

Chiral measurements in the electric-dipole approximation

vorgelegt von
M. Sc.
Andrés Felipe Ordóñez Lasso
ORCID: 0000-0001-5274-4413

von der Fakultät II – Mathematik und Naturwissenschaften
der Technischen Universität Berlin
zur Erlangung des akademischen Grades

Doktor der Naturwissenschaften
Dr. rer. nat.

genehmigte Dissertation

Promotionsausschuss:

Vorsitzender: Prof. Dr. Andreas Knorr

Gutachterin: Prof. Dr. Olga Smirnova

Gutachterin: Prof. Dr. Christiane Koch

Gutachter: Prof. Dr. Thomas Baumert

Tag der wissenschaftlichen Aussprache: 29.11.2019

Berlin 2020

This thesis is dedicated to my father, who 14 years ago suggested me to consult a physics book.

Abstract

In this thesis, we present a unified perspective on chiral measurements in the electric-dipole approximation spanning rotational, vibrational, and electronic dynamics, taking place in bound states and in unbound continuum states, and covering a wide range of experimental configurations with light sources ranging from microwaves to synchrotron radiation to state-of-the-art noncollinearly propagating multifrequency femtosecond laser pulses. In all of these situations molecular handedness is imprinted either on the photoelectrons or on the photons emitted by the chiral sample. We develop a theoretical description which not only reveals but also highlights the physical features that all of these effects share. Our description encompasses established as well as several new techniques.

Starting from our investigation of one-photon photoelectron circular dichroism, which provides elementary instances of chiral wavefunctions that revealed insightful mechanisms for the emergence of the forward-backward asymmetry in the photoelectron angular distribution, we move on to pump probe schemes which reveal that the spin of the pump photon can be stored in the molecule and then read out at a later time in the photoelectron angular distribution resulting from photoionization by linearly or unpolarized probe photons. We then address the role of the detector in defining the chirality of the setup, and how it allows enantiosensitive detection in the absence of chiral light. Taking this into account we develop the basis for the unifying framework mentioned above and derive new equations for several chiral effects. In the case of photoionization the new description allows a deeper understanding of photoelectron circular dichroism and reveals its connections to Berry-curvature-related effects.

We realize that we can take advantage of the time dependence of the electric field to produce electric fields chiral within the electric-dipole approximation, which unlocks the full potential of light to control the enantiosensitive response of chiral matter, and present the theory to characterize and manipulate these fields at the microscopic and macroscopic scale.

Zusammenfassung

In dieser Arbeit präsentieren wir eine einheitliche Perspektive auf chirale Messungen in der elektrischen Dipolnäherung, die Rotations-, Schwingungs- und elektronische Dynamiken umfasst, die in gebundenen Zuständen und in ungebundenen Kontinuumszuständen stattfinden, und eine große Bandbreite experimenteller Konfigurationen mit Lichtquellen abdeckt, die von Mikrowellen über Synchrotronstrahlung bis hin zu modernsten sich nicht kollinear ausbreitenden Multifrequenz-Femtosekundenlaserpulsen reichen. In all diesen Situationen wird die molekulare Händigkeit entweder auf die Photoelektronen oder auf die von der chiralen Probe emittierten Photonen aufgeprägt. Wir entwickeln eine theoretische Beschreibung, die die physikalischen Eigenschaften nicht nur offenbart, sondern auch hervorhebt, die alle diese Effekte miteinander teilen. Unsere Beschreibung umfasst sowohl etablierte als auch mehrere neue Techniken.

Ausgehend von unserer Untersuchung des Ein-Photonen Photoelektronen-Zirkulardichroismus, die elementare Beispiele chiraler Wellenfunktionen liefert, welche wiederum aufschlussreiche Mechanismen für die Entstehung der Vorwärts-Rückwärts-Asymmetrie in der Photoelektronen-Winkelverteilung aufdecken, gehen wir zu Pump-Probe Anordnungen über, die zeigen, dass der Spin des Pump-Photons im Molekül gespeichert und zu einem späteren Zeitpunkt in der Photoelektronen-Winkelverteilung, die sich aus der Photoionisierung durch linear- oder unpolarisierte Probe-Photonen ergibt, ausgelesen werden kann. Wir befassen uns dann mit der Rolle des Detektors bei der Definition der Chiralität des Aufbaus und wie er den enantiosensitiven Nachweis in Abwesenheit von chiralem Licht ermöglicht. Unter Berücksichtigung dessen entwickeln wir die Grundlage für den oben genannten einheitlichen Rahmen und leiten neue Gleichungen für mehrere chirale Effekte ab. Im Falle der Photoionisation ermöglicht die neue Beschreibung ein tieferes Verständnis des Photoelektronen-Zirkulardichroismus und zeigt seine Verbindungen zu Berry-Krümmungsverwandten Effekten auf.

Wir erkennen, dass wir die Zeitabhängigkeit des elektrischen Feldes nutzen können, um elektrische Felder zu erzeugen, die innerhalb der elektrischen Dipolnäherung chiral sind, was das volle Potenzial des Lichts freisetzt, um die enantiosensitive Reaktion chiraler Materie zu kontrollieren, und stellen die Theorie zur Charakterisierung und Manipulation dieser Felder auf mikroskopischer und makroskopischer Skala vor.

Publications

This cumulative thesis is based on the following publications:

- Andres F. Ordonez and Olga Smirnova. Propensity rules in photoelectron circular dichroism in chiral molecules. I. Chiral hydrogen. **Physical Review A** **99**, 043416 (2019). DOI: [10.1103/PhysRevA.99.043416](https://doi.org/10.1103/PhysRevA.99.043416)
- S. Beaulieu, A. Comby, D. Descamps, B. Fabre, G. A. Garcia, R. Généaux, A. G. Harvey, F. Légaré, Z. Mašín, L. Nahon, A. F. Ordonez, S. Petit, B. Pons, Y. Mairesse, O. Smirnova, and V. Blanchet. Photoexcitation circular dichroism in chiral molecules. **Nature Physics** **14**, 484489 (2018). DOI: [10.1038/s41567-017-0038-z](https://doi.org/10.1038/s41567-017-0038-z)
- Andres F. Ordonez and Olga Smirnova. Generalized perspective on chiral measurements without magnetic interactions. **Physical Review A** **98**, 063428 (2018). DOI: [10.1103/PhysRevA.98.063428](https://doi.org/10.1103/PhysRevA.98.063428)
- Andres F. Ordonez and Olga Smirnova. Propensity rules in photoelectron circular dichroism in chiral molecules. II. General picture. **Physical Review A** **99**, 043417 (2019). DOI: [10.1103/PhysRevA.99.043417](https://doi.org/10.1103/PhysRevA.99.043417)
- David Ayuso, Ofer Neufeld, Andres F. Ordonez, Piero Decleva, Gavriel Lerner, Oren Cohen, Misha Ivanov, and Olga Smirnova. Synthetic chiral light for efficient control of chiral light matter interaction. **Nature Photonics** **13**, 866 (2019). DOI: [10.1038/s41566-019-0531-2](https://doi.org/10.1038/s41566-019-0531-2)

The accepted version of these papers can be found in Sections 4.1 - 4.5 respectively.

Acknowledgments

I acknowledge support from the MEDEA project, which has received funding from the European Union's Horizon 2020 research and innovation programme under the Marie Skłodowska-Curie grant agreement No 641789. I acknowledge support from the DFG SPP 1840 "Quantum Dynamics in Tailored Intense Fields" and DFG grant SM 292/5-2.

I would like to thank my supervisor Olga Smirnova for guiding me through these exhilarating last four years. Besides your immense contribution to this work, your contribution to my growth as a physicist is absolutely invaluable. You are a true Doktormutter and it's been an honor and a pleasure to be your PhD student.

I am grateful to all the excellent scientists that took part in one way or another in the publications presented here, especially to David Ayuso and Misha Ivanov, with whom it's been a pleasure to collaborate in our latest paper. I am also very grateful to Misha Ivanov for his comments during the course of this thesis and for his helpfulness as director of the theory department of the Max-Born-Institut.

I thank my friends in the Max-Born-Institut for the great working environment they create. In particular Felipe Morales, Serguei Patchkovskii, and Sergey Solovov for all their support, advice, and company. I am very grateful to Maria Richter among other things for making sure I have a perfectly written Zusammenfassung.

Last but not least I would like to thank my family who has always supported me in all possible ways. I am especially grateful to my wife for filling my life with love and happiness during every stage of this work.

Contents

1	Introduction	1
1.1	Chirality: a symmetric asymmetry	1
1.2	The interaction between light and chiral molecules	3
1.3	Chiral effects in the electric-dipole approximation	9
1.3.1	Enantiosensitive photon emission	9
1.3.2	Enantiosensitive photoelectron emission	16
2	Summary of publications	21
2.1	Propensity rules in photoelectron circular dichroism in chiral molecules. I. Chiral hydrogen	21
2.2	Photoexcitation circular dichroism in chiral molecules	23
2.3	Generalized perspective on chiral measurements without magnetic interactions	24
2.4	Propensity rules in photoelectron circular dichroism in chiral molecules. II. General picture	27
2.5	Synthetic chiral light for efficient control of chiral light matter interaction	28
3	Conclusions and outlook	29
	References	31
4	Publications	37
4.1	Propensity rules in photoelectron circular dichroism in chiral molecules. I. Chiral hydrogen	37
4.2	Photoexcitation circular dichroism in chiral molecules	51
4.3	Generalized perspective on chiral measurements without magnetic interactions	99
4.4	Propensity rules in photoelectron circular dichroism in chiral molecules II. General picture	121
4.5	Synthetic chiral light for efficient control of chiral light matter interaction	135

List of abbreviations

ATI: Above-threshold ionization.

CD: Circular dichroism.

CPL: Circularly polarized light.

DFG: Difference frequency generation.

FID: Free induction decay.

HHG: High-harmonic generation.

LCP: Left circularly polarized.

OA: Optical activity.

PAD: Photoelectron angular distribution.

PECD: Photoelectron circular dichroism.

RCP: Right circularly polarized.

REMPI: Resonantly-enhanced multiphoton ionization.

SFG: Sum frequency generation.

SHG: Second harmonic generation.

1 Introduction

This introduction aims to provide the reader with the fundamental background necessary to understand and assess the publications that resulted from this thesis. At the risk of trivializing the results in these publications, I have decided to write this introduction in such a way that it incorporates from the outset the main concepts and the core of the understanding that we have achieved during the course of this thesis. Concepts such as *chiral setup* and *locally chiral light* as well as several equations describing different chiral effects will be introduced as soon as they become relevant for the discussion, regardless of the fact that they were developed only recently by us. We do this with the objective of sharing with the reader in a smooth and compact way the unified view of different chiral effects that we have achieved over the last four years. We have nevertheless tried to clearly differentiate our contribution from the contributions of others whenever necessary.

The introduction is organized as follows, first we introduce chirality and how it can be quantified. Then, we introduce the quintessential chiral effects of optical activity and circular dichroism. Afterwards, we introduce several (and mostly very recent) chiral effects taking place within the electric-dipole approximation. These we divide into a group where the observables are photons and another where the observables are photoelectrons.

1.1 Chirality: a symmetric asymmetry

Chirality (handedness) is the geometrical feature that we perceive as the difference between a left hand and a right hand. Like left and right hands, a chiral object and its mirror image (a pair of enantiomorphs) have distinct shapes. Since rotations do not affect shapes, a chiral object is usually defined as an object which cannot be transformed into its reflection (a discrete parity-inverting transformation) by a rotation (a continuous parity-conserving transformation). In other words, one cannot transform a chiral object into its mirror image without changing the relative position between its points (the shape). This particular lack of symmetry can be formulated in the language of group theory by stating that the point group of a chiral object lacks improper rotational axes. Some examples of chiral objects are shown in Fig. 1.

The handedness of an object can be quantified by pseudoscalars, that is, scalar numbers which change sign upon inversion $\vec{r} \rightarrow -\vec{r}$. Pseudoscalars usually occur as the product of a vector and a pseudovector. Pseudovectors are in turn vectors that do not change direction upon spatial inversion and usually occur as the cross product between two (polar) vectors¹. We can draw pseudovectors as curved arrows indicating a rotation (\odot or \oslash). For example, the chirality of the object in Fig. 1b, which consists of four distinguishable points forming a tetrahedron, can be characterized through the triple scalar product

$$\chi = \vec{r}_{1,0} \cdot (\vec{r}_{2,0} \times \vec{r}_{3,0}), \quad (1)$$

where $\vec{r}_{i,j} = \vec{r}_i - \vec{r}_j$ are relative positions, and \vec{r}_i with $i = 0, 1, 2, 3$ are the positions of the red, green, blue, and black points, respectively. Upon spatial inversion all position vectors transform

¹From here on we will write simply “vector” when we refer to a polar vector.

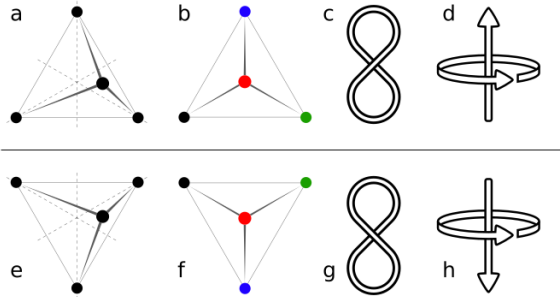


Figure 1: Examples of chiral objects: a) Four indistinguishable points forming a chiral non-regular tetrahedron. The point inside the equilateral triangle is above the plane of the page. The relative positions of the points make them distinguishable. b) Four distinguishable and non-coplanar points forming a regular tetrahedron. The red point is above the plane of the page. c) Indistinguishable points forming a three-dimensional curve. d) A combination of a vector (straight arrow) and a pseudovector (curved arrow). e) to h) show the mirror images of a) to d).

as $\vec{r}_i \rightarrow -\vec{r}_i$ so that all relative positions transform as $\vec{r}_{i,j} \rightarrow -\vec{r}_{i,j}$, the pseudovector $\vec{r}_{2,0} \times \vec{r}_{3,0}$ remains invariant, and therefore $\chi \rightarrow -\chi$. The pseudoscalar χ depends only on the relative positions between the points and is fully independent of the reference frame, which is exactly what we expect from a property that depends only on the shape of the object and neither on its position nor orientation. Furthermore, since $|\chi|$ is proportional to the volume of the tetrahedron, it vanishes when the three vectors are coplanar, which appropriately reflects the lack of chirality in that case. Note that the definition of right handedness and left handedness or of positive and negative χ is arbitrary.

In physics, chirality plays a very prominent role in at least two scenarios: when dealing with the weak force² and when dealing with chiral molecules. In the latter case, which is the only one we will treat here, the positions of the nuclei form stable³ chiral structures of either handedness (pairs of enantiomers) as for example those shown in Fig. 2. As a consequence of the parity symmetry of the electromagnetic interaction holding the molecule together, opposite enantiomers share the same energy spectrum⁴, which in practice makes their distinction and separation considerably more involved than otherwise. A guiding principle in the study of enantiomeric recognition is that

$$\textit{two opposite enantiomorphs behave differently only when} \\ \textit{they are probed by a third chiral object} \quad (2)$$

²The weak interaction is the only fundamental interaction that is not parity symmetric [1]. This striking violation of symmetry implies that there are phenomena that occur in nature but whose mirror image does not occur in nature!

³Like in the nitrogen inversion occurring in ammonia, the nuclear configurations of two opposite enantiomers correspond to degenerate potential energy minima separated by a potential energy barrier. In many chiral molecules the barrier can be such that the enantiomers can be considered stable for all practical purposes.

⁴Extremely tiny energy differences due to the weak interaction have been predicted but they have not been observed so far (see Sec. 8 in Ref. [2] and references therein).

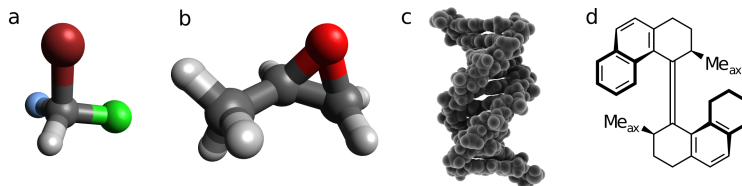


Figure 2: Examples of chiral molecules: a) Bromochlorofluoromethane CHBrClF , one of the simplest chiral molecules b) Propylene oxide $\text{CH}_3\text{CHCH}_2\text{O}$, the first chiral molecule detected in the interstellar medium [7]. c) DNA [8] d) A synthetic molecular rotary motor [9].

i.e., given two opposite enantiomers L and R , and a chiral probe L' , the interaction between L and L' is in principle different from that between R and L' . Whether such a difference can be readily measured is a different matter, which in general depends on the situation at hand.

Chiral molecules are not only very abundant in nature, but they also play a very important role in living organisms, where puzzling enough, they always show up with the same handedness. For example, the essential amino acid phenylalanine, which is a precursor of the neurotransmitters dopamine (pleasure), noradrenaline, and adrenaline (fight or flight), is always left handed. This marked asymmetry between the occurrence of the left and right versions of biological molecules is known as homochirality and, although several hypotheses have been proposed (see e.g. Ref. [3] and references therein), its origin remains an open question. Regardless of how it came about, homochirality has very important practical consequences for us (living beings) because the enantiopurity of our bodies makes us automatically enantiosensitive, that is, our bodies, or more specifically, our biological receptors, react differently when exposed to either left or right versions of a given external molecule. In some cases such difference can be rather manifest and appear as a difference in taste [4], smell [5], or pharmacological activity [6].

Now, instead of the interaction between chiral molecules with other chiral molecules, we will discuss the interaction between chiral molecules and electromagnetic fields.

1.2 The interaction between light and chiral molecules

The beginnings of the study of molecular chirality are intimately related with the development of the wave theory of light and in particular with the realization that light is a transverse wave that can be polarized⁵. As monochromatic linearly polarized light traverses a chiral medium, its plane of polarization rotates around the axis of propagation as shown in Fig. 3. In this phenomenon, known as optical rotation or optical activity (OA) [10, 12, 13], the rotation of the plane of polarization is a manifestation of the breaking of inversion symmetry due to the chirality of the medium. According to the parity symmetry of the electromagnetic interaction, which is the only relevant interaction in this case, if a phenomenon is possible then its mirror image is equally possible. For OA this means that if the plane of polarization rotates by an angle θ in one

⁵For a historical review see Refs. [10] and [11].

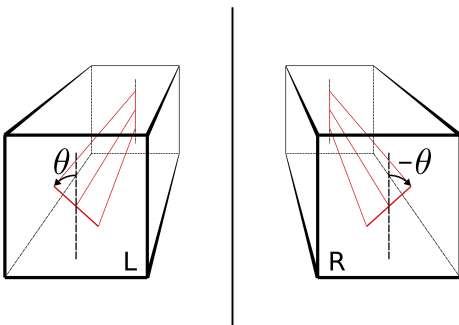


Figure 3: Optical activity: rotation of the plane of polarization of linearly polarized light (shown in red) as it propagates across either a left- (L) or a right-handed (R) medium. The systems are mirror images of each other.

$$\begin{array}{c} \vec{E} \uparrow \\ \text{L} + \odot \vec{k} = \curvearrowright \vec{\theta} \\ \vec{E} \downarrow \end{array} \quad \Bigg| \quad \begin{array}{c} \vec{E} \uparrow \\ \text{R} + \odot \vec{k} = \curvearrowleft \vec{\theta} \\ \vec{E} \downarrow \end{array}$$

Figure 4: Symmetry of optical activity. An isotropic chiral molecular sample L interacts with a linearly polarized electric field \vec{E} with wave vector \vec{k} (coming out of the page) and as a result of this interaction the electric field is rotated by an angle $\vec{\theta}$ (a pseudovector). A reflection in the plane defined by \vec{E} and \vec{k} changes the handedness from L to R, leaves \vec{E} and \vec{k} unaffected, and reverses the rotation $\vec{\theta}$.

enantiomer, it must rotate by an angle $-\theta$ in the opposite enantiomer, so that both situations are indeed mirror images of each other (see Fig. 3). In general, if the behavior of one enantiomer is known, one must only take a mirror image of the whole system to figure out the behavior of the opposite enantiomer. Figure 4 shows a simplified scheme of OA in terms of “reactants” and “product”, where the reactants are the chiral medium and the monochromatic linearly polarized light, and the product is the rotation by which the plane of polarization is rotated. Later we will be more careful regarding the role of light as a “reactant”.

To understand better the role of molecular chirality in OA, Fig. 5 shows how the absence of chirality leads to reflection symmetry of the whole system, which precludes optical rotation. In addition, Fig. 5 also shows that OA can occur only when the wave vector \vec{k} is taken into account. In a monochromatic plane wave, \vec{k} encodes the propagation direction in the spatial dependence $e^{i\vec{k}\cdot\vec{r}}$ of the field. This is very important because in many cases the wavelength of the radiation is very large compared to the molecular size and therefore the effects of taking the spatial dependence of the field into account are rather small at the single-molecule level ($e^{i\vec{k}\cdot\vec{r}} \approx 1$). In such cases the observation of OA requires the light to interact with many molecules in order for the small single-molecule effect to accumulate into a readily measurable signal.

As originally recognized by Fresnel, by decomposing linearly polarized light into a coherent superposition of left and right circularly polarized light (CPL), OA can be understood as resulting from a difference in the phase velocities for each helicity of the CPL in the given chiral medium

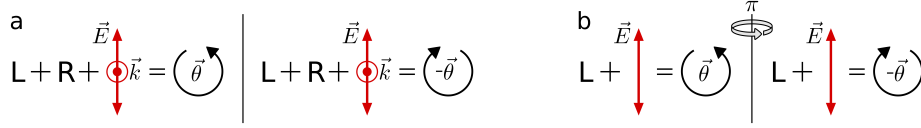


Figure 5: **a)** If we assume that as a result of the interaction between an isotropic achiral medium (L+R) and a linearly polarized field (\vec{E}, \vec{k}) we obtain an angle of rotation $\vec{\theta}$, then reflection across the plane of polarization yields the same “reactants” but an opposite angle of rotation, which can only be true when $\theta = 0$. In other words, the reflection symmetry of the “reactants” with respect to the plane of polarization rules out any pseudovector observable in that plane. **b)** If we assume that as a result of the interaction between an isotropic chiral medium (L) and a \vec{k} -independent (e.g. a standing wave or a field in the electric-dipole approximation) linearly polarized field \vec{E} we obtain an angle of rotation $\vec{\theta}$, then rotation by π around the polarization axis yields the same “reactants” but an opposite angle of rotation, which can only be true when $\theta = 0$. In other words, the rotation symmetry of the “reactants” around \vec{E} rules out any vector or pseudovector observable in the plane perpendicular to \vec{E} .

(see e.g. Ref. [10] and page 19 in Ref. [11]). Such difference is a manifestation of the chirality of CPL, which is encoded in the handedness of the helix formed by circularly polarized light in space (see Fig. 6). The handedness of CPL (a pseudoscalar) is given by the projection of the photon’s spin (i.e. the pseudovector indicating the direction of rotation of the CPL) on the propagation direction \hat{k} (a vector). The chirality of the CPL also implies that for wavelengths in the vicinity of an absorption band of a chiral molecule⁶, left and right CPL is absorbed by different amounts in a given enantiomer, which is known as circular dichroism (CD)⁷ [10, 12, 13]. In this case, there are four possible combinations of molecular handedness and CPL handedness [(R, R), (R, L), (L, R), (L, L)], however, since absorption is a scalar (i.e. a number which does not change sign upon inversion), the parity symmetry of the electromagnetic interaction implies that $A(R, R) = A(L, L)$ and $A(R, L) = A(L, R)$, where A is the amount of absorption, the first argument is the molecular handedness, and the second argument is the CPL handedness. Since the propagation direction \vec{k} is required to define the CPL handedness, the emergence of CD requires taking into account the spatial dependence of the field (which enters together with \vec{k} as $e^{i\vec{k}\cdot\vec{r}}$), and like OA, it is also a very small effect when the wavelength is much larger than the molecular dimensions.

To formalize a little bit what we have just stated, let’s consider the potential energy V describing the interaction of a system of charges with an electromagnetic field. A multipolar expansion of the electric and magnetic fields yields [10]

$$V(t) = q\phi(0, t) - \vec{d} \cdot \vec{E}(0, t) - \vec{m} \cdot \vec{B}(0, t) - \frac{1}{3} \vec{\nabla} \cdot [Q\vec{E}(\vec{r}, t)] \Big|_{\vec{r}=0} + \dots, \quad (3)$$

where q (scalar), \vec{d} (vector), \vec{m} (pseudovector), and Q (2nd rank tensor) are the monopole, electric dipole, magnetic dipole, and electric quadrupole of the charge distribution, respectively,

⁶Remember that both molecular enantiomers share the same spectrum.

⁷Although the word *dichroism* literally stands for two different photon energies (colors), circular dichroism refers to the difference in absorption between left and right CPL at the same photon energy.

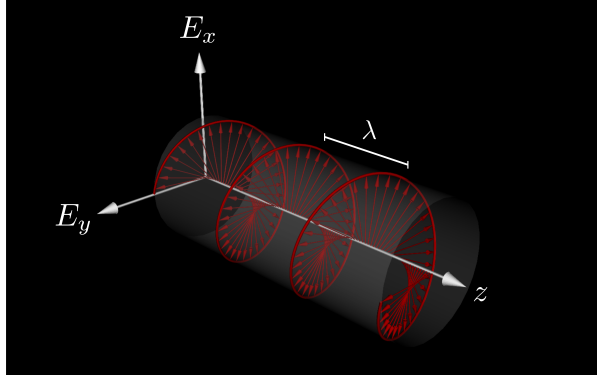


Figure 6: Circularly polarized light propagating in the z direction forms a helix in (E_x, E_y, z) space. Its helicity (handedness) is given by the scalar product between the rotation direction pseudovector (photon's spin) and the propagation direction. Its characteristic scale is given by the wavelength.

and $\phi(\vec{r}, t)$, $A(\vec{r}, t)$, $\vec{E}(\vec{r}, t) = -\vec{\nabla}\phi - \partial_t \vec{A}(\vec{r}, t)$, and $\vec{B}(\vec{r}, t) = \vec{\nabla} \times \vec{A}(\vec{r}, t)$ are the scalar potential, vector potential, electric field, and magnetic field, respectively. To get a feeling for the relative magnitude of the different terms consider a particle with charge q , distance to the origin r_0 , and speed v_0 interacting with a plane wave $\vec{E} = \vec{E}_0 e^{i(\vec{k}\cdot\vec{r} - \omega t)} + \text{c.c.}$ A crude classical approximation yields $|\vec{d} \cdot \vec{E}| \sim |qr_0 E_0|$, $|\vec{m} \cdot \vec{B}| \sim |qr_0 \frac{v_0}{c} E_0|$, and $|\vec{\nabla} \cdot Q\vec{E}|_{\vec{r}=0} = |qr_0^2 k E_0|$, and therefore

$$\frac{|\vec{m} \cdot \vec{B}|}{|\vec{d} \cdot \vec{E}|} \sim \frac{v_0}{c}, \quad \frac{|\vec{\nabla} \cdot [Q\vec{E}(\vec{r}, t)]|}{|\vec{d} \cdot \vec{E}|} \sim \frac{r_0}{\lambda}, \quad (4)$$

where $\lambda = 2\pi/k$ is the wavelength and c is the speed of light. This shows that, at least for classical charges which move at speeds well below the speed of light and for wavelengths far bigger than the characteristic scale of the charge distribution, the electric-dipole interaction clearly dominates over the magnetic-dipole and electric-quadrupole interactions. Quantum mechanically this is also the case, except for particular situations such as when selection rules forbid the electric-dipole transition. Note also that, since for a plane wave $\omega\vec{B} = \vec{k} \times \vec{E}$, a theoretical description including both electric- and magnetic-dipole interactions implicitly includes \vec{k} as well.

As discussed above, already from symmetry arguments it is clear that OA and CD require taking the wave vector \vec{k} into account. Formally, this corresponds to taking the magnetic dipole and the electric quadrupole terms in Eq. (3) into account. For the case of CD, one needs to consider only the interaction of a chiral molecule initially in the ground state with light resonant with a transition between the ground state $|g\rangle$ and an excited state $|e\rangle$. The probability amplitude of the excited state then contains contributions from the electric-dipole, magnetic-dipole, and electric-quadrupole terms (the latter we do not write explicitly)

$$a_e = -\vec{d}_{eg} \cdot \vec{\mathcal{E}} - \vec{m}_{eg} \cdot \vec{\mathcal{B}} - \dots, \quad (5)$$

where $\vec{d}_{eg} = \langle e|\vec{d}|g\rangle$, $\vec{m}_{eg} = \langle e|\vec{m}|g\rangle$, $\vec{E}(0, t) = \vec{\mathcal{E}}e^{-i\omega t} + \text{c.c.}$, $\vec{B}(0, t) = \vec{\mathcal{B}}e^{-i\omega t} + \text{c.c.}$ The lowest order terms contributing to the population of the excited state $|a_e\rangle^2$ correspond to the direct electric-dipole, the interference between electric-dipole and magnetic-dipole, and the interference between the electric-dipole and the electric-quadrupole (the latter we do not write explicitly)

$$|a_e|^2 = |\vec{d}_{eg} \cdot \vec{\mathcal{E}}|^2 + 2\text{Re} \left\{ (\vec{d}_{eg} \cdot \vec{\mathcal{E}})^* (\vec{m}_{eg} \cdot \vec{\mathcal{B}}) \right\} + \dots, \quad (6)$$

which after orientation averaging over all molecular orientations (denoted by ϱ) becomes⁸

$$\int d\varrho |a_e|^2 = \frac{1}{3} |\vec{d}_{eg}|^2 |\vec{\mathcal{E}}|^2 + \frac{2}{3} \text{Re} \left\{ (\vec{d}_{eg}^* \cdot \vec{m}_{eg}) (\vec{\mathcal{E}}^* \cdot \vec{\mathcal{B}}) \right\} + \dots \quad (7)$$

The interference term between the electric-dipole and the electric-quadrupole vanishes exactly after orientation averaging. Note that the interference term (scalar) is the product of a rotationally-invariant⁹ molecular pseudoscalar ($\vec{d}_{eg}^* \cdot \vec{m}_{eg}$) and a field pseudoscalar ($\vec{\mathcal{E}}^* \cdot \vec{\mathcal{B}}$), therefore it changes sign for either opposite enantiomers or opposite helicities of the light and is zero when the molecule is achiral or the field is achiral (e.g. linearly polarized). In fact, since we can represent the unperturbed states $|g\rangle$ and $|e\rangle$ by real wavefunctions, \vec{d}_{eg} is a real vector and $\vec{m}_{eg} \equiv i\vec{m}'_{eg}$ is a purely imaginary vector, and since $c\vec{\mathcal{B}} = \hat{k} \times \vec{\mathcal{E}}$, then we can write

$$\int d\varrho |a_e|^2 = \frac{1}{3} |\vec{d}_{eg}|^2 |\vec{\mathcal{E}}|^2 + \frac{2}{3c} (\vec{d}_{eg} \cdot \vec{m}'_{eg}) \left[\hat{k} \cdot (i\vec{\mathcal{E}} \times \vec{\mathcal{E}}^*) \right], \quad (8)$$

where $\hat{k} = \vec{k}/k$ is the propagation direction and $i\vec{\mathcal{E}} \times \vec{\mathcal{E}}^*$ is a real vector parallel to the photon's spin¹⁰. The population of the excited state and therefore the light absorption will be modulated by an interference term which is the product of the molecular handedness and the electromagnetic field handedness (helicity). The molecular handedness in Eq. (8) is defined by the sign of $\vec{d}_{eg} \cdot \vec{m}'_{eg}$ and for a different pair of states this sign can be different. This reflects the fact that a sufficiently complex object can have several parts, each with its own handedness. A basic example is shown in Fig. 7. Quantum mechanical examples are discussed in Sec. IV of Ref. [16] (see Sec. 4.3). Of course, which handedness we probe depends on how we probe the object. In the case of chiral molecules, there is an infinite number of ways of combining the transition dipoles between all the available states to form pseudoscalars, and therefore an infinite number of handedness can be associated with a single molecule. We will see some examples of these possible pseudoscalars below. Circularly polarized light resonant with a given transition allows us to probe exactly one of these handedness. The interference term in Eq. (8) is the mathematical manifestation of the fundamental statement (2). Equation (8) mathematically expresses how the result of an interaction between two chiral objects depends on their relative handedness.

⁸See Ref. [14] to learn how to do orientation averaging analytically and our work [15] (see Secs. 2.3 and 4.3 here) for several applications relevant to chirality.

⁹Scalar or vector products between two vectors are independent of the frame of reference. In isotropic samples, such rotational invariants are the only molecular properties that survive orientation averaging.

¹⁰For circular polarization in the xy plane $\vec{\mathcal{E}} = \mathcal{E}(\hat{x} \pm i\hat{y})/\sqrt{2}$, which yields $i\vec{\mathcal{E}} \times \vec{\mathcal{E}}^* = \pm\hat{z}$.

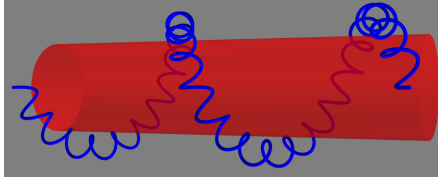


Figure 7: An object displaying two independent handedness: a helix made of a more tightly bound helix.

At this point, and in the light of statement (2) one might find it paradoxical that in OA, linearly polarized light, which is evidently not chiral¹¹, can be used to probe the handedness of a molecular sample. While in CD the chirality of the probe is evidently encoded in the helicity of the circularly polarized light, in OA the chirality of the probe relies on taking into account not only the light but also the configuration of the detector measuring the rotation angle. In contrast to an absorption measurement where the output is always positive (slightly bigger for one enantiomer than for the other), in an angle measurement the output can be either positive or negative. In particular, the experimenter must arbitrarily define what rotation direction is positive and what rotation direction is negative. By doing this, the experimenter establishes a reference pseudovector $\hat{\theta}_{\text{ref}}$ that allows the angles to be written as $\vec{\theta} = \theta \hat{\theta}_{\text{ref}}$ and determines whether θ (a scalar) is positive or negative. Analogously to how in CD the handedness of the probe was given by the projection of \hat{k} (vector) on the photon's spin $i\vec{\mathcal{E}} \times \vec{\mathcal{E}}^*$ (pseudovector), in OA the handedness of the probe will be given by the projection of \hat{k} on $\hat{\theta}_{\text{ref}}$. That is, instead of having chiral light we have a *chiral setup* (see Fig. 8) acting as the chiral probe. Although the arbitrariness of choosing $\hat{\theta}_{\text{ref}}$ looks somewhat artificial, the same arbitrariness takes place when in a CD spectrum, which only shows the difference between absorption of right-circularly-polarized light (RCP) and left-circularly-polarized (LCP) light [the interference term in Eq. (8)], the experimenter defines if he is going to subtract the RCP spectrum from the LCP spectrum or vice versa. Formally, by using the potential energy in Eq. (3), a semiclassical description of the light-matter interaction, and first order perturbation theory, one can show that the induced polarization in the isotropic sample has a term proportional to the time derivative of $\vec{B}(0, t)$ and the induced magnetization has a term proportional to the time derivative of $\vec{E}(0, t)$. The resulting constitutive relations in Maxwell's equations lead to an angle of rotation per unit length given by an expression of the form [12]¹²

$$\theta = C \sum_i \left(\frac{1}{\omega_{ig}^2 - \omega^2} \right) (\vec{d}_{gi} \cdot \vec{m}'_{ig}) (\hat{k} \cdot \hat{\theta}_{\text{ref}}) \quad (9)$$

where C is a (scalar) constant which depends on the wavelength of the incoming light and the density of the medium, and the sum is over all states $|i\rangle$. The quantity θ is the product of a molecular pseudoscalar $\sum_i (\vec{d}_{gi} \cdot \vec{m}'_{ig}) / (\omega_{ig}^2 - \omega^2)$ and a *setup* pseudoscalar $(\hat{k} \cdot \hat{\theta}_{\text{ref}})$. This shows

¹¹The electromagnetic field of a linearly polarized wave $\{\vec{E}(\vec{r}, t), \vec{B}(\vec{r}, t)\}$ is symmetric with respect to reflections in the plane perpendicular to $\vec{B}(\vec{r}, t)$. \vec{E} is contained in that plane and \vec{B} is a pseudovector which is invariant under such reflection.

¹²Use equations 22, 55, 56 β in Ref. [12], and then take into account that in Ref. [12] it is assumed (as is usual) that $\hat{\theta}_{\text{ref}}$ points in the same direction as \hat{k} . Note however that $\hat{\theta}_{\text{ref}}$ is a pseudovector arbitrarily defined while \hat{k} is a vector with a fixed physical meaning.

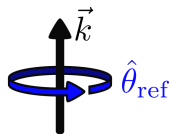


Figure 8: Chiral setup in optical activity. \vec{k} is the propagation direction of the light and $\hat{\theta}_{\text{ref}}$ is the rotation direction defined as positive.

how, by helping to form a *chiral setup*, the detection scheme can allow chiral discrimination of an isotropic sample in the absence of chiral light. Although at the time we did not consider OA, we have discussed chiral setups and their role in the absence of chiral light in Ref. [15] (see Secs. 2.3 and 4.3 here). There we focused on vector observables as opposed to pseudovector observables such as $\vec{\theta}$, but the idea is essentially the same.

1.3 Chiral effects in the electric-dipole approximation

As illustrated in the previous section, both optical activity (OA) and circular dichroism (CD) rely on the wave vector \vec{k} , which is encoded in the spatial dependence $e^{i\vec{k}\cdot\vec{r}}$ of the propagating wave. OA and CD are therefore usually small effects whenever the wavelength is much greater than the molecular dimensions. To bypass such limitation it is desirable to find chiral effects which do not rely on the spatial dependence of the light, that is, effects which do occur even in the limit where $e^{i\vec{k}\cdot\vec{r}} = 1$, i.e. in the so-called electric-dipole approximation where terms beyond the electric monopole and electric dipole in Eq. (3) are neglected. The first of these effects was predicted by Giordmaine in the context of nonlinear optics [17] and the second by Ritchie in the context of photoionization [18]. The essence of both effects is that, analogously to OA, the breaking of reflection symmetry caused by the presence of the chiral medium allows for a response which is perpendicular to the plane of polarization of the incident radiation, and is directed in opposite directions for opposite enantiomers.

For the readers familiar with the “coupled-oscillator model” used to model CD and OA in large molecules made of two groups (see e.g. Ref. [19]), it must be remarked that although this model uses the electric-dipole approximation for each group in the chromophore, the electric field at the position of each group is different, and therefore the model explicitly takes into account the variation of the electric field in space. That is, the model describes the interaction between the molecule and the light beyond the electric-dipole approximation.

1.3.1 Enantiosensitive photon emission

A few years after the first observation of second-harmonic generation [20], Giordmaine realized that the processes of sum- and difference-frequency generation (SFG and DFG) could take place in an isotropic medium within the electric-dipole approximation provided the medium was chiral [17]. Specifically, he found that, *after orientation averaging* (see e.g. Refs. [14, 15] and Sec. 4.3), the second order polarization at the sum frequency takes the form¹³

¹³For an introduction to nonlinear optics see e.g. Ref. [21].

$$\vec{P}^{(2)}(\omega_1 + \omega_2) = \chi^{(2)} \left[\vec{\mathcal{E}}(\omega_1) \times \vec{\mathcal{E}}(\omega_2) \right] \quad (10)$$

where $\vec{P}^{(2)}(\omega)$ is the Fourier amplitude of the second-order polarization at the frequency ω , $\vec{\mathcal{E}}(\omega)$ is the Fourier amplitude of the electric field at the frequency ω , and $\chi_+^{(2)}$ is a second-order susceptibility-like term for sum-frequency generation which contains a sum of expressions involving terms of the form $\vec{d}_{gm} \cdot (\vec{d}_{mk} \times \vec{d}_{kg})$ [cf. Eqs. (8) and (9)], where $\vec{d}_{ij} \equiv \langle i | \vec{d} | j \rangle$, \vec{d} is the electric-dipole vector operator [see Eq. (3)], $|g\rangle$ is the ground state, and $|m\rangle$ and $|k\rangle$ are excited states which are summed over. Since both the electric field and the polarization are vectors, $\vec{\mathcal{E}}(\omega_1) \times \vec{\mathcal{E}}(\omega_2)$ is a pseudovector and $\chi_+^{(2)}$ is a *pseudoscalar* (i.e. $\chi_{+,R}^{(2)} = -\chi_{+,L}^{(2)}$) encoding the response of the medium [cf. Eq. (9)]. Furthermore, since Eq. (10) has been already averaged over all possible molecular orientations, then $\chi_+^{(2)}$ contains only *molecular information which is reference-frame independent* (i.e. rotationally invariant). In short, $\chi_+^{(2)}$ encodes the handedness of the medium. We can also see in Eq. (10) that $\vec{P}^{(2)}(\omega_1 + \omega_2)$ is perpendicular to $\vec{\mathcal{E}}(\omega_1)$ and $\vec{\mathcal{E}}(\omega_2)$ and has opposite signs for left and right enantiomers, i.e. $\vec{P}^{(2)}(\omega_1 + \omega_2)$ is enantiosensitive. In the time domain this means that the induced polarization at the sum frequency in one enantiomer is delayed by π with respect to the other enantiomer. Figure 9 shows the total incident field and the sum frequency polarization for a specific incident field. In this figure we can clearly see how the π phase difference between $\vec{P}_L^{(2)}(\omega_1 + \omega_2)$ and $\vec{P}_R^{(2)}(\omega_1 + \omega_2)$ follows from applying a mirror reflection of the whole system across the plane defined by the incident fields. An analogous reasoning can be made for difference-frequency generation. Importantly, the enantiosensitive information is encoded in the phase of the induced polarization but not in its intensity. This means that an intensity measurement is able to distinguish a chiral medium from an achiral medium, but it is not able to distinguish left enantiomers from right enantiomers.

As we discuss in Ref. [15] (see Secs. 2.3 and 4.3 here), enantiosensitive effects which rely on observing a vector (as opposed to a scalar) and which occur in the absence of a chiral field rely on a *chiral setup* consisting of the electric field and the detection scheme together. The enantiosensitive polarization in Eq. (10) is one of these effects. In comparison to Eq. (9), we see that in Eq. (10) we have not yet projected the observable on a reference vector \vec{v}_{ref} defined in the laboratory frame. Such projection would yield a scalar number $P^{(2)}(\omega_1 + \omega_2)$ which is the product of the molecular handedness and the chiral setup handedness. For the moment we will however leave Eq. (10) as it is to emphasize the vector character of the observable and refer the reader to Ref. [15] (see Secs. 2.3 and 4.3 here).

The chiral/achiral distinction via sum frequency generation was experimentally confirmed shortly afterwards by Rentzepis et al. [22]¹⁴, however, the interpretation of Rentzepis' experiment has been challenged by recent numerical and experimental works [23] according to which the magnitude of the effect is, although readily measurable [24, 25], considerably smaller than originally thought.

¹⁴An important point in these experiments is that in order for the induced polarization of the molecules to add constructively a condition known as phase matching must be satisfied [21]. Phase matching requires that $\vec{k}_+ = \vec{k}_1 + \vec{k}_2$, where \vec{k}_1 , \vec{k}_2 , and \vec{k}_+ are the wave vectors of the waves with frequencies ω_1 , ω_2 , and $\omega_1 + \omega_2$, respectively. The longer the length across which the sum generation occurs, the more precisely this condition must be satisfied. This is the reason why the sum frequency experiments take place with non-collinear beam geometries.

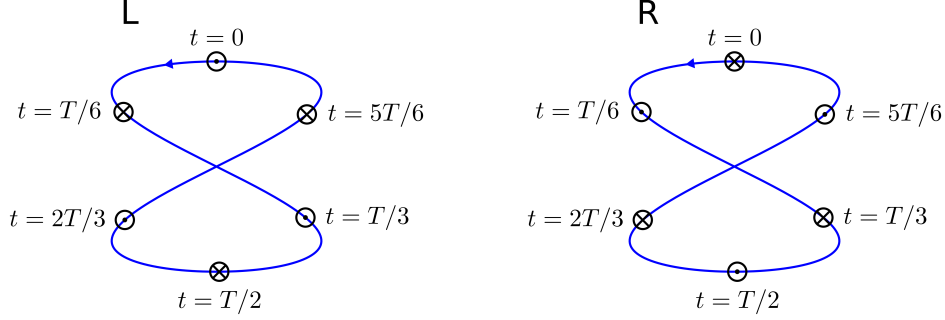


Figure 9: Second order induced polarization at the sum frequency in left and right enantiomers. The blue line indicates the Lissajous figure of the total incident field $\vec{E}(t) = \cos(2\omega t + \pi/2)\hat{x} + \cos(\omega t)\hat{y}$, and the symbols \odot and \otimes indicate the second order induced polarization at the sum frequency 3ω pointing out of and into the page, respectively, at intervals of $1/6$ of the fundamental period $T = 2\pi/\omega$ (half of the period associated with the 3ω frequency). Note that the left and the right figures are mirror images of each other across the plane of the page.

An alternative direction was taken by Hicks et al. [26, 27, 28] who measured the analogues of CD and OA for second harmonic generation (SHG) in chiral monolayers. The monolayers are formed at the interface between two achiral media such as water and air. Although SHG-CD and SHG-OA vanish for isotropic samples in the electric-dipole approximation, the anisotropy of the interface imposes a certain degree of orientation¹⁵ on the chiral molecules that make up the chiral monolayer, which leads to electric-dipole-allowed SHG-CD and SHG-OA. This explains the striking values measured by Hicks et al., which are thousand times bigger than those for linear CD and OA¹⁶, which stem from interferences between electric-dipole and magnetic-dipole transitions. Although strictly valid for monolayers, the theoretical analyses of Hicks et al. [28, 27] revealed a general mechanism. They found that the induced polarization in the case of SHG-CD was of the form¹⁷

$$\vec{P}^{(2)}(2\omega) = \vec{P}_{\text{chiral}}^{(2)}(2\omega) + \vec{P}_{\text{achiral}}^{(2)}(2\omega), \quad (11)$$

where $\vec{P}_{\text{chiral}}^{(2)}$ is enantiosensitive (it has opposite signs for opposite enantiomers) and $\vec{P}_{\text{achiral}}^{(2)}$ is not enantiosensitive (it has the same sign for opposite enantiomers). Crucially, the (at first sight undesirable) presence of $\vec{P}_{\text{achiral}}^{(2)}$ leads to an intensity of the form (we drop the 2ω argument for simplicity)

$$\left| \vec{P}^{(2)} \right|^2 = \left| \vec{P}_{\text{chiral}}^{(2)} \right|^2 + \left| \vec{P}_{\text{achiral}}^{(2)} \right|^2 + 2\text{Re} \left\{ \vec{P}_{\text{chiral}}^{(2)*} \cdot \vec{P}_{\text{achiral}}^{(2)} \right\}, \quad (12)$$

¹⁵The surface has C_∞ symmetry with respect to the normal to the surface. If additional anisotropy is present then the effect takes place even for achiral molecules [29].

¹⁶A more detailed description of the great results obtained in the nonlinear response of chiral surfaces goes beyond the scope of this work.

¹⁷The actual expressions in Refs. [28, 27] are for the intensity of specific components of $\vec{P}^{(2)}(2\omega)$ in terms of the components of second order susceptibility tensors $\chi_{ijk}^{(2)}$.

where the interference term and therefore also the intensity at the second harmonic are enantiosensitive. This is in contrast to what we have in Eq. (10), where $\vec{P}^{(2)}(\omega_1 + \omega_2)$ is enantiosensitive but $|\vec{P}^{(2)}(\omega_1 + \omega_2)|^2$ is not, and it shows how an achiral (not enantiosensitive) amplitude can be used to resolve the enantiomers in intensity measurements. Like in any interference effect, the amount of modulation of the signal will depend on the relative magnitude and on the angle between $\vec{P}_{\text{chiral}}^{(2)}$ and $\vec{P}_{\text{achiral}}^{(2)}$. The enantiosensitivity in systems of uniaxially oriented chiral molecules, not necessarily in a monolayer, will display the same physics (in terms of chirality) as the monolayers.

In the light of the results of Hicks et al. [26, 27, 28] and coming back to SFG in isotropic media, Belkin et al. [24] realized that if one takes into account the effect of the magnetic-dipole and the electric-quadrupole interactions then one also obtains an expression of the form,

$$\vec{P}^{(2)}(\omega_1 + \omega_2) = \vec{P}_{\text{chiral}}^{(2)}(\omega_1 + \omega_2) + \vec{P}_{\text{achiral}}^{(2)}(\omega_1 + \omega_2), \quad (13)$$

where $\vec{P}_{\text{chiral}}^{(2)}$ is caused by the electric-dipole interaction and is given by Eq. (10) and $\vec{P}_{\text{achiral}}^{(2)}$ is caused by the magnetic-dipole and electric-quadrupole interactions. Then, they relied on the (at first sight undesirable) smallness of $\vec{P}_{\text{chiral}}^{(2)}(\omega_1 + \omega_2)$, which opportunely turns out to be (at least in some cases) of the same order of magnitude as $\vec{P}_{\text{achiral}}^{(2)}(\omega_1 + \omega_2)$, to experimentally obtain huge differences of up to $\sim 30\%$ in the intensities of SFG resulting from opposite enantiomers. One can show that the interference term will have the form¹⁸

$$2\text{Re} \left\{ \vec{P}_{\text{chiral}}^{(2)*} \vec{P}_{\text{achiral}}^{(2)} \right\} = -2\text{Re} \left\{ \chi_{ee}^{(2)*} \chi_{em}^{(2)} \left[\vec{\mathcal{E}}^*(\omega_1) \cdot \vec{\mathcal{B}}(\omega_2) \right] \left[\vec{\mathcal{E}}^*(\omega_2) \cdot \vec{\mathcal{E}}(\omega_1) \right] \right. \\ \left. + \chi_{ee}^{(2)*} \chi_{me}^{(2)} \left[\vec{\mathcal{B}}(\omega_1) \cdot \vec{\mathcal{E}}^*(\omega_2) \right] \left[\vec{\mathcal{E}}^*(\omega_1) \cdot \vec{\mathcal{E}}(\omega_2) \right] \right\} + \dots \quad (14)$$

where each term is the product of a molecular pseudoscalar (e.g. $\chi_{ee}^{(2)*} \chi_{em}^{(2)}$) associated with the molecular handedness and a field pseudoscalar (e.g. $[\vec{\mathcal{E}}^*(\omega_1) \cdot \vec{\mathcal{B}}(\omega_2)][\vec{\mathcal{E}}^*(\omega_2) \cdot \vec{\mathcal{E}}(\omega_1)]$) associated with the field handedness. In comparison with Eqs. (8) and (9) where the field pseudoscalar was between the electric field and the magnetic field at the same frequency, in this configuration the field pseudoscalars involve scalar products between the electric field of one frequency with the magnetic field of the other frequency. There are also electric-quadrupole contributions to Eq. (14) which we do not write here for simplicity.

A couple of years before the work of Belkin et al. [24], Buckingham and Fischer [30] theoretically obtained an expression like Eq. (13) but instead of relying on the magnetic-dipole and the electric-quadrupole to obtain $\vec{P}_{\text{achiral}}^{(2)}(\omega_1 + \omega_2)$ they relied on a static electric field to obtain $\vec{P}_{\text{achiral}}^{(3)}(\omega_1 + \omega_2 + 0)$. In this case, the enantiosensitive signal is linear in the amplitude of the static electric field and the effect occurs within the electric-dipole approximation. Fischer et al. then proceeded to confirm this higher-order electro-optic (Pockels) effect experimentally [31] and with a ~ 2.5 kV/cm static field they were able to achieve an intensity signal of up to $\sim 20\%$ of

¹⁸This requires taking into account that $\vec{P}_{\text{achiral}}^{(2)}(\omega_1 + \omega_2) = \chi_{em}^{(2)} \vec{\mathcal{E}}(\omega_1) \times \vec{\mathcal{B}}(\omega_2) + \chi_{me}^{(2)} \vec{\mathcal{B}}(\omega_1) \times \vec{\mathcal{E}}(\omega_2) + \dots$ and some vector algebra.

the of the SFG signal in the absence of the static electric field. In this case one can show that the interference term takes the form

$$\begin{aligned}
2\text{Re} \left\{ \vec{P}_{\text{chiral}}^{(2)*} \cdot \vec{P}_{\text{achiral}}^{(3)} \right\} = & 2\text{Re} \left\{ \chi^{(2)*} \chi_1^{(3)} \left(\left[\vec{\mathcal{E}}(\omega_1) \times \vec{\mathcal{E}}(\omega_2) \right]^* \cdot \vec{\mathcal{E}}(\omega_1) \right) \left[\vec{\mathcal{E}}(\omega_2) \cdot \vec{\mathcal{E}}_2(0) \right] \right. \\
& + \chi^{(2)*} \chi_2^{(3)} \left(\left[\vec{\mathcal{E}}(\omega_1) \times \vec{\mathcal{E}}(\omega_2) \right]^* \cdot \vec{\mathcal{E}}(\omega_2) \right) \left[\vec{\mathcal{E}}(\omega_1) \cdot \vec{\mathcal{E}}_2(0) \right] \\
& \left. + \chi^{(2)*} \chi_3^{(3)} \left(\left[\vec{\mathcal{E}}(\omega_1) \times \vec{\mathcal{E}}(\omega_2) \right]^* \cdot \vec{\mathcal{E}}(0) \right) \left[\vec{\mathcal{E}}(\omega_1) \cdot \vec{\mathcal{E}}_2(\omega_2) \right] \right\} \quad (15)
\end{aligned}$$

where again each term is the product of a molecular pseudoscalar associated with the molecular handedness and a field pseudoscalar associated with the field handedness [cf. Eqs. (8), (14)]. A review of nonlinear optical effects in chiral media discussing the effects we have considered so far can be found in Ref. [32].

More recently, Patterson et al. [33] conducted an experiment where they exposed a chiral medium to a static electric field $\vec{\mathcal{E}}(0)$ and resonantly excited a perturbed rotational level with a linearly polarized field $\vec{\mathcal{E}}(\omega)$. Once the fields $\vec{\mathcal{E}}(\omega)$ and $\vec{\mathcal{E}}(0)$ were removed, the oscillating electric field emitted by the free oscillations of the medium polarization (free induction decay) was measured (including phase) and its component perpendicular to the fields $\vec{\mathcal{E}}(\omega)$ and $\vec{\mathcal{E}}(0)$ was observed to oscillate with opposite phases in opposite enantiomers. Similarly to SFG, if the medium were achiral the whole system would be reflection symmetric with respect to the plane defined by $\vec{\mathcal{E}}(\omega)$ and $\vec{\mathcal{E}}(0)$ and therefore no response perpendicular to this plane could occur. A chiral medium breaks this symmetry and allows the emergence of such a response. Also like in SFG, the opposite phase in opposite enantiomers follows from considering the mirror image of the whole system across the plane defined by the incident fields. The general mechanism leading to this enantiosensitive free induction decay (FID) will be explained in one of the publications that are part of this work (see section IV.C.1 in Ref. [15] and Sec. 4.3 here). For the sake of offering a consistent picture to the reader we anticipate that in this case we found that the amplitude of the polarization responsible for this effect has the form

$$\sum_{M_g, M_m, M_n} \sum_{m \neq n} \frac{1}{\omega_{mn}} \left[\vec{d}_{gn} \cdot \left(\vec{d}_{nm} \times \vec{d}_{mg} \right) \right] \left[\vec{\mathcal{E}}(0) \times \vec{\mathcal{E}}(\omega) \right] \quad (16)$$

where $\vec{d}_{i,j} = \langle J_i, \tau_i, M_i | \vec{d} | J_j, \tau_j, M_j \rangle$ is the electric-dipole matrix element between asymmetric rotor states¹⁹, $|n\rangle$ and $|m\rangle$ are unperturbed states of the molecule separated by an energy difference ω_{mn} , and we made no assumption on the polarization of $\vec{\mathcal{E}}(\omega)$ nor on the direction of $\vec{\mathcal{E}}(0)$. Equation (16) is, like Eq. (10), a product between a pseudoscalar that encodes the molecular handedness, and a pseudovector depending on the incident electric fields. It is also an example of a *chiral setup* effect, where the incident electric field is not chiral by itself but the setup defined by the electric field and the detection scheme together is chiral.

In comparison to Eq. (10) one could say that this is the FID version of the enantiosensitive SFG in Eq. (10) for one of the frequencies equal to zero, i.e. a FID version of the electro-optic (Pockels)

¹⁹See Ref. [34] to learn more about asymmetric rotors.

effect²⁰. We highlight that the effect takes place only after the incident fields are removed and therefore cannot be described within a nonlinear optics formalism, where at any time the response is proportional to some power of the incident fields. Another important difference is that, since there is only a single frequency involved, there is no phase matching condition that needs to be satisfied. In comparison with vibrational and electronic transitions, the frequencies in rotational transitions are such that the extraction of the phase of the FID electric field is relatively simple.

In the same year Patterson and Doyle [35] replaced the static field by an oscillating field to achieve a resonant SFG scheme with three rotational levels, where the two lowest levels are resonantly coupled by a linearly polarized field $\vec{\mathcal{E}}(\omega_1)$ and the two higher levels are resonantly coupled by a field $\vec{\mathcal{E}}(\omega_2)$ linearly polarized perpendicular to $\vec{\mathcal{E}}(\omega_1)$. Then, like for the previous experiment, they observed a FID signal perpendicular to the plane defined by the incident fields which had opposite phases for opposite enantiomers, this time at the frequency $\omega_1 + \omega_2$. As expected from the previous works in nonlinear optics and unlike the previous experiment, the signal occurs even in the presence of the incident pulses and one can confidently say that they observed the SFG predicted by Giordmaine (but now for rotational transitions) followed by FID due to the resonant character of the excitation. In comparison to other SFG experiments probing vibrational or electronic transitions, their SFG signal benefited from the proximity of the two upper rotational levels, which could be excited by a field with a wavelength of the order of 1 meter, ensuring in this way an approximately constant phase relation between the two frequencies across an interaction region with a scale on the order of centimeters, in spite of the fact that the two incident fields propagate in perpendicular directions. To illustrate this, consider the total field resulting from two beams propagating with directions \vec{k}_1 and \vec{k}_2 ,

$$\vec{E}(\vec{r}, t) = \vec{E}_1 \cos(\vec{k}_1 \cdot \vec{r} - \omega_1 t) + \vec{E}_2 \cos(\vec{k}_2 \cdot \vec{r} - \omega_2 t). \quad (17)$$

If we evaluate it at a different position $\vec{r} + \vec{\delta}$ we get

$$\vec{E}(\vec{r} + \vec{\delta}, t) = \vec{E}_1 \cos[\vec{k}_1 \cdot \vec{r} - \omega_1(t - \tau)] + \vec{E}_2 \cos[\vec{k}_2 \cdot \vec{r} - \omega_2(t - \tau) + \phi] \quad (18)$$

where $\tau = \frac{1}{\omega_1} \vec{k}_1 \cdot \vec{\delta}$, $\phi = k_2(\hat{k}_2 - \hat{k}_1) \cdot \vec{\delta}$, and $\hat{k}_i = \vec{k}_i/|k_i|$. Only when $\hat{k}_1 = \hat{k}_2$ we get $\phi = 0$ and a spatial displacement is simply equivalent to a temporal displacement $\vec{E}(\vec{r} + \vec{\delta}, t) = \vec{E}(\vec{r}, t - \tau)$ for any displacement $\vec{\delta}$, i.e. no extra relative phase is induced by the displacement. For the case $\hat{k}_1 \perp \hat{k}_2$ and an arbitrary $\vec{\delta}$, a small phase $\phi \ll 1$ requires in general that $|\vec{\delta}|/\lambda_2 \ll 1$. This means that two different molecules will see approximately the same relative phase between the two frequencies as long as the distance δ between them is much smaller than the largest of the two wavelengths. Unlike in the work of Patterson and Doyle, this was not taken into account in the very interesting theoretical works of Brumer, Shapiro, and collaborators (see Ref. [36] and references therein) which we will now consider.

In Ref. [37], Gerbasi, Shapiro, and Brumer showed numerically that it was possible to drive extremely efficient enantiosensitive population transfer between vibrational levels in isotropic chiral molecules within the electric-dipole approximation by using three mutually orthogonal

²⁰See e.g. Ref. [21] for the usual Pockels effect.

linear polarizations²¹, setting each polarization at resonance with one of the transitions in a three level system. Namely, they showed that by controlling the relative phases between the different frequencies it was possible to move up to 95% of the population to the highest level in one enantiomer and only 4% of the population to the highest level (and 94% to the middle level) in the other enantiomer, using the same field and starting in the lowest level in both enantiomers.

Regardless of the interesting details about how the population is transferred from one vibrational level to the other (see Ref. [37]), the deciding factor for enantiosensitive population transfer in general is that, by definition, the two enantiomers behave differently when they interact with the same field. In the light of statement (2) this means that the electric field itself is chiral. Remarkably, since the effect takes place within the electric-dipole approximation, the chirality is not encoded in the spatial dependence of the field in space (as for circularly polarized light). Instead as we show in this thesis, it must be encoded in the time evolution of the field. The tip of the electric field has to trace a chiral trajectory in (E_x, E_y, E_z) -space as it evolves in time. This simple fact, which as far as we know has not been pointed out in the literature²² preceding our work [40] (see Secs. 2.5 and 4.5), underlies the physics of all phenomena occurring in the electric-dipole approximation where an isotropic sample of chiral molecules leads to a scalar (as opposed to a vector or a tensor) observable that is enantiosensitive. More on this, and in particular on how to deal with the problem of the relative phases changing across space when the beams propagate noncolinearly, is discussed in Ref. [40] (see Secs. 2.5 and 4.5 here).

Coming back to rotational transitions, a couple of years ago Eibenberger et al. [41] added a third oscillating field to their previous setup in Ref. [35]. This field is linearly polarized perpendicular to the other two fields and resonantly couples the remaining uncoupled transition in the three level rotational system they considered earlier in Ref. [35]. Besides the fact that the details (from the point of view of chirality) of how the population transfer occurs are different, this is the same level and coupling scheme considered by Gerbasi et al. in Ref. [37] (see also Ref. [42]). It must be clarified that what is a detail and what is not a detail is evident only in hindsight of our work²³ [40] (see Secs. 2.5 and 4.5 here). We stress that the fact that Patterson and Doyle recognized the importance of keeping the relative phase between the perpendicular polarizations constant [35] was a game changer which allowed the enantiosensitive population transfer between rotational levels in Ref. [41] by relying on the proximity (~ 100 Mhz) of two of the levels. As pointed out in Refs. [37] and [41], the enantiosensitive population transfer is the result of interference between two quantum pathways. Using the results that we derived for rotational averaging in Ref. [15] (see Secs. 2.3 and 4.3 here), one can show that for perturbative fields, the interference term is of the form

$$\frac{1}{3}\text{Re} \left\{ \sum_{M_0, M_1, M_2} \left\{ \vec{d}_{0,1} \cdot (\vec{d}_{1,2} \times \vec{d}_{2,0}) \right\} \left\{ \vec{\mathcal{E}}(\omega_{10}) \cdot [\vec{\mathcal{E}}(\omega_{21}) \times \vec{\mathcal{E}}(\omega_{20})] \right\} \right\}, \quad (19)$$

²¹Note that this requires at least one of the fields to propagate perpendicular to the other two.

²²One could think that this was implicitly suggested by Brumer et al. in Ref. [38], however their comment regarding the impossibility of achieving a different population in isotropic samples of opposite enantiomers reveals that they were not considering the full trajectory of the electric field in time and were therefore unaware of the chirality of the field. Afterwards when they disproved themselves in Ref. [39] regarding such impossibility, they also did not mention the chirality of the field.

²³In fact, at the time when Ref. [41] was published, although Patterson and Doyle were aware of the works by Brumer, Shapiro, et al. (they cite several of these works in Ref. [33]), they considered their work so different that they did not cite it in Ref. [41].

where $\vec{d}_{i,j} = \langle J_i, \tau_i, M_i | \vec{d} | J_j, \tau_j, M_j \rangle$ is the electric-dipole matrix element between asymmetric rotor states. As the reader should by now recognize, the expression above is the product of a molecular pseudoscalar characterizing the handedness of the molecule and a field pseudoscalar characterizing the handedness of the total electric field at the position of the molecule [cf. Eqs. (8), (14), (15)]. There is also a previous alternative theoretical description due to Lehmann [43] for the three works by Patterson et al. [33, 35, 41] we discussed here, however it was developed specifically to formalize Patterson’s et al. work and is not written in a way that fits into the big picture that we are trying to convey here.

With this we conclude the discussion of enantiosensitive nonlinear optical phenomena and move on to the discussion of enantiosensitive effects in photoionization.

1.3.2 Enantiosensitive photoelectron emission

After this brief overview of chiral effects in nonlinear optics it might be surprising to learn that one can also distinguish opposite enantiomers already in a one-photon process (i.e., first-order perturbation theory in the semiclassical treatment) within the electric-dipole approximation and in isotropic media. In 1976 Ritchie [18] theoretically predicted that one-photon ionization of an isotropic sample of chiral molecules with circularly polarized light (CPL) would yield a photoelectron angular distribution (PAD) that is asymmetric with respect to the plane of polarization of the light and where the direction of the asymmetry can be changed by either changing the rotation direction of the electric field or the handedness of the chiral medium. This effect is now known as photoelectron circular dichroism (PECD). Crucially, since PECD takes place within the electric-dipole approximation, Ritchie correctly estimated that it would yield enantiosensitive signals of about 10% of the total signal, much higher than in linear circular dichroism and optical activity. An example of the effect is shown in Fig. 10. Ritchie’s estimations were first reproduced by more elaborate numerical models developed by Powis [44] more than two decades later and then experimentally confirmed by Böwering et al. [45] shortly after. Since then, a very considerable number of calculations and experiments in several different chiral molecules have confirmed that the magnitude of the effect consistently reaches magnitudes on the order of 10% of the total signal and that the asymmetry is remarkably sensitive to molecular details, which makes it particularly interesting as a diagnostic tool. Reviews of one-photon PECD can be found in Refs. [13, 46, 47].

Specifically, what Ritchie found was that the PAD resulting from one-photon ionization of isotropic samples of chiral molecules using CPL has the form

$$W(\theta) = A + B \cos \theta + C \cos^2 \theta \tag{20}$$

$$= b_0 P_0(\cos \theta) + b_1 P_1(\cos \theta) + b_2 P_2(\cos \theta) \tag{21}$$

where θ is the angle indicating the direction of the photoelectron with respect to the $+z$ axis, the polarization of the CPL lies in the xy plane ($\theta = \pi/2$), and B is nonzero for chiral molecules. The second line shows an equivalent and more commonly used expression in terms of Legendre polynomials (note that $b_1 = B$), where b_0 corresponds to the angle integrated $W(\theta)$ and b_1/b_0 is the parameter usually reported in experiments reaching values of about 0.1. Clearly, any term

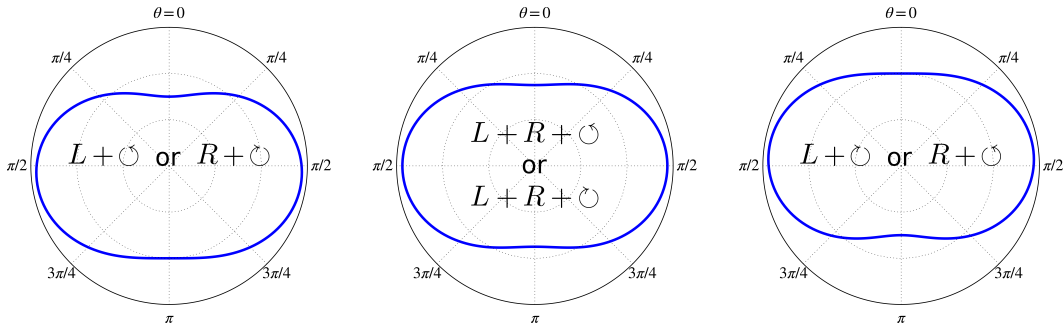


Figure 10: Example of a photoelectron angular distribution in one-photon ionization of an isotropic medium at a fixed photoelectron energy. The field is circularly polarized in the xy plane and θ indicates the polar angle measured from the $+z$ direction. The angular distribution has cylindrical symmetry. L and R stand for the handedness of the chiral medium, \circlearrowright and \circlearrowleft stand for clockwise and counterclockwise polarization as seen from the $+z$ direction. Note that the left and the right panels have opposite asymmetries with respect to the xy plane ($\theta = \pi/2$) while the central panel, which corresponds to an achiral medium ($L + R$), displays no asymmetry.

odd in $\cos\theta$ will cause an asymmetry with respect to the plane of polarization $\theta = \pi/2$. In fact, as we pointed out in Ref. [15] (see Secs. 11 and 4.3 here), b_1 is proportional to the net photoelectron current (the vector sum of the currents emitted in all directions). In contrast, in the absence of molecular chirality the photoelectron current emitted in direction (θ, φ) is exactly matched by an opposite current in direction $(\pi - \theta, \varphi + \pi/2)$ and therefore, although the total emitted current (i.e. sum of the magnitudes) is not zero, the net photoelectron current (i.e. the vector sum) vanishes. Figure 2 in Ref. [15] (see Sec. 4.3 here) explains enantiosensitivity and dichroism in terms of a “reactants” and “product” symmetry analysis, where the “product” is the photoelectron current. A useful if rather mechanical analogy due to Powis [46] which captures the essence of PECD is the behavior of a nut (electron) on a threaded rod (chiral molecular potential) under the action of a force inducing rotation of the nut (circularly polarized light). The helical thread transforms the rotational motion of the nut into motion perpendicular to the the plane of rotation. Because the helical thread is the same for two opposite orientations of the rod, then clockwise rotation produces motion along the rod in the same direction for both orientations but in opposite directions for opposite helical threads.

Now that the essence of the phenomenon has been described, we will give an overview of the underlying theoretical description. In contrast to the effects described in the previous sections, in photoionization one has to deal with unbound states, i.e., with states that describe the motion of electrons which are not confined by the Coulomb attraction of the nuclei to a finite region in space. Because they are unbound, these states form a continuous energy spectrum. And because they represent states where there is flow of electrons and therefore nonzero probability currents, their wave function is necessarily complex. As we will see below, this a determining factor for the emergence of PECD. In photoionization, these states have boundary conditions such that asymptotically far away from the rest of the molecule (i.e. $r \rightarrow \infty$ and the center of the molecule is located at $r = 0$) they behave as outgoing plane waves $e^{i\vec{k}\cdot\vec{r}}$ when \vec{r} points in the

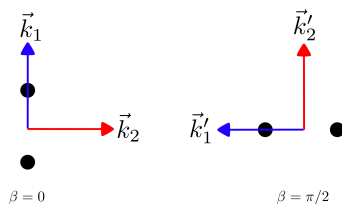


Figure 11: Two orientations of a diatomic molecule. The black circles indicate the nuclei. The scattering state depends on the relative angle between the molecular axis and the propagation direction \vec{k} of the outgoing (asymptotically plane) wave. Therefore, while the states $|\vec{k}_1\rangle$ and $|\vec{k}'_1\rangle$ are the same in the molecular frame and are related to each other by a simple rotation in the laboratory frame, the states $|\vec{k}_1\rangle$ and $|\vec{k}'_2\rangle$ are truly different from each other.

same direction as \vec{k} . This asymptotic behavior, which corresponds to a photoelectron momentum $\vec{p} = \hbar\vec{k}$ in the detector, is used to label these states as $|\vec{k}\rangle$. For smaller r , the behavior of the wave function $\psi_{\vec{k}}(\vec{r}) \equiv \langle \vec{r} | \vec{k} \rangle$ differs from molecule to molecule. The outgoing part of the scattering state requires an incoming part in order to conserve probability, which, since we only observe outgoing electrons, raises questions about the physical meaning of populating such a state. In fact, if one takes into account that the radiation has a certain bandwidth then it can be shown that the ionized wave packet formed by the superposition of the scattering states with different energies contains only an outgoing component [48] and the incoming wave only plays a role in the calculation of the transition matrix elements. Besides the continuity of the energy spectrum, for each energy level $E = p^2/2m_e$, there are an infinite number of degenerate states $|\vec{k}\rangle$, each pointing in a different direction specified by the spherical angles (θ_k, φ_k) .

For a given photon energy $\hbar\omega$, photoionization can take place from one or more orbitals provided the photon energy is high enough so that in general, a single photon energy will yield photoelectrons with different energies depending on which orbital they came from according to energy conservation, i.e., higher photoelectron energies correspond to higher energy orbitals. Like for transitions between bound states, for a given initial state $|i\rangle$ and final state $|\vec{k}\rangle$, the transition amplitude within the electric-dipole approximation will be given by $\vec{d}_{\vec{k}i} \cdot \vec{\mathcal{E}}(\omega)$, where $\vec{d}_{\vec{k}i} \equiv \langle \vec{k} | \vec{d} | i \rangle$ is the electric-dipole transition matrix element and $\vec{\mathcal{E}}(\omega)$ is the Fourier amplitude of the field at the frequency ω . As mentioned previously, the wave function of the scattering state $|\vec{k}\rangle$ is complex and therefore $\vec{d}_{\vec{k}i}$ is complex as well. Although a full specification of the state includes information about the state in which the molecule is left, for simplicity we only indicate the photoelectron momentum $\hbar\vec{k}$ in the label of the final state $|\vec{k}\rangle$. Because nuclear motion is usually much slower than electronic motion, we can in most cases safely assume that the photoionization takes place at a fixed molecular orientation. The importance of distinguishing between \vec{k} in the molecular and in the laboratory frame is illustrated in Fig. 11, where we can see that, just like the bound wave functions are clamped to the nuclei (within the Born-Oppenheimer approximation), the scattering wave functions for \vec{k} fixed in the molecular frame are also clamped to the nuclei. This in turn means that, provided \vec{k} remains constant in the molecular frame, $\vec{d}_{\vec{k}i}$ is also clamped to the nuclei, i.e. it rotates rigidly with the molecule, just like one would expect from any other purely molecular property. In contrast if one keeps \vec{k} fixed in the laboratory frame, the transition electric-dipole vector for different orientations will not be related to each other in any simple way.

For a single molecular orientation one can always choose the molecular frame coincident with the laboratory frame (even when it is not practical to do so). In this case the quantity $W(\vec{k}) = |\vec{d}_{\vec{k}i}^* \cdot \vec{\mathcal{E}}(\omega)|^2$ will determine the probability that an electron is ionized and flies away in direction \vec{k} with energy $\hbar^2 k^2 / 2m_e$, i.e. it will determine the photoelectron spectrum. The photoelectron angular distribution is simply the photoelectron spectrum at a fixed energy. When multiple orientations must be taken into account one really needs to make a clear distinction between molecular and laboratory frames. This is the case, for example, when one is interested in the photoelectron spectrum resulting from an isotropic sample, which requires averaging over all molecular orientations. As we show in Ref. [15] (see Sec. 4.3 here), the result of such procedure yields a net photoelectron current of the form²⁴

$$\vec{j}(k) = \frac{1}{6} \int d\Omega_k \left[\vec{k} \cdot \left(\vec{d}_{\vec{k}i}^* \times \vec{d}_{\vec{k}i} \right) \right] \left[\vec{\mathcal{E}}^*(\omega) \times \vec{\mathcal{E}}(\omega) \right], \quad (22)$$

where \vec{k} is the photoelectron momentum, $\vec{d}_{\vec{k},g} = \langle \vec{k} | \vec{d} | g \rangle$ is the transition matrix element between the ground state $|g\rangle$ and the scattering state $|\vec{k}\rangle$, the integral is over all directions of \vec{k} , and $\vec{\mathcal{E}}(\omega)$ is the Fourier amplitude of the electric field at frequency ω . Equation (22) makes no assumption on the polarization of the electric field. The triple scalar product $\vec{k} \cdot (\vec{d}_{\vec{k}i}^* \times \vec{d}_{\vec{k}i})$ is non-zero thanks to the fact that $\vec{d}_{\vec{k}i}^*$ is a complex vector. Like the previous expressions for the effects in Eqs. (10) and (16), the vector response is the product of a molecular pseudoscalar and a field pseudovector (in the direction of the spin of the photon). Note that by projecting \vec{j} on a reference vector \vec{v}_{ref} defined by the detection scheme, the field pseudovector in Eq. (22) turns into the pseudoscalar $\vec{v}_{\text{ref}} \cdot [\vec{\mathcal{E}}^*(\omega) \times \vec{\mathcal{E}}(\omega)]$ which describes the handedness of the chiral setup. Contrary to what is loosely written unfortunately too often, we stress that the helicity, which is the projection of the photon's spin $\vec{\mathcal{E}}^*(\omega) \times \vec{\mathcal{E}}(\omega)$ on the propagation direction of the light²⁵, does not play any role in PECD because PECD occurs in the electric-dipole approximation where the propagation direction of the light is not taken into account at all. Such misunderstanding may have originated because \vec{v}_{ref} is usually chosen parallel to the propagation direction of the light, however \vec{v}_{ref} is actually defined by the detector. In fact, one would also obtain PECD in a rotating standing wave where the propagation direction of the light is undefined, or from the rotating electric field at a given point resulting from crossing two linearly polarized fields that propagate noncollinearly and have the same frequency. In the latter case one would need to make sure that the interaction region is small enough [see Eq. (18)]. A detailed discussion of Eq. (22) can be found in Refs. [15, 49] (see Secs. 4.3 and 4.4 here).

In 2012 Lux et al. [50] observed PECD in resonantly enhanced multiphoton (three-photon) ionization²⁶ and in (four-photon) above-threshold-ionization²⁷ (ATI) with asymmetries comparable

²⁴Since the expression originally derived by Ritchie for b_1 in Ref. [18] is rather unintelligible for the non-specialist and since in Appendix 5 of Ref. [15] (see Sec. 4.3 here) we proved that Eq. (22) is exactly equivalent to Ritchie's expression, we decided not to include Ritchie's expression here. The interested reader can find it in Eq. (11) of Ref. [18].

²⁵Note that the \vec{k} in Eq. (22) stands for the photoelectron momentum and not for direction of propagation of the light like in Eqs. (8) and (9).

²⁶Resonantly enhanced multiphoton ionization (REMPI) refers to the process where N photons are absorbed and there is an integer number of photons $n < N$ such that $n\hbar\omega$ is resonant with a transition. This considerably increases the ionization yield in comparison to the case where there is no intermediate resonance.

²⁷Above threshold ionization (ATI) is the process where electrons absorb more photons than required to escape

to those found in one-photon ionization. This was important not only because it extended PECD to the multiphoton regime, but also because, unlike previous experiments, it was achieved using a table-top femtosecond laser instead of a synchrotron, opening the way for time-resolved experiments on the one hand and making PECD experiments accessible to a much wider community on the other hand. Since the absorption of N photons by an isotropic sample leads to an angular distribution with Legendre polynomials $P_l(\cos\theta)$ of order l up to $2N$ ²⁸, then not only b_1 , but also b_3, b_5, \dots (the coefficients associated with odd powers of $\cos\theta$) are enantiosensitive. This experiment therefore revealed new enantiosensitive observables beyond b_1 . We can anticipate that while b_1 is associated with a vector observable (the net photoelectron current), higher order coefficients are associated with tensor observables of rank l describing the correlations between the photoelectron emission in different directions and encoding molecular information in the form of higher order scalar (for even l) and pseudoscalar (for odd l) rotational invariants. The expression for b_3 for the case of two-photon absorption through an intermediate state $|j\rangle$ is for example of the form

$$b_3 = C \left\{ \int d\Omega_k [\vec{k} \cdot (\vec{d}_{kj}^* \times \vec{d}_{ji})] (\vec{k} \cdot \vec{d}_{ji}) (\vec{k} \cdot \vec{d}_{ji}) \right\} \left\{ \left[\hat{z} \cdot (\vec{\mathcal{E}}^* \times \vec{\mathcal{E}}) \right] (\hat{z} \cdot \vec{\mathcal{E}}) (\hat{z} \cdot \vec{\mathcal{E}}^*) \right\} + \dots \quad (23)$$

where C is a constant depending on things such as detuning and bandwidth of the radiation, and the sum is over terms which are products of molecular pseudoscalars and chiral setup pseudoscalars, where we took $\vec{v}_{\text{ref}} = \hat{z}$. A discussion of these higher order coefficients is the subject of a paper in the process of submission.

On the experimental side, the progress of Lux et al. in using table-top lasers to measure PECD was complemented by the work of Ferré et al. [52] who produced almost circularly polarized pulses with photon energies on the order of tens of electron volts via high harmonic generation²⁹, allowing them to observe one-photon PECD with a table-top setup.

Beaulieu et al. [53] observed PECD on the order of 1% in the many-photon tunneling regime³⁰ in Fenchone, demonstrating that PECD occurs in all ionization regimes (one-photon, multiphoton, ATI, and tunneling). This result is interesting because while the physics underlying one- and few-photon ionization is very similar and can be described using standard perturbation theory, the physics in the presence of the strong non-resonant fields required to reach the tunneling regime is fundamentally different [55]. Shortly after, Comby et al. [56] performed the first time-resolved PECD measurement. They used a linear pump - circular probe setup, where the linear pump excited the molecule into a bound state and the circular probe ionized it. The recorded

the parent ion which leads to several peaks in the photoelectron spectrum at energies $E_n = p^2/2m_e = n\hbar\omega - I_p$ for n such $E_n > 0$, where I_p is the ionization potential.

²⁸This follows from the fact that for N -photon absorption (N th-order perturbation theory in a semiclassical treatment), the probability amplitude is proportional to $(\vec{d} \cdot \vec{\mathcal{E}})^N$ and the probability to $|\vec{d} \cdot \vec{\mathcal{E}}|^{2N}$. Since \vec{d} is a rank-1 spherical tensor, $|\vec{d} \cdot \vec{\mathcal{E}}|^{2N}$ is a superposition of spherical tensors with ranks up to $2N$. This means that when the angular distribution, which is proportional to $|\vec{d} \cdot \vec{\mathcal{E}}|^{2N}$, is written in terms of spherical harmonics Y_l^m (spherical tensors of rank l), the maximum value of l will be $2N$. For an introduction to spherical tensors see Ref. [51].

²⁹High harmonic generation (HHG) is an extremely nonlinear process where a medium is irradiated with intense light at frequency ω and it emits light at integer multiples of this frequency.

³⁰The tunneling regime refers to ionization in a very strong low frequency field that deforms the potential energy so much that the electron can tunnel ionize. See Ref. [54] for an introduction.

enantiosensitive dynamics took place on the order of 1 ps and were attributed to vibrational relaxation followed by electronic relaxation. A particular complication that arises in this setup is that the polarization of the linear pump lies in the polarization plane of the circular probe and therefore breaks the cylindrical symmetry of the system and prevents a proper reconstruction of a VMI image using the inverse Abel transform.

We remark that in the absence of chiral light, as is the case for PECD effects, the enantiomers can only differ in their behavior by a phase. While for bound states this is reflected by polarization oscillations of the same magnitude with opposite phase for opposite enantiomers [see e.g. Eq. (10)], in photoionization this is reflected as PAD asymmetries of the same magnitude pointing in opposite directions for opposite enantiomers. This must be clearly distinguished from the enantiosensitive population dynamics observed in effects involving chiral light, as in e.g. CD and Refs. [37, 41], where the populations (magnitudes) of the levels differ from one enantiomer to the other. Note that even if in PECD experiments the light used is usually chiral (CPL), the chirality of the light does not play any role.

Finally, we would like to bring the attention of the reader to the work of Beaulieu et al. [57] where they measured angularly resolved photoionization time delays in chiral molecules, the works of Demekhin et al. [58] and Rozen et al. [59] where they observe novel asymmetries in the photoionization of chiral molecules, and the work of Goetz. et al. [60] where PECD is optimized via quantum control techniques. These recent papers inspired our follow-up work devoted to further development of our theoretical framework. These latest developments are not a part of this thesis.

2 Summary of publications

2.1 Propensity rules in photoelectron circular dichroism in chiral molecules. I. Chiral hydrogen

This paper³¹ stems from our longing to identify physical mechanisms that lead to photoelectron circular dichroism (PECD), that go beyond the well known (but not particularly insightful) fact that PECD results from interference between the contribution of partial waves of opposite parity. In particular we are interested in trying to understand what makes a photoelectron more likely to go “forwards” than “backwards”, i.e. we are interested in the question of what determines the sign of the so-called forward-backward asymmetry (FBA) in PECD. Since the calculation of PECD requires knowledge of the initial and the final state, we are also interested in the question of what is the simplest chiral wave function. We found elementary chiral wave functions that result from the superposition of only two hydrogenic orbitals. These wave functions illustrate three fundamental ways in which chirality can be encoded in a wave function. It can either appear as i) the combination of static polarization (vector) with a circular probability current

³¹We begin with this paper, which was the third publication that resulted from this thesis, because it was meant to be the first one to be published and contains the germ of several key ideas that contributed to all the other papers that resulted from this thesis.

(pseudovector) perpendicular to it, ii) a chiral (toroidal-knot) probability current without density polarization iii) a chiral (torus-link) density with zero probability current. Analogously to how a standing wave can be constructed from two oppositely directed plane waves, we have shown how the chiral density can be constructed from two oppositely directed chiral currents. These hydrogenic chiral wave functions show that achiral systems, like atoms, can be made chiral if excited appropriately; a first step towards laser-sculpted chiral matter³².

After illustrating the elementary chiral wave functions, we study their photoelectron angular distributions (PADs) for circularly polarized light. The calculation of the PADs is done exactly by using the achiral scattering states of hydrogen. This allows us to trace back any chiral effect to the chirality of the initial wave function. The analysis of these molecular-frame PADs yields propensity rules which correlate the direction and the magnitude of the FBA to two distinct features of the chiral wave function. For example, in the case of the chiral probability current wave functions, the probability current has both an azimuthal and a polar component (see Fig. 2 in the paper), and while the sign of the FBA is determined by the polar component, the magnitude of the FBA is determined by the relative direction of the azimuthal component with respect to the spin of the ionizing photon.

We then simulate the different orientations of a chiral molecule by changing the orientation of the initial state. Since symmetry arguments show that a FBA in an uniaxially aligned system with the alignment axis either parallel or perpendicular to the polarization plane of the circularly polarized light can only occur in the presence of chiral molecules (Sec. IV A in Ref. [49]), we can limit the analysis to uniaxially aligned samples in these configurations³³. Continuing with the example of the chiral probability current wave functions, if we consider two opposite orientations of the same initial state, they will have opposite azimuthal and opposite polar probability current components. The opposite polar components will lead to opposite signs of the FBA and the opposite azimuthal components to opposite magnitudes of the FBA. Since the magnitudes are different, the FBA of one orientation will not be compensated by that of the opposite orientation, and there will be a remaining non-zero FBA. Our propensity rules therefore explain how PECD in aligned samples takes place and how one sign or the other occurs.

If we consider an isotropic sample instead of an aligned one the resulting FBA in our model vanishes. This is because the scattering states that we are using do not change when we “change the orientation”. If wanted, this could be remedied by introducing perturbations in the scattering wave functions so that they become orientation aware.

The elementary chiral wave functions yield a FBA that does not change sign as a function of the photoelectron energy. However, we show that if one considers chiral wave functions of increasing complexity, then such sign changes can occur. Such sign changes are due to the fact that as the complexity of the wave function increases it can accommodate more than a single handedness (like the helix made of a tighter helix in Fig. 7). Furthermore, if these different handedness lead to different signs and if they are associated with structures of different scales in the wave function, the photoelectron energy will probe the structures differently for different photoelectron energies. Higher photoelectron energies will probe smaller structures more efficiently and lower photoelectron energies will probe bigger structures more efficiently. This allows for sign changes of the FBA.

³²See also the recent work by Owens et al. [61] in the realm of rotational states.

³³This summary will only describe the case where the alignment axis is perpendicular to the polarization plane of the circularly polarized light. The other case can be found in Appendix 3 of the paper.

There are basically three distinct paths that can be followed starting from these results. First, the further development of these chiral states along the lines of e.g. what fields are necessary to populate them, how they interact with each other and with chiral matter, and what consequences would bring considering chiral Rydberg atoms. Second, the development of a more elaborate model based on the ideas presented here, and which takes into account the chirality of the scattering state. Third, given its single center character, this model is particularly well suited for the analysis of the strong field regime PECD. This latter path has already been taken and we are in the process of submission.

2.2 Photoexcitation circular dichroism in chiral molecules

This paper is the result of a theoretical and experimental collaboration where the theoretical work was divided into an analytical and a numerical component. We restrict this summary to the analytical results due to my doctoral advisor and myself.

In this paper we consider a pump-probe scheme where a circularly polarized pump excites bound states of an isotropic ensemble of chiral molecules and a linearly polarized probe ionizes the excited molecules after a certain time delay. Remarkably, although the ionization step proceeds using linearly polarized light, PECD with respect to the polarization of the pump pulse is observed. In very simple terms this means that the photon’s spin in the pump can be recorded in the molecule and then read out at a later time by applying a linearly polarized probe pulse and looking at the asymmetry in the photoelectron spectrum.

Consider a simple model with three bound states and one photoelectron level (with infinite energy degenerate states $|\vec{k}\rangle$, one for each direction). First, the circularly polarized pump coherently excites the two excited bound states. This can be done by having a pump with a bandwidth that covers the energies of both transitions. Once the pulse is over and after taking the isotropy of the sample into account, the oscillations of the expected value of the electric dipole are a combination of two types of motion (see inset in Fig. 1 of the paper³⁴). On the one hand, it displays circular motion in the direction determined by the pump. This circular motion consists of two frequency components (which produces beating), each corresponding to the energy difference between the ground state and one of the excited states. This circular motion is identical in opposite enantiomers. On the other hand, there is a linear motion in the direction perpendicular to the plane of polarization of the pump with a frequency corresponding to the energy difference between the two excited states. The expression for this linear motion [Eq. (1) of the paper shows its time derivative] is proportional to the product between the rotation direction of the electric field and a molecular pseudoscalar given by the scalar triple product between the transition electric-dipoles between the three states. At any given time the z component of the expected value of the electric dipole has opposite signs for opposite enantiomers and fixed polarization (enantiosensitivity) or fixed enantiomer and opposite polarizations (circular dichroism). The oscillation of the expected value of the electric dipole leads to the emergence of a current which oscillates correspondingly (up to a phase delay). We call this effect photoexcitation circular dichroism³⁵ (PXCD). It is conceivable that photoionization (with linearly polarized light) from

³⁴Note the similarity with the structure of the chiral probability current states presented in in Fig. 2d of the previous paper.

³⁵At the time we were not aware of Giordmaine’s work [17] and its close relation to PXCD. We became aware of it during the preparation of the next paper, which was largely motivated by the results we found here.

such an excited state could lead to a forward-backward asymmetry in the resulting photoelectron angular distribution.

Consider now photoionization from the excited states using a probe pulse with a bandwidth such that there is an energy band in the photoelectron spectrum where there is interference between the quantum pathway passing through one of the excited states and the quantum pathway passing through the other excited state. The net photoelectron current in this case [Eq. (3) in the paper] is given by a product between the rotation direction of the pump and a molecular pseudoscalar involving the transition electric-dipoles associated with the quantum paths leading to photoionization and the photoelectron momentum itself. Like the PXCD current, it is enantiosensitive and circularly dichroic. Furthermore, it oscillates as a function of the pump-probe delay with the same frequency as the PXCD current. We call this effect photoexcitation-photoelectron circular dichroism (PXECD). In the plane-wave limit for the scattering states, the energy integrated PXCD and PXECD currents are proportional to each other.

Besides illustrating how PECD-like effects can occur even when the ionizing pulse is not circularly polarized and providing a first example of a vectorial formulation of PECD where the enantiosensitivity appears explicitly in the form a scalar triple product between molecular vectors, this paper also motivated a thorough investigation of enantiosensitive effects occurring in the electric-dipole approximation which resulted in the next paper.

2.3 Generalized perspective on chiral measurements without magnetic interactions

In this paper we present a unified picture of several enantiosensitive effects taking place within the electric-dipole approximation. A very considerable fraction of the concepts and equations presented in the introduction of this thesis were originally developed in this paper. The aim of this paper is to show that there are several novel enantiosensitive effects occurring in physical situations spanning a somewhat broad spectrum (nonlinear optics, microwave spectroscopy, photoionization) that have more in common than what the original theoretical descriptions developed for each of them reveals. We provide a unified picture for five effects: photoelectron circular dichroism (PECD), enantiosensitive microwave spectroscopy (EMWS), photoexcitation circular dichroism (PXCD), photoexcitation-photoelectron circular dichroism (PXECD), and enantiosensitive sum-frequency generation (SFG), and derive new expressions for PECD, EMWS, PXCD, and PXECD, which have the same fundamental structure as that for SFG, and clearly reveal the similarities between them. With the exception of PXECD all expressions result from first-order perturbation theory, the PXECD expression results from second-order (PXECD) perturbation theory.

We begin by discussing the measurement process in enantiosensitive effects, where despite the chirality of the medium, the quantity that is directly measured is nevertheless a scalar (a click in a detector). This scalar results from the product of two pseudoscalar quantities. One encodes the molecular handedness and the other encodes the handedness of the probe. In the case of circular dichroism (CD), the prototypical chiro-optical effect, the handedness of the probe is given by the helicity of the circularly polarized light (CPL), which is in turn given by the projection of the spin of the photon on its propagation direction. Only after we know both the handedness of the probe and the result of the measurement can we obtain the molecular

handedness. For the effects of interest here the light is not chiral and therefore the directionality of the detection setup must be brought into the picture. In the case of PECD, where the output is a net photoelectron current pointing in one of the two directions perpendicular to the polarization plane, the detector must consist of two plates, one in each perpendicular direction. Although these plates are otherwise indistinguishable, we treat them asymmetrically because, in order to calculate the net photoelectron current, we must subtract the output of one of them (usually called backward) from the output of the other (usually called forward). This effectively defines a reference vector \hat{u}_{ref} that allows us to assign a sign to the photoelectron current. The spin of the photon projected on the reference vector is what defines the handedness of the setup used to probe the chiral medium. Crucially, the fact that we use such a directional detector follows from the fact that we are measuring a vector observable. All the electric-dipole effects discussed here rely on the measurement of such a vector observable. Furthermore, we show that a symmetry analysis of how a vector observable resulting from interaction between CPL and a chiral isotropic medium reveals that vector observables are automatically enantiosensitive and circularly dichroic. Vector observables have the same magnitude but opposite directions when either the enantiomer or the polarization is swapped, and are invariant under simultaneous swapping of enantiomer and polarization. This can be extended to other polarization schemes such as e.g. two different frequencies linearly polarized at a certain angle. In that case a change of π in the phase of one of the frequencies plays the role of changing the rotation direction of CPL.

Two clarifications are due here. First, although a typical CD experiment may seem directional in the sense that the detector must be put behind the sample, the measurement of CD does not in principle require a directional detection, as one can simply surround the sample by a single spherical detector and count the fluorescence photons in all directions. Second, although in PECD the reference vector is usually taken to coincide with the propagation direction of the light, which leads to the deceitful name “forward-backward asymmetry”, the FBA is in reality defined with respect to how the detectors are labeled and is fully independent of the direction of propagation of the light. To convince yourself of this, note that PECD can in principle be achieved using a standing rotating wave, where the direction of propagation of the light is undefined.

Having established the global picture we proceed to the derivation of the expressions for each of the effects. In the case of PECD we begin by showing that b_1 is simply the signed magnitude of the net photoelectron current. As far as we know, this simple but insightful fact has not been stated previously in the literature. Then, taking into account that, similarly to a bound wave function, the scattering wave function rotates rigidly with the molecule, we choose to keep the photoelectron momentum \vec{k} fixed in the molecular frame throughout the derivation (see introduction of this thesis). This allows us to apply the orientation averaging techniques in Ref. [14] (see also Appendix 2 of the present paper), which are well known in the nonlinear optics and in the CD communities but apparently not in the photoionization community. After a few relatively simple steps which we explain in detail in the paper we obtain Eq. (22) [Eq. (14) in the paper]. This equation is valid for any polarization and has the promised structure. In comparison,³⁶ the expression originally derived by Ritchie [18] is expressed, as usual for photoionization, in terms of sums over several indices which result from a partial wave expansion of the scattering wave function and a fair amount of angular momentum algebra that produces a product of several 3j-symbols. As pioneering as it is, it is a rather complicated expression that can very unlikely be appreciated as having anything in common with that describing the enantiosensitive SFG [see

³⁶A rather unfair comparison given that Ritchie derived this almost 50 years earlier!

Eq. (10)] found by Giordmaine [17] a decade earlier. The equivalence of our expression and Ritchie’s original expression is demonstrated in Appendix 5 of the paper.

We then move on to a general description of the PXCD effect introduced in the previous paper [62]. In this case, we begin by pointing out that in order to form a molecular pseudoscalar that encodes the molecular handedness it is necessary to have at least three molecular vectors (equivalently one vector and one pseudovector). Any enantiosensitive effect must somehow probe these vectors in such a way that they end up forming a triple product. In the case of photoionization these vectors are the photoelectron momentum and the real and imaginary parts of the transition electric-dipole. For bound transitions, where there is no scattering direction and the transition electric-dipoles can be chosen real, one can instead rely on the three transition electric-dipole vectors in a three-level system³⁷. We derive an expression for the expected value of the electric-dipole which results from coherent excitation of the two excited states for arbitrary polarizations. The expression derived in the previous paper for PXCD is a particular case of the expression in this paper. This expression shows that the interference term, which is second order in the field amplitudes, is enantiosensitive and describes an oscillation in a direction perpendicular to the polarization vectors defined by the incident fields at the frequency corresponding to the energy difference between the two excited states. In essence this is the free induction decay (FID) version of the enantiosensitive difference-frequency generation (DFG) predicted by Giordmaine [17]. Nevertheless, besides occurring in the absence of the exciting fields, the fact that one can use a broad band pulse centered at a single frequency to populate both excited states coherently requires a rather relaxed interpretation of what DFG means.

We also show that the DFG variant of the EMWS results obtained by Patterson et al. in Ref. [35] for rotational transitions can be written in virtually the same way as the PXCD signal [cf. Eqs. (17) and (22) in the paper³⁸]. In other words, PXCD and EMWS are essentially the electronic/vibrational and rotational expressions of the same underlying phenomenon. While in hindsight this might seem evident, the noteworthy aspect of this is that, while for PXCD the molecular orientation is treated as a parameter of the wave function, in EMWS the orientation itself is the main degree of freedom of the wave function. The equations required to achieve this equivalence are derived in Appendix 3 of this paper. Furthermore, the expressions derived using the usual machinery for rotational states [43], which were specifically derived to account for Patterson’s et al. experiment, hardly reveal this connection.

The expression presented in the introduction [Eq. (16)] for the enantiosensitive effect obtained by Patterson et al. [33] with the static electric field is also derived in this paper. Furthermore we show that it works not only for rotational but also for electronic and vibrational states [cf. Eq. (28) in the paper].

Finally, we derive the expression for the PECD net photoelectron current in pump probe setups with two intermediate states for arbitrary polarizations of pump and probe [see Eqs. (30)-(35) in the paper]. The equations for PXECD derived in the previous paper are a particular case of the equations in this paper. Unlike the previous expressions where there is a single product between a molecular pseudoscalar and a field pseudovector, in these expressions we obtain a sum of such products. This happens because this photoionization scheme probes five molecular

³⁷An enantiosensitive effect is achieved with only two levels in CD because there the transition magnetic-dipole pseudovector is taken into account.

³⁸There is a typo in Eq. (22). The M superscripts on the transition dipoles should be replaced by L superscripts.

vectors (four transition dipoles and the photoelectron momentum) and there are ten ways to form different pseudoscalars with five vectors. In fact, we have recently learned that only six of this ten pseudoscalars are really independent from each other [see Eq. (24) in Ref. [14]]. Nevertheless, the expressions in this paper are written in a particularly practical form that connects a single molecular pseudoscalar with a single field pseudovector [see Eq. (31) in Ref. [14]]. Even for six instead of ten different pseudoscalars, our expressions reveal how rapidly the complexity of the enantiosensitive response increases by adding a second photon. This complexity makes Eqs. (30)-(35) very valuable because they show which combinations of the pump and probe polarizations address which molecular pseudoscalars. In Eqs. (33)-(35) we classify these terms according to their polarization selection rules in three main groups. The first group is nonzero only for chiral fields and has not yet been tested experimentally. The second group is nonzero for circular or elliptical fields. The third group contains the remaining contributions. In particular, the third group shows that two-photon PECD can occur even when the pump and probe pulses are both linearly polarized, provided the fields are neither parallel nor orthogonal to each other [see Eq. (35)]. This third group has not been tested experimentally yet. Importantly, the contributions to the interference term do not depend on the relative phase between the two pulses and therefore the pump and probe do not need to be phase-locked. Nevertheless, it must be kept in mind that we ignore any nuclear motion between pump and pulse, and therefore the expressions are valid only for short enough pump-probe time delays.

In summary, besides recognizing the importance of measuring vectors (as opposed to scalars) that allow the use of chiral setups in the absence of chiral light, we have achieved a clear common theoretical framework enantiosensitive effects occurring within the electric-dipole approximation across the fields of nonlinear optics, photoionization, and microwave spectroscopy. A further generalization of the reasoning presented in this work towards the topic of tensor observables [see e.g. Eq. (23)] is in the process of submission.

2.4 Propensity rules in photoelectron circular dichroism in chiral molecules. II. General picture

This paper reveals the geometrical origin of photoelectron circular dichroism, which becomes evident from the structure of the expression we found for photoelectron circular dichroism (PECD) in the previous paper. In contrast to the original expression derived by Ritchie in Ref. [18], our expression accentuates the underlying physics and attenuates the technicalities without abandoning scientific rigor. Here we take a closer look at this expression and discuss the physics it encodes.

We begin by demonstrating that the \vec{k} -dependent vector field that results from the vector product between the photoionization transition electric-dipole vector and its complex conjugate encodes the absorption circular dichroism corresponding to a transition from the ground state to the scattering state with photoelectron momentum \vec{k} . Each component of this vector field is associated with a particular orientation of the circularly polarized light in the molecular frame. Then we show that this vector field is mathematically analogous to the Berry curvature in a two-band solid and that the net photoelectron current in PECD can be therefore interpreted as resulting from a Hall-like conductivity given by the flux of this Berry-like field across the surface of radius k in the space of photoelectron momentum (k_x, k_y, k_z) . The connection of the Berry-like field with

the angular momentum associated with the photoionization transition is also derived. Propensity rules, like those discussed in part I of this paper for the particular case of chiral hydrogen, are encoded in this Berry-like field.

Next, using our expression for one-photon PECD, we demonstrate that the net photoelectron current resulting from full orientation averaging can be obtained by limiting the averaging to only six orientations. Then we discuss the symmetry properties of uniaxially aligned samples interacting with circularly polarized light when the alignment axis is either perpendicular or parallel to the polarization plane of the light and show that, except for a very anomalous case, these aligned samples can only display PECD if the sample is chiral. The circular dichroism in the angular distribution displayed by achiral oriented samples is also discussed (see also Refs. [63]). In particular it is shown that the vectorial observables resulting from achiral oriented samples lies in the polarization plane of the light while that resulting from aligned chiral molecules is perpendicular to the polarization plane of the light.

Finally, we derive formulas for PECD in the presence of molecular uniaxial alignment described by an arbitrary function alignment distribution $w(\beta)$, where β is the angle between the laboratory axis and the molecular axis being aligned. This means that all situations from perfect alignment to perfect anti-alignment are taken into account. The formulas reduce to our PECD expression discussed before in the isotropic limit where $w(\beta) = 1$. Alignment perpendicular to the polarization plane as well as alignment parallel to the polarization plane are considered. These formulas, which constitute a vast generalization of the isotropic formula, clearly show that the effect of alignment is to produce an effective stretching of the Cartesian components of the propensity field. The enhancement of the PECD effect via alignment will then be determined by the relative magnitudes and signs of the different Cartesian components of the propensity field. PECD of anisotropic samples has been recently measured [64] and our results appear to be in line with the experimental findings.

A continuation of this work in the direction of a numerical investigation of the structure of the propensity Berry-like fields of molecules is in progress.

2.5 Synthetic chiral light for efficient control of chiral light matter interaction

This paper originated from efforts towards a high harmonic generation (HHG) based enantiosensitive effect taking place in the electric-dipole approximation and from the realization that the key physical element necessary for enantiosensitivity at the level of total number of photons absorbed or emitted in this approximation is the chirality of the electric field. This summary will be mostly restricted to the latter point, which is the one I contributed to.

First we point out the difference between measurements which rely on light's chirality, as e.g. circular dichroism (CD), and measurements which rely on chiral setups and occur in the absence of chiral light, as e.g. optical activity (OA) and photoelectron circular dichroism (PECD). As discussed in the introduction of this thesis and as originally formulated in Ref. [15] (see Sec. 2.3), chiral setups rely on vector observables. Such directionality of the observable is not required in effects which rely on the chirality of the light. The main point of this paper is that the chirality of light, which in the case of circularly polarized light relies on its spatial dependence, can instead

be entirely encoded in the temporal dependence of the electric field. That is, in the form of a chiral polarization, where the electric field traces a chiral trajectory in (E_x, E_y, E_z) space as it oscillates³⁹. This type of chirality does not rely on the spatial dependence of the field and it is therefore local in space and hence, unlike circularly polarized light, it has an enantiosensitive effect on chiral matter even within the electric-dipole approximation. We call this type of light locally chiral light (LCL). We show that the handedness of the LCL can be characterized via the pseudoscalars that can be formed with its vector Fourier components, and its sign can be reversed by changing the relative phase between the different frequencies. As shown in the introduction [see Eq. ([41])], these field pseudoscalars emerge naturally in interference terms in the perturbative description of light-matter interaction and can be used to control the enantiosensitive response of chiral matter already at the interference between one-photon and two-photon transitions.

Although this type of chirality has not been recognized before, LCL was unknowingly present in the works of Gerbasi et al. [37] and Eibenberger et al. [41]. However, only now it is clear that LCL was the key physical element explaining the enantiosensitive population transfer in those works. On the one hand, Gerbasi et al. did not recognize that the relative phase between the frequencies (and therefore the handedness) would typically change rapidly across the interaction region, condemning experimental measurements to failure. On the other hand, Eibenberger et al. knew of this problem but their solution is severely limited to having one of the wavelengths considerable bigger than the interaction region. Here we show that a chiral electric field can be obtained with only two frequencies ω and 2ω , where ω is elliptically polarized and 2ω is linearly polarized perpendicular to the plane defined by the ω ellipse. In addition, we devise an experimental setup consisting of two noncollinear beams that keeps the handedness of the field constant across space (i.e. it is globally chiral) without imposing restrictions on the frequencies. Since the enantiosensitivity takes place within the electric-dipole approximation and the setup is not restricted in terms of frequencies, our work unlocks the full potential of light to control the enantiosensitive response of chiral matter at the level of angle-integrated signals, i.e. without relying on the directionality of the detection (chiral setup).

As an example of what can be achieved using the proposed setup this paper shows calculations of HHG where a given set of even harmonics display perfect destructive interference in one enantiomer, and perfect constructive interference in the opposite enantiomer. The behavior can be completely reversed by reversing the handedness of the field. This corresponds to perfect chiral discrimination, an accomplishment unparalleled in the field of chiro-optical techniques.

Because of the generality of our findings, we expect our work to have a strong impact on the field of chiral discrimination as a whole, and in particular to the investigation of ultrafast processes in chiral molecules. The experimental confirmation of our results is underway.

3 Conclusions and outlook

We have discussed a broad range of effects that take place within the electric-dipole approximation, which are typically orders of magnitude stronger than optical activity and circular dichroism. Several of these effects were introduced here.

³⁹In fact we have already seen how one of these trajectories may look like when we considered PXCD (see inset of Fig. 1 in Ref. [62]), where it described the FID of the expected value of the electric dipole after the pump.

We have introduced elementary instances of chiral wave functions which exemplify three basic forms in which chirality can be encoded in a wave function. These chiral wave functions can be formed as superpositions of atomic states, which points the way towards laser-sculpted chirality of initially achiral systems. Using these chiral wave functions we found a concrete mechanism showing how the interplay of two propensity rules can lead to the formation of net photoelectron currents (forward-backward asymmetries) in the photoionization of aligned chiral systems.

We have developed an analytical formulation that reveals helical (more precisely torus-knot-like) electronic currents formed in isotropic chiral molecules after excitation with a circularly polarized electric field. This formulation was extended to describe how net photoelectron currents (forward-backward asymmetries) result from subsequent photoionization with linearly polarized and even unpolarized light.

We have introduced a classification of chiral effects that distinguishes two groups. The first group relies on the chirality of the electromagnetic field and yields enantiosensitive scalar observables. The second group relies on the chirality of the setup, can take place in the absence of chiral electromagnetic fields, and yields enantiosensitive vector observables.

We have derived new mathematical expressions for the description of several chiral effects taking place within the electric-dipole approximation and relying on chiral setups and vector observables. These expressions are considerably simpler than previous ones, provide a deeper physical insight into each of these chiral effects, and reveal the intimate connection between all these chiral effects.

The expression we derived for photoelectron circular dichroism reveals that the net photoelectron current results from the \vec{k} -averaged absorption circular dichroism encoded in the propensity field $i\vec{d}_{ki}^* \times \vec{d}_{ki}$ (\vec{d}_{ki} is the transition electric-dipole). The propensity field turns out to have the same form as the Berry curvature in two-band solids. First, this reveals an unexpected connection to solid state physics and the property often referred to as *geometrical magnetism* (Berry curvature) which ultimately leads to topological phases of matter. Second, it also reveals the geometrical origin of photoelectron circular dichroism. Furthermore, the generalization of our PECD expression to aligned samples shows how alignment is equivalent to an effective stretching of the propensity field.

We introduced a new type of chirality of light which is fully encoded in the Lissajous figure traced by the electric field at a single point in space. The local character of this chirality means that it can interact with the molecular chirality within the electric-dipole approximation. We introduced chiral measures to quantify the chirality of this light and propose an experimental arrangement for its production. Furthermore, we show that it can be made to have the same chirality at every point across the focus, and have numerical evidence of its incredible potential to control the enantiosensitive response of chiral matter.

All of these advancements provide a rather broad range of directions that can be followed in the future. These include:

- First, the development of laser-sculpted chiral matter from achiral matter using locally-chiral light.
- Second, the application of locally-chiral light to nanostructured materials to explore the interplay between chirality-ordering in matter and in light.

- Third, the investigation of geometrical and topological features of the propensity field in chiral molecules and its connections to effects in condensed matter physics.
- Fourth, the analysis of second and higher rank tensor observables and their application to chiral discrimination.
- Fifth, the application of locally-chiral light to different intensity regimes and spectral regions.
- Sixth, the exploration of chiral distillation techniques using locally-chiral light.
- Seventh, the application of coherent control techniques with locally-chiral light setups.
- Eighth, the investigation of ultrafast processes occurring in chiral molecules using locally-chiral light.
- Finally, it is important to explore other locally-chiral light setups.

This list suggests that the work described in this thesis has the potential to open a new and rich field of research based on the concepts introduced here, namely synthetic chiral matter, synthetic chiral light, chiral setups, and the connection between geometrical/topological effects and chiral effects.

References

- [1] Yang, C. N. The Law of Parity Conservation and Other Symmetry Laws of Physics. *Nobel Prize Lecture* (1957). URL <https://www.nobelprize.org/prizes/physics/1957/yang/lecture/>.
- [2] Berger, R. & Stohner, J. Parity violation. *Wiley Interdisciplinary Reviews: Computational Molecular Science* **9**, e1396 (2019). URL <https://onlinelibrary.wiley.com/doi/abs/10.1002/wcms.1396>.
- [3] Korenić, A., Perović, S., Ćirković, M. M. & Miquel, P.-A. Symmetry breaking and functional incompleteness in biological systems. *Progress in Biophysics and Molecular Biology (in press)* (2019). URL <http://www.sciencedirect.com/science/article/pii/S0079610718302530>.
- [4] Gal, J. The Discovery of Stereoselectivity at Biological Receptors: Arnaldo Piutti and the Taste of the Asparagine Enantiomers—History and Analysis on the 125th Anniversary. *Chirality* **24**, 959–976 (2012). URL <https://onlinelibrary.wiley.com/doi/abs/10.1002/chir.22071>.
- [5] Leitereg, T. J., Guadagni, D. G., Harris, J., Mon, T. R. & Teranishi, R. Chemical and sensory data supporting the difference between the odors of the enantiomeric carvones. *Journal of Agricultural and Food Chemistry* **19**, 785–787 (1971). URL <https://doi.org/10.1021/jf60176a035>.

- [6] Lin, G.-Q., You, Q.-D. & Cheng, J.-F. *Chiral Drugs: chemistry and biological action* (Wiley, Hoboken, New Jersey, 2011).
- [7] McGuire, B. A. *et al.* Discovery of the interstellar chiral molecule propylene oxide (CH₃CHCH₂O). *Science* **352**, 1449–1452 (2016). URL <https://science.sciencemag.org/content/352/6292/1449>.
- [8] Hays, F. A. *et al.* How sequence defines structure: A crystallographic map of dna structure and conformation. *Proceedings of the National Academy of Sciences* **102**, 7157–7162 (2005). URL <https://www.pnas.org/content/102/20/7157>. PDB ID: 1ZEW, <https://www.pnas.org/content/102/20/7157.full.pdf>. Tarini, M., Cignoni, P. & Montani, C. Ambient occlusion and edge cueing for enhancing real time molecular visualization. *IEEE Transactions on Visualization and Computer Graphics* **12**, 1237–1244 (2006).
- [9] Feringa, B. L. The Art of Building Small: from Molecular Switches to Motors. *Nobel Prize Lecture* (2016). URL <https://www.nobelprize.org/prizes/chemistry/2016/feringa/lecture/>.
- [10] Barron, L. D. *Molecular light scattering and optical activity* (Cambridge University Press, 2004), 2 edn.
- [11] Lowry, T. M. *Optical Rotatory Power* (Dover Publications, New York, 1964).
- [12] Condon, E. U. Theories of Optical Rotatory Power. *Reviews of Modern Physics* **9**, 432–457 (1937). URL <https://link.aps.org/doi/10.1103/RevModPhys.9.432>.
- [13] Berova, N., Polavarapu, P. L., Nakanishi, K. & Woody, R. W. *Comprehensive Chiroptical Spectroscopy*, vol. 1 (Wiley, Hoboken, New Jersey, 2012).
- [14] Andrews, D. L. & Thirunamachandran, T. On three-dimensional rotational averages. *The Journal of Chemical Physics* **67**, 5026–5033 (1977). URL <http://aip.scitation.org/doi/citedby/10.1063/1.434725>.
- [15] Ordonez, A. F. & Smirnova, O. Generalized perspective on chiral measurements without magnetic interactions. *Physical Review A* **98**, 063428 (2018). URL <https://link.aps.org/doi/10.1103/PhysRevA.98.063428>.
- [16] Ordonez, A. F. & Smirnova, O. Propensity rules in photoelectron circular dichroism in chiral molecules. I. Chiral hydrogen. *Physical Review A* **99**, 043416 (2019). URL <https://link.aps.org/doi/10.1103/PhysRevA.99.043416>.
- [17] Giordmaine, J. A. Nonlinear Optical Properties of Liquids. *Physical Review* **138**, A1599–A1606 (1965). URL <https://link.aps.org/doi/10.1103/PhysRev.138.A1599>.
- [18] Ritchie, B. Theory of the angular distribution of photoelectrons ejected from optically active molecules and molecular negative ions. *Physical Review A* **13**, 1411 (1976). URL <http://journals.aps.org/pr/abstract/10.1103/PhysRevA.13.1411>.
- [19] Craig, D. P. & Thirunamachandran, T. *Molecular Quantum Electrodynamics* (Academic Press, London, 1984).

- [20] Franken, P. A., Hill, A. E., Peters, C. W. & Weinreich, G. Generation of Optical Harmonics. *Physical Review Letters* **7**, 118–119 (1961). URL <https://link.aps.org/doi/10.1103/PhysRevLett.7.118>.
- [21] Boyd, R. *Nonlinear Optics* (Academic Press, 2008), 3 edn.
- [22] Rentzepis, P. M., Giordmaine, J. A. & Wecht, K. W. Coherent Optical Mixing in Optically Active Liquids. *Physical Review Letters* **16**, 792–794 (1966). URL <https://link.aps.org/doi/10.1103/PhysRevLett.16.792>.
- [23] Fischer, P., Wiersma, D. S., Righini, R., Champagne, B. & Buckingham, A. D. Three-Wave Mixing in Chiral Liquids. *Physical Review Letters* **85**, 4253–4256 (2000). URL <http://link.aps.org/doi/10.1103/PhysRevLett.85.4253>.
- [24] Belkin, M. A., Kulakov, T. A., Ernst, K.-H., Yan, L. & Shen, Y. R. Sum-Frequency Vibrational Spectroscopy on Chiral Liquids: A Novel Technique to Probe Molecular Chirality. *Physical Review Letters* **85**, 4474–4477 (2000). URL <https://link.aps.org/doi/10.1103/PhysRevLett.85.4474>.
- [25] Belkin, M. A., Han, S. H., Wei, X. & Shen, Y. R. Sum-Frequency Generation in Chiral Liquids near Electronic Resonance. *Physical Review Letters* **87**, 113001 (2001). URL <https://link.aps.org/doi/10.1103/PhysRevLett.87.113001>.
- [26] Petralli-Mallow, T., Wong, T. M., Byers, J. D., Yee, H. I. & Hicks, J. M. Circular dichroism spectroscopy at interfaces: a surface second harmonic generation study. *The Journal of Physical Chemistry* **97**, 1383–1388 (1993). URL <http://dx.doi.org/10.1021/j100109a022>.
- [27] Byers, J. D., Yee, H. I., Petralli-Mallow, T. & Hicks, J. M. Second-harmonic generation circular-dichroism spectroscopy from chiral monolayers. *Physical Review B* **49**, 14643–14647 (1994). URL <https://link.aps.org/doi/10.1103/PhysRevB.49.14643>.
- [28] Byers, J. D., Yee, H. I. & Hicks, J. M. A second harmonic generation analog of optical rotatory dispersion for the study of chiral monolayers. *The Journal of Chemical Physics* **101**, 6233–6241 (1994). URL <https://aip.scitation.org/doi/abs/10.1063/1.468378>.
- [29] Verbiest, T., Kauranen, M., Van Rompaey, Y. & Persoons, A. Optical Activity of Anisotropic Achiral Surfaces. *Physical Review Letters* **77**, 1456–1459 (1996). URL <https://link.aps.org/doi/10.1103/PhysRevLett.77.1456>.
- [30] Buckingham, A. D. & Fischer, P. Linear electro-optic effect in optically active liquids. *Chemical Physics Letters* **297**, 239–246 (1998). URL <http://www.sciencedirect.com/science/article/pii/S0009261498011440>.
- [31] Fischer, P., Buckingham, A. D., Beckwitt, K., Wiersma, D. S. & Wise, F. W. New Electro-Optic Effect: Sum-Frequency Generation from Optically Active Liquids in the Presence of a dc Electric Field. *Physical Review Letters* **91**, 173901 (2003). URL <https://link.aps.org/doi/10.1103/PhysRevLett.91.173901>.
- [32] Fischer, P. & Hache, F. Nonlinear optical spectroscopy of chiral molecules. *Chirality* **17**, 421–437 (2005). URL <https://onlinelibrary.wiley.com/doi/abs/10.1002/chir.20179>.

- [33] Patterson, D., Schnell, M. & Doyle, J. M. Enantiomer-specific detection of chiral molecules via microwave spectroscopy. *Nature* **497**, 475–477 (2013). URL <http://www.nature.com/nature/journal/v497/n7450/full/nature12150.html#author-information>.
- [34] Kroto, H. W. *Molecular Rotation Spectra*. Dover Books on Physics and Chemistry (Dover Publications, 1992).
- [35] Patterson, D. & Doyle, J. M. Sensitive Chiral Analysis via Microwave Three-Wave Mixing. *Physical Review Letters* **111**, 023008 (2013). URL <http://link.aps.org/doi/10.1103/PhysRevLett.111.023008>.
- [36] Shapiro, M. & Brumer, P. *Quantum Control of Molecular Processes* (Wiley-VCH, Weinheim, 2012), 2 edn.
- [37] Gerbasi, D., Brumer, P., Thanopoulos, I., Král, P. & Shapiro, M. Theory of the two step enantiomeric purification of 1,3 dimethylallene. *The Journal of Chemical Physics* **120**, 11557–11563 (2004). URL <https://aip.scitation.org/doi/abs/10.1063/1.1753552>.
- [38] Brumer, P., Frishman, E. & Shapiro, M. Principles of electric-dipole-allowed optical control of molecular chirality. *Physical Review A* **65**, 015401 (2001). URL <https://link.aps.org/doi/10.1103/PhysRevA.65.015401>.
- [39] Frishman, E., Shapiro, M., Gerbasi, D. & Brumer, P. Enantiomeric purification of nonpolarized racemic mixtures using coherent light. *The Journal of Chemical Physics* **119**, 7237–7246 (2003). URL <https://aip.scitation.org/doi/abs/10.1063/1.1603732>.
- [40] Ayuso, D. *et al.* Synthetic chiral light for efficient control of chiral light-matter interaction. *Nature Photonics* **13**, 866 (2019). URL <https://www.nature.com/articles/s41566-019-0531-2>.
- [41] Eibenberger, S., Doyle, J. & Patterson, D. Enantiomer-Specific State Transfer of Chiral Molecules. *Physical Review Letters* **118**, 123002 (2017). URL <https://link.aps.org/doi/10.1103/PhysRevLett.118.123002>.
- [42] Hirota, E. Triple resonance for a three-level system of a chiral molecule. *Proceedings of the Japan Academy, Series B* **88**, 120–128 (2012). URL https://www.jstage.jst.go.jp/article/pjab/88/3/88_3_120/_article.
- [43] Lehmann, K. K. Chapter 21 - Theory of Enantiomer-Specific Microwave Spectroscopy. In Laane, J. (ed.) *Frontiers and Advances in Molecular Spectroscopy*, 713–743 (Elsevier, 2018). URL <https://www.sciencedirect.com/science/article/pii/B9780128112205000228>.
- [44] Powis, I. Photoelectron circular dichroism of the randomly oriented chiral molecules glyceraldehyde and lactic acid. *The Journal of Chemical Physics* **112**, 301–310 (2000). URL <http://scitation.aip.org/content/aip/journal/jcp/112/1/10.1063/1.480581>.
- [45] Böwering, N. *et al.* Asymmetry in Photoelectron Emission from Chiral Molecules Induced by Circularly Polarized Light. *Physical Review Letters* **86**, 1187–1190 (2001). URL <http://link.aps.org/doi/10.1103/PhysRevLett.86.1187>.

- [46] Powis, I. Photoelectron Circular Dichroism in Chiral Molecules. In Rice, S. A. (ed.) *Advances in Chemical Physics*, 267–329 (John Wiley & Sons, Inc., 2008). URL <http://onlinelibrary.wiley.com/doi/10.1002/9780470259474.ch5/summary>.
- [47] Nahon, L., Garcia, G. A. & Powis, I. Valence shell one-photon photoelectron circular dichroism in chiral systems. *Journal of Electron Spectroscopy and Related Phenomena* **204**, Part B, 322–334 (2015). URL <https://www.sciencedirect.com/science/article/pii/S0368204815000766>.
- [48] Bethe, H. Über die nichtstationäre Behandlung des Photoeffekts. *Annalen der Physik* **396**, 443–449 (1930). URL <https://onlinelibrary.wiley.com/doi/abs/10.1002/andp.19303960404>.
- [49] Ordonez, A. F. & Smirnova, O. Propensity rules in photoelectron circular dichroism in chiral molecules. II. General picture. *Physical Review A* **99**, 043417 (2019). URL <https://link.aps.org/doi/10.1103/PhysRevA.99.043417>.
- [50] Lux, C. *et al.* Circular Dichroism in the Photoelectron Angular Distributions of Camphor and Fenchone from Multiphoton Ionization with Femtosecond Laser Pulses. *Angewandte Chemie International Edition* **51**, 5001–5005 (2012). URL <https://onlinelibrary.wiley.com/doi/abs/10.1002/anie.201109035>.
- [51] Brink, D. M. & Satchler, G. R. *Angular Momentum* (Clarendon Press, Oxford, 1968), 2 edn.
- [52] Ferré, A. *et al.* A table-top ultrashort light source in the extreme ultraviolet for circular dichroism experiments. *Nature Photonics* **9**, 93–98 (2015). URL <http://www.nature.com/nphoton/journal/v9/n2/full/nphoton.2014.314.html>.
- [53] Beaulieu, S. *et al.* Universality of photoelectron circular dichroism in the photoionization of chiral molecules. *New Journal of Physics* **18**, 102002 (2016). URL <http://stacks.iop.org/1367-2630/18/i=10/a=102002>.
- [54] Smirnova, O. & Ivanov, M. Multielectron High Harmonic Generation: simple man on a complex plane. *arXiv:1304.2413 [physics, physics:quant-ph]* (2013). URL <http://arxiv.org/abs/1304.2413>. ArXiv: 1304.2413. Smirnova, O. & Ivanov, M. Multielectron High Harmonic Generation: Simple Man on a Complex Plane. In *Attosecond and XUV Physics*, 201–256 (John Wiley & Sons, Ltd, 2014). URL <https://onlinelibrary.wiley.com/doi/abs/10.1002/9783527677689.ch7>.
- [55] Ivanov, M. Y., Spanner, M. & Smirnova, O. Anatomy of strong field ionization. *Journal of Modern Optics* **52**, 165–184 (2005). URL <http://dx.doi.org/10.1080/0950034042000275360>.
- [56] Comby, A. *et al.* Relaxation Dynamics in Photoexcited Chiral Molecules Studied by Time-Resolved Photoelectron Circular Dichroism: Toward Chiral Femtochemistry. *The Journal of Physical Chemistry Letters* **7**, 4514–4519 (2016). URL <http://dx.doi.org/10.1021/acs.jpcllett.6b02065>.
- [57] Beaulieu, S. *et al.* Attosecond-resolved photoionization of chiral molecules. *Science* **358**, 1288–1294 (2017). URL <http://science.sciencemag.org/content/358/6368/1288>.

- [58] Demekhin, P. V., Artemyev, A. N., Kastner, A. & Baumert, T. Photoelectron Circular Dichroism with Two Overlapping Laser Pulses of Carrier Frequencies ω and 2ω Linearly Polarized in Two Mutually Orthogonal Directions. *Physical Review Letters* **121**, 253201 (2018). URL <https://link.aps.org/doi/10.1103/PhysRevLett.121.253201>.
- [59] Rozen, S. *et al.* Controlling Subcycle Optical Chirality in the Photoionization of Chiral Molecules. *Physical Review X* **9**, 031004 (2019). URL <https://link.aps.org/doi/10.1103/PhysRevX.9.031004>.
- [60] Goetz, R. E., Koch, C. P. & Greenman, L. Quantum Control of Photoelectron Circular Dichroism. *Physical Review Letters* **122**, 013204 (2019). URL <https://link.aps.org/doi/10.1103/PhysRevLett.122.013204>.
- [61] Owens, A., Yachmenev, A., Yurchenko, S. N. & Küpper, J. Climbing the Rotational Ladder to Chirality. *Physical Review Letters* **121**, 193201 (2018). URL <https://link.aps.org/doi/10.1103/PhysRevLett.121.193201>.
- [62] Beaulieu, S. *et al.* Photoexcitation circular dichroism in chiral molecules. *Nature Physics* **14**, 484–489 (2018). URL <https://www.nature.com/articles/s41567-017-0038-z>.
- [63] Dubs, R. L., Dixit, S. N. & McKoy, V. Circular Dichroism in Photoelectron Angular Distributions from Oriented Linear Molecules. *Physical Review Letters* **54**, 1249–1251 (1985). URL <http://link.aps.org/doi/10.1103/PhysRevLett.54.1249>. Dubs, R. L., Dixit, S. N. & McKoy, V. Circular dichroism in photoelectron angular distributions from adsorbed atoms. *Physical Review B* **32**, 8389–8391 (1985). URL <http://link.aps.org/doi/10.1103/PhysRevB.32.8389>.
- [64] Tia, M. *et al.* Observation of Enhanced Chiral Asymmetries in the Inner-Shell Photoionization of Uniaxially Oriented Methyloxirane Enantiomers. *The Journal of Physical Chemistry Letters* **8**, 2780–2786 (2017). URL <https://doi.org/10.1021/acs.jpcllett.7b01000>.

Propensity rules in photoelectron circular dichroism in chiral molecules I: Chiral hydrogen

Andres F. Ordonez^{1,2,*} and Olga Smirnova^{1,2,†}

¹*Max-Born-Institut, Berlin, Germany*

²*Technische Universität Berlin, Berlin, Germany*

This is the accepted version of an article published in Physical Review A 99, 043416 (2019). The published version is available online at <http://dx.doi.org/10.1103/PhysRevA.99.043416>

Photoelectron circular dichroism results from one-photon ionization of chiral molecules by circularly polarized light and manifests itself in forward-backward asymmetry of electron emission in the direction orthogonal to the light polarization plane. What is the physical mechanism underlying asymmetric electron ejection? How “which way” information builds up in a chiral molecule and maps into forward-backward asymmetry?

We introduce instances of bound chiral wave functions resulting from stationary superpositions of states in a hydrogen atom and use them to show that the chiral response in one-photon ionization of aligned molecular ensembles originates from two propensity rules: (i) Sensitivity of ionization to the sense of electron rotation in the polarization plane. (ii) Sensitivity of ionization to the direction of charge displacement or stationary current orthogonal to the polarization plane. In the companion paper [Phys. Rev. A 99, 043417 (2019)] we show how the ideas presented here are part of a broader picture valid for all chiral molecules and arbitrary degrees of molecular alignment.

I. INTRODUCTION

Photoelectron circular dichroism (PECD) [1–4] heralded the “dipole revolution” in chiral discrimination: chiral discrimination without using chiral light. PECD belongs to a family of methods exciting rotational [5–8], electronic, and vibronic [9, 10] chiral dynamics without relying on relatively weak interactions with magnetic fields. In all these methods the chiral response arises already in the electric-dipole approximation and is significantly higher than in conventional techniques, such as e.g. absorption circular dichroism or optical rotation, known since the XIX century (see e.g. [11]). The connection between these electric-dipole-approximation-based methods is analyzed in [12]. The key feature that distinguishes them from standard techniques is that chiral discrimination relies on a chiral observer - the chiral reference frame defined by the electric field vectors and detector axis [12]. In PECD, ionization with circularly polarized light of a non-racemic mixture of randomly-oriented chiral molecules results in a forward-backward asymmetry (FBA) in the photoelectron angular distribution and is a very sensitive probe of photoionization dynamics and of molecular structure and conformation [13, 14]. PECD yields a chiral response as high as few tens of percent of the total signal and the method is quickly expanding from the realm of fundamental research to innovative applications, becoming a new tool in analytical chemistry [15–17]. PECD is studied extensively both experimentally [4, 18–44] and theoretically [2, 3, 12, 45–57] and was recently pioneered in the multiphoton [58–67], pump-probe [68], and strong-field ionization regimes [69, 70].

In this work we focus on the physical mechanisms underlying the chiral response in one-photon ionization at the level of electrons and introduce “elementary chiral instances” - chiral electronic wave functions of the hydrogen atom.

In molecules, with the exception of the ground electronic state, the chiral configuration of the nuclei is not a prerequisite for obtaining a chiral electronic wave function. Thus, one may consider using a laser field to imprint chirality on the electronic wave function of an achiral nuclear configuration. The ability to create a chiral electronic wave function in an atom via a chiral laser field [71] implies the possibility of creating perfectly oriented (and even stationary) ensembles of *synthetic chiral molecules* (atoms with chiral electronic wave functions) with a well defined handedness in a time-resolved fashion from an initially isotropic ensemble of atoms. Such time-resolved chiral control may open new possibilities in the fields of enantiomeric recognition and enrichment if the ensemble of synthetic chiral atoms is made to interact with actual chiral molecules. From a more fundamental point of view, the elementary chiral instances could be excited in atoms arranged in a lattice of arbitrary symmetry to explore an interplay of electronic chirality and lattice symmetry possibly leading to interesting synthetic chiral phases of matter.

Here our goal is to understand how molecular properties such as the probability density and the probability current give rise to PECD and how they affect the sign of the FBA in the one-photon ionization regime. In a forthcoming publication we will use the hydrogenic chiral wave functions to extend this study into the strong-field regime. As a first step towards our goal, we consider the case of photoionization from a bound chiral state into an achiral Coulomb continuum, and restrict the analysis to aligned samples.

* ordonez@mbi-berlin.de

† smirnova@mbi-berlin.de

As can be seen in Fig. 2 of [12] and in Figs. 3 and 5 of the companion paper [1], within the electric-dipole approximation, the photoelectron angular distribution of isotropic or aligned samples can display a FBA only if the sample is chiral. This is in contrast with other dichroic effects observed in oriented or aligned achiral systems (see e.g. [72, 73]).

An isotropic continuum such as that of the hydrogen atom cannot yield a FBA in an isotropically oriented ensemble (see [45] and Appendix VII A), because in this case the continuum is not able to keep track of the molecular orientations and therefore the information about the chirality of the bound state is completely washed out by the isotropic orientation averaging. However, this does not rule out the emergence of the FBA in an aligned ensemble, where only a restricted set of orientations comes into play. Therefore, the fact that we use an isotropic continuum shall not affect our discussion on the origins of PECD in any way beyond what is already obvious, namely, that the FBA we discuss relies entirely on the chirality of the bound state and that it vanishes if we include all possible molecular orientations.

In Sec. II we introduce the chiral hydrogenic states. In Sec. III we use the chiral hydrogenic states to focus on physical mechanisms underlying PECD in aligned molecules. In Sec. IV we discuss effects on the FBA that result from increasing the complexity of the initial state. In the companion paper [1] we show that optical propensity rules also underlie the emergence of the chiral response in photoionization in the general case of arbitrary chiral molecules and arbitrary degree of molecular alignment, and we also expose the link between the chiral response in aligned and unaligned molecular ensembles. Section V concludes this paper.

II. HYDROGENIC CHIRAL WAVE FUNCTIONS

We will describe three types of hydrogenic chiral wave functions. The first type (p-type) is of the form

$$|\chi_p^\pm\rangle = \frac{1}{\sqrt{2}} (|3p_{\pm 1}\rangle + |3d_{\pm 1}\rangle), \quad (1)$$

where $|nl_m\rangle$ denotes a hydrogenic state with principal quantum number n , angular momentum l , and magnetic quantum number m . $\chi_p^+(\vec{r})$ is shown in Fig. 1. The superposition of states with even and odd values of l breaks the inversion symmetry and leads to a wave function polarized (hence the subscript p) along the z axis, which is indicated by an arrow pointing down in Fig. 1. $m = \pm 1$ implies a probability current in the azimuthal direction and is indicated by a circular arrow in Fig. 1. The combination of these two features results in a chiral wave function, as is evident from its compound symbol. The sign of m determines the *enantiomer* and, as usual, the two *enantiomers* are related to each other through a re-

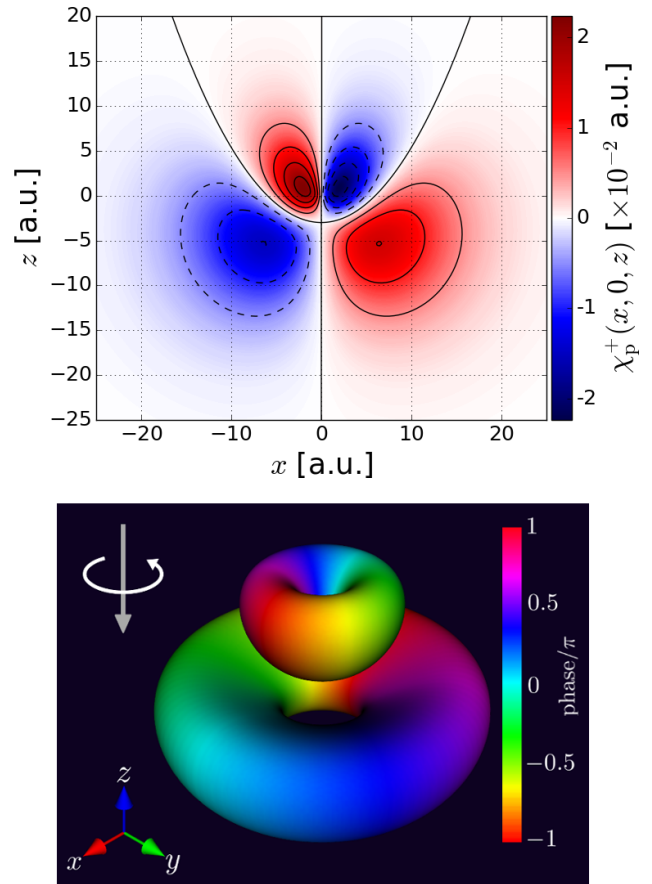


Figure 1. Top: contour map of $\chi_p^+(\vec{r})$ [Eq. (1)] on the $y = 0$ plane, where it only takes real values. Dashed (solid) lines indicate negative (zero or positive) contours. Bottom: isosurface $|\chi_p^+(\vec{r})| = 0.01$ a.u. colored according to the phase. The chiral symbol on the upper left corner indicates the polarization of the density (vertical arrow) and the probability current in the azimuthal direction (curved arrow).

flexion; in this case, across the $x = 0$ plane, as follows from the symmetry of spherical harmonics¹.

The second type (c-type) is given by

$$|\chi_c^\pm\rangle = \frac{1}{\sqrt{2}} (|3p_{\pm 1}\rangle + i|3d_{\pm 1}\rangle), \quad (2)$$

which differs from $|\chi_p\rangle$ only in the imaginary coefficient in front of $|3d_{\pm 1}\rangle$. At first sight, since $\langle \vec{r} | 3p_{\pm 1} \rangle$ and

¹ We could have also defined opposite enantiomers through an inversion, and in this case instead of changing m we would change the relative sign between $|3p_1\rangle$ and $|3d_1\rangle$. Both definitions of the opposite enantiomer are equivalent and are related to each other via a rotation.

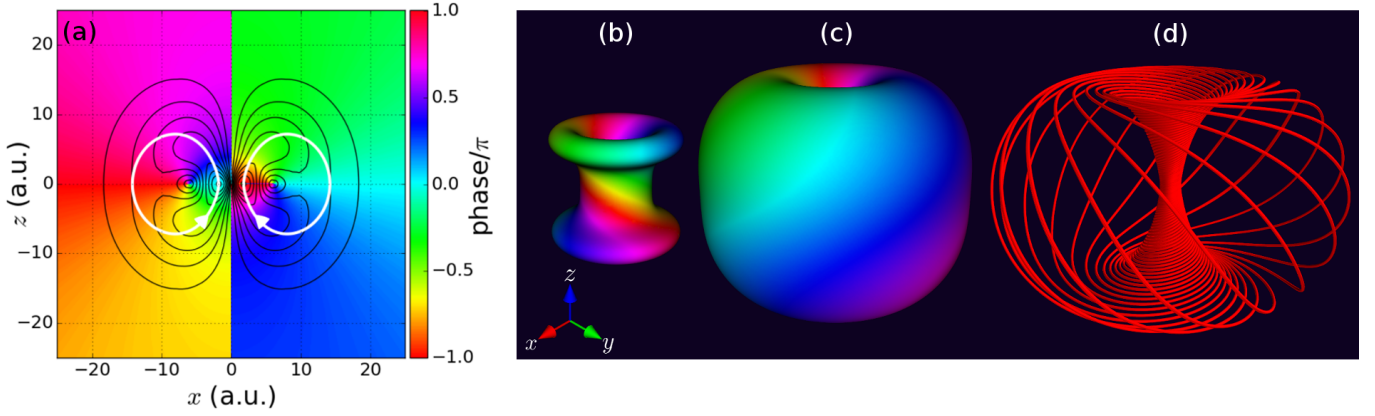


Figure 2. (a) Cut of $\chi_c^+(\vec{r})$ [Eq. (2)] on the $y = 0$ plane. The black lines indicate the contours of $|\chi_c^+(\vec{r})|$ while the colors indicate its phase. The white arrows indicate the direction of the component of the probability current in the $y = 0$ plane. (b) Isosurfaces $|\chi_c^+(\vec{r})| = 0.011$ a.u. and (c) $|\chi_c^+(\vec{r})| = 0.005$ a.u. colored according to the phase. (d) Trajectory followed by an element of the probability fluid $|\chi_c^+(\vec{r})|^2$. The rotation around the z axis is counterclockwise. The radial distance in this specific trajectory varies between 1 and 18.5 a.u.

$\langle \vec{r} | 3d_{\pm 1} \rangle$ are complex functions, one would not expect important differences between p and c states, however, as shown in Fig. 2, the p and c states are qualitatively different. We can see that instead of the polarization along z , there is probability current circulating around a nodal circle of radius 6 a.u. in the $z = 0$ plane, as indicated by the two circular arrows in Fig. 2 (a). Analogously to the p states, where the polarization of the probability density is determined by the relative sign between $|3p_{\pm 1}\rangle$ and $|3d_{\pm 1}\rangle$, in the c states the direction of the probability current is determined by the relative sign between $|3p_{\pm 1}\rangle$ and $i|3d_{\pm 1}\rangle$. This *out-of-plane* (polar) current combined with the *in-plane* (azimuthal) current due to $m = \pm 1$ leads to a chiral probability current (hence the c subscript), visualized in Fig. 2 (d) via the trajectory followed by an element of the probability fluid $|\chi_c^+(\vec{r})|^2$. This single trajectory (also known as a streamline in the context of fluids) clearly shows how, although pure helical motion of the electron is not compatible with a bound state, helical motion can still take place in a bound state via opposite helicities in the *inner* and *outer* regions². As can be inferred from the cut of $\chi_c^+(\vec{r})$ in the $y = 0$ plane [Fig. 2 (a)], trajectories passing far from the nodal circle, like that shown in Fig. 2 (d), circulate faster in the azimuthal direction than around the nodal circle while those close to the nodal circle have the opposite behavior and look like the wire in a toroidal solenoid. Interestingly, a probability current with the same topology was found in Ref. [74] when analyzing the effect of the (chiral) weak interaction on the hydrogenic state $2p_{1/2}$.

So far we have only considered wave functions with achiral probability densities whose chirality relies on non-

zero probability currents. The helical phase structure of $\chi_c^{\pm}(\vec{r})$ [see Figs. 2 (b) and (c)] suggests that we can construct a wave function $\chi_{\rho}^{\pm}(\vec{r})$ with chiral probability density (hence the subscript ρ) by taking the real part of $\chi_c^{\pm}(\vec{r})$, i.e.

$$\begin{aligned} |\chi_{\rho}^{\pm}\rangle &= \frac{1}{\sqrt{2}} (|\chi_c^{\pm}\rangle + \text{c.c.}) \\ &= \frac{1}{2} (|3p_{\pm 1}\rangle + i|3d_{\pm 1}\rangle - |3p_{\mp 1}\rangle + i|3d_{\mp 1}\rangle) \\ &= \frac{1}{\sqrt{2}} (\mp |3p_x\rangle + |3d_{yz}\rangle). \end{aligned} \quad (3)$$

It turns out that this wave function is not chiral. Nevertheless, increasing the l values by one results in the wave function we are looking for³. The third type (ρ -type) of chiral wave function is given by

$$\begin{aligned} |\chi_{\rho(421)}^{\pm}\rangle &= \frac{1}{\sqrt{2}} (|\chi_{c(421)}^{\pm}\rangle + \text{c.c.}) \\ &= \frac{1}{2} (|4d_{\pm 1}\rangle + i|4f_{\pm 1}\rangle - |4d_{\mp 1}\rangle + i|4f_{\mp 1}\rangle) \\ &= \frac{1}{\sqrt{2}} (\mp |4d_{xz}\rangle + |4f_{yz^2}\rangle) \end{aligned} \quad (4)$$

² We will say that a point is in the inner/outer region if the z component of its probability current is positive/negative.

³ It is also possible to obtain a chiral ρ state without increasing the value of l by replacing the c state in Eq. (3) by a superposition of the p [Eq. (1)] and c [Eq. (2)] states. However, the resulting state is less symmetric and does not provide any more insight than the one obtained in Eq. (4) so we decided to skip it in favor of clarity.

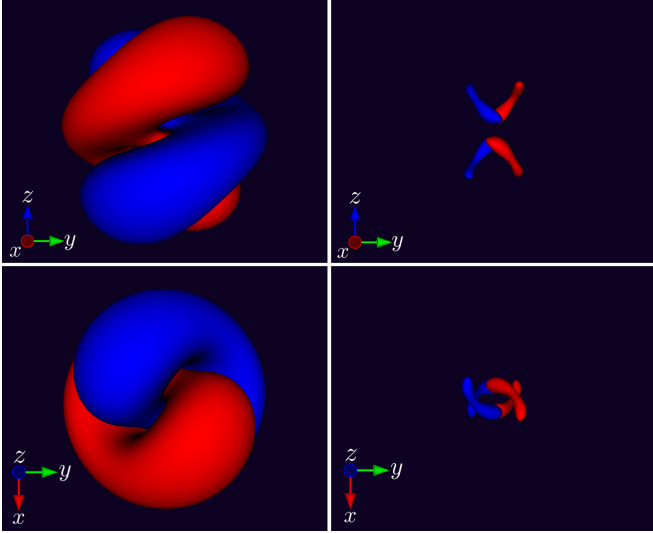


Figure 3. Isosurfaces $\chi_{\rho(421)}^+(\vec{r}) = \pm 0.001$ a.u. (left) and $\chi_{\rho(421)}^+(\vec{r}) = \pm 0.008$ a.u. (right) [Eq. (4)] viewed along the x (top) and z (bottom) axes.

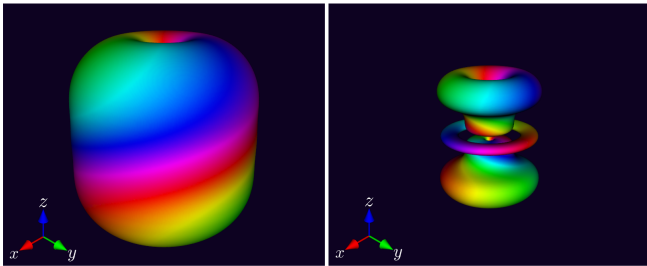
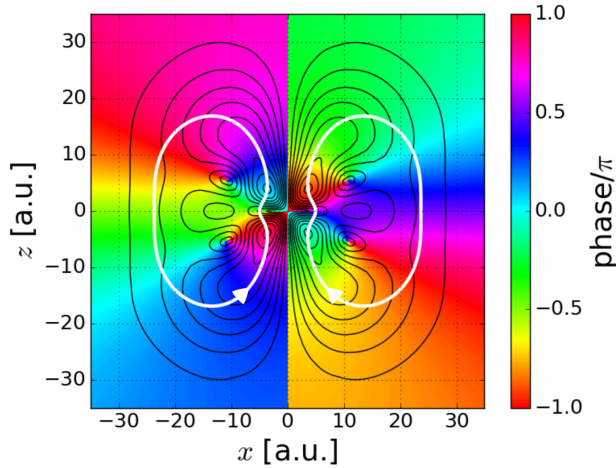


Figure 4. Top: cut of $\chi_{c(421)}^+(\vec{r})$ [Eq. (6)] on the $y = 0$ plane. The black lines indicate the contours of $|\chi_{c(421)}^+(\vec{r})|$ while the colors indicate its phase. The white arrows indicate the direction of the component of the probability current in the $y = 0$ plane. Bottom: isosurfaces $|\chi_{c(421)}^+(\vec{r})| = 0.001$ a.u. (left) and $|\chi_{c(421)}^+(\vec{r})| = 0.004$ a.u. (right) colored according to the phase.

and is shown in Fig. 3 for $m = 1$. In Eq. (4) we introduced the notation

$$|\chi_{p(nl|m)}^\pm\rangle \equiv \frac{1}{\sqrt{2}}(|n, l, \pm|m|\rangle + |n, l+1, \pm|m|\rangle) \quad (5)$$

$$|\chi_{c(nl|m)}^\pm\rangle \equiv \frac{1}{\sqrt{2}}(|n, l, \pm|m|\rangle + i|n, l+1, \pm|m|\rangle) \quad (6)$$

$$|\chi_{\rho(nl|m)}^\pm\rangle \equiv \frac{1}{\sqrt{2}}(|\chi_{c(nl|m)}^\pm\rangle + \text{c.c.}), \quad l \geq 2, \quad (7)$$

which includes straightforward modifications to the simplest cases in Eqs. (1), (2), and (4) that we have already considered. Figure 4 shows $\chi_{c(421)}^+(\vec{r})$, which was used in Eq. (4), and Figs. 5 and 6 the $m = 2$ variations $\chi_{c(422)}^+(\vec{r})$ and $\chi_{\rho(422)}^+(\vec{r}) = (\langle \vec{r} | 4d_{x^2-y^2} \rangle - \langle \vec{r} | 4f_{xyz} \rangle) / \sqrt{2}$ ⁴, which will be used for the analysis of PECD in the next subsection. As can be seen in Figs. 3 and 6, like the c states, the ρ states also have helical structures of opposite handedness in the *inner* and *outer* regions.

The ρ states are particularly meaningful because they mimic the electronic ground state of an actual chiral molecule in the sense that unlike the p and the c states, their chirality is completely encoded in the probability density and does not rely on probability currents. The decomposition of ρ states into c states is the chiral analogue of the decomposition of a standing wave into two waves traveling in opposite directions, and, as we shall see in the next subsection, it will provide the corresponding advantages.

Finally, note that according to Barron's definition of true and false chirality [75], the p states display false chirality because a time reversal yields the opposite enantiomer, while the c and ρ states display true chirality because a time-reversal yields the same enantiomer.

III. THE SIGN OF THE FORWARD-BACKWARD ASYMMETRY IN ALIGNED CHIRAL HYDROGEN

Now we consider photoionization from the chiral bound states just introduced via circularly polarized light. For this, we require the scattering wave function $\psi_k^{(-)}$. In the case of hydrogen, this wave function is known analytically [76]. $\psi_k^{(-)}$ has cylindrical symmetry with respect to \vec{k} and is shown in Fig. 7 for $k = 0.3$ a.u. in a

⁴ Interestingly, when plotted as in Fig. 6, the states $\chi_{\rho(l+1,l,l)}^\pm(\vec{r})$ form a topological structure known as torus link with linking number $\pm l$.

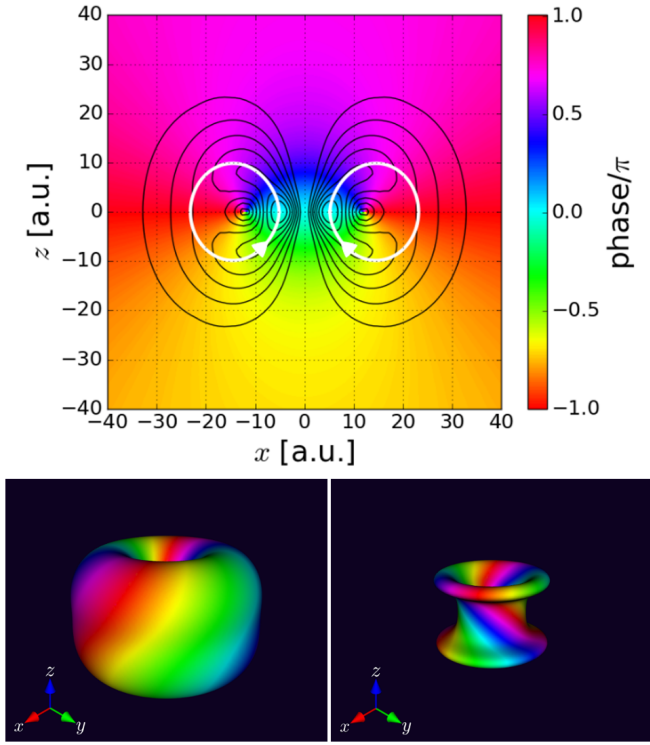


Figure 5. Top: cut of $\chi_{c(422)}^+(\vec{r})$ [Eq. (6)] on the $y = 0$ plane. The white arrows indicate the direction of the component of the probability current in the $y = 0$ plane. Bottom: isosurfaces $|\chi_{c(422)}^+(\vec{r})| = 0.003$ a.u. (left) and $|\chi_{c(422)}^+(\vec{r})| = 0.005$ a.u. (right) colored according to the phase.

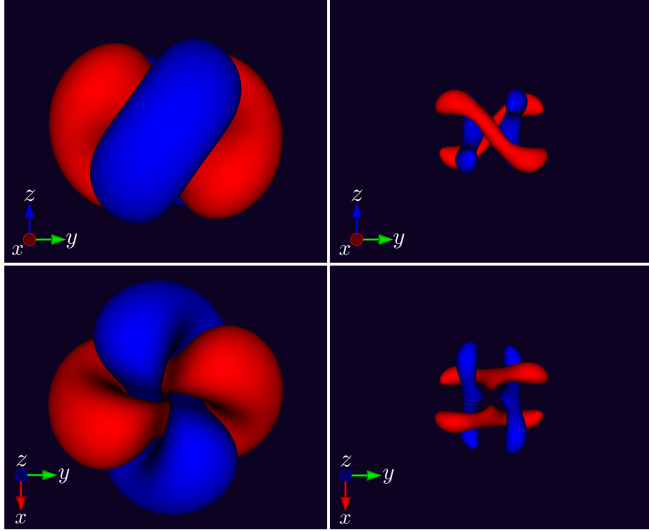


Figure 6. Isosurfaces $\chi_{\rho(422)}^+(\vec{r}) = \pm 0.001$ a.u. (left) and $\chi_{\rho(422)}^+(\vec{r}) = \pm 0.006$ a.u. (right) [Eq. (7)] viewed along the x (top) and z (bottom) axes.

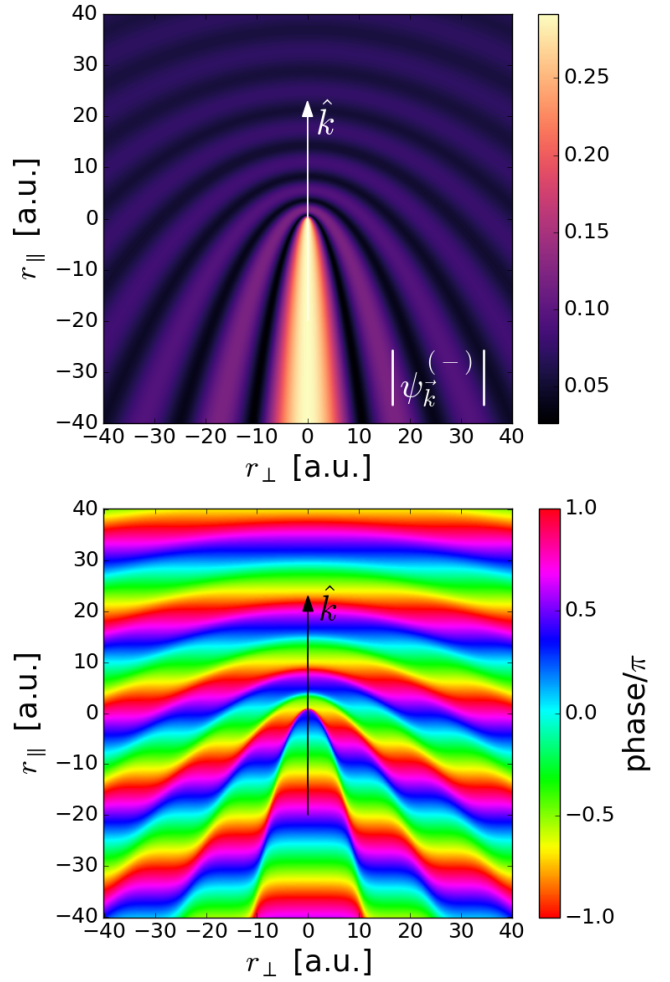


Figure 7. Absolute value (top) and phase (bottom) of the scattering wave function $\psi_{\vec{k}}^{(-)}(\vec{r})$ evaluated in a plane containing \vec{k} for $k = 0.3$ a.u. r_{\parallel} and r_{\perp} are the coordinates parallel and perpendicular to \vec{k} , respectively.

plane containing \vec{k} . Since only hydrogenic functions are involved, the calculation of the transition dipole matrix element $\langle \psi_{\vec{k}}^{(-)} | \vec{r} | \chi \rangle$ can be carried out analytically. The angular integrals reduce to 3-j symbols [77] and the radial integrals can be calculated using the method of contour integration described in [76].

The angle-integrated photoelectron current $\vec{j}(k)$ can be extracted from the angular and energy dependent ionization probability $W_{\sigma} \equiv |\langle \psi_{\vec{k}}^{(-)} | \vec{r} \cdot \vec{\mathcal{E}}_{\sigma} | \chi \rangle|^2$, where $\vec{\mathcal{E}}$ is the Fourier transform of the field and $\sigma = \pm 1$ indicates the rotation direction of the field (see also Ref. [12]). First we do a partial wave expansion of W_{σ} ,

$$W_{\sigma}(\vec{k}) = \sum_{l,m} b_{l,m}(k, \sigma) Y_l^m(\hat{k}), \quad (8)$$

and then we replace it in the expression for the z com-

ponent of the angle-integrated photoelectron current,

$$j_z(k, \sigma) = \int d\Omega_k W_\sigma(\vec{k}) k_z = \sqrt{\frac{4\pi}{3}} k b_{1,0}(k, \sigma). \quad (9)$$

For normalization purposes, one can also consider the radial component of the angle-integrated photoelectron current, which yields

$$j_r(k, \sigma) = \int d\Omega_k W_\sigma(\vec{k}) k = \sqrt{4\pi} k b_{0,0}(k, \sigma) \quad (10)$$

Figures 8 (a), 8 (b), and 9 show $j_z(k, \sigma)$ and $j_r(k, \sigma)$ for the case of photoionization from the initial states $|\chi_{p(311)}^\pm\rangle$ [see Eq. (1)] with their z molecular axis perpendicular to the plane of polarization of the ionizing light. We can clearly see two propensity rules that also hold for any other $|\chi_{p(nlm)}^\pm\rangle$ state: (i) the direction of j_z is determined by the electronic polarization direction of $\chi_{p(nlm)}^\pm(\vec{r})$ and (ii) the magnitudes of j_r and j_z are bigger when the bound electron rotates in the same direction as the electric field in comparison to when they rotate in opposite directions. The first propensity rule is a consequence of the non-plane-wave nature of the continuum wave function $\psi_k^{(-)}(\vec{r})$ (see Fig. 7), which resembles a bound polarized structure and leads to improved overlap between $\psi_k^{(-)}(\vec{r})$ and $\chi_{p(nlm)}^\pm(\vec{r})$ in the dipole matrix element when the direction of electronic polarization and the direction of the photoelectron coincide as compared to when they are opposite to each other. The polarized structure of $\psi_k^{(-)}(\vec{r})$ decays monotonously with increasing k and vanishes in the plane-wave limit, which explains the monotonous decay of $j_z(k)$. The second propensity rule is well known in the 1-photon-absorption atomic case [76]. This rule changes with the ionization regime [73, 78, 79].

In the aligned case, thanks to the vector nature of the photoelectron current, it is enough to consider only two opposite orientations (see Sec. III in our companion paper [1]). In view of the first propensity rule we have that for the two opposite orientations the polarization will point in opposite directions and therefore j_z will have opposite signs. However, since for opposite orientations the bound electron current also rotates in opposite directions while the light polarization remains fixed, the magnitude of j_z will be different for each orientation, thus avoiding a complete cancellation of the asymmetry. Furthermore, as can be seen in Fig. 8 (c), the sign of the orientation-averaged j_z will be that of the orientation where the electron co-rotates with the electric field of the light. That is, the propensity rule for the aligned case is that the total photoelectron current $\vec{j} = j_z \hat{z}$ will point in the direction of electronic polarization associated to the orientation where the bound electronic current co-rotates with the ionizing electric field.

A similar analysis can be carried out for the case of photoionization from the initial states $|\chi_{c(nlm)}^\pm\rangle$, shown

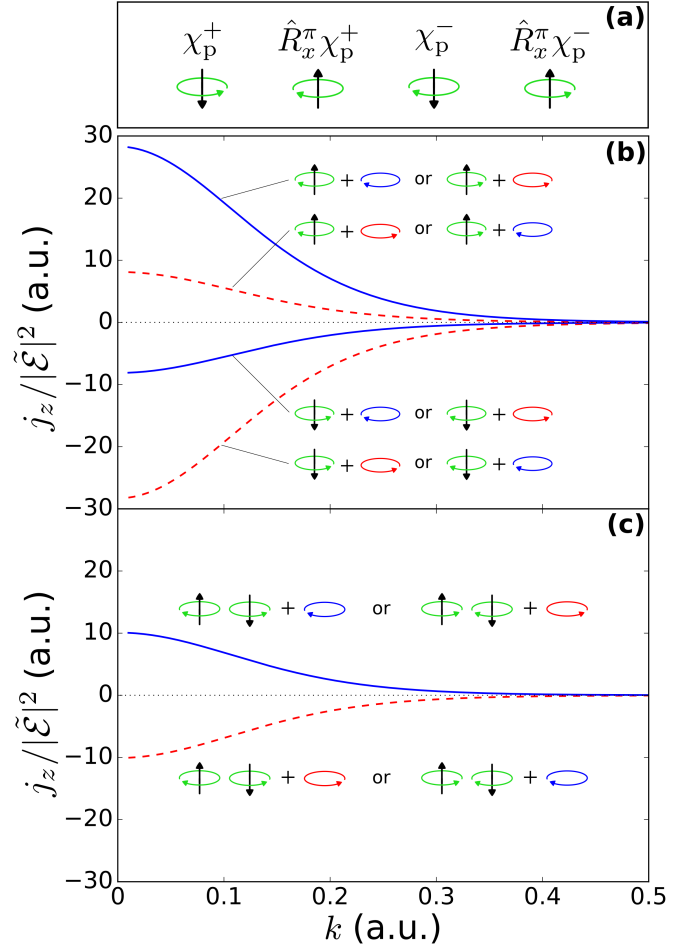


Figure 8. Photoelectron current along z as a function of photoelectron momentum resulting from photoionization of a p-type chiral state [see Eq. (5)] via light circularly polarized in the xy plane. (a) Diagrams indicating the electronic polarization (vertical arrow) and the electronic current (circular arrow) in the p-type chiral states for two opposite enantiomers and two opposite orientations. \hat{R}_x^π is the operator that rotates the wave function by π radians around the x axis. (b) Photoelectron current [Eq. (9)] for different enantiomer, orientation, and light polarization combinations. The enantiomer and its orientation is indicated by the diagrams explained in (a), and the light polarization is indicated by the circular arrows after the plus signs. Note that the sign of j_z is determined by the direction of the electronic polarization and that the magnitude of j_z is determined by the relative direction between the electronic current and the light polarization. (c) Photoelectron current averaged over two opposite orientations (equivalent to the aligned case) for different combinations of enantiomer and light polarization. There is no cancellation of the asymmetry because for one orientation the bound electron co-rotates with the field, while for the opposite orientation it counter-rotates. The calculations shown are for the states $\chi_{p(311)}^\pm$ but the conclusions are valid for any $\chi_{p(nlm)}^\pm$ state.

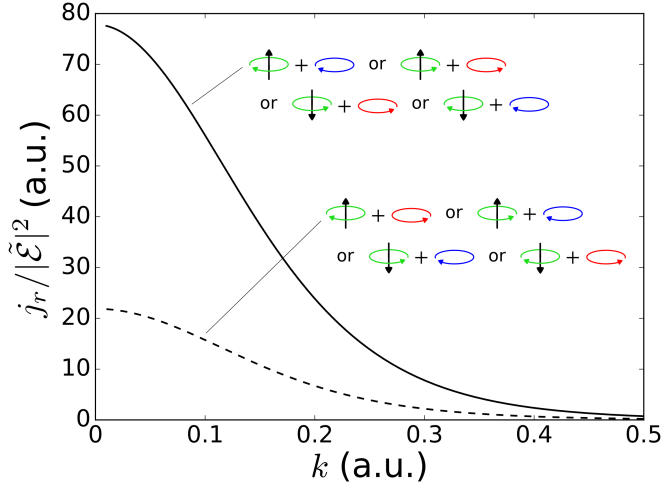


Figure 9. Total photoelectron current resulting from photoionization of a p-type chiral state [see Eq. (5)] via light circularly polarized in the xy plane for different enantiomer, orientation, and light polarization combinations. Diagrams are explained in Fig. 8 (a). Only the relative direction between the bound electronic current and the rotating electric field determines j_r . The calculations shown are for the states $\chi_{p(311)}^\pm$ but the conclusions are valid for any $\chi_{p(nlm)}^\pm$ state.

in Fig. 10 for the specific case where $(nlm) = (422)$ but valid for any other values of (nlm) . The only difference is that in this case the role which was played by the electronic polarization in the p-type states is now played by the vertical component of the electronic current in the inner region. Like before, this result can be understood by considering the overlap between the initial and final states. The polarized structure of the continuum state determines the region contributing more to the dipole matrix element (see $|\psi_k^{(-)}(\vec{r})|$ in Fig. 7) and the relative direction between the probability currents in the initial and final states in this region determines the amount of overlap. When the direction of the probability current of $\chi_{c(nlm)}^+(\vec{r})$ in the inner region (which is where $|\psi_k^{(-)}(\vec{r})|$ is greatest) is parallel to the direction of \vec{k} the overlap is maximized. Therefore, the propensity rule in this case is that the sign of j_z is positive/negative when the out-of-plane component of the electronic current in the inner region points up/down. The non-monotonous behavior of j_z as a function of k obeys the fact that this propensity rule not only relies on the polarized nature of $|\psi_k^{(-)}(\vec{r})|$, but also on the direction of the continuum probability current, therefore, for $k \rightarrow 0$, although the density of the continuum state is maximally polarized, its probability current tends to zero, rendering it unable to distinguish the direction of the probability current of the bound state, which is the feature responsible for the FBA in the first place. At an intermediate photoelectron momentum $k \approx 0.1$ a.u. the probability current of the continuum state matches that of the bound state and the sensitivity of the continuum state to the direction

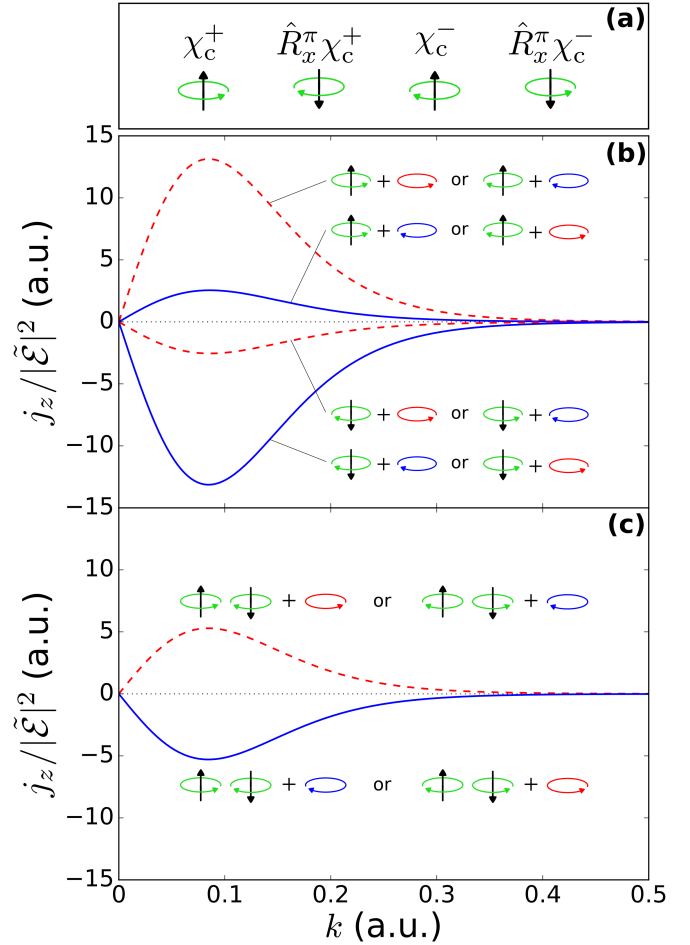


Figure 10. Same as Fig. 8 but for the c-type chiral states [see Eq. (6)]. The role played by the electronic polarization in the p-type states is replaced by the out-of-plane component of the probability current in the inner region in the c-type states. The results in (c) are also valid for photoionization from ρ -type chiral states (see text). The calculations shown are for the states $\chi_{c(422)}^\pm$ but the conclusions are valid for any $\chi_{c(nlm)}^\pm$ state.

of the probability current of the bound state is optimal. For larger values of k , the match worsens and the continuum also becomes less and less polarized leading to a monotonic decay of the FBA. The other propensity rule regarding the relative rotation of the bound current and the electric field remains the same as in the case of the p states and, again, the contributions from opposite orientations to j_z do not completely cancel each other.

Finally, in the case where the photoionization takes place from the states $|\chi_{\rho(nlm)}^\pm\rangle$ [see Eq. (7)], there is neither any probability current nor any net polarization that we can rely on. Furthermore, one can see from Figs. 3 and 6 that the wave function $\chi_{\rho(nlm)}^\pm(\vec{r})$ is invariant with respect to rotations by π either around the x or the y axis, so that j_z is the same for both orientations. Thus the situation appears to be quite different from what we

had for the states $|\chi_{p(nlm)}^\pm\rangle$ and $|\chi_{c(nlm)}^\pm\rangle$. However, we know that the chiral probability density of $|\chi_{\rho(nlm)}^\pm\rangle$ is the result of the superposition of the chiral currents from $|\chi_{c(nlm)}^\pm\rangle$ and its complex conjugate. These two chiral currents flow in opposite directions therefore, when we subject $|\chi_{\rho(nlm)}^\pm\rangle$ to a field circularly polarized in the xy plane, one part of $|\chi_{\rho(nlm)}^\pm\rangle$ will be counter-rotating and the other part will be co-rotating with the field. One part will have an upwards out-of-plane current in the inner region and the other will have a downwards out-of-plane current in the inner region. Thus the situation for a single orientation of $|\chi_{\rho(nlm)}^\pm\rangle$ is very similar to what we had before when we considered two opposite orientations of $|\chi_{c(nlm)}^\pm\rangle$. In fact, as shown in Appendix VII B, both situations are exactly equivalent in the case of an isotropic continuum like that of hydrogen. That is, the z component of the photoelectron current resulting from photoionization from the state $|\chi_{\rho(nlm)}^\pm\rangle$ is equal to that obtained from $|\chi_{c(nlm)}^\pm\rangle$ after averaging over two opposite orientations. The results plotted in Fig. 10 (c) are not only those obtained for $|\chi_{c(422)}^\pm\rangle$, but also those obtained for $|\chi_{\rho(422)}^\pm\rangle$. This shows that although the ρ -type states do not display any bound probability current, we can still make sense of the sign of the FBA displayed by their photoelectron angular distribution through their decomposition into c -type states.

An example of how to use these propensity rules for the less symmetric cases where the orientation of the molecular z axis is in the plane of the light polarization is given in Appendix VII C.

IV. EXTENSIONS OF THE MODEL

So far we have restricted our discussion to bound wave functions involving only two different consecutive angular momenta l with a specific phase between them of $0, \pi$ (p -type states), or $\pm\pi/2$ radians (c -type states). To get an idea of how increasing the complexity of the bound wave function may affect the FBA and the corresponding propensity rules we will consider what happens when we introduce either a third l component or an arbitrary phase shift between the two l components.

A third l component simply introduces the possibility of having a single wave function with more than one handedness (like a helix made of a tighter bound helix) and therefore a FBA which may change sign as a function of energy, a feature seen in actual molecules but absent in the simplest possible chiral wave functions we have presented. Consider for example the c -type wave function with three l values given by

$$|\chi_c^{+-}\rangle = \sqrt{\frac{9}{19}} \left\{ \frac{i}{3} |4p_1\rangle + |4d_1\rangle + i |4f_1\rangle \right\}, \quad (11)$$

which is a superposition of $|4p_1\rangle$ and the state $|\chi_{c(421)}\rangle$

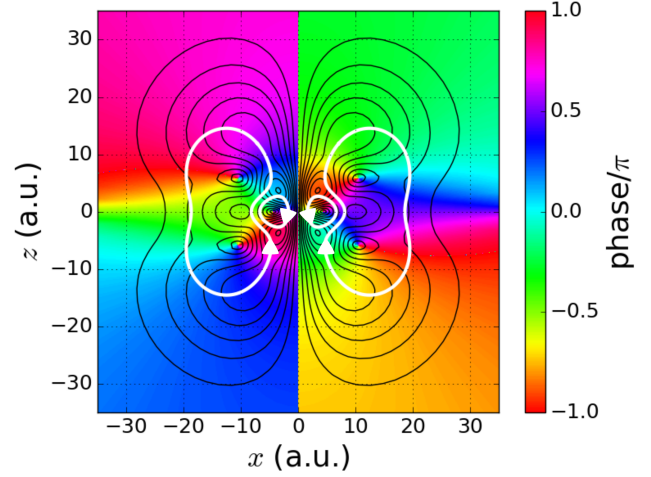


Figure 11. Cut of $\chi_c^{+-}(\vec{r})$ [Eq. (11)] on the $y = 0$ plane. The white arrows indicate the direction of the component of the probability current in the $y = 0$ plane. The extra loops in the innermost region (cf. Fig. 4) allow for an extra degree of handedness. One handedness is associated to the big loops (+) and the other to the small loops (-).

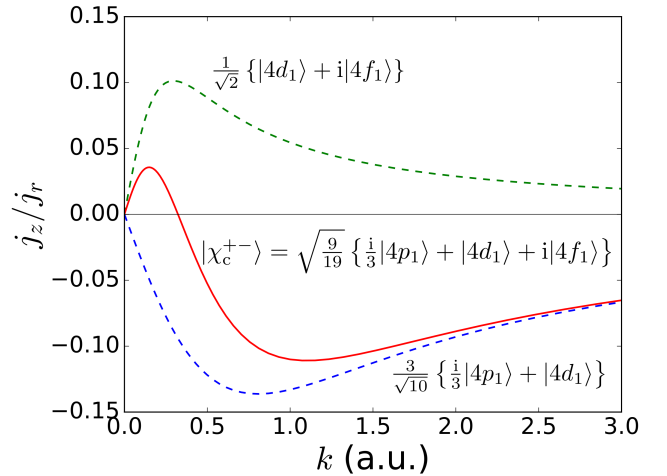


Figure 12. Normalized photoelectron current [Eqs. (9) and (10)] as a function of photoelectron momentum resulting from photoionization of the initial state $|\chi_c^{+-}\rangle$ in Eq. (11) (solid red line) via light left circularly polarized (rotating counter-clockwise as viewed from the $+z$ direction) and alignment perpendicular to the light polarization plane. The FBA changes sign as a function of photoelectron energy $k^2/2$ reflecting the ambivalent handedness of $|\chi_c^{+-}\rangle$ (see Fig. 11). The dashed lines show the corresponding currents for the ‘single-handed’ states that make up $|\chi_c^{+-}\rangle$.

[see Eq. (6)]. A plot of this wave function on the plane $y = 0$ is shown in Fig. 11 (compare with Fig. 4). Unlike the states $|\chi_{c(nml)}^\pm\rangle$, where the chiral current displays a single handedness, the state $|\chi_c^{+-}\rangle$ displays two possible handedness, one associated with the big current loops and the other one associated with the small current loops

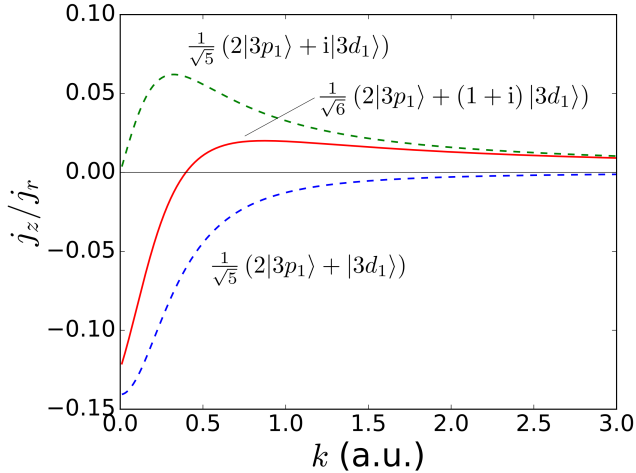


Figure 13. Normalized photoelectron current [Eqs. (9) and (10)] as a function of photoelectron momentum resulting from photoionization of the initial state $|\chi_{p(311)}^+\rangle + |\chi_{c(311)}^+\rangle$ (solid red line) via light left circularly polarized (rotating counterclockwise as viewed from the $+z$ direction) and alignment perpendicular to the light polarization plane. The FBA changes sign as a function of photoelectron energy $k^2/2$ reflecting the p-like (lower dashed line) and c-like character (upper dashed line) at lower and higher photoelectron energies, respectively.

in Fig. 11. Since the two chiral currents are confined to regions of different sizes, high (low) energy photoelectrons will probe more efficiently the chirality associated to the smaller (bigger) loops, and therefore one may observe a change of sign in the FBA as the photoelectron energy is increased. Figure 12 shows how each chiral component contributes to the total FBA. An analogous behavior is observed for the case of p-type states.

Clearly, closed current loops like those shown in Fig. 11 can only occur around a zero of the wave function, and the emergence of the small loops in Fig. 11 is associated with the emergence of a zero at $r \approx 4.4$ a.u., $\theta = \pi/2$. At the same time, the change of sign of the FBA is linked to the existence of the small loops, which suggests an interesting link between the topology of the wave function (zeros and currents around them) and the zeros of the FBA as a function of photoelectron energy. Further investigation of this point will be presented in a forthcoming publication.

Introduction of phases differing from zero or $\pi/2$ between consecutive l components simply means that instead of having a pure p- or a pure c-type state we have a superposition of both. This can also lead to a FBA that changes sign as a function of energy because the behavior of the FBA as a function of energy is different for p and c states. For example, as shown in Fig. 13, a state $|\chi_{p(311)}^+\rangle + |\chi_{c(311)}^+\rangle$ displays a FBA which is negative at lower energies and positive at higher energies,

i.e. it reflects the p character at lower energies and the c character at higher energies.

Although the concepts of polarization, current, and wave-function overlap, underlying the propensity rules are general, the assignment of specific propensity rules to chiral molecules can be impeded due to their considerably more complex electronic structure than the elementary chiral wave-functions introduced here. In the companion paper [1] we develop an alternative route, bypassing the specific propensity rules and introducing a more general measure, which simply indicates the presence thereof. This measure –propensity field– controls the sign of forward-backward asymmetry in PECD.

V. CONCLUSIONS

We have introduced three families of hydrogenic chiral wave functions that serve as basic tools for the analysis of electronic chiral effects. The chirality of these wave functions may be due either to a chiral density, a chiral probability current, or a combination of achiral density and achiral probability current.

We have used the chiral hydrogenic wave functions as a tool to explore the basic physical mechanisms underlying the chiral response in photoionization at the level of electrons. We have shown that two basic photoionization propensity rules determine the sign of the forward-backward asymmetry in photoelectron circular dichroism (PECD) in aligned molecules. One propensity rule selects the molecular orientations in which the electron and the electric field rotate in the same direction, and the other propensity rule determines whether the photoelectrons are emitted preferentially forwards or backwards. This simple picture illustrates that the propensity rules lie at the heart of photoelectron circular dichroism. In the companion paper [1] we show how these ideas can be extended to the case of randomly oriented molecules, where another layer of effects of geometrical origin add to this simple picture.

Note added in proof. Recently, the authors have been made aware of Ref. [80], where perturbed superpositions of two c-type states yield wave functions with nodal structures that display links and trefoils.

VI. ACKNOWLEDGEMENTS

A.F.O. and O.S. gratefully acknowledge the MEDEA project, which has received funding from the European Union’s Horizon 2020 research and innovation programme under the Marie Skłodowska-Curie grant agreement 641789. O.S. acknowledges support from the DFG SPP 1840 “Quantum Dynamics in Tailored Intense Fields” and the DFG grant SM 292/5-2.

VII. APPENDIX

A. Vanishing of the FBA for an orientation-independent continuum and an isotropically oriented ensemble

In this appendix we give a simple demonstration that an orientation-independent continuum yields a zero FBA when all molecular orientations are equally likely (see also [45]). Consider the lab-frame orientation-averaged photoelectron angular distribution

$$W_\sigma(\vec{k}) = \int d\lambda \left| \langle \psi_{\vec{k}}^{(-)} | \hat{\epsilon}_\sigma | \hat{D}(\lambda) \chi \rangle \right|^2, \quad (12)$$

where $\hat{\epsilon}_\sigma \equiv (\hat{x} + \sigma i \hat{y})$, $\sigma = \pm 1$, and $\hat{D}(\lambda)$ is the operator that rotates the bound wave function $\chi(\vec{r})$ by the Euler angles $\lambda \equiv \alpha\beta\gamma$. We assumed that the scattering wave function $\psi_{\vec{k}}^{(-)}(\vec{r})$ is independent of the molecular orientation λ and therefore there is no need to rotate it. Here we consider rotations in the active sense, i.e. we always have the same frame of reference (the lab frame) and we rotate the functions. If we expand the bound wave function in spherical harmonics as

$$\chi(\vec{r}) = \sum_{l,m} u_{l,m}(r) Y_l^m(\hat{r}), \quad (13)$$

then the rotation operator $\hat{D}(\lambda)$ acts on $\chi(\vec{r})$ through the Wigner D-matrices $D_{m',m}^{(l)}(\lambda)$ according to

$$\hat{D}(\lambda) \chi(\vec{r}) = \sum_{l,m,m'} D_{m',m}^{(l)}(\lambda) u_{l,m}(r) Y_l^{m'}(\hat{r}) = \sum_{l,m,m'} D_{m',m}^{(l)}(\lambda) \chi_{l,m,m'}(\vec{r}). \quad (14)$$

Replacing this expansion in the expression for the photoelectron angular distribution we obtain

$$\begin{aligned} W_\sigma(\vec{k}) &= \sum_{l_1, m_1, m'_1, l_2, m_2, m'_2} \left[\int d\lambda D_{m'_2, m_2}^{(l_2)*}(\lambda) D_{m'_1, m_1}^{(l_1)}(\lambda) \right] \langle \psi_{\vec{k}}^{(-)} | \hat{\epsilon}_\sigma | \chi_{l_2, m_2, m'_2} \rangle^* \langle \psi_{\vec{k}}^{(-)} | \hat{\epsilon}_\sigma | \chi_{l_1, m_1, m'_1} \rangle \\ &= \sum_{l_1, m_1, m'_1} \frac{8\pi^2}{2l_1 + 1} \left| \langle \psi_{\vec{k}}^{(-)} | \hat{\epsilon}_\sigma | \chi_{l_1, m_1, m'_1} \rangle \right|^2 \end{aligned} \quad (15)$$

where we used the orthogonality relation for the Wigner D-matrices [77]. Now we expand the scattering wave function in spherical harmonics with respect to \hat{k}

$$\psi_{\vec{k}}^{(-)}(\vec{r}) = \sum_{l,m} \psi_{k,l,m}(\vec{r}) Y_l^{m*}(\hat{k}), \quad (16)$$

and replace it in the expression for the photoelectron angular distribution

$$W_\sigma(\vec{k}) = \sum_{l,m,l_1,m_1,m'_1} \frac{8\pi^2}{2l_1 + 1} \left| \langle \psi_{k,l,m} | \hat{\epsilon}_\sigma | \chi_{l_1, m_1, m'_1} \rangle Y_l^m(\hat{k}) \right|^2 = \sum_{l,m} f_{\sigma,l,m}(k) \left| Y_l^m(\hat{k}) \right|^2 \quad (17)$$

where

$$f_{\sigma,l,m}(k) = \sum_{l_1, m_1, m'_1} \frac{8\pi^2}{2l_1 + 1} \left| \langle \psi_{k,l,m} | \hat{\epsilon}_\sigma | \chi_{l_1, m_1, m'_1} \rangle \right|^2. \quad (18)$$

Since $|Y_l^m(\hat{k})|^2$ is symmetric with respect to the xy plane for every l and m , Eq. (17) shows that $W_\sigma(\vec{k})$ is also symmetric with respect to the xy plane, and thus exhibits no FBA, irregardless of the values of the coefficients $f_{\sigma,l,m}(k)$ which encode the information about the chiral bound state and the light polarization. Any deviation from an orientation-independent scattering wave function will introduce cross-terms in Eqs. (15) and (17), and therefore will open the possibility of non-zero FBA.

B. Absence of m-coupling in the photoelectron current for isotropic continua

Consider the photoelectron angular distribution resulting from a single molecular orientation

$$W_\sigma(\vec{k}) = \left| \left\langle \psi_{\vec{k}}^{(-)} \left| \hat{\epsilon}_\sigma \right| \chi \right\rangle \right|^2, \quad (19)$$

where $\hat{\epsilon}_\sigma \equiv (\hat{x} + \sigma i \hat{y})$, $\sigma = \pm 1$, χ is the bound wave function that has already been rotated by the Euler angles $\lambda \equiv \alpha\beta\gamma$, and the scattering wave function is molecular-orientation independent, i.e. it only depends on the relative direction between the position vector \vec{r} and the photoelectron momentum \vec{k} . Both wave functions can be expanded as

$$\chi(\vec{r}) = \sum_{l,m} \chi_{l,m}(\vec{r}) \quad (20)$$

$$\psi_{\vec{k}}^{(-)}(\vec{r}) = \sum_{l,m} \psi_{l,m}(k, \vec{r}) Y_l^{m*}(\hat{k}), \quad (21)$$

where $\chi_{l,m}(\vec{r}) = u_{l,m}(r) Y_l^m(\hat{r})$ and $\psi_{l,m}(k, \vec{r}) = v_{l,m}(k, r) Y_l^m(\hat{r})$. Replacing these expansions in $W_\sigma(\vec{k})$ we get

$$W_\sigma(\vec{k}) = \sum_{l_1, m_1, l_2, m_2, l'_1, l'_2} \langle \psi_{l'_1, m_1 + \sigma} | \hat{\epsilon}_\sigma | \chi_{l_1, m_1} \rangle^* \langle \psi_{l'_2, m_2 + \sigma} | \hat{\epsilon}_\sigma | \chi_{l_2, m_2} \rangle Y_{l'_1}^{m_1 + \sigma*}(\hat{k}) Y_{l'_2}^{m_2 + \sigma}(\hat{k}) \quad (22)$$

where we used the selection rules $m'_1 = m_1 + \sigma$ and $m'_2 = m_2 + \sigma$ for the electric-dipole transitions. The product of the spherical harmonics $Y_{l'_1}^{m_1 + \sigma*} Y_{l'_2}^{m_2 + \sigma}$ can be rewritten as a superposition of spherical harmonics Y_l^m with $m = -m_1 + m_2$, and the calculation of j_z only requires the term $l, m = 1, 0$ [see Eq. (9)]. Therefore we must only consider the terms in Eq. (22) where $m_1 = m_2$, which means that the different m components in the bound wave function χ do not interfere in j_z . That is, the calculation of j_z for a coherent superposition $\chi_{l_1, m_1} + \chi_{l_2, m_2}$ yields the same result as the sum of the j_z 's obtained for each state of the superposition separately.

C. An example of propensity rules for the in-plane orientation.

Consider the state $|\chi_{\text{p}(311)}^+\rangle$ when the molecular frame is related to the lab frame by a rotation of $\pi/2$ around \hat{y}^{L} . In this case, the electronic polarization points along $-\hat{x}^{\text{L}}$ and the bound probability current is in the $\hat{y}^{\text{L}}\hat{z}^{\text{L}}$ plane. For light circularly polarized in the $\hat{x}^{\text{L}}\hat{y}^{\text{L}}$ plane, neither the asymmetry of the initial state (i.e. its electronic polarization) is along the direction perpendicular to the light polarization nor the bound probability current is in the plane of the light polarization. Nevertheless, with the help of the Wigner rotation matrices [77] we can write the rotated spherical harmonics in terms of unrotated spherical harmonics as

$$\hat{R}_y^{\pi/2} Y_1^1 = \frac{1}{2} Y_1^1 + \frac{1}{\sqrt{2}} Y_1^0 + \frac{1}{2} Y_1^{-1}, \quad (23)$$

$$\hat{R}_y^{\pi/2} Y_2^1 = -\frac{1}{2} Y_2^2 - \frac{1}{2} Y_2^1 + \frac{1}{2} Y_2^{-1} + \frac{1}{2} Y_2^{-2}. \quad (24)$$

Replacing Eqs. (23) and (24) in the expression for $\chi_{\text{p}(311)}^+$ [Eq. (1)] and using $\hat{R}_y^\pi Y_l^m = (-1)^{l+m} Y_l^{-m}$ we obtain

$$\begin{aligned} \hat{R}_y^{\pi/2} \chi_{\text{p}(311)}^+ &= \frac{1}{2} \frac{1}{\sqrt{2}} [R_{3,1} Y_1^1 - R_{3,2} Y_2^1 - R_{3,2} Y_2^2] + \frac{1}{2} \frac{1}{\sqrt{2}} [R_{3,1} Y_1^{-1} + R_{3,2} Y_2^{-1} + R_{3,2} Y_2^{-2}] + \frac{1}{2} R_{3,1} Y_1^0 \\ &= \frac{1}{2} \hat{R}_y^\pi \chi_{\text{p}(311)}^- + \frac{1}{2} \chi_{\text{p}(311)}^- + \frac{1}{\sqrt{2}} \Phi \end{aligned} \quad (25)$$

where $R_{n,l}(r)$ are the bound radial functions of hydrogen and we defined

$$\Phi(\vec{r}) = \frac{1}{\sqrt{2}} \left\{ R_{3,1}(r) Y_1^0(\hat{r}) + \frac{1}{\sqrt{2}} R_{3,2}(r) [Y_2^{-2}(\hat{r}) - Y_2^2(\hat{r})] \right\}. \quad (26)$$

In analogy to what we did before with the ρ state, we separated the wave function according to the direction of its probability current with respect to the z axis, i.e. into positive, negative, and zero m 's. In general, this is as far as we can go with the simplification, and at this point we must only figure out the sign of the asymmetry that the part co-rotating with the electric field yields to tell the sign of the FBA asymmetry that the full wave function yields. However, in this particularly simple case we can recognize that not only the $m = 0$ but also the $m = \pm 2$ terms do not contribute to the chirality of neither the co-rotating nor the counter-rotating parts. We have grouped this achiral terms into Φ . Furthermore, the remaining terms can be rewritten in terms of p states with their polarizations pointing along \hat{z}^L and $-\hat{z}^L$.

From the discussion of the propensity rules in Sec. III and from Fig. 8 we already know the j_z^L that will result from each of the p states appearing in Eq. (25). Furthermore, from Appendix VII B we know that each m component will have an independent effect on j_z . Therefore, although the unrotated state $\chi_{p(311)}^+(\vec{r}^L)$ exhibits a negative j_z^L for both left and right circularly polarized light, once we rotate this state by $\pi/2$ around \hat{y}^L Eq. (25) shows that it will exhibit a negative/positive j_z^L for right/left circularly polarized light because the signal from the second/first term will dominate.

We can also use Eq. (25) to verify that j_z vanishes in the isotropically-oriented case [see Eq. (17) of the companion paper [1]] by taking into account the 6 orientations of $|\chi_{p(311)}^+\rangle$ displayed in Fig. 2 of [1]

$$\begin{aligned} j_z &= \frac{1}{6} \left[j_z(\chi_p^+) + j_z(\hat{R}_y^\pi \chi_p^+) + 4j_z(\hat{R}_y^{\pi/2} \chi_p^+) \right] \\ &= \frac{1}{6} \left[j_z(\chi_p^+) + j_z(\hat{R}_y^\pi \chi_p^+) + j_z(\hat{R}_y^\pi \chi_p^-) + j_z(\chi_p^-) \right] \\ &= 0 \end{aligned} \quad (27)$$

where the arguments of j_z on the right hand side of Eq. (27) indicate the orientation of the initial wave function, and from symmetry we know that the four orientations where \hat{z}^M lies on the $\hat{x}^L \hat{y}^L$ plane yield the same photoelectron current.

-
- [1] A. F. Ordonez and O. Smirnova, *Physical Review A* **99**, 043417 (2019).
[2] B. Ritchie, *Physical Review A* **13**, 1411 (1976).
[3] I. Powis, *The Journal of Chemical Physics* **112**, 301 (2000).
[4] N. Böwering, T. Lischke, B. Schmidtke, N. Müller, T. Khalil, and U. Heinzmann, *Physical Review Letters* **86**, 1187 (2001).
[5] D. Patterson, M. Schnell, and J. M. Doyle, *Nature* **497**, 475 (2013).
[6] D. Patterson and J. M. Doyle, *Physical Review Letters* **111**, 023008 (2013).
[7] A. Yachmenev and S. N. Yurchenko, *Phys. Rev. Lett.* **117**, 033001 (2016).
[8] S. Eibenberger, J. Doyle, and D. Patterson, *Phys. Rev. Lett.* **118**, 123002 (2017).
[9] P. Fischer, A. D. Buckingham, and A. C. Albrecht, *Phys. Rev. A* **64**, 053816 (2001).
[10] S. Beaulieu, A. Comby, D. Descamps, B. Fabre, G. A. Garcia, R. Géneaux, A. G. Harvey, F. Lègaré, Z. Masín, L. Nahon, A. F. Ordonez, S. Petit, B. Pons, Y. Mairesse, O. Smirnova, and V. Blanchet, *Nature Physics* **14**, 484 (2018).
[11] E. U. Condon, *Reviews of Modern Physics* **9**, 432 (1937).
[12] A. F. Ordonez and O. Smirnova, *Physical Review A* **98**, 063428 (2018).
[13] I. Powis, in *Advances in Chemical Physics*, edited by S. A. Rice (John Wiley & Sons, Inc., 2008) pp. 267–329.
[14] L. Nahon, G. A. Garcia, and I. Powis, *Journal of Electron Spectroscopy and Related Phenomena Gas phase spectroscopic and dynamical studies at Free-Electron Lasers and other short wavelength sources*, **204, Part B**, 322 (2015).
[15] M. M. R. Fanoood, N. B. Ram, C. S. Lehmann, I. Powis, and M. H. M. Janssen, *Nature Communications* **6**, 7511 (2015).
[16] U. Boesl and A. Kartouzian, *Annual Review of Analytical Chemistry* **9**, 343 (2016).
[17] R. Hadidi, D. K. Bozanic, G. A. Garcia, and L. Nahon, *Advances in Physics: X* **3**, 1477530 (2018).
[18] G. A. Garcia, L. Nahon, M. Lebeck, J.-C. Houver, D. Doweck, and I. Powis, *The Journal of Chemical Physics* **119**, 8781 (2003).
[19] S. Turchini, N. Zema, G. Contini, G. Alberti, M. Alagia, S. Stranges, G. Fronzoni, M. Stener, P. Decleva, and T. Prosperi, *Phys. Rev. A* **70**, 014502 (2004).
[20] U. Hergenhahn, E. E. Rennie, O. Kugeler, S. Marburger, T. Lischke, I. Powis, and G. Garcia, *The Journal of*

- Chemical Physics* **120**, 4553 (2004).
- [21] T. Lischke, N. Böwering, B. Schmidtke, N. Müller, T. Khalil, and U. Heinzmann, *Phys. Rev. A* **70**, 022507 (2004).
- [22] S. Stranges, S. Turchini, M. Alagia, G. Alberti, G. Contini, P. Decleva, G. Fronzoni, M. Stener, N. Zema, and T. Prosperi, *The Journal of Chemical Physics* **122**, 244303 (2005).
- [23] A. Giardini, D. Catone, S. Stranges, M. Satta, M. Tacconi, S. Piccirillo, S. Turchini, N. Zema, G. Contini, T. Prosperi, P. Decleva, D. D. Tommaso, G. Fronzoni, M. Stener, A. Filippi, and M. Speranza, *ChemPhysChem* **6**, 1164 (2005).
- [24] C. J. Harding, E. Mikajlo, I. Powis, S. Barth, S. Joshi, V. Ulrich, and U. Hergenbahn, *The Journal of Chemical Physics* **123**, 234310 (2005).
- [25] L. Nahon, G. A. Garcia, C. J. Harding, E. Mikajlo, and I. Powis, *The Journal of Chemical Physics* **125**, 114309 (2006).
- [26] G. Contini, N. Zema, S. Turchini, D. Catone, T. Prosperi, V. Carravetta, P. Bolognesi, L. Avaldi, and V. Feyer, *The Journal of Chemical Physics* **127**, 124310 (2007).
- [27] G. A. Garcia, L. Nahon, C. J. Harding, and I. Powis, *Phys. Chem. Chem. Phys.* **10**, 1628 (2008).
- [28] V. Ulrich, S. Barth, S. Joshi, U. Hergenbahn, E. Mikajlo, C. J. Harding, and I. Powis, *The Journal of Physical Chemistry A* **112**, 3544 (2008).
- [29] I. Powis, C. J. Harding, G. A. Garcia, and L. Nahon, *ChemPhysChem* **9**, 475 (2008).
- [30] I. Powis, C. J. Harding, S. Barth, S. Joshi, V. Ulrich, and U. Hergenbahn, *Phys. Rev. A* **78**, 052501 (2008).
- [31] S. Turchini, D. Catone, G. Contini, N. Zema, S. Irrera, M. Stener, D. D. Tommaso, P. Decleva, and T. Prosperi, *ChemPhysChem* **10**, 1839 (2009).
- [32] G. A. Garcia, H. Soldi-Lose, L. Nahon, and I. Powis, *The Journal of Physical Chemistry A* **114**, 847 (2010), pMID: 20038111.
- [33] L. Nahon, G. A. Garcia, H. Soldi-Lose, S. Daly, and I. Powis, *Phys. Rev. A* **82**, 032514 (2010).
- [34] S. Daly, I. Powis, G. A. Garcia, H. Soldi-Lose, and L. Nahon, *The Journal of Chemical Physics* **134**, 064306 (2011).
- [35] D. Catone, M. Stener, P. Decleva, G. Contini, N. Zema, T. Prosperi, V. Feyer, K. C. Prince, and S. Turchini, *Phys. Rev. Lett.* **108**, 083001 (2012).
- [36] D. Catone, S. Turchini, M. Stener, P. Decleva, G. Contini, T. Prosperi, V. Feyer, K. C. Prince, and N. Zema, *Rendiconti Lincei* **24**, 269 (2013).
- [37] G. A. Garcia, L. Nahon, S. Daly, and I. Powis, *Nature Communications* **4**, 2132 (2013).
- [38] S. Turchini, D. Catone, N. Zema, G. Contini, T. Prosperi, P. Decleva, M. Stener, F. Rondino, S. Piccirillo, K. C. Prince, and M. Speranza, *ChemPhysChem* **14**, 1723 (2013).
- [39] M. Tia, B. Cunha de Miranda, S. Daly, F. Gaie-Levrel, G. A. Garcia, I. Powis, and L. Nahon, *The Journal of Physical Chemistry Letters* **4**, 2698 (2013).
- [40] I. Powis, S. Daly, M. Tia, B. Cunha de Miranda, G. A. Garcia, and L. Nahon, *Phys. Chem. Chem. Phys.* **16**, 467 (2014).
- [41] M. Tia, B. Cunha de Miranda, S. Daly, F. Gaie-Levrel, G. A. Garcia, L. Nahon, and I. Powis, *The Journal of Physical Chemistry A* **118**, 2765 (2014), pMID: 24654892.
- [42] L. Nahon, L. Nag, G. A. Garcia, I. Myrgorodska, U. Meierhenrich, S. Beaulieu, V. Wanie, V. Blanchet, R. Geneaux, and I. Powis, *Phys. Chem. Chem. Phys.* **18**, 12696 (2016).
- [43] G. A. Garcia, H. Dossmann, L. Nahon, S. Daly, and I. Powis, *ChemPhysChem* **18**, 500 (2016).
- [44] D. Catone, S. Turchini, G. Contini, T. Prosperi, M. Stener, P. Decleva, and N. Zema, *Chemical Physics* **482**, 294 (2017), electrons and nuclei in motion - correlation and dynamics in molecules (on the occasion of the 70th birthday of Lorenz S. Cederbaum).
- [45] N. A. Cherepkov, *Chemical Physics Letters* **87**, 344 (1982).
- [46] I. Powis, *The Journal of Physical Chemistry A* **104**, 878 (2000).
- [47] M. Stener, G. Fronzoni, D. D. Tommaso, and P. Decleva, *The Journal of Chemical Physics* **120**, 3284 (2004).
- [48] C. J. Harding and I. Powis, *The Journal of Chemical Physics* **125**, 234306 (2006).
- [49] D. D. Tommaso, M. Stener, G. Fronzoni, and P. Decleva, *ChemPhysChem* **7**, 924 (2006).
- [50] M. Stener, D. Di Tommaso, G. Fronzoni, P. Decleva, and I. Powis, *The Journal of Chemical Physics* **124**, 024326 (2006).
- [51] I. Dreissigacker and M. Lein, *Physical Review A* **89**, 053406 (2014).
- [52] A. N. Artemyev, A. D. Müller, D. Hochstuhl, and P. V. Demekhin, *The Journal of Chemical Physics* **142**, 244105 (2015).
- [53] R. E. Goetz, T. A. Isaev, B. Nikoobakht, R. Berger, and C. P. Koch, *The Journal of Chemical Physics* **146**, 024306 (2017).
- [54] M. Ilchen, G. Hartmann, P. Rupprecht, A. N. Artemyev, R. N. Coffee, Z. Li, H. Ohldag, H. Ogasawara, T. Osipov, D. Ray, P. Schmidt, T. J. A. Wolf, A. Ehresmann, S. Moeller, A. Knie, and P. V. Demekhin, *Phys. Rev. A* **95**, 053423 (2017).
- [55] M. Tia, M. Pitzer, G. Kastirke, J. Gatzke, H.-K. Kim, F. Trinter, J. Rist, A. Hartung, D. Trabert, J. Siebert, K. Henrichs, J. Becht, S. Zeller, H. Gassert, F. Wiegandt, R. Wallauer, A. Kuhlins, C. Schober, T. Bauer, N. Wechselberger, P. Burzynski, J. Neff, M. Weller, D. Metz, M. Kircher, M. Waitz, J. B. Williams, L. P. H. Schmidt, A. D. Müller, A. Knie, A. Hans, L. Ben Ltaief, A. Ehresmann, R. Berger, H. Fukuzawa, K. Ueda, H. Schmidt-Böcking, R. Dörner, T. Jahnke, P. V. Demekhin, and M. Schöffler, *The Journal of Physical Chemistry Letters* **8**, 2780 (2017), pMID: 28582620.
- [56] S. Daly, I. Powis, G. A. Garcia, M. Tia, and L. Nahon, *The Journal of Chemical Physics* **147**, 013937 (2017).
- [57] J. Miles, D. Fernandes, A. Young, C. Bond, S. Crane, O. Ghafur, D. Townsend, J. Sá, and J. Greenwood, *Analytica Chimica Acta* **984**, 134 (2017).
- [58] C. Lux, M. Wollenhaupt, T. Bolze, Q. Liang, J. Koehler, C. Sarpe, and T. Baumert, *Angewandte Chemie International Edition* **51**, 5001 (2012).
- [59] C. S. Lehmann, R. B. Ram, I. Powis, and M. H. M. Janssen, *The Journal of Chemical Physics* **139**, 234307 (2013).
- [60] M. M. Rafiee Fanood, I. Powis, and M. H. M. Janssen, *The Journal of Physical Chemistry A* **118**, 11541 (2014), pMID: 25402546.
- [61] M. M. Rafiee Fanood, M. H. M. Janssen, and I. Powis, *Phys. Chem. Chem. Phys.* **17**, 8614 (2015).

- [62] C. Lux, M. Wollenhaupt, C. Sarpe, and T. Baumert, *ChemPhysChem* **16**, 115 (2015).
- [63] C. Lux, A. Senftleben, C. Sarpe, M. Wollenhaupt, and T. Baumert, *Journal of Physics B: Atomic, Molecular and Optical Physics* **49**, 02LT01 (2016).
- [64] M. M. R. Fanoood, M. H. M. Janssen, and I. Powis, *The Journal of Chemical Physics* **145**, 124320 (2016).
- [65] A. Kastner, C. Lux, T. Ring, S. Züllighoven, C. Sarpe, A. Senftleben, and T. Baumert, *ChemPhysChem* **17**, 1119 (2016).
- [66] S. Beaulieu, A. Comby, A. Clergerie, J. Caillat, D. Descamps, N. Dudovich, B. Fabre, R. Généaux, F. Légaré, S. Petit, B. Pons, G. Porat, T. Ruchon, R. Taïeb, V. Blanchet, and Y. Mairesse, *Science* **358**, 1288 (2017).
- [67] A. Kastner, T. Ring, B. C. Krüger, G. B. Park, T. Schäfer, A. Senftleben, and T. Baumert, *The Journal of Chemical Physics* **147**, 013926 (2017).
- [68] A. Comby, S. Beaulieu, M. Boggio-Pasqua, D. Descamps, F. Legare, L. Nahon, S. Petit, B. Pons, B. Fabre, Y. Mairesse, and V. Blanchet, *The Journal of Physical Chemistry Letters* **7**, 4514 (2016).
- [69] S. Beaulieu, A. Ferre, R. Geneaux, R. Canonge, D. Descamps, B. Fabre, N. Fedorov, F. Legare, S. Petit, T. Ruchon, V. Blanchet, Y. Mairesse, and B. Pons, *New Journal of Physics* **18**, 102002 (2016).
- [70] S. Beaulieu, A. Comby, B. Fabre, D. Descamps, A. Ferre, G. Garcia, R. Geneaux, F. Legare, L. Nahon, S. Petit, T. Ruchon, B. Pons, V. Blanchet, and Y. Mairesse, *Faraday Discuss.* **194**, 325 (2016).
- [71] D. Ayuso, O. Neufeld, A. F. Ordonez, P. Declava, G. Lerner, O. Cohen, M. Ivanov, and O. Smirnova, *Nature Photonics* **13**, 866 (2019).
- [72] R. L. Dubs, S. N. Dixit, and V. McKoy, *Physical Review B* **32**, 8389 (1985).
- [73] M. Ilchen, N. Douguet, T. Mazza, A. Rafipoor, C. Callegari, P. Finetti, O. Plekan, K. Prince, A. Demidovich, C. Grazioli, L. Avaldi, P. Bolognesi, M. Coreno, M. Di Fraia, M. Devetta, Y. Ovcharenko, S. D'Estéer, K. Ueda, K. Bartschat, A. Grum-Grzhimailo, A. Bozhevolnov, A. Kazansky, N. Kabachnik, and M. Meyer, *Physical Review Letters* **118**, 013002 (2017).
- [74] R. A. Hegstrom, J. P. Chamberlain, K. Seto, and R. G. Watson, *American Journal of Physics* **56**, 1086 (1988).
- [75] L. D. Barron, *Chemical Physics Letters* **123**, 423 (1986).
- [76] Hans A. Bethe and Edwin Salpeter, *Quantum mechanics of one- and two-electron atoms* (Springer Verlag, 1957).
- [77] D. M. Brink and G. R. Satchler, *Angular Momentum*, 2nd ed. (Clarendon Press, Oxford, 1968).
- [78] I. Barth and O. Smirnova, *Physical Review A* **84**, 10.1103/PhysRevA.84.063415 (2011).
- [79] I. Barth and O. Smirnova, *Physical Review A* **87**, 013433 (2013).
- [80] M. Berry, *Foundations of Physics* **31**, 659 (2001).

Photoexcitation Circular Dichroism in Chiral Molecules

S. Beaulieu,^{1,2} A. Comby,¹ D. Descamps,¹ B. Fabre,¹ G. A. Garcia,³ R. Géneaux,⁴ A. G. Harvey,⁵ F. Légaré,² Z. Mašín,⁵ L. Nahon,³ A. F. Ordóñez,^{5,6} S. Petit,¹ B. Pons,^{1,*} Y. Mairesse,^{1,†} O. Smirnova,^{5,6,‡} and V. Blanchet¹

¹ *Université de Bordeaux - CNRS - CEA, CELIA, UMR5107, F33405 Talence, France*

² *Institut National de la Recherche Scientifique, Varennes, Quebec, Canada*

³ *Synchrotron Soleil, l'orme des Merisiers, BP48, St Aubin, 91192 Gif sur Yvette, France*

⁴ *LIDYL, CEA, CNRS, Université Paris-Saclay, CEA Saclay, 91191 Gif-sur-Yvette France*

⁵ *Max-Born-Institut, Max-Born-Str. 2A, 12489 Berlin, Germany*

⁶ *Technische Universität Berlin, Ernst-Ruska-Gebäude, Hardenbergstr. 36 A, 10623, Berlin, Germany*

This is the accepted version of an article published in Nature Physics 14, 484 (2018). The published version is available online at <http://dx.doi.org/10.1038/s41567-017-0038-z>

Chirality is ubiquitous in nature and fundamental in science, from particle physics to metamaterials. The standard technique of chiral discrimination - photoabsorption circular dichroism - relies on the magnetic properties of a chiral medium and yields an extremely weak chiral response. We propose and demonstrate a new, orders of magnitude more sensitive type of circular dichroism in neutral molecules: photoexcitation circular dichroism. It does not rely on weak magnetic effects, but takes advantage of the coherent helical motion of bound electrons excited by ultrashort circularly polarized light. It results in an ultrafast chiral response and the efficient excitation of a macroscopic chiral density in an initially isotropic ensemble of randomly oriented chiral molecules. We probe this excitation without the aid of further chiral interactions using linearly polarized laser pulses. Our time-resolved study of vibronic chiral dynamics opens a way to the efficient initiation, control and monitoring of chiral chemical change in neutral molecules at the level of electrons.

The macro-world gives us many examples of chiral dynamics created by helical structures which convert rotations in a plane into translational motion orthogonal to it, from the Archimedes screw to plane propellers and household fans. In the micro-world, the electrons bound inside chiral molecules should develop a similar helical motion when excited by planar rotation of the electric field of circularly polarized light. Electronic excitation by circularly polarized light has been used to distinguish right-handed from left-handed molecules since 1896 [1]. This technique, called the photoabsorption circular dichroism (CD) [2], is based on the difference in the absorption of left- and right-circularly polarized light in chiral molecules and remains the go-to tool [3] for analysing properties of biological molecules, providing indispensable information on their structure, kinetics and thermodynamics, interaction with their environment and with other molecules. However, it does not rely on the helical nature of bound electron currents, but uses the helical pitch of the light wave instead. This pitch, given by the wavelength of the absorbed light, $\lambda \gtrsim 2500\text{\AA}$ ($1\text{\AA} = 10^{-8}$ cm), is barely noticeable on the molecular scale of $\sim 1\text{\AA}$, leading to very weak signals, three to four orders of magnitude less than the light absorption itself. Formally, the chiral-sensitive part of the light-induced excitation requires the excited electrons to respond to both the electric and the magnetic field of the light wave, see Fig. 1(a).

Remarkably, in spite of extraordinary recent advances in developing new methods for chiral discrimination that do not rely on the magnetic properties of the medium [4–15], none has relied on using the helical motion of bound electrons. Is it possible to excite and probe such motion without the help of magnetic field effects?

Exciting chiral dynamics in bound states

A hallmark of helical motion of bound electrons is the appearance of an induced dipole orthogonal to the polarization plane of the exciting circular light. We first show that an ultrashort pulse creates such a dipole in a randomly oriented molecular ensemble. Let the electric field of the pulse, rotating in the x-y plane, coherently excite two electronic states (Fig. 1(b)) of a chiral molecule. As shown in the Methods, the orientation-averaged induced dipole acquires the desired component along the light propagation direction z :

$$d_z^{\text{PXCD}} \propto \sigma [\vec{d}_{01} \times \vec{d}_{02}] \cdot \vec{d}_{12} \sin(\Delta E_{21}t), \quad (1)$$

Here $\sigma = \pm 1$ is the light helicity, \vec{d}_{01} , \vec{d}_{02} and \vec{d}_{12} are the dipole transition vectors connecting the ground $|0\rangle$ and the two excited electronic states $|1\rangle$, $|2\rangle$ (Fig. 1(b)), ΔE_{21} is the energy spacing between the two excited states. For more than two states, Eq. (1) will contain the sum over all pairs of excited states n, m , leading to oscillations at all relevant frequencies ΔE_{nm} . As a function of time the induced dipole vector \vec{d}^{PXCD} maps out a helix (Fig. 1(b)) and the z -component of the helical current is

$$j_z^{\text{PXCD}} \propto \sigma [\vec{d}_{01} \times \vec{d}_{02}] \cdot \vec{d}_{12} \Delta E_{21} \cos(\Delta E_{21}t). \quad (2)$$

Both d_z^{PXCD} and j_z^{PXCD} are quintessential chiral observables (see e.g. [16, 17]). Indeed, both are proportional

* bernard.pons@u-bordeaux.fr

† yann.mairesse@u-bordeaux.fr

‡ Olga.Smirnova@mbi-berlin.de

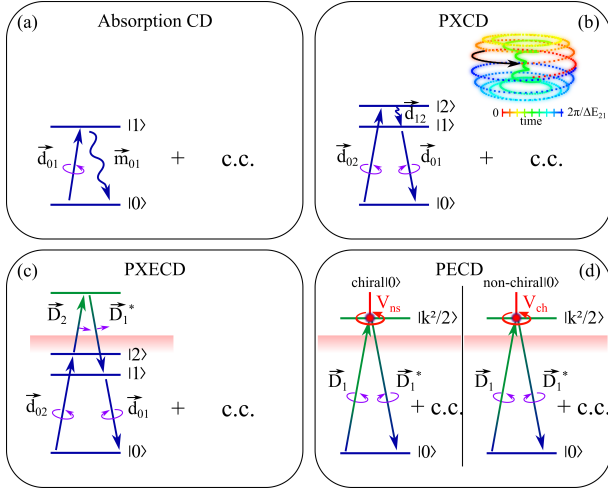


FIG. 1. **Chiral discrimination schemes in randomly oriented molecular ensembles.** The complex conjugated diagrams, complementing those presented, are omitted. Down-arrows denote complex-conjugation of driving fields. (a) CD requires an electric dipole transition up and a magnetic dipole transition down and vice-versa. (b) PXCD (Eq. (1)) requires a coherent excitation of two states by ultrashort circularly polarized pulse. The excitation dipole transition to state $|2\rangle$ is followed by a dipole transition to state $|1\rangle$ and a stimulated dipole transition to state $|0\rangle$. Inset: Induced dipole maps out a helix as a function of time. (c) In PXECD (Eq. (3)) the two excited states $|1\rangle$ and $|2\rangle$ are connected by Raman-type transitions via the continuum, stimulated by a linearly polarized probe pulse. (d) PECD requires circularly polarized light and a photoelectron scattering in a chiral V_{ch} (right panel) or non-spherically symmetric V_{ns} potential (left panel). Red arrows indicate a torque (imparted on the emitted photoelectron) which survives the orientational averaging and induces the chiral response in PECD.

to the light helicity $\sigma = \pm 1$ and to the triple product of three vectors $[\vec{d}_{01} \times \vec{d}_{02}] \cdot \vec{d}_{12}$. The latter product is a pseudo-scalar and as such presents a fundamental measure of chirality: it changes sign upon reflection and thus has an opposite sign for left and right enantiomers. For randomly oriented non-chiral molecules $d_z^{\text{PXCD}} = j_z^{\text{PXCD}} = 0$.

Eqs. (1,2) lead to the following conclusions. First, the coherent excitation of electronic states leads to a charge displacement along the light propagation direction. Hence, a macroscopic dipole d_z^{PXCD} and the corresponding chiral density are created in the excited states, with a chiral current oscillating out of phase for the two enantiomers. Second, PXCD requires no magnetic or quadrupole effects, and so, it is orders of magnitude stronger than standard photoabsorption CD. While photoabsorption CD exploits the helical pitch of the laser field in space, PXCD takes advantage of the sub-cycle rotation of the light field in time and is inherently ultrafast. PXCD arises only if the excitation dipoles \vec{d}_{01} , \vec{d}_{02} are non-collinear: for the angle ϕ between the two tran-

sition dipoles, the PXCD (Eqs. (1,2)) is proportional to $\sigma \sin(\phi)$. Since $\sigma = \pm 1$, $\sigma \sin(\phi) = \sin(\sigma\phi) = \sin(\sigma\omega\tau)$, where ω is the light frequency and $\tau = \phi/\omega$ is the time required by the light field to rotate by the angle ϕ . PXCD vanishes if the coherence between excited states $|1\rangle$ and $|2\rangle$ is lost and it reflects the dynamical symmetry breaking in an isotropic medium. Our compact formulation of chiral response forms a common basis for understanding and linking together several different phenomena involving rotational [11] and bound-continuum dipole transitions [4] for chiral discrimination or dichroic phenomena [18]. The common requirement linking all of them is the non-collinearity of the excitation dipoles.

Is it possible to create PXCD from purely vibrational excitation of a chiral molecule? Theoretically, vibrational states within the same electronic state can also fulfil the PXCD condition as long as their dipoles are not collinear, see Eqs. (1,2). As shown in the Supplementary Information (SI), this requires the breakdown of the Franck-Condon approximation, i.e. strong dependence of the electronic wave-function on the position of the nuclei. In turn, such dependence leads to the appearance of electronic currents stimulated by the nuclear motion, which is triggered by the pump pulse. Thus, vibrational PXCD is intertwined with the underlying chiral motion of electrons. The PXCD current can be induced with circularly polarized light either by direct coherent excitation of electronic states or by vibrational excitations with a strong coupling between electronic and vibrational degrees of freedom.

We now show that time-resolving PXCD does not require a chiral probe. The coherence underlying PXCD allows a chiral object to 'interact with itself', albeit in a different quantum state, thus mimicking interaction with "another chiral object" and removing any need for other chiral interactions during the probe step (Fig. 1). One such non-chiral probe, termed PhotoExcitation-induced photo-Electron Circular Dichroism (PXECD), is introduced below.

Probing chiral dynamics in bound states

One way to probe the excited chiral density is to promote the chiral wave-packet to the electronic continuum using a linearly polarized pulse (Fig. 1(c)). As shown in the Methods, the standard photoionization observable, the photoelectron current averaged over molecular orientations, is:

$$J_z^{\text{PXECD}}(k) \propto \sigma [\vec{d}_{01} \times \vec{d}_{02}] \cdot \vec{D}_{12}^r(k) \sin(\Delta E_{21}\tau) + \sigma [\vec{d}_{01} \times \vec{d}_{02}] \cdot \vec{D}_{12}^i(k) \cos(\Delta E_{21}\tau), \quad (3)$$

with $J_x^{\text{PXECD}}(k) = J_y^{\text{PXECD}}(k) = 0$. Here τ is the pump-probe delay, k is the photoelectron momentum, $\vec{D}_{12}(k) = \vec{D}_{12}^r(k) + i\vec{D}_{12}^i(k)$ is the Raman-type photoionization vector (see Fig. 1(c) and the Methods) which connects the excited bound states via the common continuum and plays the role of \vec{d}_{12} of Eqs. (1,2).

The electron current Eq. (3) contains two triple products. Just like the triple product $[\vec{d}_{01} \times \vec{d}_{02}] \cdot \vec{d}_{12}$ earlier,

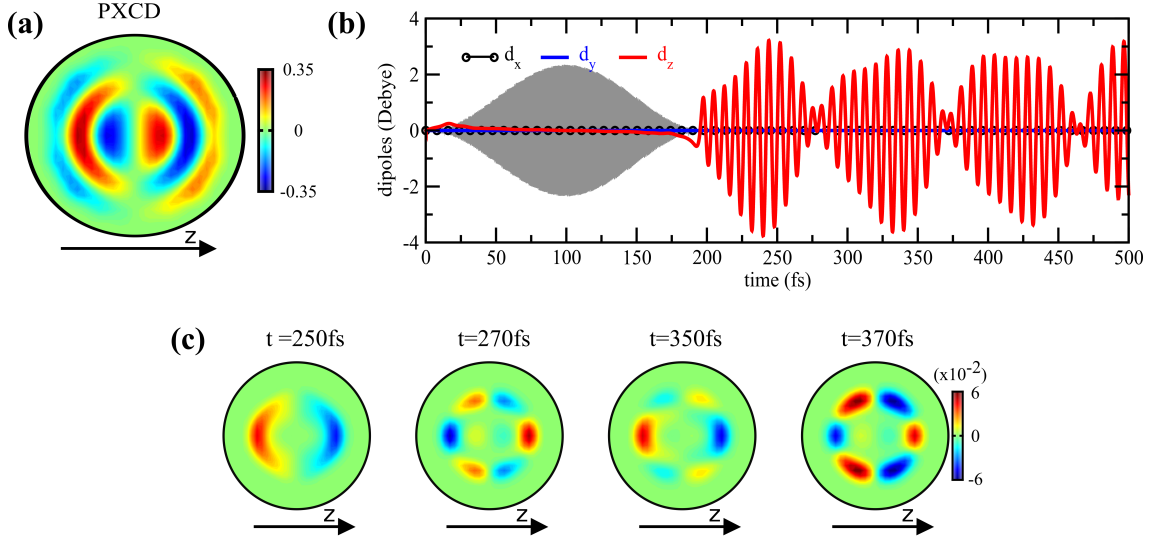


FIG. 2. **Theoretical analysis of the electron chiral dynamics in (1S)-(+)-fenchone.** (a) Momentum space electron density underlying PXCD. The asymmetry resulting from the chirality of the electron density is formed along the light propagation direction z . (b) Temporal evolution of the x -, y - and z -components of the macroscopic dipole associated with the $(3s,3p)$ Rydberg wave-packet created by the pump pulse (the shaded area). Only the z -component, along the direction of propagation of the pump and probe pulses, survives orientational averaging. (c) Momentum space PXECD signals at various pump-probe delays t calculated with a probe duration of 36 fs (FWHM in intensity).

both $[\vec{d}_{01} \times \vec{d}_{02}] \cdot \vec{D}_{12}^r$ and $[\vec{d}_{01} \times \vec{d}_{02}] \cdot \vec{D}_{12}^i$ will change sign upon reflection. Thus, the electron current in Eq. (3) is a pseudo-scalar observable; it reverses its direction if the handedness σ of the pump pulse or of the enantiomer is swapped, showing that PXECD is a genuine chiral effect. The chiral nature of the response arises only if the participating bound states are coherently excited. Once the coherence is lost, the chiral signal will also disappear.

Importantly, the state of the continuum does not need to be chiral, as it only provides a link between the two chiral bound states $|1\rangle$ and $|2\rangle$ (Fig. 1(c)). $J_z^{\text{PXECD}}(k)$ remains chiral even for a plane wave continuum (see the Methods), in this case $\vec{D}_{12}(k)$ only has an imaginary component:

$$J_{z,\text{PW}}^{\text{PXECD}}(k) \propto -\sigma[\vec{d}_{01} \times \vec{d}_{02}] \vec{D}_{12}^{i,\text{PW}}(k) \cos(\Delta E_{21}\tau). \quad (4)$$

Note also that the total PXECD photoelectron current $J_{\text{tot}}^{\text{PXECD}} \equiv \int J_{z,\text{PW}}^{\text{PXECD}}(k) dk$ measures the helical current excited in bound states j_z^{PXCD} (Eq. 2), i.e. $J_{\text{tot}}^{\text{PXECD}} \propto j_z^{\text{PXCD}}$ (see the SI), because $-1/2 \int \vec{D}_{12}^{i,\text{PW}}(k) dk \equiv \Delta E_{12} \vec{d}_{12}$. In particular, for $\Delta E_{12} = 0$ both the PXCD bound and the PXECD continuum currents vanish.

One might think that partial alignment of the excited molecular ensemble could already be fully responsible for enabling non-chiral probes of chiral dynamics. However, it is not true in our case. Indeed, the effect of alignment persists for a single excited electronic state and for the two excited electronic states with collinear dipoles, but in both cases it leads to zero PXECD current. Finally, removing the effect of partial alignment shows that the

PXECD current remains chiral for every k (see the Methods).

Probing the created chiral excitation using photoelectron imaging with linearly polarized light constitutes yet another new phenomenon. The PXECD is reminiscent of the Photoelectron Circular Dichroism (PECD) [4–6, 13–15, 19], which arises when circularly polarized light is used to photoionize a chiral molecule. However, there is a fundamental difference. PECD can only exist if the molecular potential felt by the emitted electron is either chiral [4] or, at least, non-spherically symmetric [20] (both effects quickly disappearing for photoelectron energies above 10 to 20 eV), while the initial orbital may or may not be chiral at all [21] (see Fig. 1(d) and the SI).

In contrast to PECD, PXECD requires neither chiral light, nor chiral or asymmetric scattering of the photoelectron. It can be observed both at low and high photoelectron energies. If one chooses to observe it at low energies, the chiral continuum may affect imaging of the bound chiral current. Nevertheless, if the bound dynamics is excited but the PXCD helical current (electronic or vibronic) is absent, i.e. the excited dynamics is not chiral, its measurement with linear light will yield zero chiral response. Thus, if the experiment detects time dependent chiral signal, it demonstrates the presence of bound chiral dynamics: the PXECD measurement detects PXCD. This contrasts PXECD with time-resolved PECD measurement, which uses circularly polarized probe: it will yield non-zero chiral response even if the excited dynamics is not chiral.

Since time-resolved PXECD does not require the tech-

nically challenging use of ultrashort circularly polarized XUV pulses [22–26], it opens unique perspectives for ultrafast chiral-sensitive measurements using readily available ultrashort linearly polarized XUV light.

We shall now confirm both numerically and experimentally that our scheme provides a sensitive time-resolved probe of chiral molecular dynamics in bound states.

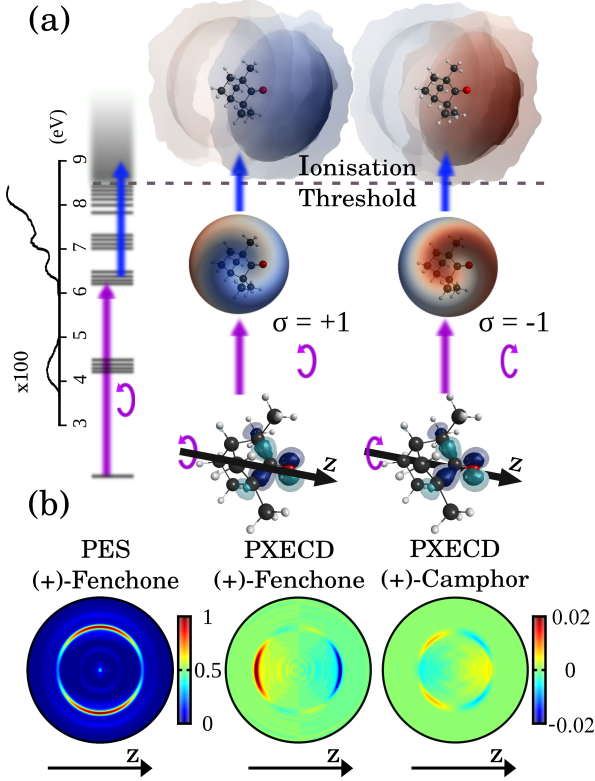


FIG. 3. **PXECD in fenchone molecules.** (a) Artist view of PXECD. Absorption of circularly polarized femtosecond pulse at 201 nm with helicity $\sigma = \pm 1$ promotes an electron from the highest occupied molecular orbital to Rydberg bands, creating a chiral vibronic wave-packet. A linearly polarized femtosecond probe pulse at 405 nm photoionizes the molecule, revealing the chiral asymmetry of the Rydberg wave-packet in the angular distribution of the photoelectrons. The absorption spectrum of fenchone is adapted from [39] (b) Experimental images of $(L+R)$ image (PES) and $(L-R)$ images (PXECD) at the 200 fs pump-probe delay for (1S)-(+)-fenchone and (1R)-(+)-camphor. The characteristic forward-backward asymmetry of the photoelectron is observed along the light propagation direction z . The PXECD image of (1R)-(-)-fenchone is shown in the figure 4 of the SI.

Theoretical analysis in fenchone

To quantify the PXECD effect we performed quantum mechanical calculations on fenchone molecules (see the

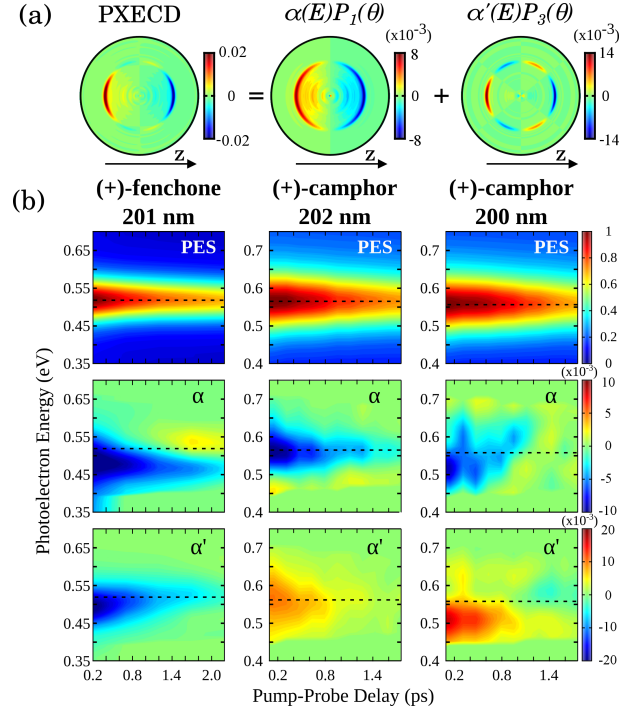


FIG. 4. **Time-resolved PXECD in fenchone and camphor.** (a) Legendre polynomials decomposition of the PXECD image for (1S)-(+)-Fenchone at 200 fs pump-probe delay. The α, α' coefficients, already normalized to the maximum value of $(L+R)/2$ image, are multiplied by their associated Legendre polynomials $P_i(\theta)$: $P_1 = \cos(\theta)$, $P_3 = (5/2 \cdot \cos^3(\theta) - 3/2 \cdot \cos(\theta))$ to reconstruct the PXECD image. (b) Evolution of the PES and PXECD coefficients as a function of the pump-probe delay and the photoelectron kinetic energy, in (1S)-(+)-fenchone with a 201 nm pump, (1R)-(+)-camphor with a 202 nm pump or with a 200 nm pump. The black dotted lines represent the kinetic energy of the photoelectron corresponding to the maximum of PES. The decay times of the main PES component are 3.28 ± 0.05 and 2.36 ± 0.07 ps for fenchone and camphor respectively

SI). First, we simulated the PXCD phenomenon and calculated the excitation of the s- and p-manifold of Rydberg states in fenchone by a circular pump pulse. Upon averaging over random initial orientation of molecules, the resulting electron density of the Rydberg wave-packet is asymmetric in the z -direction in the momentum space. The asymmetry reverses if the helicity of the pump pulse or the handedness of the molecule is reversed. The strength of the PXCD can be quantified by the magnitude of the chiral component of the excited electron density. It is obtained by subtracting the momentum space density D obtained with right (R) and left (L) circularly polarized light: $PXCD = 2(D(L) - D(R))/(D(L) + D(R))$. The calculated PXCD reaches very high values (35%, Fig. 2(a)). The asymmetry of the charge distribution describes a macroscopic dipole moment d_z^{PXCD} which reaches 3 Debye (Fig. 2(b)) and oscillates at frequencies determined

by the energy differences between the states forming the electronic wave-packet. The pump-probe PXECD signal, calculated as $(D(L) - D(R))$ and normalized to the maximum of $(D(L) + D(R))/2$, reveals temporal oscillations (Fig. 2(c)) and 6% asymmetry, thanks to the short duration of the probe pulse (36 fs FWHM in intensity). The asymmetry scales with the probe bandwidth ΔW_{FWHM} as $e^{-[\Delta E_{12}\sqrt{\ln 2}/\Delta W_{\text{FWHM}}]^2}$ (see the SI), decreasing for longer probe pulses such as used in the experiment.

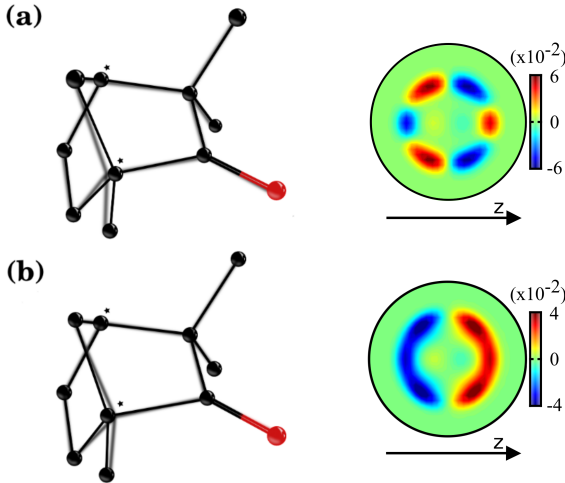


FIG. 5. **Sensitivity of PXECD in (1S)-(+)-fenchone to the evolution of the chiral molecular structure.** (a) The equilibrium geometries of the ground (dark) and 3s (shaded) electronic states, and the PXECD signal computed at $t = 370$ fs using the ground state geometry for both the pump excitation and the probe ionization. (b) The representation of the geometries are exchanged and the PXECD is now calculated for a probe ionization that occurs from a vibronic wave-packet localised at the 3s equilibrium geometry. The PXECD image is averaged over random molecular orientations and calculated with a 36 fs duration of the probe pulse.

Observation of PXECD in fenchone

In our experiment, a circularly polarized femtosecond pump pulse at 201 nm (6.17 eV photon energy, 80 meV at $1/e^2$ electric field bandwidth) photoexcites enantiopure fenchone molecules from a supersonic gas jet in the interaction zone of a velocity map imaging spectrometer. The molecules are excited to Rydberg bands through single-photon absorption (Fig. 3(a), see the SI). A time-delayed, linearly polarized probe pulse at 405 nm (3.1 eV photon energy, 85 meV at $1/e^2$ of the electric field bandwidth) induces one-photon ionization of the excited molecules. The cross-correlation of the pump and the probe pulses is 170 fs. The photoelectrons are accelerated and projected by an electrostatic lens onto a set of dual microchannel plates and imaged by a phosphor

screen and a CCD camera. The (L) and (R) photoelectron images are recorded alternatively using left and right circularly polarized pump pulses respectively. The difference (L-R) and sum (L+R) of these two images are fitted by a linear combination of Legendre polynomials using a least-square fitting algorithm (p-Basex, see the SI for details). The PXECD is given by (L-R) image while the (L+R) image reflects the angle resolved photoelectron spectrum (PES). These two images shown in Fig. 3(b) for a 200 fs pump-probe delay are both normalized by the peak of the (L+R)/2 image. As expected, a significant amplitude of the PXECD image is observed, reaching 2%. The asymmetry reverses for the other enantiomer of (1S)-(+)-fenchone, (see Fig. 4 in the SI), proving the enantio-sensitivity of the effect, originating from the pseudo-scalar nature of the PXECD current, see Eq. (3). The forward-backward asymmetry, i.e. the normalized difference of photoelectron counts between the forward and the backward hemispheres relative to the z-axis is $-1.86\% \pm 0.14\%$ for (1S)-(+)-fenchone and $+1.68\% \pm 0.34\%$ for (1R)-(-)-fenchone, at 700 fs delay.

The photoelectron spectrum, obtained from the first even term of the Legendre decomposition (see SI), contains a single broad component in energy, corresponding to ionization from the outermost orbital (vertical ionization potential 8.72 eV). This component does not shift in energy with the pump-probe delay (Fig. 4(b)) and decays exponentially in 3.3 ps, reflecting a simple vibronic relaxation of the Rydberg population onto lower states which cannot be photoionized by one probe photon alone. The temporal evolution of the PXECD image shows much richer spectroscopic features, which can be analyzed by decomposing it in odd Legendre polynomials (Fig. 4(a)). We note that a sum of first- and third-order Legendre polynomials, with coefficients α and α' , is enough to fit the PXECD images. Both coefficients maximize around ~ 50 meV below the maximum of the PES. The PXECD signal (Fig. 4(b)) can be decomposed into two components: below and above the maximum of the PES. The low-energy component of α undergoes a rather smooth decay. On the contrary, its high-energy component decays very quickly and even changes sign around 1 ps. For α' the behaviour is opposite, *i.e.* the high-energy component shows much slower dynamics than the low-energy part. Such time- and electron energy- dependent behaviour is characteristic of internal vibrational torsional motion and may indicate the change of the chiral structure of the molecule induced by such motion. Indeed, the electronic excitation of the molecules is expected to be accompanied by a significant vibrational excitation, since the equilibrium geometries of Rydberg states are quite different from that of the ground state. The molecules will tend to relax towards the equilibrium geometry of the Rydberg states, and oscillate around it. Figure 5 illustrates the influence of this change of molecular geometry on the calculated PXECD signal. Even small bond length changes ($\leq 7\%$) lead to significant

modification of the PXECD signal. This demonstrates the remarkable sensitivity of PXECD to molecular vibrations, which follow the electronic excitation. The ensuing vibrational dynamics will inevitably blur the purely electronic oscillations shown in Fig. 2(c). At 4 ps (not shown), the PXECD completely vanishes while the Rydberg population is still 30% of its initial value. This result unambiguously reflects the loss of wave-packet coherence which halts chiral dynamics in our experiment.

Observation of PXECD in camphor

According to numerical simulations (see the SI), the coherence between the two Rydberg bands could eventually in fenchone. However, the *s*- and *p*- Rydberg bands of camphor are upshifted by additional several tens of meV compared to fenchone, preventing direct excitation of the *p*- states by the pump pulse. The experiment still reveals a strong PXECD signal, indicating that a chiral vibronic wave-packet has been created in camphor. Both PXCD and PXECD are highly molecular specific (Fig. 3(b)): the PXECD images from the two isomers (camphor and fenchone) are drastically different. The α' coefficients in camphor and fenchone are of opposite sign as seen in multiphoton [27] and one-photon PECD [14]. In our experiment, this could be a consequence of PXECD sensitivity to isomerism (see Fig. 5 to gauge the sensitivity to nuclear configuration), but it might also be a signature of the different nature of the excited chiral electronic currents in fenchone and camphor. Changing the excitation wavelength from 202 nm to 200 nm does not affect the monoexponential decay of the PES. In contrast, a strong change is observed in the PXECD: the α' magnitude is almost twice as large and it is shifted in energy towards the red wing of the photoelectron spectrum. The drastic change observed in the PXECD signal in camphor once the pump photon energy is increased by only 60 meV illustrates the extreme sensitivity of this measurement to the excited vibrational dynamics.

Conclusions and outlook

The ensemble-averaged chiral charge density arising in PXCD implies asymmetry in the charge distribution along the light propagation direction, induced by the planar rotation of light polarization but not by light's helical structure. Depending on the medium density, this could lead to a very large coherently oscillating macroscopic dipole. The phase of this oscillation is opposite for two enantiomers, leading to macroscopic enantio-sensitive effects. The existence of the enantio-sensitive macroscopic dipole, which also occurs for purely rotational excitation [11, 28], opens a way to laser-driven separation of enantiomers in isotropic racemic mixtures in the gas phase.

The application of a linearly polarized X-ray probe in PXECD would enable genuine probing of ultrafast chiral bound dynamics, since PXECD does not require chiral interaction in the continuum, which becomes negligible for sufficiently high-energy electrons. Therefore, the PXCD phenomenon opens the way to direct visualization of chiral electronic density using time-resolved X-ray diffraction imaging, both in the gas and condensed phase. Intense ultrafast sources of X-ray radiation, such as Free Electron Lasers, combined with measurements sensitive to valence-shell dynamics in the gas phase [29] should lead to few-fs time resolution of chiral charge dynamics.

Finally, PXCD could be used to drive molecular reactions in chiral systems in a stereo-specific way, by imprinting a chiral torque via the helicity of the exciting circularly polarized pulse. The ultrafast charge dynamics triggered by coherent electronic excitation is reminiscent of ultrafast charge migration triggered by photoionization [30–33, 35–37] recently observed in ref. [38] and speculated to underlie charge-directed reactivity in cations [34]. Chiral electron stereo-dynamics in neutral molecules may open similar opportunities for controlling charge and energy flow in molecules at the level of electrons, offering new perspectives for such intriguing problems as asymmetric synthesis, a major challenge in stereochemistry.

-
- [1] Cotton, A. Recherches sur l'absorption et la dispersion de la lumière par les milieux doués du pouvoir rotatoire. *J. Phys. Theor. Appl.* **5**, 237–244 (1896).
- [2] Barron, L. D. *Molecular light scattering and optical activity* (Cambridge University Press, Cambridge, UK ; New York, 2004), 2nd ed., rev. and enl edn.
- [3] Berova, N., Nakanishi, K. & Woody, R. *Circular dichroism: principles and applications* (Wiley-VCH, New York, 2000), 2nd edn.
- [4] Ritchie, B. Theory of the angular distribution of photoelectrons ejected from optically active molecules and molecular negative ions. *Phys. Rev. A* **13**, 1411–1415 (1976). URL <http://dx.doi.org/10.1103/PhysRevA.13.1411>.
- [5] Powis, I. Photoelectron circular dichroism of the randomly oriented chiral molecules glyceraldehyde and lactic acid. *The Journal of Chemical Physics* **112**, 301–310 (2000). URL <http://dx.doi.org/10.1063/1.480581>.
- [6] Böwering N., T. Lischke, B. Schmidtke, N. Müller, T. Khalil & U. Heinzmann Asymmetry in Photoelectron Emission from Chiral Molecules Induced by Circularly Polarized Light. *Physical Review Letters* **86**, 1187–1190 (2001). URL <http://dx.doi.org/10.1103/PhysRevLett.86.1187>.
- [7] Lux C., Wollenhaupt M., Bolze T., Liang Q., Köhler J., Sarpe C. & Baumert T. Circular dichroism in the photoelectron angular distributions of camphor and fenchone from multiphoton ionization with femtosecond laser pulses. *Angewandte Chemie International Edition* **51**, 5001–5005 (2012). URL <http://dx.doi.org/10.1002/anie.201109035>.
- [8] Lehmann, C. S., Ram, N. B., Powis, I. & Janssen, M. H. M. Imaging photoelectron circular dichroism of chiral molecules by femtosecond multiphoton coincidence de-

- tection. *The Journal of Chemical Physics* **139**, 234–307 (2013). URL <http://dx.doi.org/10.1063/1.4844295>.
- [9] Pitzer, M., Kunitski, M., Johnson, A. S., Jahnke, T., Sann, H., Sturm, F., Schmidt, L. Ph. H., Schmidt-Böcking, H., Dörner, R., Stohner, J., Kiedrowski, J., Reggelin, M., Marquardt, S., Schießer, A., Berger, R. & Schöffler, M. S. Direct determination of absolute molecular stereochemistry in gas phase by coulomb explosion imaging. *Science* **341**, 1096–1100 (2013). URL <http://dx.doi.org/10.1126/science.1240362>.
- [10] Herwig, P., Zawatzky, K., Grieser, M., Heber, O., Jordon-Thaden, B., Krantz, C., Novotný, O., Repnow, R., Schurig, V., Schwalm, D., Vager, Z., Wolf, A., Trapp, O., Kreckel, H. Imaging the absolute configuration of a chiral epoxide in the gas phase. *Science* **342**, 1084–1086 (2013). URL <http://dx.doi.org/10.1126/science.1246549>.
- [11] Patterson, D., Schnell, M. & Doyle, J. M. Enantiomer-specific detection of chiral molecules via microwave spectroscopy. *Nature* **497**, 475–477 (2013). URL <http://dx.doi.org/10.1038/nature12150>.
- [12] Yachmenev, A. & Yurchenko, S. N. Detecting Chirality in Molecules by Linearly Polarized Laser Fields. *Physical Review Letters* **117**, 033001 (2016). URL <http://dx.doi.org/10.1103/PhysRevLett.117.033001>.
- [13] Comby, A., Beaulieu, S., Boggio-Pasqua, M., Descamps, D., Légaré, F., Nahon, L., Petit, S., Pons, B., Fabre, B., Mairesse, Y. & Blanchet, V. Relaxation Dynamics in Photoexcited Chiral Molecules Studied by Time-Resolved Photoelectron Circular Dichroism: Toward Chiral Femtochemistry. *The Journal of Physical Chemistry Letters* **7**, 4514–4519 (2016). URL <http://dx.doi.org/10.1021/acs.jpcllett.6b02065>.
- [14] Nahon, L., Garcia, G. A. & Powis, I. Valence shell one-photon photoelectron circular dichroism in chiral systems. *Journal of Electron Spectroscopy and Related Phenomena* **204**, 322–334 (2015). URL <http://dx.doi.org/10.1016/j.elspec.2015.04.008>.
- [15] Nahon, L., Nag, L., Garcia, G. A., Myrgorodska, I., Meierhenrich, U., Beaulieu, S., Wanie, V., Blanchet, V., Geneaux, R. & Powis, I. Determination of accurate electron chiral asymmetries in fenchone and camphor in the vuv range: Sensitivity to isomerism and enantiomeric purity. *Phys. Chem. Chem. Phys.* **18**, 12696–12706 (2016). URL <http://dx.doi.org/10.1039/C6CP01293K>.
- [16] Barron, L. D. True and false chirality and absolute asymmetric synthesis. *Journal of the American Chemical Society* **108**, 5539–5542 (1986). URL <http://dx.doi.org/10.1021/ja00278a029>.
- [17] Tang, Y. & Cohen, A. E. Optical chirality and its interaction with matter. *Physical Review Letters* **104**, 163901 (2010). URL <http://dx.doi.org/10.1103/PhysRevLett.104.163901>.
- [18] Cherepkov, N. A. & Rašeev, G. Linear Dichroism in the Angular Distribution of Photoelectrons. *The Journal of Chemical Physics* **103**, 8238–8246 (1995). URL <http://dx.doi.org/10.1063/1.470188>.
- [19] Garcia, G. A., Nahon, L., Daly, S. & Powis, I. Vibrationally induced inversion of photoelectron forward-backward asymmetry in chiral molecule photoionization by circularly polarized light. *Nature Communications* **4**, 2132 (2013). URL <http://dx.doi.org/10.1038/ncomms3132>.
- [20] Stener, M., Di Tommaso, G., Fronzoni, P., Declewa, & I. Powis Theoretical study on the circular dichroism in core and valence photoelectron angular distributions of camphor enantiomers. *The Journal of Chemical Physics* **124**, 024326 (2006). URL <http://dx.doi.org/10.1063/1.2150438>.
- [21] Ulrich, V., Barth, S., Joshi, S., Hergenhahn, U., Mikajlo, E., Harding, C.J. & I. Powis Giant Chiral Asymmetry in the C1s Core Level Photoemission from Randomly Oriented Fenchone Enantiomers. *The Journal of Physical Chemistry A* **112**, 3544–3549 (2008). URL <http://dx.doi.org/10.1021/jp709761u>.
- [22] Wang, T. *et al.* Femtosecond single-shot imaging of nanoscale ferromagnetic order in Co/Pd multilayers using resonant x-ray holography. *Phys. Rev. Lett.* **108**, 267403 (2012) URL <http://dx.doi.org/10.1103/PhysRevLett.108.267403>.
- [23] Spezzani, C., Allaria, E., Coreno, M., Diviacco, B., Ferrari, E., Geloni, G., Karantzoulis, E., Mahieu, B., Vento, M. & De Ninno, G. Coherent light with tunable polarization from single-pass free-electron lasers. *Phys. Rev. Lett.* **107**, 084801 (2011) URL <http://dx.doi.org/10.1103/PhysRevLett.107.084801>.
- [24] Allaria, E. *et al.*, Highly coherent and stable pulses from the FERMI seeded free-electron laser in the extreme ultraviolet. *Nat. Photon.* **6**, 699–704 (2012) URL <http://dx.doi.org/10.1038/nphoton.2012.233>.
- [25] Fleischer, A., Kfir, O., Diskin, T., Sidorenko, P. & Cohen, O. Spin angular momentum and tunable polarization in high-harmonic generation. *Nat. Photon.* **8**, 543–549 (2014) URL <http://dx.doi.org/10.1038/nphoton.2014.108>.
- [26] Ferré, A. *et al.* A table-top ultrashort light source in the extreme ultraviolet for circular dichroism experiments. *Nature Photonics* **9**, 93–98 (2015). URL <http://dx.doi.org/10.1038/nphoton.2014.314>.
- [27] Lux, C., Wollenhaupt, M., Sarpe, C. & Baumert, T. Photoelectron circular dichroism of bicyclic ketones from multiphoton ionization with femtosecond laser pulses. *ChemPhysChem* **16**, 115–137 (2015). URL <http://dx.doi.org/10.1002/cphc.201402643>.
- [28] Eibenberger, S., Doyle, J., Patterson, D. Enantiomer-Specific State Transfer of Chiral Molecules. *Physical Review Letters* **118**, 123002 (2017). URL <http://dx.doi.org/10.1103/PhysRevLett.118.123002>.
- [29] Bredtmann, T., Ivanov, M. & Dixit, G. X-ray imaging of chemically active valence electrons during a pericyclic reaction. *Nat Commun* **5**, 5589 (2014). URL <http://dx.doi.org/10.1038/ncomms6589>.
- [30] Lunnemann, S., Kuleff, A.I. & Cederbaum, L.S. Ultrafast charge migration in 2-phenylethyl-N, N-dimethylamine. *Chem. Phys. Lett.* **450**, 232–235 (2008).
- [31] Breidbach, J. & Cederbaum, L.S. Universal attosecond response to the removal of an electron. *Phys. Rev. Lett.* **94**, 033901 (2005). URL <http://dx.doi.org/10.1103/PhysRevLett.94.033901>.
- [32] Remele, F. & Levine, R.D. An electronic time scale in chemistry. *Proc. Natl. Acad. Sci. USA* **103**, 6793–6798 (2006). URL <http://dx.doi.org/10.1073/pnas.0601855103>.
- [33] Kuleff, A.I. & Cederbaum, L.S. Charge migration in different conformers of glycine: The role of nuclear geometry. *Chem. Phys.* **338**, 320–328 (2007). URL <https://doi.org/10.1016/j.chemphys.2007.04.012>.
- [34] Weinkauff, R., Schlag, E.W., Martinez, T.J. & Levine, R.D. Nonstationary electronic states and site-selective

- reactivity. *J. Phys. Chem. A* **101**, 7702–7710 (1997). URL <https://doi.org/10.1021/jp9715742>
- [35] Lepine, F., Ivanov, M.Y., Vrakking, M.J.J. Attosecond molecular dynamics: Fact or fiction? *Nat. Phot.* **8**, 195–204 (2014). URL <https://doi.org/doi:10.1038/nphoton.2014.25>
- [36] Leone, S.R. *et al.* What will it take to observe processes in ‘real time’?. *Nat. Phot.* **8**, 162–166 (2014).
- [37] Kuleff, A.I. & Cederbaum, L.S. Ultrafast correlation-driven electron dynamics. *J. Phys. B* **47**, 124002 (2014). URL <https://doi.org/10.1088/0953-4075/47/12/124002>
- [38] Calegari, F. *et al.* Ultrafast electron dynamics in phenylalanine initiated by attosecond pulses. *Science* **346**, 336–339 (2014). URL <https://doi.org/10.1126/science.1254061>
- [39] Pulm, F., Schramm, J., Hormes, J., Grimme, S. & Peyerimhoff, S. D. Theoretical and experimental investigations of the electronic circular dichroism and absorption spectra of bicyclic ketones. *Chemical Physics* **224**, 143–155 (1997). URL [http://dx.doi.org/10.1016/S0301-0104\(97\)00258-9](http://dx.doi.org/10.1016/S0301-0104(97)00258-9).

Acknowledgements

We thank Rodrigue Bouillaud and Laurent Merzeau for technical assistance. We thank M. Ivanov, F. Morales, A. Stolow and T. Elsaesser for stimulating discussions. We acknowledge financial support of the Agence Nationale pour la Recherche (ANR-14-CE32-0014 MISFITS), the University of Bordeaux and the Conseil Regional de Nouvelle-Aquitaine (2.1.3-09010502 COLA2 project). Z.M. and O.S. gratefully acknowledge the support from Deutsche Forschungsgemeinschaft, project Sm 292-5/1, A.H. gratefully acknowledges the support from Deutsche Forschungsgemeinschaft, projects IV 152/7-1 and HA

8552/2-1. A.F.O. and O.S. gratefully acknowledge EU ITN MEDEA -AMD-641789-17 project. S.B. acknowledges the support of a NSERC Vanier Canada Graduate Scholarship. R.G. acknowledges financial support from the Agence Nationale pour la Recherche through the XSTASE project (ANR-14-CE32-0010). The authors gratefully acknowledge the support of their collaboration through European Cooperation in Science and Technology (COST), program CM1204 XLIC. This project has received funding from the European Research Council (ERC) under the European Union’s Horizon 2020 research and innovation program no. 682978 - EXCITERS.

Author contributions

S.B., A.C., R.G., Y.M., V.B., performed the experiment. D.D. and S.P. operated the laser system. S.B., A.C., B.F., G.G., L.N., B.P., Y.M. and V.B. analyzed the data. B.F. and B.P. performed the molecular geometry and dynamical calculations. A.H., A.F.O., Z.M. and O.S. developed the analytical theory, A.F.O. and O.S. derived triple-product chirality measures for PXCD and PXECD and analyzed their connection and properties. S.B. wrote the first version of the manuscript, all authors contributed to writing the manuscript.

Competing Interests

The authors declare that they have no competing financial interests.

Additional information

Correspondence should be addressed to B.P. or Y.M. or O.S.

METHODS

A. Exciting Chiral Currents.

To derive Eqs. (1,2) for the z components of the induced dipole and current we use standard time-dependent perturbation theory, assuming two excited states $i = 1, 2$ coupled to the ground state. The pump field in the laboratory frame (superscript L) is:

$$\vec{E}^L(t) = \frac{1}{\sqrt{2}} F(t) \hat{\varepsilon}_\sigma^L e^{-i(\omega t + \delta)} + \text{c.c.}, \quad (5)$$

where ω is the carrier frequency, $F(t)$ is the field amplitude, δ is the carrier-envelope phase, and

$$\hat{\varepsilon}_\sigma^L = \frac{\hat{x}^L + \sigma i \hat{y}^L}{\sqrt{2}} \quad (6)$$

describes the pulse polarization. The excitation amplitudes are:

$$a_i(\varrho) = -i \left[R(\varrho) \hat{\varepsilon}_\sigma^L \cdot \vec{d}_{i,0} \right] \mathcal{E}(\omega_{i0}), \quad (7)$$

where $i = 1, 2$ labels the excited states, $\mathcal{E}(\omega_{i0})$ are the spectral amplitudes at the transition frequencies ω_{i0} , $\vec{d}_{i,0}$ are the excitation dipole matrix elements in the molecular frame, and the pump field is rotated into the molecular frame via the rotation matrix $R(\varrho)$, with the Euler angles $\varrho \equiv (\alpha, \beta, \gamma)$ (see SI for explicit expressions). The induced dipole in the molecular frame is:

$$\vec{d}_\varrho(\tau) = \sum_{i,j=0}^2 a_i^*(\varrho) a_j(\varrho) e^{-i\omega_{ji}\tau} \vec{d}_{i,j}, \quad (8)$$

where $\vec{d}_{i,j} = \langle i | \hat{d} | j \rangle$ and $\omega_{ij} = \omega_i - \omega_j$. Transforming to the lab frame and averaging over all orientations ϱ yields

$$\begin{aligned} \overline{\vec{d}^L}(\tau) &= \int d\varrho R^t(\varrho) \vec{d}_\varrho(\tau) \\ &= \sum_{i,j=0}^2 e^{-i\omega_{ji}\tau} \left\{ \int d\varrho a_i^*(\varrho) a_j(\varrho) R^t(\varrho) \right\} \vec{d}_{i,j}, \end{aligned} \quad (9)$$

where $R^t = R^{-1}$ is the transpose of the rotation matrix R . Details of the integration are presented in the SI. The final result is:

$$\overline{\vec{d}^L}(\tau) = \frac{1}{3} \left(\begin{array}{c} \sqrt{2} \left[|\mathcal{E}(\omega_{10})| (d_{1,0})^2 \cos(\omega_{10}\tau - \phi_1 - \frac{\pi}{2}) + |\mathcal{E}(\omega_{20})| (d_{2,0})^2 \cos(\omega_{20}\tau - \phi_2 - \frac{\pi}{2}) \right] \\ \sigma \sqrt{2} \left[|\mathcal{E}(\omega_{10})| (d_{1,0})^2 \sin(\omega_{10}\tau - \phi_1 - \frac{\pi}{2}) + |\mathcal{E}(\omega_{20})| (d_{2,0})^2 \sin(\omega_{20}\tau - \phi_2 - \frac{\pi}{2}) \right] \\ |\mathcal{E}(\omega_{10})| |\mathcal{E}(\omega_{20})| \sigma \left[\vec{d}_{1,0} \times \vec{d}_{2,0} \right] \cdot \vec{d}_{1,2} \sin(\omega_{21}\tau - \phi_{21}) \end{array} \right), \quad (10)$$

where $\mathcal{E}(\omega_{i0}) = |\mathcal{E}(\omega_{i0})| \exp(i\phi_i)$, $\phi_{21} = \phi_2 - \phi_1$. The $\pi/2$ phase shift reflects the resonance. Eq. (1) of the paper shows the z -component, for $\phi_{21} = 0$. Note that d_z^L is a time-even pseudo-scalar, i.e. the quintessential chiral observable. Together with the x and y components, which describe rotation in the polarization plane, d_z^L describes the helical charge motion induced in a randomly oriented chiral ensemble. The planar rotation stems from the coherence with the ground state, the motion along the z -axis from the coherence between the excited states. The bound current is obtained by differentiating the dipole:

$$\overline{\vec{j}^L}(\tau) = \frac{1}{3} \left(\begin{array}{c} -\sqrt{2} \left[|\mathcal{E}(\omega_{10})| \omega_{10} (d_{1,0})^2 \sin(\omega_{10}\tau - \phi_1 - \frac{\pi}{2}) + |\mathcal{E}(\omega_{20})| \omega_{20} (d_{2,0})^2 \sin(\omega_{20}\tau - \phi_2 - \frac{\pi}{2}) \right] \\ \sigma \sqrt{2} \left[|\mathcal{E}(\omega_{10})| \omega_{10} (d_{1,0})^2 \cos(\omega_{10}\tau - \phi_1 - \frac{\pi}{2}) + |\mathcal{E}(\omega_{20})| \omega_{20} (d_{2,0})^2 \cos(\omega_{20}\tau - \phi_2 - \frac{\pi}{2}) \right] \\ |\mathcal{E}(\omega_{10})| |\mathcal{E}(\omega_{20})| \omega_{21} \sigma \left[\vec{d}_{1,0} \times \vec{d}_{2,0} \right] \cdot \vec{d}_{1,2} \cos(\omega_{21}\tau - \phi_{21}) \end{array} \right). \quad (11)$$

The strength of the chiral response in PXCD depends on the efficiency of conversion of the planar current excited by the pump field into the helical current with the chiral component along the z axis. The conversion is performed by the chiral molecule itself. In the example shown in the SI (Fig. 1) the conversion is 100%.

B. Probing Chiral Currents.

The photoelectron current Eq. (3) is derived by applying perturbation theory to the coherent excitation amplitudes calculated above. The ionizing probe field with frequency ω' is linearly polarized along the laboratory \hat{x}^L axis and is delayed (delay τ) from the pump field. The current for the photo-electron momentum \vec{k} in the molecular frame is

$$\vec{J}'(\vec{k}) = \frac{1}{2} a_{\vec{k}}^* a_{\vec{k}} \vec{k} + \text{c.c.} \quad (12)$$

where the population amplitude of the continuum state $|\vec{k}\rangle$ is (see the SI)

$$a_{\vec{k}} = - \left(R(\varrho) \hat{\varepsilon}_\sigma^L \cdot \vec{d}_{1,0} \right) \left(R(\varrho) \hat{x}^L \cdot \vec{D}_1 \right) e^{-i\omega_1\tau} \mathcal{E}(\omega_1) \mathcal{E}'(\omega'_{\vec{k}1}) - \left(R(\varrho) \hat{\varepsilon}_\sigma^L \cdot \vec{d}_{2,0} \right) \left(R(\varrho) \hat{x}^L \cdot \vec{D}_2 \right) e^{-i\omega_2\tau} \mathcal{E}(\omega_2) \mathcal{E}'(\omega'_{\vec{k}2}) \quad (13)$$

Here $\mathcal{E}'(\omega_{\vec{k},i})$ is the spectral amplitude of the probe at the required transition frequency, $\vec{D}_i(\vec{k})$ are bound-free transition dipoles in the molecular frame.

The current includes both diagonal contributions and the Raman-type coupling of states $i = 1, 2$ via the continuum. Only the latter survives the orientation averaging (see the SI). Substituting expressions for the continuum amplitudes, and keeping only the off-diagonal terms, we obtain the current in the molecular frame:

$$\vec{J}(\vec{k}, \varrho) = \left(R(\varrho) \hat{\varepsilon}_{-\sigma}^L \cdot \vec{d}_{2,0}^* \right) \left(R(\varrho) \hat{x}^L \cdot \vec{D}_2^* \right) \times \left(R(\varrho) \hat{\varepsilon}_{\sigma}^L \cdot \vec{d}_{1,0} \right) \left(R(\varrho) \hat{x}^L \cdot \vec{D}_1 \right) \times \mathcal{E}(\omega, \omega') e^{i\omega_{21}\tau} \vec{k} + \text{c.c.} \quad (14)$$

where the $\mathcal{E}(\omega, \omega')$ includes all spectral amplitudes of the pump and probe pulses for the relevant transition frequencies,

$$\mathcal{E}(\omega, \omega') = \mathcal{E}^*(\omega_2) \mathcal{E}(\omega_1) \mathcal{E}'^*(\omega'_{\vec{k}2}) \mathcal{E}'(\omega'_{\vec{k}1}) \quad (15)$$

Note that $\vec{J}(\vec{k})$ is independent of the carrier-envelope phase δ of the pump. Hence, it also does not matter whether the probe is linearly polarized along the x or the y axis.

After transforming the current into the laboratory frame $\vec{J}^L(\vec{k}, \varrho) = R^t(\varrho) \vec{J}$, averaging over all molecular orientations, and over all directions of \vec{k} we obtain:

$$\vec{J}_z^L(k) = -\frac{\sigma}{60} \mathcal{E}(\omega, \omega') \left[\vec{d}_{1,0} \times \vec{d}_{2,0} \right] \cdot \vec{D}_{12}(k) e^{i(\omega_{21}\tau - \frac{\pi}{2})} + \text{c.c.} \quad (16)$$

$$\vec{J}_x^L(k) = \vec{J}_y^L(k) = 0, \quad (17)$$

$$\vec{D}_{12}(k) = \int d\Omega_k \vec{D}_{12}(\vec{k}) \quad (18)$$

and the Raman-type photoionization vector $\vec{D}_{12}(\vec{k})$ is defined below. Writing $\vec{D}_{12}(k)$ as a sum of its real and imaginary parts, we obtain Eq. (3), up to constant factors (omitted there for compactness):

$$\begin{aligned} \vec{J}_z^L(k) &= -\frac{\sigma}{60} |\mathcal{E}(\omega, \omega')| \left[\vec{d}_{1,0} \times \vec{d}_{2,0} \right] \cdot \left(\vec{D}_{12}^r(k) + i \vec{D}_{12}^i(k) \right) \times e^{i(\omega_{21}\tau + \phi(\omega, \omega') - \frac{\pi}{2})} + \text{c.c.} \\ &= -\frac{\sigma}{30} |\mathcal{E}(\omega, \omega')| \left[\vec{d}_{1,0} \times \vec{d}_{2,0} \right] \cdot \left[\vec{D}_{12}^r(k) \sin(\omega_{21}\tau + \phi(\omega, \omega')) + \vec{D}_{12}^i(k) \cos(\omega_{21}\tau + \phi(\omega, \omega')) \right] \end{aligned} \quad (19)$$

Here the phases and amplitudes of the pump and probe fields are denoted $\phi(\omega, \omega')$ and $|\mathcal{E}(\omega, \omega')|$. For $\vec{D}_{12}(\vec{k})$ we find (see the SI)

$$\vec{D}_{12}(\vec{k}) = -4 \left(\vec{D}_1 \cdot \vec{D}_2^* \right) \vec{k} + \left(\vec{D}_2^* \cdot \vec{k} \right) \vec{D}_1 + \left(\vec{D}_1 \cdot \vec{k} \right) \vec{D}_2^* \quad (20)$$

This general expression shows that every available vector $(\vec{D}_1, \vec{D}_2^*, \vec{k})$ can be used to ‘‘complete’’ the triple product. We show below that the last two terms in this equation can be associated with partial alignment of the molecular ensemble by the pump pulse, and disappear if the unpolarized probe is used. However, the PXECD effect remains due to the first term in the above equation.

C. PXECD for unpolarized probe pulse

Theoretically, it is instructive to consider completely unpolarized light as a probe of the excited chiral dynamics. Since the probe is completely isotropic, it can not be sensitive to the initial alignment by the pump. Thus, considering an unpolarized probe, we can find out how a partial alignment of the initially isotropic ensemble by the pump transition affects the chiral continuum current (the PXECD effect). Below we show that the PXECD effect does not vanish, if the alignment by the pump is excluded. Thus, the PXECD effect does not originate solely from a partial alignment by the pump pulse.

Consider an arbitrary direction of the linear probe in the laboratory frame. Instead of a single vector characterizing the direction of polarization \hat{x}^L of the probe pulse, we introduce

$$\hat{p}^L = \begin{pmatrix} \sin \theta_p \cos \varphi_p \\ \sin \theta_p \sin \varphi_p \\ \cos \theta_p \end{pmatrix}$$

Then the current in Eq. (14) takes the form

$$\vec{J}(\vec{k}, \varrho, \hat{p}^L) = \sum_{i,j} \left(R(\varrho) \hat{\varepsilon}_{-\sigma}^L \cdot \vec{d}_{2,0} \right) \left(R(\varrho) \hat{j}^{L*} \cdot \vec{D}_2^* \right) \left(R(\varrho) \hat{\varepsilon}_{\sigma}^L \cdot \vec{d}_{1,0} \right) \left(R(\varrho) \hat{i}^L \cdot \vec{D}_1 \right) p_i p_j^* \mathcal{E}(\omega, \omega') \vec{k} e^{i\omega_{21}\tau} + \text{c.c.}, \quad (21)$$

where i and j take values x, y, z . From this expression we can see that cross terms $i \neq j$ vanish after averaging over probe-polarization directions, therefore we only need to calculate the terms corresponding to a probe polarized along directions \hat{x}^L , \hat{y}^L and \hat{z}^L independently. We already calculated the expression for a probe polarized along \hat{x}^L and demonstrated that it is valid for all probe polarizations in the $x^L y^L$ plane, and in particular to probe polarization along \hat{y}^L . For a probe polarized along \hat{z}^L we obtain expressions identical to Eqs. (16,17,18,19) for the current, except that \vec{D}_{12} in Eq. (20) is now given by

$$\vec{D}_{12}(\vec{k}, \hat{z}^L) = -2 \left[\left(\vec{D}_1 \cdot \vec{D}_2 \right) \vec{k} + \vec{D}_1 \left(\vec{D}_2^* \cdot \vec{k} \right) + \vec{D}_2^* \left(\vec{D}_1 \cdot \vec{k} \right) \right]. \quad (22)$$

From Eqs. (20), (21), and (22), the expression for the current in the lab frame reads as

$$\vec{J}_z^L(\vec{k}, \hat{p}^L) = -\frac{\sigma}{60} |\mathcal{E}(\omega, \omega')| \left(\vec{d}_{1,0} \times \vec{d}_{2,0} \right) \cdot \vec{D}_{12}(\vec{k}; \hat{p}^L) e^{i(\omega_{21}\tau - \frac{\pi}{2} + \phi(\omega, \omega'))} + \text{c.c.} + \text{cross terms}, \quad (23)$$

$$\begin{aligned}\vec{D}_{12}(\vec{k}, \hat{p}^L) &= (|p_x|^2 + |p_y|^2) \vec{D}_{12}(\vec{k}, \hat{x}^L) + |p_z|^2 \vec{D}_{12}(\vec{k}, \hat{z}^L) \\ &= -2 \left[2 - (\hat{n}^L \cdot \hat{p}^L)^2 \right] (\vec{D}_1 \cdot \vec{D}_2^*) \vec{k} + \left[1 - 3(\hat{n}^L \cdot \hat{p}^L)^2 \right] \left[(\vec{D}_2^* \cdot \vec{k}) \vec{D}_1 + (\vec{D}_1 \cdot \vec{k}) \vec{D}_2^* \right],\end{aligned}\quad (24)$$

where $\hat{n}^L = \hat{z}^L$ is the propagation direction of the pump. The coefficient $[1 - 3(\hat{n}^L \cdot \hat{p}^L)^2]$ vanishes after averaging over orientations of the probe and we obtain the simple expression

$$\vec{D}_{12}^u(\vec{k}) = \int d\varphi_P \int d\theta_P \sin\theta_P \vec{D}_{12}(\vec{k}, \hat{p}^L) = -\frac{10}{3} (\vec{D}_1 \cdot \vec{D}_2^*) \vec{k}, \quad (25)$$

which, once integrated over orientations of \vec{k} [see Eq. (18)], gives the Raman-type photoionization vector that goes into the final expression for the current Eq. (19). Note that, once the partial alignment by the pump is excluded, only the vector \vec{k} can be used to “complete” the triple product.

D. PXECD in the plane wave continuum.

So far, all our calculations have been general. We now consider the case of the plane wave continuum, eliminating any possibility of chiral contributions from the continuum (i.e. the photoelectron scattering from the chiral potential of the core). We write the photoionization dipoles in the velocity gauge,

$$\vec{D}_i = \langle \vec{k} | \vec{p} | \psi_i \rangle = \vec{k} \tilde{\psi}_i(\vec{k}), \quad i = 1, 2 \quad (26)$$

The photoionization matrix elements are proportional to the wave functions of the excited states in the momentum space, $\tilde{\psi}_i(\vec{k})$. Putting these expressions in Eq. (20), we obtain

$$\vec{D}_{12}(\vec{k}) = -2k^2 \tilde{\psi}_1(\vec{k}) \tilde{\psi}_2^*(\vec{k}) \vec{k} \quad (27)$$

Thus, the Raman-type photoionization vector $\vec{D}_{12}(k) = \int d\Omega_k \vec{D}_{12}(\vec{k})$ becomes:

$$\vec{D}_{12}^{\text{PW}}(k) = -2 \int d\Omega_k k^2 \tilde{\psi}_1(\vec{k}) \tilde{\psi}_2^*(\vec{k}) \vec{k}. \quad (28)$$

We now show that $\vec{D}_{12}^{\text{PW}}(k)$ is purely imaginary. We split the electronic wave-functions $\psi_{1,2}(\vec{r})$ of the bound states $|1\rangle, |2\rangle$ in coordinate space into their symmetric and antisymmetric components:

$$\psi_{1,2}(\vec{r}) = \psi_{1,2}^S(\vec{r}) + \psi_{1,2}^A(\vec{r}) \quad (29)$$

Their Fourier transforms are

$$\tilde{\psi}_{1,2}(\vec{k}) \equiv \int d\vec{r} \psi_{1,2}(\vec{r}) e^{i\vec{k}\vec{r}} = \int d\vec{r} \psi_{1,2}^S(\vec{r}) \cos(\vec{k} \cdot \vec{r}) + i \int d\vec{r} \psi_{1,2}^A(\vec{r}) \sin(\vec{k} \cdot \vec{r}) \equiv \tilde{\psi}_{1,2}^S(\vec{k}) + i\tilde{\psi}_{1,2}^A(\vec{k}), \quad (30)$$

where both $\tilde{\psi}_{1,2}^A(\vec{k})$ and $\tilde{\psi}_{1,2}^S(\vec{k})$ are real functions. After simple algebra we get:

$$\vec{D}_{12}^{\text{PW}}(k) = 2i \int d\Omega_k k^2 \left(\tilde{\psi}_1^S(\vec{k}) \tilde{\psi}_2^A(\vec{k}) - \tilde{\psi}_1^A(\vec{k}) \tilde{\psi}_2^S(\vec{k}) \right) \vec{k} \quad (31)$$

Thus, $\vec{D}_{12}^{\text{PW}}(k)$ is purely imaginary:

$$\vec{D}_{12}^{\text{PW}}(k) = i\vec{D}_{12}^{i,\text{PW}}(k) \quad (32)$$

Taking into account Eq. (32) and using explicitly the imaginary component of the Raman-type photoionization vector $\vec{D}_{12}^{i,\text{PW}}(k)$ we obtain Eq. (4) of the main text:

$$\vec{J}_z^{L,\text{PW}}(k) = -\frac{\sigma}{30} \frac{|\mathcal{E}(\omega, \omega')|}{\omega'_k \omega'_k} \left[\vec{d}_{1,0} \times \vec{d}_{2,0} \right] \cdot \vec{D}_{12}^{i,\text{PW}}(k) \cos(\omega_{21}\tau + \phi(\omega, \omega')). \quad (33)$$

The constants as well as the phases and amplitudes of the pump and probe fields $\phi(\omega, \omega')$, $|\mathcal{E}(\omega, \omega')|$ at the excitation and probe frequencies, appearing in Eq. (33), were omitted in Eq. (4) of the main text for compactness and clarity of our equations. Importantly, Eq. (33) shows that the PXECD current remains chiral for every k , even when the effects of chirality in the continuum are removed by using a plane wave continuum. Thus, PXECD can be used as a probe exclusively sensitive to chiral bound dynamics.

We now establish the relationship between the PXCD current and the total PXECD current integrated over all k . First, we compare the Raman-type photoionization vector integrated over all k ($d\vec{k} \equiv d\Omega_k k^2$):

$$-\frac{1}{2} \int dk \vec{D}_{12}^{\text{PW}}(k) \equiv \int d\vec{k} \tilde{\psi}_1(\vec{k}) \tilde{\psi}_2^*(\vec{k}) \vec{k}, \quad (34)$$

and the bound transition dipole between the two excited states $\vec{d}_{1,2}$. The latter can be written in a strikingly similar form:

$$i\omega_{21} \vec{d}_{1,2} \equiv \int d\vec{k} \tilde{\psi}_1(\vec{k}) \tilde{\psi}_2^*(\vec{k}) \vec{k} \quad (35)$$

The right hand sides of Eqs. (34,35) are equivalent. Thus, $i\omega_{21}\vec{d}_{1,2}$ and $-\int dk \vec{D}_{12}^{\text{PW}}(k)/2$ are also equivalent. If $\omega_{21} = 0$, the Raman-type photoionization vector integrated over all k is also zero.

Thus we recover a simple connection between the bound transition dipole $\vec{d}_{1,2}$ and the integrated Raman-type photoionization vector:

$$\omega_{21}\vec{d}_{1,2} \equiv -\frac{1}{2} \int dk \vec{D}_{12}^{i,\text{PW}}(k) \quad (36)$$

Here we explicitly used that $\vec{D}_{12}^{\text{PW}}(k)$ is purely imaginary. This is evident from Eqs. (32,35). Using this simple connection and integrating the continuum current over all k (assuming adjustable strength of the probe pulse at all frequencies, so that $C_{\mathcal{E}} = \frac{1}{5} \frac{\mathcal{E}'^*(\omega'_{\vec{k}_2})\mathcal{E}'(\omega'_{\vec{k}_1})}{\omega'_{\vec{k}_1}\omega'_{\vec{k}_2}}$ is independent of k) we obtain a simple relationship between the bound and total (integrated over all k) continuum currents:

$$J_{\text{tot}}^{\text{PXECD}} \equiv \int dk \overline{J_z^{\text{L,PW}}}(k), \quad (37)$$

$$J_{\text{tot}}^{\text{PXECD}} = C_{\mathcal{E}} J_z^{\text{PXCD}}. \quad (38)$$

Here we used Eqs.(11,33,36). Despite its simplicity, Eq. (38) is important for understanding the PXECD phenomenon. It shows that even if one explicitly removes the effects associated with the chirality of the molecular continuum or effects associated with the non-spherical symmetry of the molecular continuum (by using a plane wave continuum instead), the PXECD current remains chiral, not only for every k (see Eq. (33)), but also integrally for all k , because in this case it directly reflects the chirality of the bound PXCD current. If the bound current is equal to zero (e.g. when the two bound states are degenerate), then the total continuum current is also equal to zero.

E. The nature of the PXECD current.

We can now address the question about the mechanisms leading to the PXECD current more broadly. The PXECD continuum current may arise due to the following reasons: (a) due to bound PXCD current; (b) due to partial alignment of the molecular ensemble by the pump pulse, (c) due to the degenerate PXECD process, even in the absence of bound PXCD current, i.e. when $\omega_{12} = 0$. Degenerate PXECD is the PXECD for degenerate excited states.

Eq. (19) is general, it contains all three effects. The set of examples that we have considered in previous subsections allows us to identify and to isolate each of these effects. The effect of partial alignment due to the pump pulse can be "removed" by considering an unpolarized probe. Eq. (25) shows that chiral response does not vanish in this case. Finally, to isolate the degenerate PXECD process, one can remove the effects (a,b) by considering unpolarized light and setting $\omega_{12} = 0$. When the effects (a,b) are removed, for $\omega_{12} = 0$ and an unpolarized probe, the Raman-type photoionization vector is

$$\vec{D}_{12}^{\text{u}}(\vec{k}) = -\frac{10}{3} (\vec{D}_1(\vec{k}) \cdot \vec{D}_2^*(\vec{k})) \vec{k} \quad (39)$$

and the PXECD current is:

$$\overline{J_z^{\text{L}}}(k) = \frac{\sigma}{9} |\mathcal{E}(\omega, \omega')| \int d\Omega_k [\vec{d}_{1,0} \times \vec{d}_{2,0}] \cdot \vec{k} \cdot (\vec{D}_1^i(\vec{k}) \cdot \vec{D}_2^*(\vec{k}) - \vec{D}_1^*(\vec{k}) \cdot \vec{D}_2^i(\vec{k})) \quad (40)$$

In this expression, for simplicity we set the phases $\phi(\omega, \omega') = 0$.

In the previous subsection we have demonstrated that in the case of a plane wave continuum, the total PXECD current (integrated over all k) vanishes if we set $\omega_{12} = 0$. However, each momentum component of this current remains finite as long as the excited states |1> and |2> do not have definite parity, and $d_{12} \neq 0$. Note that the triple product in Eq. (40) is formed by the two bound dipoles and the vector \vec{k} of the continuum electron.

F. Inverse Abel transform of the two-photon chiral signal.

Here we show how the Abel-inverted quantities α and α' (Fig.4 of the main text) are connected to the conventional asymmetry parameters of the 3D photo-electron signal.

Experimentally, the photo-electron spectrum closely follows the spectrum of the probe: the spectra are located within a bell-shaped 3D sphere $G_0(k, k_0)$, where $E_0 = k_0^2/2$ is the central energy, with width $\Delta E \ll E_0$. In the geometry of our experiment, the 3D chiral asymmetry signal can be written as

$$R_{3D}^{\text{PXECD}} = CG_0(k, k_0) [q_{1,0}P_1^0(\cos\theta) + q_{2,-2}P_2^2(\cos\theta)\sin(2\phi) + q_{3,0}P_3^0(\cos\theta) + q_{3,2}P_3^2(\cos\theta)\cos(2\phi)] \quad (41)$$

where C depends on the gas density, etc. The Legendre polynomials P_2^2 and P_3^2 reflect the geometry of the experiment, where the pump field is propagating along the z axis. The parameters $q_{2,-2}$ and q_{32} appear due to the breaking of the cylindrical symmetry in our experimental setup; q_{32} reflects the chiral asymmetry, changing sign with changing light helicity or enantiomer handedness. The 3D signal is projected onto the 2D x-z plane, simulating the measurement, and then raised back to 3D, simulating the reconstruction. The modeling is done numerically using the experimentally measured $G_0(k, k_0)$. The analytical model will be described elsewhere. The presence of q_{32} modifies the reconstructed 3D image in two ways. First, α and α' (Fig. 4 of the main text) contain q_{32} : $\alpha = q_{10} + 6q_{32}$ and $\alpha' = q_{10} - 6q_{32}$. Secondly, a characteristic signal $\propto q_{32}(k/k_0)P_1^0(\cos\theta)$ for $k < k_0$ lying outside of the spectral bandwidth of the pulse may appear as signature of q_{32} . This background allows us to give the upper estimate to q_{32} from the 3D images directly obtained via the inverse Abel transform of the measured 2D spectra (see SI).

G. Numerical simulations.

The numerical results for PXCD and PXECD in fenchone, presented in Figs. 2 and 4, have been obtained using perturbative quantum-mechanical calculations which mimic the experimental pump-probe setup. These calculations employ bound and continuum Configuration-Interaction Single (CIS) states in the framework of frozen nuclei and single-active electron approximations. Our simulations have shown that molecular chiral Rydberg wavepackets can be formed by absorption of a circularly polarized photon. In addition, (i) the population of this wavepacket does not depend on the helicity within the dipole approximation, (ii) this wavepacket is inherently chiral, as imaged by the photoexcitation circular dichroism which survives orientation averaging within a set of randomly aligned targets as long as there is an electronic coherence between the excited states, (iii) when a linearly polarized probe is switched on, this chiral dichroism is transferred into the continuum and mapped onto the (usual) photoelectron circular dichroism, even in the plane-wave approximation, (iv) the electronic beating between the underlying wavepacket states is noticeable in the excitation and the related ionization dichroisms, as function of the pump-probe delay, but the beating is blurred in the total photo-ionization signal. All of this sheds new light on the origin of chirality, whose signature is no more constrained to molecular ionization but extends to the whole electronic spectrum, within the usual and intuitive dipole approximation. Extended details regarding the simulations are given in Section III of the SI.

H. Vibrational coherence in PXECD.

Section V of the SI discusses the role that the excitation of the vibrational wavepackets plays in PXECD. Our analytical results presented above are general and can be applied to both electronic and vibrational (vibronic) states. However, the non-collinearity of the excitation dipoles required in PXCD leads to the following conditions for observing vibrational PXECD. Firstly, it requires the breakdown of the Franck-Condon approximation. This is expected to be the case for large molecules exhibiting broad vibrational lines. Indeed, the essence of this approximation is that the vibrational wave-functions are sufficiently compact in coordinate space, so that the electronic transition dipoles do not change as a function of the vibrational coordinates within this compact region. If, however, the vibrational wave-functions spread over considerable distances, the breakdown of the Franck-Condon approximation is expected and natural. Secondly, it requires multidimensional, at least two dimensional, potential energy surfaces (PES), which is certainly the case for chiral molecules.

Data availability The data that support the plots within this paper and other findings of this study are available from the corresponding author upon reasonable request.

Photoexcitation Circular Dichroism in Chiral Molecules: Supplementary Information

S. Beaulieu^{1,2}, A. Comby¹, D. Descamps¹, B. Fabre¹, G. A. Garcia³,
R. Généaux⁴, A. G. Harvey⁵, F. Légaré², Z. Mašín⁵, L. Nahon³, A. F.
Ordonez^{5,6}, S. Petit¹, B. Pons¹, Y. Mairesse¹, O. Smirnova^{5,6}, V. Blanchet¹

¹ *Université de Bordeaux - CNRS - CEA,
CELIA, UMR5107, F33405 Talence, France*

² *Institut National de la Recherche Scientifique, Varennes, Quebec, Canada*

³ *Synchrotron Soleil, l'orme des Merisiers,
BP48, St Aubin, 91192 Gif sur Yvette, France*

⁴ *LIDYL, CEA, CNRS, Université Paris-Saclay,
CEA Saclay, 91191 Gif-sur-Yvette France.*

⁵ *Max-Born-Institut, Max-Born-Str. 2A, 12489 Berlin.*

⁶ *Technische Universität Berlin, Ernst-Ruska-Gebäude,
Hardenbergstr. 36A, 10623, Berlin, Germany.*

This Supplementary Information describes the details of the analytical, numerical and experimental analysis of Photoexcitation Circular Dichroism (PXCD) and its probing.

First, we show how helical electron motion can be excited in an isotropic ensemble of randomly oriented neutral chiral molecules without the help of magnetic or quadrupole interactions. The underlying ensemble-averaged chiral charge displacement and chiral electron density in excited states of neutral molecules constitute a new phenomenon we call PXCD. We derive Eqs. (1,2) of the main text, which prove that PXCD is a quintessential chiral effect, as its observables, such as the induced dipole and current, are time-even pseudoscalars.

Second, we show how PXCD can be probed without the aid of further chiral interactions. We derive Eqs. (3,4) of the main text, which describe one such probe – Photoexcitation induced photoElectron Circular Dichroism (PXECD). We prove that the averaged over molecular orientations photo-electron current - the PXECD observable - is also a time-even pseudoscalar. We demonstrate the unique sensitivity of PXECD to chiral dynamics in bound states.

Third, we give some technical details about the experimental conditions and we describe the analysis of the experimental images presented in Fig.4 of the main text. PXECD images recorded in the two enantiomers of fenchone are also shown.

Fourth, we present the numerical quantum-mechanical calculations that describe the PXCD and PXECD phenomena in fenchone, mimicking the experiments performed at CELIA. These calculations reveal how the absorption of a circularly polarized photon leads to the formation of a Rydberg wavepacket in fenchone molecules whose chiral dynamics is mapped onto the continuum through absorption of a second, linearly polarized, photon.

Finally, we discuss the role that the excitation of vibrational wavepackets plays in PXECD.

I. EXCITING CHIRAL CURRENTS

In this section we show how macroscopic chiral electron currents can be excited in neutral molecules without the help of magnetic field or quadrupole interactions. Specifically, we show how the interaction of an ultrashort circularly polarized light (pump pulse) and a randomly oriented ensemble of chiral molecules results in the helical motion of the ensemble-averaged induced electric dipole and the excitation of an ensemble-averaged coherent helical current.

We derive Eqs. (1,2) of the main text, which describe the components of the induced dipole and current in the propagation direction z of the circularly polarized pump pulse. Eqs. (1,2) of the main text show that the z components of the induced dipole and current are **time-even pseudoscalars**, i.e. are quintessential chiral observables. Here we also derive other components (x, y) of the induced dipole and current, which also survive the orientational averaging. These two components of the dipole and the current describe rotation in the polarization plane and together with the chiral-sensitive component along the z -axis describe helical charge motion in a randomly oriented ensemble of chiral molecules, arising upon excitation by the pump pulse (see Fig. 1 below and Fig. 1 (b) of the main text).

Fundamentally, the excitation of a chiral current and density in an initially isotropic ensemble using circularly polarized light without relying on light's chiral properties is due to the coherent excitation of a superposition of chiral eigenstates. We call this new phenomenon PhotoExcited Circular Dichroism (PXCD). PXCD is an example of spontaneous symmetry breaking, which has a dynamical origin. We show how ultrafast pulses can be used to induce it and to resolve it in time. Spontaneous symmetry breaking plays a key role in understanding many-body phenomena (see e.g. [1]) and often has a dynamical origin: from the "inversion" of the ammonia molecule to temporal variations of the shape of atomic nucleus. In such cases one needs an ultrafast camera to catch its ever evolving image. It is very exciting to imagine the role that ultrafast measurements can play in time-resolving this ubiquitous phenomenon in many-body systems.

We now turn to the formal description of the PXCD phenomenon. Due to the resonant nature of the excitation, the molecule is modeled as a three level system and the interaction between the electric field and the molecule is treated using first order perturbation theory and the dipole approximation.

We define the pump field in the laboratory reference frame as:

$$\vec{E}^L(t) = F(t) [\cos(\omega t + \delta) \hat{x}^L + \sigma \sin(\omega t + \delta) \hat{y}^L] \quad (1)$$

where ω is the carrier frequency, $F(t)$ includes the field amplitude and the envelope, and the carrier-envelope phase δ determines the orientation of the electric field vector at the moment $t = 0$. Finally, the helicity $\sigma = \pm 1$ determines whether the field is left or right polarized. This pump field can be written in the compact notation

$$\vec{E}^L(t) = \frac{1}{\sqrt{2}} F(t) \hat{\epsilon}_\sigma^L e^{-i(\omega t + \delta)} + \text{c.c.} \quad (2)$$

where the rotation of the field is characterized by the operator

$$\hat{\epsilon}_\sigma^L = \frac{\hat{x}^L + \sigma i \hat{y}^L}{\sqrt{2}} \quad (3)$$

The superscript L indicates vectors in the laboratory (lab) frame, while the vectors in molecular frame do not have a superscript. The transformation of vectors from the lab frame to the molecular frame is performed according to $\vec{v} = R(\varrho) \vec{v}^L$ where

$$R(\varrho) = Z(\alpha) Y(\beta) Z(\gamma)$$

$$= \begin{pmatrix} \cos \alpha \cos \beta \cos \gamma - \sin \alpha \sin \gamma & -\cos \alpha \cos \beta \sin \gamma - \sin \alpha \cos \gamma & \cos \alpha \sin \beta \\ \sin \alpha \cos \beta \cos \gamma + \cos \alpha \sin \gamma & -\sin \alpha \cos \beta \sin \gamma + \cos \alpha \cos \gamma & \sin \alpha \sin \beta \\ -\sin \beta \cos \gamma & \sin \beta \sin \gamma & \cos \beta \end{pmatrix} \quad (4)$$

with $\varrho \equiv (\alpha, \beta, \gamma)$ the Euler angles in the z - y - z convention. Using perturbation theory, after the end of the pump pulse of duration T_1 , we find the wave function at a time τ :

$$\psi_\varrho(\tau) = a_0 \psi_0 e^{-i\omega_0 \tau} + a_1(\varrho) \psi_1 e^{-i\omega_1 \tau} + a_2(\varrho) \psi_2 e^{-i\omega_2 \tau}, \quad (5)$$

where $a_0 \approx 1$ and the expressions for the excitation amplitudes are standard:

$$a_i(\varrho) = -i \left[R(\varrho) \hat{\varepsilon}_\sigma^L \cdot \vec{d}_{i,0} \right] \mathcal{E}(\omega_{i0}) \quad (6)$$

$i = 1, 2$ labels the excited states, $\vec{d}_{i,0}$ are the transition dipole matrix elements to these states from the ground state, in the molecular frame, and the pump field is rotated into the molecular frame via the rotation matrix $R(\varrho)$. The excitation amplitude is proportional to the spectral component of the pump at the corresponding transition frequency ω_{i0} , $\mathcal{E}(\omega_{i0})$.

The induced dipole is:

$$\vec{d}_\varrho(\tau) = \langle \psi_\varrho(\tau) | \hat{\vec{d}} | \psi_\varrho(\tau) \rangle = \sum_{i,j=0}^2 a_i^*(\varrho) a_j(\varrho) e^{-i\omega_{ji}\tau} \vec{d}_{i,j}. \quad (7)$$

where $\vec{d}_{i,j} = \langle i | \hat{\vec{d}} | j \rangle$ and $\omega_{ij} = \omega_i - \omega_j$.

Now we move to the lab frame and average over all molecular orientations

$$\begin{aligned} \overline{\vec{d}^L}(\tau) &= \int d\varrho \vec{d}_\varrho^L(\tau) \\ &= \int d\varrho R^t(\varrho) \vec{d}_\varrho(\tau) \\ &= \sum_{i,j=0}^2 e^{-i\omega_{ji}\tau} \left\{ \int d\varrho a_i^*(\varrho) a_j(\varrho) R^t(\varrho) \right\} \vec{d}_{i,j}, \end{aligned} \quad (8)$$

where $\int d\varrho \equiv \frac{1}{8\pi^2} \int_0^{2\pi} d\alpha \int_0^\pi d\beta \int_0^{2\pi} d\gamma \sin \beta$ and $R^t = R^{-1}$ is the transpose of the rotation matrix R , $8\pi^2$ is the normalization coefficient.

Let us begin with the evaluation of the term $i, j = 0, 0$. In the perturbative regime, $a_0 \approx 1$ and therefore the only dependence on ϱ in the integrand is in $R^t(\varrho)$. Inspection of $R(\varrho)$ in Eq. (4) shows that the integral vanishes.

The terms $i = 0, j = 1, 2$ arising due to coherence between the ground $|0\rangle$ and excited states $|1\rangle, |2\rangle$ of the molecule, read

$$\begin{aligned}
\left[\overline{d^L}(\tau)\right]_{i=0;j=1,2} &\equiv e^{-i\omega_{j0}\tau} \left\{ \int d\varrho a_j(\varrho) R^t(\varrho) \right\} \vec{d}_{0,j} \\
&= i\mathcal{E}(\omega_{j0}) e^{-i\omega_{j0}\tau} \left\{ \int d\varrho \left[R(\varrho) \hat{\varepsilon}_\sigma^L \cdot \vec{d}_{j,0} \right] R^t(\varrho) \right\} \vec{d}_{0,j} \\
&= \frac{i\mathcal{E}(\omega_{j0}) e^{-i\omega_{j0}\tau}}{3\sqrt{2}} \begin{pmatrix} (\vec{d}_{j,0})_x & (\vec{d}_{j,0})_y & (\vec{d}_{j,0})_z \\ i\sigma (\vec{d}_{j,0})_x & i\sigma (\vec{d}_{j,0})_y & i\sigma (\vec{d}_{j,0})_z \\ 0 & 0 & 0 \end{pmatrix} \vec{d}_{0,j} \\
&= \frac{i\mathcal{E}(\omega_{j0}) e^{-i\omega_{j0}\tau}}{3\sqrt{2}} (d_{j,0})^2 \begin{pmatrix} 1 \\ i\sigma \\ 0 \end{pmatrix}, \tag{9}
\end{aligned}$$

where we made use of $\vec{d}_{i,j} = \vec{d}_{j,i} \in \mathbb{R}^3$, i.e. all components of transition dipole vectors are real quantities.

Now we add the complex conjugate of the expression above, to obtain the final result for the averaged induced dipole between the ground and excited states (corresponding to the terms $j = 0, i = 1, 2$):

$$\begin{aligned}
\left[\overline{d^L}(\tau)\right]_{i=0;j=1,2} + \left[\overline{d^L}(\tau)\right]_{i=1,2;j=0} &= \left[\overline{d^L}(\tau)\right]_{i=0;j=1,2} + \text{c.c.} \\
&= \frac{\sqrt{2}}{3} |\mathcal{E}(\omega_{j0})| (d_{j,0})^2 \begin{pmatrix} \cos(\omega_{j0}\tau - \phi_j - \frac{\pi}{2}) \\ \sigma \sin(\omega_{j0}\tau - \phi_j - \frac{\pi}{2}) \\ 0 \end{pmatrix} \tag{10}
\end{aligned}$$

where $\mathcal{E}(\omega_{j0}) = |\mathcal{E}(\omega_{j0})| e^{i\phi_j}$. Note that this term corresponds to a dipole in the xy plane rotating in the same direction as the field, with frequency ω_{j0} , and delayed by $\phi_j + \frac{\pi}{2}$, where $\frac{\pi}{2}$ appears due

to the resonance nature of the interaction with the pump pulse.

Finally, the terms $i = 1, 2, j = 1, 2$ involving only the coherence induced between the excited states yield:

$$\begin{aligned}
\left[\overline{d^L}(\tau) \right]_{i=1,2;j=1,2} &= e^{-i\omega_{ji}\tau} \left\{ \int d\varrho a_i^*(\varrho) a_j(\varrho) R^t(\varrho) \right\} \vec{d}_{i,j} \\
&= \mathcal{E}^*(\omega_{i0}) \mathcal{E}(\omega_{j0}) e^{-i\omega_{ji}\tau} \left\{ \int d\varrho \left[R(\varrho) \hat{\varepsilon}_{-\sigma}^L \cdot \vec{d}_{i,0} \right] \left[R(\varrho) \hat{\varepsilon}_{\sigma}^L \cdot \vec{d}_{j,0} \right] R^t(\varrho) \right\} \vec{d}_{i,j} \\
&= \frac{i}{6} \mathcal{E}^*(\omega_{i0}) \mathcal{E}(\omega_{j0}) e^{-i\omega_{ji}\tau} \sigma \begin{pmatrix} 0 & 0 & 0 \\ 0 & 0 & 0 \\ \left[\vec{d}_{i,0} \times \vec{d}_{j,0} \right]_x & \left[\vec{d}_{i,0} \times \vec{d}_{j,0} \right]_y & \left[\vec{d}_{i,0} \times \vec{d}_{j,0} \right]_z \end{pmatrix} \vec{d}_{j,i} \\
&= \frac{i}{6} \mathcal{E}^*(\omega_{i0}) \mathcal{E}(\omega_{j0}) e^{-i\omega_{ji}\tau} \begin{pmatrix} 0 \\ 0 \\ \sigma \left[\vec{d}_{i,0} \times \vec{d}_{j,0} \right] \cdot \vec{d}_{i,j} \end{pmatrix}. \tag{11}
\end{aligned}$$

From the triple product in the result we see that the diagonal terms $i = j$ vanish, while the sum of the cross terms reads

$$\begin{aligned}
\left[\overline{d^L}(\tau) \right]_{i=1,j=2} + \left[\overline{d^L}(\tau) \right]_{i=2,j=1} &= \left[\overline{d^L}(\tau) \right]_{i=1,j=2} + \text{c.c.} \\
&= \frac{1}{3} |\mathcal{E}(\omega_{10})| |\mathcal{E}(\omega_{20})| \sin(\omega_{21}\tau - \phi_{21}) \begin{pmatrix} 0 \\ 0 \\ \sigma \left[\vec{d}_{1,0} \times \vec{d}_{2,0} \right] \cdot \vec{d}_{1,2} \end{pmatrix} \tag{12}
\end{aligned}$$

Combining Eqs. (10,12) we obtain the expression for the molecular-orientation-averaged electric

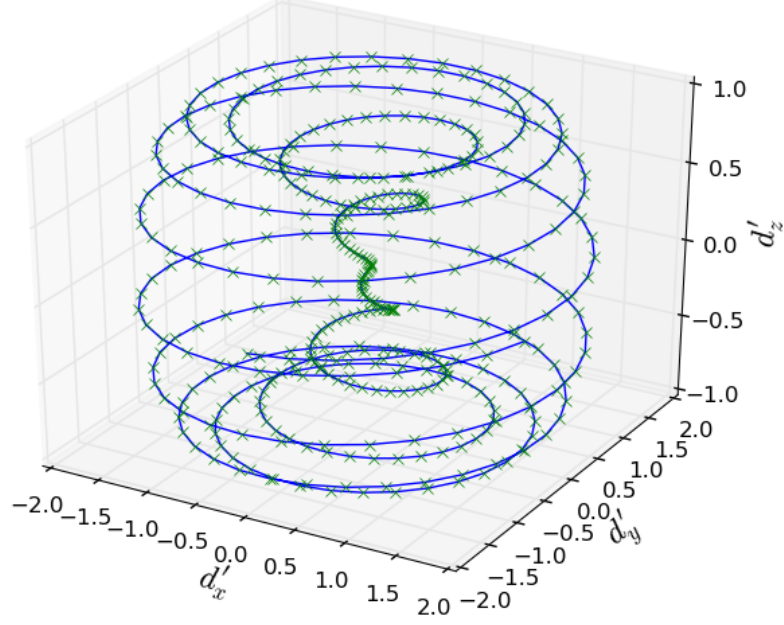


Figure 1. Trajectory of the dipole during the first period ($2\pi/\omega_{21} \sim 8$ fs) of linear oscillation along z for $\omega_{20} = 6.6$ eV, $\omega_{10} = 6.1$ eV, $\sigma = 1$, $\phi_1 = \phi_2 = 0$. The \times 's are equally spaced in time, which means that the higher the density of \times 's the lower the velocity. The coordinates are scaled according to $d'_x = \left[\frac{2\sqrt{2}}{3} |\mathcal{E}_1(\omega)| (d_{1,0})^2 \right]^{-1} [\bar{d}^L(\tau)]_x$, $d'_y = \left[\frac{2\sqrt{2}}{3} |\mathcal{E}_1(\omega)| (d_{1,0})^2 \right]^{-1} [\bar{d}^L(\tau)]_y$, $d'_z = \left[\frac{1}{3} |\mathcal{E}_1(\omega)|^2 [\bar{d}_{1,0} \times \bar{d}_{2,0}] \cdot \bar{d}_{1,2} \right]^{-1} [\bar{d}^L(\tau)]_z$.

dipole in the lab frame:

$$\bar{d}^L = \frac{1}{3} \begin{pmatrix} \sqrt{2} \left[|\mathcal{E}(\omega_{10})| (d_{1,0})^2 \cos(\omega_{10}\tau - \phi_1 - \frac{\pi}{2}) + |\mathcal{E}(\omega_{20})| (d_{2,0})^2 \cos(\omega_{20}\tau - \phi_2 - \frac{\pi}{2}) \right] \\ \sigma\sqrt{2} \left[|\mathcal{E}(\omega_{10})| (d_{1,0})^2 \sin(\omega_{10}\tau - \phi_1 - \frac{\pi}{2}) + |\mathcal{E}(\omega_{20})| (d_{2,0})^2 \sin(\omega_{20}\tau - \phi_2 - \frac{\pi}{2}) \right] \\ |\mathcal{E}(\omega_{10})| |\mathcal{E}(\omega_{20})| \sigma [\bar{d}_{1,0} \times \bar{d}_{2,0}] \cdot \bar{d}_{1,2} \sin(\omega_{21}\tau - \phi_{21}) \end{pmatrix} \quad (13)$$

Note that chirality is encoded in the z -component of the averaged dipole, which contains the triple product of the three transition dipole vectors "connecting" three states of a chiral molecule. This pseudoscalar vanishes for achiral molecules, and changes sign for opposite enantiomers or alternatively for opposite helicity of the pump pulse. Eq. (1) of the main text reproduces this result for the z -component of the averaged induced dipole and for the specific case when $\phi_{21} = 0$. Pump field components at the excitation frequencies $|\mathcal{E}(\omega_{10})| |\mathcal{E}(\omega_{20})|$ appearing in the expression for the z -component were omitted in Eq. (1) of the main text for compactness and clarity of our equations.

In the case of our experiment, the energy separation between the excited states is small compared to the separation between each excited state and the ground state. Thus, we have $\omega_{21} \ll \omega_{10}$ and $\omega_{21} \ll \omega_{20}$, which means a "low" frequency linear oscillation of the dipole along z combined with the "high" frequency circular rotation in the xy plane, which corresponds to helical-like motion of the charge density. This motion switches helicity each half period π/ω_{21} because the dipole along z direction changes sign every half period of linear oscillation while the direction of rotation in xy remains the same, as it is determined only by the helicity of the pump pulse (see Figure 1). In left and right enantiomers the induced dipoles would map out the helices of opposite helicity for every given half-period of motion along the z -axis. Assuming $\omega_{10} \approx \omega_{20}$, $\mathcal{E}(\omega_{10}) \approx \mathcal{E}(\omega_{20})$, $\phi_{12} = 0$ and $(\vec{d}_{1,0})^2 \approx (\vec{d}_{2,0})^2$, we obtain a simplified expression for the induced dipole:

$$\overline{\vec{d}}^{\text{L}}(\tau) \approx \frac{1}{3} \begin{pmatrix} 2\sqrt{2} |\mathcal{E}(\omega_{10})| (\vec{d}_{1,0})^2 \cos(\frac{\omega_{21}}{2}\tau) \cos(\omega_{10}\tau - \phi_1 - \frac{\pi}{2}) \\ \sigma 2\sqrt{2} |\mathcal{E}(\omega_{10})| (\vec{d}_{1,0})^2 \cos(\frac{\omega_{21}}{2}\tau) \sin(\omega_{10}\tau - \phi_1 - \frac{\pi}{2}) \\ |\mathcal{E}(\omega_{10})|^2 \sigma [\vec{d}_{1,0} \times \vec{d}_{2,0}] \cdot \vec{d}_{1,2} \sin(\omega_{21}\tau) \end{pmatrix}. \quad (14)$$

By definition, the expressions for the chiral current are obtained by differentiating the expression for the dipole wrt time. Thus, from Eq. (13) we obtain the expressions for the helical current:

$$\overline{\vec{j}}^{\text{L}} = \frac{1}{3} \begin{pmatrix} -\sqrt{2} \left[|\mathcal{E}(\omega_{10})| \omega_{10} (d_{1,0})^2 \sin(\omega_{10}\tau - \phi_1 - \frac{\pi}{2}) + |\mathcal{E}(\omega_{20})| \omega_{20} (d_{2,0})^2 \sin(\omega_{20}\tau - \phi_2 - \frac{\pi}{2}) \right] \\ \sigma \sqrt{2} \left[|\mathcal{E}(\omega_{10})| \omega_{10} (d_{1,0})^2 \cos(\omega_{10}\tau - \phi_1 - \frac{\pi}{2}) + |\mathcal{E}(\omega_{20})| \omega_{20} (d_{2,0})^2 \cos(\omega_{20}\tau - \phi_2 - \frac{\pi}{2}) \right] \\ |\mathcal{E}(\omega_{10})| |\mathcal{E}(\omega_{20})| \omega_{21} \sigma [\vec{d}_{1,0} \times \vec{d}_{2,0}] \cdot \vec{d}_{1,2} \cos(\omega_{21}\tau - \phi_{21}) \end{pmatrix} \quad (15)$$

In the next section, we show how the chiral dynamics induced by the pump pulse in the excited states of randomly oriented molecules can be probed without the help of any further chiral interactions.

II. PROBING CHIRAL CURRENTS

In this section we derive Eqs. (3,4) of the main text. We show how chiral electron currents excited in neutral molecules can be probed without the aid of further chiral interactions. Specifically, we show that when a coherent superposition of states is excited with a circularly polarized pump pulse in a randomly oriented ensemble of chiral molecules, photoionization from such a superposition with a linearly polarized probe pulse into the electron continuum leads to the appearance of a chiral photo-electron current. The chiral photoelectron current has been detected in our experiment. We call this new phenomenon PhotoeXcitation-induced photoElectron Circular Dichroism (PXECD).

In Section II-C we show that the PXECD current remains chiral even for a plane wave continuum, i.e. when photoelectron scattering from a chiral potential is fully excluded. This important result emphasizes that probing chiral bound dynamics does not require further chiral interactions: neither the application of chiral light, nor photoelectron scattering from the chiral potential of the core. The initial (ground) state ($|0\rangle$, see Fig 1(c) of the main text) also does not have to be chiral. As such, PXECD presents a genuine probe of chiral dynamics in bound states. We also show that the total PXECD current is proportional to PXCD current in bound states.

In Section II-B we show that the partial alignment of the excited molecular ensemble induced by the pump pulse is not responsible for creating the chiral signal in PXECD.

In Section II-D we analyze the nature of the PXECD current and compare it with the PECD current. To perform such comparison we derive PECD current using our newly developed formalism.

In Section II-E we link our formalism applied to PECD to earlier studies of the PECD and discuss Fig. 1(d) of the main text.

A. Derivation of the chiral PXECD current

In this subsection we derive Eq. (3) of the main text. To calculate the PXECD photoelectron current resulting from the photoionization of excited states, we need to consider the bound-free transitions due to the probe field, linearly polarized along the laboratory \hat{x}^L axis, carried at the frequency ω' , and delayed by a time τ from the pump field. The population amplitude of a continuum state \vec{k} after the end of the probe pulse, assuming that the pump and the probe do not overlap, is

$$a_{\vec{k}} = -ia_1 e^{-i\omega_1 \tau} \left(R(\varrho) \hat{x}^L \cdot \vec{D}_1 \right) \mathcal{E}' \left(\omega'_{\vec{k}1} \right) - ia_2 e^{-i\omega_2 \tau} \left(R(\varrho) \hat{x}^L \cdot \vec{D}_2 \right) \mathcal{E}' \left(\omega'_{\vec{k}2} \right) \quad (16)$$

where $\mathcal{E}' \left(\omega'_{\vec{k},i} \right)$ is the spectral amplitude of the probe at the required transition frequency and $\vec{D}_i(\vec{k})$ are bound-free transition dipoles in the molecular frame, \vec{k} is electron momentum vector in molecular frame. Substituting the expressions for the excitation amplitudes a_1 and a_2 (see eq. (6)) into the expression for $a_{\vec{k}}$ we obtain

$$a_{\vec{k}} = - \left(R(\varrho) \hat{\varepsilon}_\sigma^L \cdot \vec{d}_{1,0} \right) \left(R(\varrho) \hat{x}^L \cdot \vec{D}_1 \right) e^{-i\omega_1 \tau} \mathcal{E}(\omega_1) \mathcal{E}' \left(\omega'_{\vec{k}1} \right) \quad (17)$$

$$- \left(R(\varrho) \hat{\varepsilon}_{\sigma}^L \cdot \vec{d}_{2,0} \right) \left(R(\varrho) \hat{x}^L \cdot \vec{D}_2 \right) e^{-i\omega_2 \tau} \mathcal{E}(\omega_2) \mathcal{E}'\left(\omega'_{\vec{k}_2}\right)$$

We can now use these expressions to calculate the photo-electron current in the asymptotic region far away from the core, defined as

$$\vec{J}(k) = \int d\Omega_k |a_{\vec{k}}|^2 \vec{k}. \quad (18)$$

Let us look at the contribution associated with the electron momentum \vec{k}

$$\vec{J}(\vec{k}) = \frac{1}{2} a_{\vec{k}}^* a_{\vec{k}} \vec{k} + \text{c.c.} \quad (19)$$

Substituting expressions for the continuum amplitudes, we obtain the current in the molecular frame:

$$\begin{aligned} \vec{J}(\vec{k}, \varrho) = \frac{1}{2} \sum_{i,j} & \left(R(\varrho) \hat{\varepsilon}_{-\sigma}^L \cdot \vec{d}_{i,0}^* \right) \left(R(\varrho) \hat{x}^L \cdot \vec{D}_i^* \right) \left(R(\varrho) \hat{\varepsilon}_{\sigma}^L \cdot \vec{d}_{j,0} \right) \left(R(\varrho) \hat{x}^L \cdot \vec{D}_j \right) \\ & \times \mathcal{E}^*(\omega_i) \mathcal{E}(\omega_j) \mathcal{E}'^*\left(\omega'_{\vec{k}_i}\right) \mathcal{E}'\left(\omega'_{\vec{k}_j}\right) e^{i\omega_{ij}\tau} \vec{k} + \text{c.c.} \end{aligned} \quad (20)$$

Note that $\vec{J}(\vec{k})$ is independent of the phase δ of the pump field, i.e. the results do not require carrier-envelope phase stabilization or phase-locking of the pulses. In other words, it does not matter whether the probe pulse is linearly polarized along the x axis or the y axis and, vice-versa, the specific direction of the electric field vector of the circular pump pulse at the time of arrival of the probe pulse does not influence our results.

The diagonal terms do not contribute to the molecular-orientation-averaged current in the lab frame, as they correspond to probing a stationary chiral state with a linearly polarized field. This will also become clear from the derivation below. Therefore, we leave only the cross-terms

$$\begin{aligned} \vec{J}(\vec{k}, \varrho) = & \left(R(\varrho) \hat{\varepsilon}_{-\sigma}^L \cdot \vec{d}_{2,0}^* \right) \left(R(\varrho) \hat{x}^L \cdot \vec{D}_2^* \right) \left(R(\varrho) \hat{\varepsilon}_{\sigma}^L \cdot \vec{d}_{1,0} \right) \left(R(\varrho) \hat{x}^L \cdot \vec{D}_1 \right) \\ & \mathcal{E}(\omega, \omega') e^{i\omega_{21}\tau} \vec{k} + \text{c.c.} \end{aligned} \quad (21)$$

where the $\mathcal{E}(\omega, \omega')$ includes all spectral amplitudes of the pump and probe pulses for the relevant transition frequencies,

$$\mathcal{E}(\omega, \omega') = \mathcal{E}^*(\omega_2) \mathcal{E}(\omega_1) \mathcal{E}'^*\left(\omega'_{\vec{k}_2}\right) \mathcal{E}'\left(\omega'_{\vec{k}_1}\right) \quad (22)$$

So far the current is written in the molecular frame, and now we shall transform it into the laboratory frame $\vec{J}^L(\vec{k}, \varrho) = R^t(\varrho) \vec{J}$ and average over molecular orientations: $\overline{\vec{J}^L}(\vec{k}) = \int d\varrho R^t(\varrho) \vec{J}(\vec{k}, \varrho)$. This

yields the following result:

$$\overline{J_x^L(\vec{k})} = 0 \quad (23)$$

$$\overline{J_y^L(\vec{k})} = 0 \quad (24)$$

$$\overline{J_z^L(\vec{k})} = -\frac{1}{60} |\mathcal{E}(\omega, \omega')| \sigma \left[\vec{d}_{1,0} \times \vec{d}_{2,0} \right] \cdot \vec{D}_{12}(\vec{k}) e^{i(\omega_{21}\tau + \phi(\omega, \omega') - \frac{\pi}{2})} + \text{c.c.} \quad (25)$$

where we have now explicitly defined the phase and the amplitude of the spectral component $\mathcal{E}(\omega, \omega')$. Here the vector $\vec{D}_{12}(\vec{k})$ is given by the product of a second-order tensor $\hat{D}^{12}(\vec{k})$ and the vector \vec{k} :

$$\vec{D}_{12}(\vec{k}) = \hat{D}^{12}(\vec{k})\vec{k}, \quad (26)$$

The tensor arises due to partial alignment of the initially isotropic ensemble by a pump pulse. The components of the second-order tensor $\hat{D}^{12}(\vec{k})$ are given by Cartesian components of photoionization dipoles. The off-diagonal $D_{ij}^{12} = D_{ji}^{12}$ components of the tensor $\hat{D}^{12}(\vec{k})$ are:

$$\begin{aligned} D_{xy}^{12} &= D_{1x}D_{2y}^* + D_{1y}D_{2x}^* \\ D_{xz}^{12} &= D_{1x}D_{2z}^* + D_{1z}D_{2x}^* \\ D_{yz}^{12} &= D_{1y}D_{2z}^* + D_{1z}D_{2y}^* \end{aligned} \quad (27)$$

while the diagonal components are:

$$\begin{aligned} D_{xx}^{12} &= -2(D_{1,x}D_{2,x}^* + 2D_{1,y}D_{2,y}^* + 2D_{1,z}D_{2,z}^*) \\ D_{yy}^{12} &= -2(2D_{1,x}D_{2,x}^* + D_{1,y}D_{2,y}^* + 2D_{1,z}D_{2,z}^*) \\ D_{zz}^{12} &= -2(2D_{1,x}D_{2,x}^* + 2D_{1,y}D_{2,y}^* + D_{1,z}D_{2,z}^*) \end{aligned} \quad (28)$$

Averaging over all orientations of \vec{k} we obtain the final result for the lab frame PXECD current:

$$\overline{J_z^L(k)} = -\frac{\sigma}{60} |\mathcal{E}(\omega, \omega')| \left[\vec{d}_{1,0} \times \vec{d}_{2,0} \right] \cdot \vec{D}_{12}(k) e^{i(\omega_{21}\tau + \phi(\omega, \omega') - \frac{\pi}{2})} + \text{c.c.} \quad (29)$$

where the Raman-type photoionization vector is

$$\vec{D}_{12}(k) = \int d\Omega_k \vec{D}_{12}(\vec{k}). \quad (30)$$

The Raman-type photoionization vector can be written as a sum of its real and imaginary parts, $\vec{D}_{12}(k) = \vec{D}_{12}^r(k) + i\vec{D}_{12}^i(k)$, leading to the following final expression for the orientation-averaged current along the laboratory z-axis, i.e. orthogonal to the polarization plane of the pump pulse:

$$\overline{J_z^L(k)} = -\frac{\sigma}{60} |\mathcal{E}(\omega, \omega')| \left[\vec{d}_{1,0} \times \vec{d}_{2,0} \right] \cdot \left(\vec{D}_{12}^r(k) + i\vec{D}_{12}^i(k) \right) e^{i(\omega_{21}\tau + \phi(\omega, \omega') - \frac{\pi}{2})} + \text{c.c.}$$

$$= -\frac{\sigma}{30} |\mathcal{E}(\omega, \omega')| \left[\vec{d}_{1,0} \times \vec{d}_{2,0} \right] \cdot \left[\vec{D}_{12}^r(k) \sin(\omega_{21}\tau + \phi(\omega, \omega')) + \vec{D}_{12}^i(k) \cos(\omega_{21}\tau + \phi(\omega, \omega')) \right] \quad (31)$$

Up to constant multipliers, Eq. (31) reproduces Eq. (3) of the main text. The phases of the pump and probe fields $\phi(\omega, \omega')$ as well as these field components at the excitation frequencies $|\mathcal{E}(\omega, \omega')|$ appearing in the expression for the z -component of the PXECD current $\overline{J}_z^L(k)$ were omitted in Eq. (3) of the main text for compactness and clarity of our equations.

The triple products $\left[\vec{d}_{1,0} \times \vec{d}_{2,0} \right] \cdot \vec{D}_{12}^{r,i}(k)$ are characteristic measures of chirality. As pseudoscalars, they must change sign upon reflection with respect to any plane, e.g. with respect to the polarization plane of the pump pulse. Since such reflection transforms a random ensemble of left-handed molecules into a random ensemble of right-handed molecules, the triple-products will have opposite signs for left-handed and right handed ensembles. For ensembles of non-chiral molecules, the current is equal to zero. Indeed, reflection in the polarization plane will not change the ensemble and hence the z -component of the current must remain the same.

Below we derive a compact form for the vector \vec{D}_{12} in Eq. (26). First, note that the tensor \hat{D}^{12} in Eqs. (26), (27), (28) can be written as

$$\hat{D}^{12} = -4 \left(\vec{D}_1 \cdot \vec{D}_2^* \right) \mathbb{I} + \vec{D}_1 \otimes \vec{D}_2^* + \vec{D}_2^* \otimes \vec{D}_1 \quad (32)$$

where \otimes stands for the outer product. Multiplication by \vec{k} leads to

$$\vec{D}_{12}(\vec{k}) = -4 \left(\vec{D}_1 \cdot \vec{D}_2^* \right) \vec{k} + \left(\vec{D}_2^* \cdot \vec{k} \right) \vec{D}_1 + \left(\vec{D}_1 \cdot \vec{k} \right) \vec{D}_2^* \quad (33)$$

Note that this general expression shows that every available vector $(\vec{D}_1, \vec{D}_2^*, \vec{k})$ can be used to "complete" the triple product.

General expression for the PXECD current [Eq. (31)] shows that the chiral asymmetry also depends on the balance between the pulse bandwidth and the energy spacing between the excited states. For example, in case of two states with energy spacing ΔE_{12} , the reduction of asymmetry due to the narrowing of the pulse bandwidth will be minimal for the continuum energy $E_k = \frac{E_{k1} + E_{k2}}{2}$, where E_{kj} are the energies, corresponding to the peaks of the spectrum for the ionization from states $j = |1\rangle, |2\rangle$ respectively. For the Gaussian pulse with spectral amplitude $e^{-\omega^2/2\Delta W^2}$, where $2\Delta W = \Delta W_{FWHM}/\sqrt{\ln 2}$ Eq. (31) yields the current $\propto e^{-[\Delta E_{12}\sqrt{\ln 2}/\Delta W_{FWHM}]^2}$ at the continuum energy E_k . Using shorter pulses, one takes maximal advantage of the ultrafast chiral asymmetry, excited in randomly oriented molecules. Naturally, the asymmetry can also be probed with longer pulses. Such pulses probe slower chiral dynamics, involving more closely spaced states.

B. PXECD for unpolarized probe pulse

Theoretically, it is very instructive to consider completely unpolarized light as a probe of the excited chiral dynamics. Since the probe is completely isotropic, it can not be sensitive to the initial alignment by the pump. Thus, considering an unpolarized probe we can find out how partial alignment of the initially isotropic ensemble by the pump pulse affects the chiral continuum current (the PXECD effect). Below we show that the PXECD effect does not vanish, if the alignment by the pump is excluded. Thus, the PXECD effect does not originate solely from partial alignment by the pump pulse. Consider an arbitrary direction of the linear probe in the laboratory frame. Instead of a single vector characterizing the direction of polarization \hat{x}^L of the probe pulse, we introduce

$$\hat{p}^L = \begin{pmatrix} \sin \theta_p \cos \varphi_p \\ \sin \theta_p \sin \varphi_p \\ \cos \theta_p \end{pmatrix}$$

Then the current in Eq. (21) takes the form

$$\vec{J}(\vec{k}, \varrho, \hat{p}^L) = \sum_{i,j} \left(R(\varrho) \hat{\varepsilon}_{-\sigma}^L \cdot \vec{d}_{2,0} \right) \left(R(\varrho) \hat{j}^{L*} \cdot \vec{D}_2^* \right) \left(R(\varrho) \hat{\varepsilon}_{\sigma}^L \cdot \vec{d}_{1,0} \right) \left(R(\varrho) \hat{i}^L \cdot \vec{D}_1 \right) p_i p_j^* \mathcal{E}(\omega, \omega') \vec{k} e^{i\omega_{21}\tau} + \text{c.c.}, \quad (34)$$

where i and j take values x, y, z . From this expression we can see that cross terms $i \neq j$ vanish after averaging over probe-polarization directions, therefore we only need to calculate the terms corresponding to a probe polarized along directions \hat{x}^L , \hat{y}^L and \hat{z}^L independently. We already calculated the expression for a probe polarized along \hat{x}^L and demonstrated that it is valid for all probe polarizations in the $x^L y^L$ plane, and in particular to probe polarization along \hat{y}^L . For a probe polarized along \hat{z}^L we obtain expressions identical to Eqs. (23)-(25) and (31) for the current, except for \vec{D}_{12} in Eq. (33) which is now given by

$$\vec{D}_{12}(\vec{k}, \hat{z}^L) = -2 \left[\left(\vec{D}_1 \cdot \vec{D}_2 \right) \vec{k} + \vec{D}_1 \left(\vec{D}_2^* \cdot \vec{k} \right) + \vec{D}_2^* \left(\vec{D}_1 \cdot \vec{k} \right) \right]. \quad (35)$$

From Eqs. (33), (34), and (35), the expression for the current in the lab frame reads as

$$\overline{J_z^L}(\vec{k}, \hat{p}^L) = -\frac{\sigma}{60} |\mathcal{E}(\omega, \omega')| \left(\vec{d}_{1,0} \times \vec{d}_{2,0} \right) \cdot \vec{D}_{12}(\vec{k}; \hat{p}^L) e^{i(\omega_{21}\tau - \frac{\pi}{2} + \phi(\omega, \omega'))} + \text{c.c.} \\ + \text{cross terms}, \quad (36)$$

$$\vec{D}_{12}(\vec{k}, \hat{p}^L) = \left(|p_x|^2 + |p_y|^2 \right) \vec{D}_{12}(\vec{k}, \hat{x}^L) + |p_z|^2 \vec{D}_{12}(\vec{k}, \hat{z}^L)$$

$$\begin{aligned}
&= -2 \left[2 - (\hat{n}^L \cdot \hat{p}^L)^2 \right] \left(\vec{D}_1 \cdot \vec{D}_2^* \right) \vec{k} \\
&\quad + \left[1 - 3 (\hat{n}^L \cdot \hat{p}^L)^2 \right] \left[\left(\vec{D}_2^* \cdot \vec{k} \right) \vec{D}_1 + \left(\vec{D}_1 \cdot \vec{k} \right) \vec{D}_2^* \right], \tag{37}
\end{aligned}$$

where $\hat{n}^L = \hat{z}^L$ is the propagation direction of the pump. The coefficient $[1 - 3(\hat{n}^L \cdot \hat{p}^L)^2]$ vanishes after averaging over orientations of the probe and we obtain the simple expression

$$\begin{aligned}
\vec{D}_{12}^u(\vec{k}) &= \int d\varphi_p \int d\theta_p \sin\theta_p \vec{D}_{12}(\vec{k}, \hat{p}^L) \\
&= -\frac{10}{3} \left(\vec{D}_1 \cdot \vec{D}_2^* \right) \vec{k}, \tag{38}
\end{aligned}$$

which, once integrated over orientations of \vec{k} [see Eq. (30)], gives the Raman-type photoionization vector that goes into the final expression for the current Eq. (31).

Note that once partial alignment by the pump is excluded, only vector \vec{k} can be used to "complete" the triple product.

We note that from the experimental point of view, probing with an unpolarized femtosecond pulse is technically challenging. Indeed, femtosecond laser pulses are initially linearly polarized. Linearly polarized pulse can be turned into unpolarized by transmission in a diffusing medium, but this would strongly affect the femtosecond duration, making the pulse much longer. Another way would be to use a UV phase and polarization shaper to encode a random polarization output, but this would also destroy the short pulse duration.

C. PXECD in the plane wave continuum

So far, all our calculations have been general. We now consider the case of the plane wave continuum, eliminating any possibility of chiral contributions from the continuum state (i.e. photoelectron scattering from the chiral potential of the core). In the case of plane wave continuum, the photoionization matrix elements evaluated in the velocity gauge, are known to yield asymptotically correct results for the ground state of the hydrogen atom. The length gauge matrix elements are asymptotically different by a factor of 4 for the same bound state. Thus, to achieve the most accurate representation of photoionization dipoles in case of plane wave continuum, we use the velocity gauge, where the photoionization matrix elements are proportional to the wave functions of the excited states in momentum space

$$\vec{D}_i = \langle \vec{k} | \vec{p} | \psi_i \rangle = \vec{k} \tilde{\psi}_i(\vec{k}), \quad i = 1, 2 \tag{39}$$

Replacing these expressions in Eq. (33) we obtain

$$\vec{D}_{12}(\vec{k}) = -2k^2 \tilde{\psi}_1(\vec{k}) \tilde{\psi}_2^*(\vec{k}) \vec{k} \tag{40}$$

The Raman-type photoionization vector in the case of the plane wave continuum then becomes:

$$\vec{D}_{12}^{\text{PW}}(k) = -2 \int d\Omega_k k^2 \tilde{\psi}_1(\vec{k}) \tilde{\psi}_2^*(\vec{k}) \vec{k}. \quad (41)$$

It is easy to show that $\vec{D}_{12}^{\text{PW}}(k)$ is purely imaginary. Let us split the electronic wave-functions $\psi_{1,2}(\vec{r})$ of bound states $|1\rangle, |2\rangle$ in coordinate space into symmetric and antisymmetric components:

$$\psi_{1,2}(\vec{r}) = \psi_{1,2}^S(\vec{r}) + \psi_{1,2}^A(\vec{r}) \quad (42)$$

Their Fourier transforms are then given by

$$\begin{aligned} \tilde{\psi}_{1,2}(\vec{k}) &\equiv \int d\vec{r} \psi_{1,2}(\vec{r}) e^{i\vec{k}\cdot\vec{r}} = \int d\vec{r} \psi_{1,2}^S(\vec{r}) \cos(\vec{k}\cdot\vec{r}) + i \int d\vec{r} \psi_{1,2}^A(\vec{r}) \sin(\vec{k}\cdot\vec{r}) \\ &\equiv \tilde{\psi}_{1,2}^S(\vec{k}) + i \tilde{\psi}_{1,2}^A(\vec{k}), \end{aligned} \quad (43)$$

where both $\tilde{\psi}_{1,2}^A(\vec{k})$ and $\tilde{\psi}_{1,2}^S(\vec{k})$ are real functions. After simple algebra we get

$$\vec{D}_{12}^{\text{PW}}(k) = 2i \int d\Omega_k k^2 \left(\tilde{\psi}_1^S(\vec{k}) \tilde{\psi}_2^A(\vec{k}) - \tilde{\psi}_1^A(\vec{k}) \tilde{\psi}_2^S(\vec{k}) \right) \vec{k}. \quad (44)$$

Thus, we have proved that $\vec{D}_{12}^{\text{PW}}(k)$ is purely imaginary:

$$\vec{D}_{12}^{\text{PW}}(k) = i \vec{D}_{12}^{i,\text{PW}}(k) \quad (45)$$

Taking into account Eq. (45) and using explicitly the imaginary component of the Raman-type photoionization vector $\vec{D}_{12}^{i,\text{PW}}(k)$ we obtain Eq. (4) of the main text:

$$\overline{J_z^{L,\text{PW}}}(k) = -\frac{\sigma}{30} \frac{|\mathcal{E}(\omega, \omega')|}{\omega'_{\vec{k}_1} \omega'_{\vec{k}_2}} \left[\vec{d}_{1,0} \times \vec{d}_{2,0} \right] \cdot \vec{D}_{12}^{i,\text{PW}}(k) \cos(\omega_{21}\tau + \phi(\omega, \omega')). \quad (46)$$

The constants, the phases of the pump and probe fields $\phi(\omega, \omega')$ as well as the field components at the excitation and probe frequencies $|\mathcal{E}(\omega, \omega')|$ appearing in the expression for z -component of the PXECD current $\overline{J_z^{L,\text{PW}}}(k)$ were omitted in Eq. (4) of the main text for compactness and clarity of our equations. Importantly, Eq. (46) shows that the PXECD current remains chiral for every k , even when the effects of chirality in the continuum are removed (by using a plane wave continuum instead). Thus, PXECD can be used as a probe exclusively sensitive to chiral bound dynamics.

It is instructive to compare the Raman-type photoionization vector integrated over all k ($d\vec{k} \equiv d\Omega_k k^2$):

$$-\frac{1}{2} \int dk \vec{D}_{12}^{\text{PW}}(k) \equiv \int d\vec{k} \tilde{\psi}_1(\vec{k}) \tilde{\psi}_2^*(\vec{k}) \vec{k}, \quad (47)$$

and the bound transition dipole between the two excited states $\vec{d}_{1,2}$. The latter can be written in a strikingly similar form:

$$i\omega_{21}\vec{d}_{1,2} \equiv \int d\vec{k}\tilde{\psi}_1(\vec{k})\tilde{\psi}_2^*(\vec{k})\vec{k} \quad (48)$$

The right hand sides of Eqs. (47,48) are equivalent. Thus, $i\omega_{21}\vec{d}_{1,2}$ and $-\int dk\vec{D}_{12}^{\text{PW}}(k)/2$ are also equivalent. If $\omega_{21} = 0$, the Raman-type photoionization vector integrated over all k is also zero. Thus we recover a simple connection between the bound transition dipole $\vec{d}_{1,2}$ and the integrated Raman-type photoionization vector:

$$\omega_{21}\vec{d}_{1,2} \equiv -\frac{1}{2} \int dk\vec{D}_{12}^{i,\text{PW}}(k) \quad (49)$$

Here we explicitly used that $\vec{D}_{12}^{\text{PW}}(k)$ is purely imaginary. This is evident from Eqs. (45,48). Using this simple connection and integrating the continuum current over all k (assuming adjustable strength of the probe pulse at all frequencies, so that $C_{\mathcal{E}} = \frac{1}{5} \frac{\mathcal{E}'^*(\omega'_{\vec{k}2})\mathcal{E}'(\omega'_{\vec{k}1})}{\omega'_{\vec{k}1}\omega'_{\vec{k}2}}$ is independent of k) we obtain a simple relationship between the bound and total (integrated over all k) continuum currents:

$$J_{tot}^{\text{PXECD}} \equiv \int dk\overline{J_z^{L,\text{PW}}}(k), \quad (50)$$

$$J_{tot}^{\text{PXECD}} = C_{\mathcal{E}}J_z^{\text{PXCD}}. \quad (51)$$

Here we used Eqs. (15,46,49). Despite its simplicity, Eq. (51) is important for understanding the PXECD phenomenon. It shows that even if one explicitly removes the effects associated with the chirality of the molecular continuum or effects associated with the non-spherical symmetry of the molecular continuum (by using a plane wave continuum instead), the PXECD current remains chiral, not only for every k (see Eq. (46)), but also integrally for all k , because in this case it directly reflects the chirality of the bound PXCD current. If the bound current becomes equal to zero (e.g. in case of degeneracy of two bound states), then the total continuum current is also zero.

D. The nature of the PXECD current

We can now address the question about the mechanisms leading to the PXECD current more broadly. The PXECD continuum current may arise due to the following reasons: (a) due to bound PXCD current; (b) due to partial alignment of the molecular ensemble by the pump pulse, (c) due to the degenerate PXECD process, even in the absence of bound PXCD current, i.e. when $\omega_{12} = 0$. Degenerate PXECD is the PXECD for degenerate excited states.

Eq. (31) is general, it contains all three effects. The set of examples that we have considered in previous subsections allows us to identify and isolate each of these effects. The effect of partial alignment due to the pump pulse can be "removed" by considering an unpolarized probe. Eq. (38) shows that chiral response does not vanish if we remove the effects of alignment by the pump pulse.

Finally, to isolate the degenerate PXECD process, one can remove effects (a,b) by considering unpolarized light and setting $\omega_{12} = 0$.

The most important result regarding the nature of PXECD is proved in Section II C: if we consider the plane wave continuum, then the total PXECD current is directly proportional to the PXCD current. Thus, if the effect (a) is excluded the total PXECD current is zero. While the effect of alignment (effect b) may not be very surprising, the effects (a,c) are truly novel.

Consider the degenerate PXECD effect in the case when effects (a,b) are removed. For that we can consider the respective expressions for $\omega_{12} = 0$ and an unpolarized probe. In this case the PXECD becomes very similar to PECD. In the case of unpolarized light the Raman-type photoionization vector is

$$\vec{D}_{12}^u(\vec{k}) = -\frac{10}{3} \left(\vec{D}_1(\vec{k}) \cdot \vec{D}_2^*(\vec{k}) \right) \vec{k} \quad (52)$$

Then the PXECD current for $\omega_{12} = 0$ is:

$$\overline{J}_z^L(k) = \frac{\sigma}{9} |\mathcal{E}(\omega, \omega')| \int d\Omega_k \left[\vec{d}_{1,0} \times \vec{d}_{2,0} \right] \cdot \vec{k} \cdot \left(\vec{D}_1^i(\vec{k}) \cdot \vec{D}_2^r(\vec{k}) - \vec{D}_1^r(\vec{k}) \cdot \vec{D}_2^i(\vec{k}) \right) \quad (53)$$

In this expression, for simplicity we set the phases $\phi(\omega, \omega') = 0$.

In section II-C we have demonstrated that in the case of a plane wave continuum, the **total** PXECD current (integrated over all k) vanishes if we set $\omega_{12} = 0$. However, each momentum component of this current remains finite as long as the excited states $|1\rangle$ and $|2\rangle$ do not have definite parity and $d_{12} \neq 0$. Note that the triple product in Eq. (53) is formed by the two bound dipoles and the vector \vec{k} of the continuum electron.

E. Role of chiral continuum in PECD: a numerical example

In this sub-section we discuss the necessary conditions for PECD in randomly oriented ensemble of chiral molecules, although this question has been already discussed in literature. The purpose of this subsection is to confirm the diagrams presented in Fig. 1d of the main paper.

The PECD phenomenon can occur even if the initial (bound) state is not chiral. In this case the chiral response originates solely from the scattering of the photoelectron in the chiral molecular potential.

However, for a chiral bound state, the conditions on the molecular potential can be significantly relaxed. Namely, this potential does not have to be chiral, it only has to be non-spherically symmetric.

To show how the chiral asymmetry parameter of PECD depends on the strength of the non-spherical part of the molecular potential we performed the following numerical simulations. We have considered a model potential and a model chiral state. The initial chiral state was chosen as a linear combination of the hydrogenic wavefunctions: $|\psi_i\rangle = 1/\sqrt{2}(|3p_+\rangle + |3d_+\rangle)$ [4]. The strength of the non-spherical component of the potential $V(r, \theta) = -1/r - \lambda e^{-r} Y_{1,0}(\theta)$ is controlled

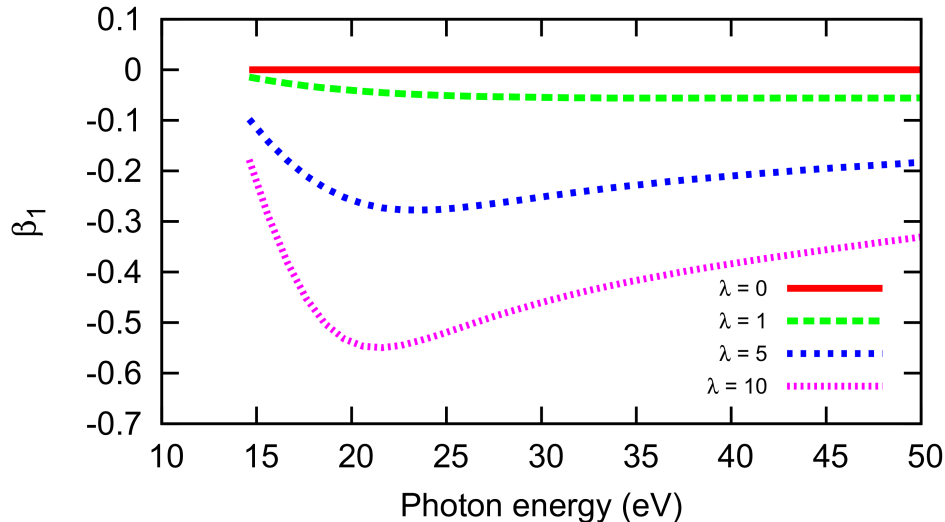


Figure 2. PECD asymmetry parameter β_1 vs photoelectron energy for model potential $V(r, \theta) = -1/r - \lambda e^{-r} Y_{1,0}(\theta)$. The strength of the non-spherical component of the potential is controlled by parameter λ and $Y_{1,0}(\theta)$ is the spherical harmonic. We have calculated the chiral asymmetry parameter for several different values of lambda: 0, 1, 5, 10. As expected, the increase in β_1 follows the increase in λ .

by the parameter λ and $Y_{1,0}(\theta)$ is the spherical harmonic. We have calculated the chiral asymmetry parameter of PECD β_1 [5] for several different values of λ : 0,1, 5, 10 (see Fig. 2).

We have used the following method for our calculation. To obtain the continuum wavefunctions we implemented the multichannel version of the renormalized Numerov method [6] and checked the correctness of the implementation against a benchmark two channel scattering calculation [7]. To solve our model problem the scattering wavefunction was expanded into partial-waves and the standard standing-wave solutions of the multichannel system were converted into photoionization (incoming-wave) boundary conditions in the asymptotic region and back-propagated to obtain the photoionization solutions in the whole radial domain spanned by the initial chiral bound state. Finally, the partial wave dipole matrix elements were calculated and inserted into Ritchie's formula for β_1 [5]. When solving the multichannel problem partial waves up to $l_{max} = 6$ were included and ionization potential of 0.5 a.u. was used when calculating the asymmetry parameter.

III. PARAMETRIZATION OF PXECD IMAGES

A. Analysis of the experimental images

An Even-Lavie valve is used as a pulsed enantiopure fenchone source with helium as carrier gas to avoid the cluster formation. (1R)-(-) and (1S)-(+)-fenchone correspond to (1R,4S) and (1S,4R) fenchone respectively. The 170 fs cross-correlation time as well as the 0 fs delay are determined on

the lightest fragment $C_4H_5O^+$ produced by dissociative ionization. The high voltage of the repeller electrode was -3kV for the experiment done in fenchone and only -2kV for the experiment done in Camphor, which increases the energy resolution. Note that the latter, along with the energy calibration, has been determined by photoionizing krypton. Typically the energy resolution is 80 meV at 0.7 eV kinetic energy. The presented results are obtained by scanning the pump-probe delays typically 30 times. At each delay, the pump helicity is permuted each 45000 laser shots (=45 seconds) to record several images.

To take into account the angular and energy dependencies of the $(L - R)$ images and in order to extract a time-dependency of asymmetric PXECD, the $(L - R)$ experimental images are fitted with a p-Basex analysis, by a sum of odd Legendre Polynomials up to the order 3[8]. The asymmetry of the PXECD is time dependent and decomposed in coefficients α and α' defined as :

$$\text{PXECD}(E_{kin}, \theta) = \frac{L(E_{kin}, \theta) - R(E_{kin}, \theta)}{\max[L(E_{kin}, \theta) + R(E_{kin}, \theta)]} = \alpha(E_{kin})P_1(\cos \theta) + \alpha'(E_{kin})P_3(\cos \theta) \quad (54)$$

where θ is the angle of emission relative to the light propagation z in Figure 3(b) of the main text. α and α' , whose temporal evolutions are displayed in Figure 4(b) of the main text, are normalized coefficients that provide a means to follow the temporal evolution of the photoelectron asymmetry. This normalization is done by the maximum of the $(L + R)/2$ images. The calculated images of Figures 2(c-d) and 5 of the article are normalized the same way that the experimental ones for an appropriate comparison.

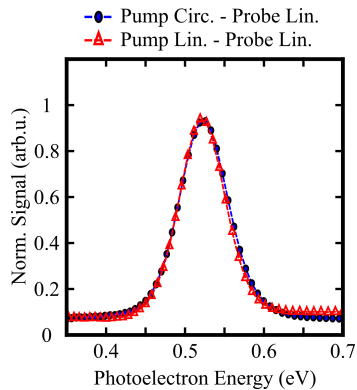


Figure 3. Photoelectron spectra (PES) obtained by a p-Basex analysis of the photoelectron images, (i.e) $(L + R)$ image, recorded at 700 fs pump-probe delay in fenchone, with a linearly polarized pump pulse (red symbol) or with a circularly polarized pump pulse (filled circle) and a linearly polarized probe pulse in both cases.

The inverse Abel transform of the p-Basex normally assumes cylindrical symmetry of the measurement geometry to get the 3D-photoelectron distribution from the recorded 2D-image. The linearly polarized probe breaks such symmetry. In order to evaluate the impact of the noncylindrical symmetry, the PES recorded in linear pump/linear probe configuration (for which the cylindrical symmetry is preserved) is compared to the one extracted from the $(L + R)$ image, in Figure 3. The perfect agreement between these two energy distributions indicates that negligible $P_{n=even}^{m=2,4}$ are in play in

the 3D-angular distribution of the $(L + R)$ photoelectron images (PES). With a 3D-detector, such as e.g. a COLTRIMS [9], no symmetry is required in the angular distribution of the photoelectrons. We will show further how α and α' could be connected to the original 3D distribution mapped onto the VMI detector despite the presence of $P_{n=odd}^{m=2}$ terms.

As a chiroptical effect, PXCD is enantio-sensitive as illustrated in Figure 4 on the mirroring effect observed on the PXECD images recorded for the two enantiomers of fenchone at a 700 fs delay. This asymmetry of photoelectron is clearly visible on both raw data (a) and (b) and of course on the fitted normalized images (c) and (d).

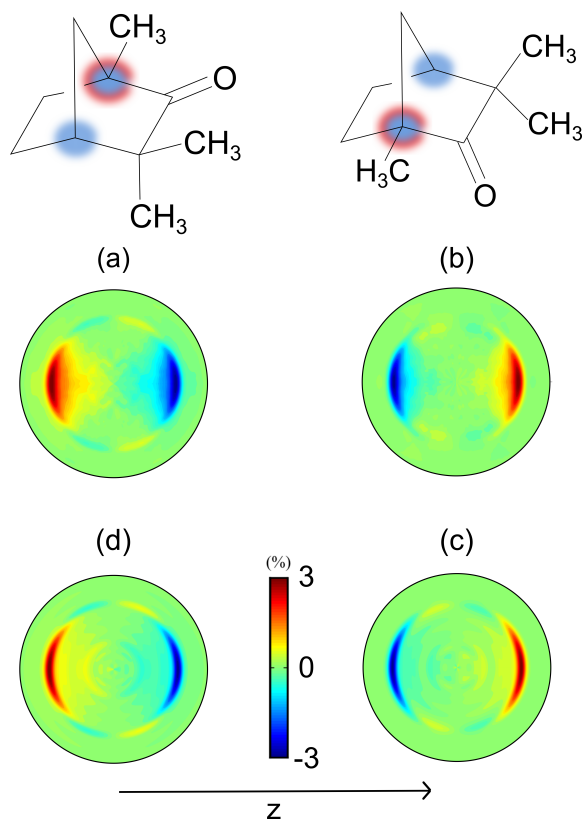


Figure 4. The photoelectron asymmetry along the optical propagation axis(z) is reversed with the handedness of the molecule, with a backward asymmetry for (a,d) (1S)-(+)-fenchone and a forward one for (b,c) (1R)-(-)-fenchone. (a) and (b) show the raw images $(L - R)$ while (c) and (d) show the fitted images $(L - R)$ once normalized by the max of $(L + R)/2$.

B. Inverse Abel transform of the two-photon chiral signal

Here we discuss Abel inversion in the geometry of our experiment and show how the Abel-inverted quantities α and α' (Fig.4 of the main text) can be connected to the conventional asymmetry parameters characterizing the chiral component of the 3D photo-electron signal.

Our experimental results confirm the expectation for the photo-ionization from a Rydberg state of the neutral to the ground state of the ion: the photo-electron spectrum closely follows the spectrum of the probe pulse, reflecting approximate conservation of vibrational excitation during photo-ionization from the Rydberg state converging to the final ionic state. As a result, the spectra are predominately located within a bell-shaped 3D sphere which we denote $G_0(k, k_0)$. Here $E_0 = k_0^2/2$ denotes the central energy of the sphere, and its width (defined by the width of the laser pulse) is sufficiently narrow, $\Delta E \ll E_0$.

In the geometry of our experiment, the 3D chiral asymmetry signal can be written as (A. Harvey et al, in preparation)

$$R_{3D}^{PXCED} = CG_0(k, k_0) \times [q_{1,0}P_1^0(\cos\theta) + q_{2,-2}P_2^2(\cos\theta)\sin(2\phi) + q_{3,0}P_3^0(\cos\theta) + q_{3,2}P_3^2(\cos\theta)\cos(2\phi)] \quad (55)$$

where C is some overall factor that depends on the density of the gas, intensities of the pump and the probe, etc. The appearance of the Legendre polynomials P_2^2 and P_3^2 reflects the geometry of the experiment, where the pump field is propagating along the z axis and the probe is polarized along the x axis. The parameters q_{lm} are related to the standard b_{lm} coefficients in the decomposition of the 3D spectrum into the real-valued spherical harmonics, $q_{lm} = N_{lm}b_{lm}$, where

$$N_{lm} = \sqrt{\frac{(2l+1)(l-|m|)!}{4\pi(l+|m|)!}} \quad (56)$$

are the normalization constants for the real-valued spherical harmonics. The parameters $q_{2,-2}$ and q_{32} appear due to breaking of cylindrical symmetry in the two-photon pump-probe setup. The parameter q_{32} also reflects chiral asymmetry: it changes sign if we change the handedness of the light or enantiomer.

The actual modeling is done numerically using the experimentally measured $G_0(k, k_0)$ from the photo-electron spectra.

The presence of q_{32} (or b_{32}) modifies the reconstructed 3D image in two ways. First, the coefficients α and α' (Fig. 4 of the main text) in front of the Legendre polynomials P_1^0, P_3^0 contain b_{32} : $\alpha = q_{10} + 6q_{32}$ and $\alpha' = q_{10} - 6q_{32}$. Secondly, the last term gives a characteristic signal $\propto b_{32}(k/k_0)P_1^0(\cos\theta)$ for $k < k_0$ lying outside of the spectral bandwidth of the pulse leading to a characteristic background at low energies, growing linearly with k towards the energy shell G_0 . The detailed derivation will be presented elsewhere (A. Ordonez, F. Morales, M. Ivanov, O.Smirnova, in preparation). These results allow us to give a rigorous upper estimate to q_{32} from the 3D images directly obtained via the inverse Abel transform of the measured 2D spectra.

Below we summarize the results of the analysis of the reconstructed experimental 3D images. The result of the analysis for fenchone, for the first delay, is shown in Fig.5. Blue (α) and red (α') are

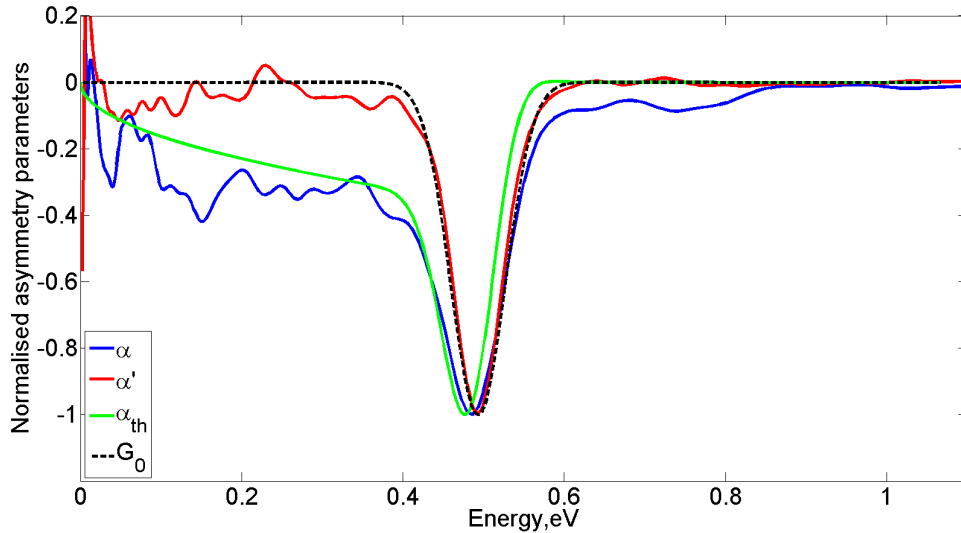


Figure 5. Normalized asymmetry parameters in Fenchone for the first delay and the effect of q_{32} : Blue (α) and red (α') are reconstructed from experiment. The black curve is the experimental $-G_0$, centered at $E_0 = 0.4932$ eV. The green curve is the theoretical α signal for $q_{32}/q_{10} = 0.09$. The tail of the green curve approximately represents the background in the low-energy tail of the blue curve (experimental α).

obtained by Abel inversion of the experimental 2D images. In contrast to α' (red), which is not affected by the loss of the cylindrical symmetry and is confined to the pulse bandwidth (G_0 , black curve, centered at $E_0 = 0.4932$ eV), the blue curve appears to have a low energy background, which can be attributed to the presence of q_{32} . This background drops rather quickly at longer pump-probe delays. Attributing this background solely to q_{32} allows us to obtain its upper estimate. The green curve corresponds to setting $q_{32}/q_{10} = 0.09$. Similar analysis can be performed for every delay, see Fig.6 for the second delay.

The estimated upper bound for q_{32}/q_{10} , as a function of the pump-probe delay, is found to be rather low and rapidly decreases with the time-delay, see Table I.

IV. NUMERICAL QUANTUM MECHANICAL CALCULATIONS FOR TWO-PHOTON ABSORPTION IN FENCHONE

A. Preliminaries

In the experiment we are dealing with a set of randomly aligned fenchone molecules embedded in time-delayed pump and probe laser pulses. As far as these pulses do not time overlap, the interaction can be split in two parts: (i) the pump step where the molecules are brought into high-lying bound states through one-photon absorption from a circularly polarized low-energy laser pulse, (ii) the

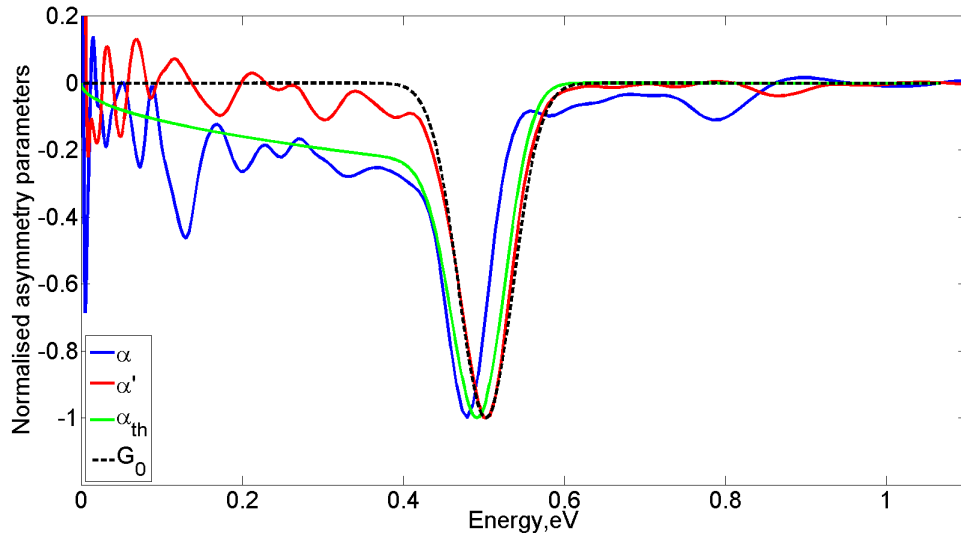


Figure 6. Normalized asymmetry parameters in fenchone for the second delay and the effect of q_{32} : Blue (α) and red (α') are reconstructed from experiment. The black curve is the experimental $-G_0$, centered at $E_0 = 0.5025$ eV. The green curve is the theoretical α signal for $q_{32}/q_{10} = 0.07$. The tail of the green curve approximately represents the background in the low-energy tail of the blue curve (experimental α).

probe step where the molecules are ionized from these bound states by absorption of a linearly polarized photon. The low intensity of both pump and probe pulses makes the description of electron dynamics easier: high-order (multiphoton) processes can be depreciated so that first-order perturbative theories can be safely applied. However this description remains rather demanding insofar as not only bound but also continuum molecular states are required to represent the pump- and probe-induced dynamics, respectively. So let's first focus on the construction of these molecular states.

B. The molecular states

Unless otherwise stated all the quantum chemistry calculations that will be described hereinafter have been performed using the GAMESS-US package [10] and atomic units will be used throughout the paper. We work within the frozen nuclei approximation where all nuclei remain located at their equilibrium positions throughout the interaction. This equilibrium geometry has been optimized at the Hartree-Fock level of theory using the 6-311++G** [11] underlying Gaussian basis. These calculations have yielded the single-determinant wavefunction Φ_0 for the ground state of the fenchone system:

$$\Phi_0 = \sqrt{\frac{1}{n!}} \det\{\phi_1 \phi_2 \dots \phi_i \dots \phi_n\} \quad (57)$$

Table 1: The upper estimate for q_{32} in fenchone	
Delay (ps)	$\frac{q_{32}}{q_{10}}$
0.2	0.09
0.7	0.07
1.2	0.05
1.7	0.03
2.2	0.01

Table I. Estimated upper bound for q_{32}/q_{10} as a function of the pump-probe delay

where n is the number of electrons and ϕ_i (with $i = 1, \dots, n$) are molecular spin-orbitals. The excited bound states are calculated by means of the CIS (Configuration Interaction-Singles, [12]) approach: singly excited determinants are built by replacing an occupied spin-orbital ϕ_i in the reference (57) by a virtual one ϕ_a , and the excited state wavefunctions are finally linear combinations of those determinants:

$$\Phi_l^{CIS} = \sum_{i \rightarrow a} c_{l,i \rightarrow a} \sqrt{\frac{1}{n!}} \det\{\phi_1 \phi_2 \dots \phi_{i \rightarrow a} \dots \phi_n\}. \quad (58)$$

We further simplified the scheme on the grounds of the experimental conditions: the absorption of photon from the pump pulse with wavelength $\lambda \sim 200$ nm allows to reach almost resonant $3s$ and $3p$'s Rydberg states which basically result from excitation of the highest occupied molecular orbital (HOMO) to virtual orbitals. We therefore imposed that the 41 inner orbitals remain frozen within the CIS procedure. This enables to follow the pump-induced electron dynamics in terms of the evolution of the outermost orbital, without requirement for Dyson orbitals. We compare in Table II the energies of the low-lying excited states resulting from our simplified CIS procedure with their counterparts resulting from time-dependent density functional theory (TDDFT) calculations and experiments by Pulm *et al.* [13] and Kastner *et al.* [14]. The energies of the CIS excited states are overestimated, and decreasing the number of frozen orbitals do not significantly improve the results. Correlations beyond the CIS framework are important and better described by TDDFT. However the excited states provided by CIS display the expected shapes, for the first valence π^* state as well as for the Rydberg $3s$ and $3p$ states (see Fig. 7). We will therefore employ these CIS excited states but we will scale the pump wavelength so that the absorption of a photon brings the fenchone system into a mixture and $3s$ and $3p$ states similar to the one expected for the experiment done at $\lambda = 201$ nm.

In this respect $3p$ Rydberg states seems at first sight out of reach by absorption of one pump photon

Transition	CIS $n_{core}=41$	CIS $n_{core}=11$	TDDFT	experiment
$n \rightarrow \pi^*$	5.91	5.16	4.24	$\sim 4.25-4.28$
$n \rightarrow 3s$	8.19	8.07	6.28	~ 5.96
$n \rightarrow 3p_1$	8.64	8.53	6.67	~ 6.27
$n \rightarrow 3p_2$	8.68	8.60	6.68	~ 6.39
$n \rightarrow 3p_3$	8.73	8.62	6.77	~ 6.83

Table II. Comparison of excited states energies (in eV) obtained by means of the CIS procedure with $n_{core} = 41$ and 11 core orbitals, with TDDFT calculations and experiments by Pulm *et al.*[13] and Kastner *et al.* [14].

with $\lambda = 201$ nm, even if one takes into account the experimental bandwidth (~ 80 meV at $1/e^2$) of the laser pump pulse. The first state of this Rydberg band by a (2+1) REMPI-PECD is found ~ 6.27 eV above the ground state(see Table 1), while 201 nm corresponds to 6.17 eV. However deeper inspection of the CD absorption spectrum of fenchone, which can be found in Fig. 4 of [13], indicates that the onset of the $3p$ manifold is located about 6.2 eV. We therefore understand that besides the main $3s$ contribution, $3p$ states can be populated under the present experimental conditions. Note that for camphor, in which all Rydberg states lie higher on the energy scale (above 6.4 eV [13]), $3p$ states remain really out of reach by absorption of one pump with either $\lambda = 202$ or 200 nm.

We now turn to the definition of the continuum states which will be employed in the description of probe-induced photoionization. Within our CIS procedure with 41 core orbitals, we simply define these continuum states by allowing excitation from the HOMO to virtual orbitals whose spatial parts consist of Bessel partial waves normalized on the energy scale

$$\phi_a(\mathbf{r}) = \sqrt{\frac{2k_a}{\pi}} j_{l_a}(k_a r) Y_{l_a}^{m_a}(\theta, \phi) \quad (59)$$

where $j_{l_a}(k_a r)$ are spherical Bessel functions of wavevector k_a and angular momentum l_a while $Y_{l_a}^{m_a}$ are usual spherical harmonics. In practice we introduce the Bessel partial waves which are resonant with the four Rydberg states ($3s, 3p_{1-3}$) through absorption of one probe photon. This sets four different values of k_a , $k_{a_i} = \sqrt{2(\epsilon_i + \omega_{probe})}$ where ϵ_i is the energy of one of the Rydberg states. Angular momenta are restricted to $l \leq l_{max} = 5$ and $-l \leq m \leq l$. Single-determinantal discretized CIS continuum states are thus built according to eq. (58). We assume that these latter are orthonormal to the ground and bound excited states, and their energies, relative to that of the ground state, are simply defined as $\epsilon_{a_i} = k_{a_i}^2/2$. We are aware that our discretized CIS continuum

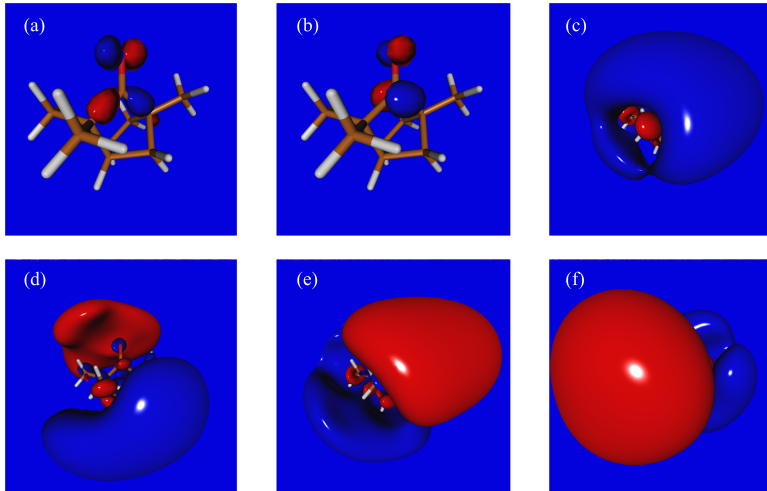


Figure 7. Isodensity maps for the ground state (a) and 5 first low-lying excited states (b-f) of fenchone obtained by means of CIS calculations with 41 core orbitals. The 3s (c), 3p1 (d), 3p2 (e) and 3p3 (f) Rydberg states basically result from excitation of one of the oxygen lone pairs of the carbonyl group to (seemingly) excited O states.

states are zero-order approximations to genuine continuum states: the ϕ_a orbitals of eq. (59) are nothing else than partial waves of plane waves with momentum k_a . In this respect they would not allow to reproduce the usual photoelectron circular dichroism inherent in ionization by circularly polarized photons. However this is particularly well suited to our aim which is to show that in our pump-probe experiments, this dichroism results from the one induced in the transient bound Rydberg wavepacket.

C. The dynamical calculations

We deal with a set of randomly aligned fenchone targets. For one molecule within this set, the electron dynamics are described by means of the time-dependent Schrödinger equation (TDSE)

$$(H_0 + V - i \frac{d}{dt}) \Psi(\{\mathbf{r}\}, t) = 0, \quad (60)$$

where H_0 is the unperturbed electronic Hamiltonian of the system, and $\Psi(\{\mathbf{r}\}, t)$ is the multielectron total wavefunction. $V = -\mathbf{d} \cdot \mathbf{E}(t)$ is the interaction term expressed in the length-gauge dipolar approximation, with \mathbf{d} the (multielectron) dipole and $\mathbf{E}(t)$ the electric field associated to the laser pulse. The TDSE can be solved by expanding $\Psi(\{\mathbf{r}\}, t)$ on the basis of time-independent CIS functions Φ_i^{CIS} with identical spin component,

$$\Psi(\{\mathbf{r}\}, t) = \sum_i a_i(t) \Phi_i^{CIS}(\mathbf{r}) e^{-i\epsilon_i t} \quad (61)$$

where $\epsilon_i = \langle \Phi_i^{CIS} | H_0 | \Phi_i^{CIS} \rangle$. Inserting eq. (61) into eq. (60) yields a set of first-order differential equations for the expansion coefficients $a_i(t)$:

$$\dot{a}_j(t) = -i \sum_i a_i(t) \mathbf{d}_{ji} \mathbf{E}(t) e^{-i(\epsilon_i - \epsilon_j)t} \quad (62)$$

where $\mathbf{d}_{ji} = \langle \Phi_j^{CIS} | \mathbf{d} | \Phi_i^{CIS} \rangle$ are the dipolar couplings. As mentioned above, we take advantage of the weakness of $\mathbf{E}(t)$ to apply first-order perturbation theory; the transition amplitude a_j associated to the transition from the entry channel i to the exit one j in the time interval $[t', t]$ simplifies to

$$a_j(t) = -i \mathbf{d}_{ji} \cdot \int_{t'}^t \mathbf{E}(t'') a_i(t'') e^{-i(\epsilon_i - \epsilon_j)t''} dt'' \quad (63)$$

Here it is worth noting that $\mathbf{E}(t)$ is defined in the laboratory-fixed frame of reference $(x^{lab}, y^{lab}, z^{lab})$ while the dipolar couplings are computed in the molecular frame $(x^{mol}, y^{mol}, z^{mol})$. For a molecule whose orientation is given in terms of the three Euler angles (α, β, γ) in the lab frame, we thus have

$$\mathbf{d}_{ji} = \mathcal{R}^{-1} \mathbf{d}_{ij}^{mol} \quad (64)$$

in the lab frame, where $\mathcal{R} = \mathcal{R}(\alpha, \beta, \gamma)$ is the rotation matrix to pass from the lab to the molecular frames of reference [15] and \mathbf{d}_{ij}^{mol} is the dipole coupling in the (natural) molecular frame.

1. PXCD in fenchone

In this part of the interaction, $a_0(t) \sim 1$ and all other amplitudes vanish. Then eq. (63) transforms into

$$a_j^p(t) = -i \mathbf{d}_{j0} \cdot \int_0^t \mathbf{E}^{pump,p}(t') e^{-i(\epsilon_0 - \epsilon_j)t'} dt', \quad (65)$$

where $\mathbf{E}^{pump,p}(t)$ is a \sin^2 -shaped field, of total duration τ^{pump} , circularly polarized in the (x^{lab}, y^{lab}) plane with either helicity $p = +1$ or $p = -1$. Because of the almost resonant irradiation conditions, only the $3s$ and $3p$'s Rydberg states are (weakly) populated, yielding for a molecular orientation associated to \mathcal{R}_l ,

$$\Psi^{l,p}(\{\mathbf{r}\}, t) = \sum_i a_i^p(t) \Psi_i^{CIS,l}(\{\mathbf{r}\}) e^{-i\epsilon_i t} \quad (66)$$

where $i \in \{3s, 3p_1, 3p_2, 3p_3\}$ and $\Phi_i^{CIS,l}$ are the associated CIS states rotated according to \mathcal{R}_l . It is worth recalling that because of our frozen core CIS description, $\{\mathbf{r}\}$ can be reduced to the coordinate \mathbf{r} of the outermost electron. We choose to display the dynamics in momentum space which is closer to the subsequent detection of freed electrons in the experiment. We accordingly take the Fourier transform \mathcal{F} of eq. (66) and define the electron density averaged over all molecular orientations as the incoherent sum

$$\rho^p(\mathbf{k}, t) = \int d\alpha_l d\beta_l d\gamma_l \sin(\beta_l) |\hat{\Psi}^{l,p}(\mathbf{k}, t)|^2 \quad (67)$$

where $\widehat{\Psi}^{l,p} = \mathcal{F}(\Psi^{l,p})$ and $t \geq \tau^{pump}$. In practice, eq. (67) is evaluated by means of a (triple) quadrature with $\Delta\alpha = \Delta\beta = \Delta\gamma$. Beyond the helicity dependence of the population of the orientation-averaged wavepacket, $P(p, t) = \|\rho^p\|^2$, we can seek whether this wavepacket presents circular dichroism patterns by looking at the so-called photo-excitation circular dichroism (PXCD)

$$PXCD(k_x, k_z, t) = 2 \frac{\rho^{p=+1}(k_x, k_z, t) - \rho^{p=-1}(k_x, k_z, t)}{\rho^{p=+1}(k_x, k_z, t) + \rho^{p=-1}(k_x, k_z, t)} \quad (68)$$

with $\rho^p(k_x, k_z, t) = \int dk_y \rho^p(\mathbf{k}, t)$ for a given value of the helicity. Recall that $p = +1$ and $p = -1$ correspond respectively to left- and right-circularly polarized fields. k_z is along the direction of propagation of the pump beam while k_y is the Time of Flight axis.

2. Pump-probe PXECD in fenchone

In this second part of the interaction, the electron is promoted into the continuum through the absorption of a photon from a \sin^2 -shaped probe field, of total duration τ^{probe} , linearly polarized in the x -direction. The delay between the maxima of pump and probe pulses is τ . The transition amplitude results from the coherent sum over the four initial states

$$a_k^p(t) = -i \sum_{i=1}^4 a_i^p(\tau^{pump}) \mathbf{d}_{ki} \cdot \int_{t_{ini}}^t \mathbf{E}^{probe}(t'') e^{-i(\epsilon_i - \epsilon_k)t''} dt'' \quad (69)$$

where $i \in \{3s, 3p_1, 3p_2, 3p_3\}$ and $t_{ini} = \tau^{pump}/2 + \tau - \tau^{probe}/2 > \tau^{pump}$. We then proceed like in the pump step, and define the PXECD for delay τ , in case where pump and probe pulses do not overlap, as

$$PXECD(k_x, k_z, \tau) = \frac{\rho^{p=+1}(k_x, k_z, t_{fin}) - \rho^{p=-1}(k_x, k_z, t_{fin})}{\mathcal{N}} \quad (70)$$

where $t_{fin} = \tau^{pump}/2 + \tau + \tau^{probe}/2$ is the time at the end of the pump-probe interaction, and ρ^p is the two-dimensional electron density finally formed in the continuum. For given τ , PXECD is normalized as in the experiment to the maximum \mathcal{N} of the half sum of the images $\rho^{p=+1}$ and $\rho^{p=-1}$ in the (k_x, k_z) plane, that is $\mathcal{N} = \max[\rho^{p=+1}(k_x, k_z, T(\tau)) + \rho^{p=-1}(k_x, k_z, T(\tau))]/2$. Note that the Fourier transform of the Bessel partial waves of eq. (59), $\widehat{\Phi}_a(k) = k^{-3/2} \delta(k - k_a)$, is computed using the generating Gaussian function $\exp(-(k - k_a)^2/\gamma^2)/\gamma\sqrt{\pi}$, with $\gamma = 0.05$ a.u., for the δ -distribution.

D. Results

In the experiment, the wavelength of the pump pulse is $\lambda \sim 200$ nm and it corresponds to an energy of 6.20 eV. The absorption of one photon from this pulse thus brings the system in between the 3s and 3p Rydberg states (see the experimental energies of these states in Table 1). Because of the upward shift of the CIS excitation energies (see again Table 1), we employ in our simulations a pump photon with energy 8.326 eV in order to fall in the same region between 3s and 3p CIS states.

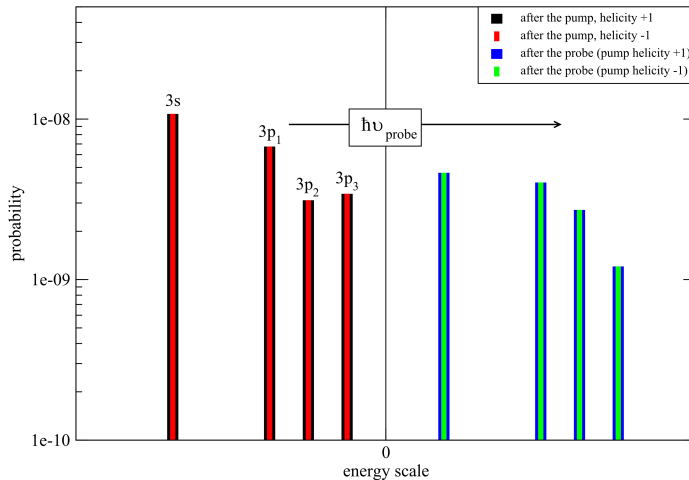


Figure 8. Orientation-averaged bound and continuum state populations at the end of the pump and/or probe pulses, in the case of adjacent but non-overlapping pump and probe pulses. State energies are referred to the ionization threshold.

The FWHM duration of the pump pulse is $\tau^{pump} = 72$ fs and its intensity is set to $I_{pump} = 10^{12}$ W/cm². For the probe field, we use the FWHM duration $\tau^{probe} = 36$ fs, $h\nu = 4.163$ eV and intensity 10^8 W/cm². The strength of the probe field does not affect the perturbative computation of the PXECD (70). All orientation averages presented hereinafter have been performed using $\Delta\alpha = \Delta\beta = \Delta\gamma = \pi/4$; we explicitly checked the convergence of the PXCD and PXECD profiles presented below.

1. Populations after pump and pump-probe excitations

We present in Fig. 8 the orientation-averaged populations $P(p, \tau^{pump})$ of bound states after the circularly polarized pump excitation. As expected, the most populated states are the $3s$ and $3p$ Rydberg ones. When the probe pulse is on, these populations are decreased because of the transfer into the continuum, as illustrated in Fig. 8 in the case of a delay $\tau = (\tau^{pump} + \tau^{probe})/2$ (which is the smallest delay for non overlapping pulses). Importantly, both the bound state populations, after pump excitation, and continuum populations, after probe ionization, are the same whether $p = +1$ or $p = -1$. Kröner found a similar behaviour in the case of pump excitation [17]. He further showed that this equality is broken beyond the dipolar approximation, and he suggested that PECD in (strictly) resonant multiphoton regime results from the interplay of dipole and non-dipole transitions within the first step of the multiphoton (ladder-type) climbing mechanism. This picture does not coincide with the usual description of one photon-induced PECD in terms of only

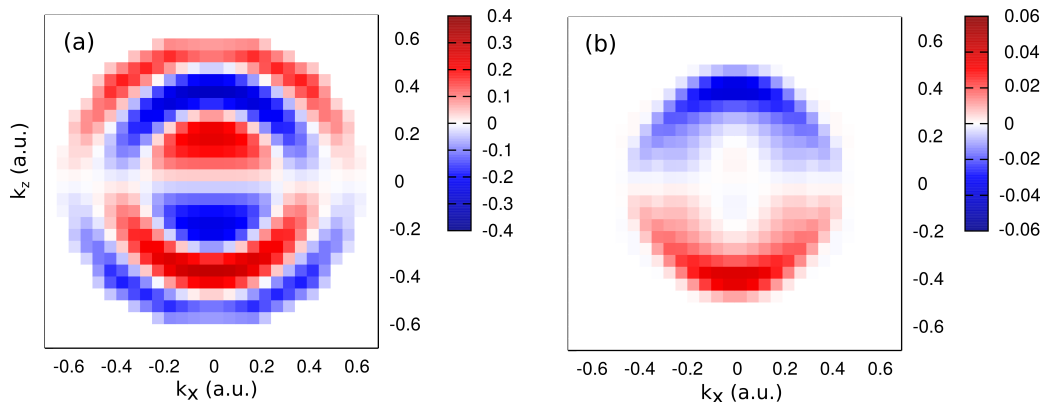


Figure 9. (a) PXCD at the end of the pump pulse. (b) PXECD at the end of the pump-probe interaction with delay $\tau = 150$ fs.

dipolar transitions [5]. Let's see what happens in our case of a Rydberg wavepacket created by a circular pump pulse and photoionized by a linear probe.

2. PXCD and PXECD

We present in Fig. 9(a) the PXCD computed according to eq. (68) at the end of the pump excitation ($t = \tau^{pump}$). It is clear that even if the transient bound state populations are insensitive to the helicity of the pump pulse within the dipolar approximation, the associated PXCD does not vanish. The occurrence of a non vanishing PXCD is intuitive for a fixed molecular orientation: the dipolar couplings are then different for $p = +1$ or $p = -1$, leading to distinct populations and related dichroism. To understand how this dichroism survives orientation averaging, we calculate it with eq. (68) by assuming that for each molecular orientation l , the bound state density $|\hat{\Psi}^{l,p}(\mathbf{k}, t)|^2$ consists of the incoherent sum over the $3s$ and $3p$ electron densities, i.e.

$$\rho^{l,p}(\mathbf{k}, t) = \sum_i |a_i^p(t)|^2 (\hat{\Phi}_i^{CIS,l}(\mathbf{k}))^2. \quad (71)$$

We find (but do not show for sake of conciseness) that the resulting PXCD vanishes: this proves that the PXCD survives orientation average because of transition amplitude cross-terms, *i.e. it is a fingerprint of helicity-dependent (chiral) electronic coherence imprinted in the molecular wavepacket by the pump pulse*. In fact, this finding is fully coherent with what is observed in the usual PECD induced by one-photon ionization: since the pioneering work of Ritchie [5], the PECD is indeed known to occur because of interferences between different partial wave ionizing pathways. As a corollary of this, we also found that the PXCD is zero if the pump populates only one excited state. The construction of a molecular wavepacket is a requisite to the observation of PXCD, at least within the dipolar approximation.

We present in Fig. 9(b) the PXECD computed at the end of the photoionization process. This theoretical result reaches $\sim 6\%$ amplitude. Even if the shape of the PXECD should not be compared

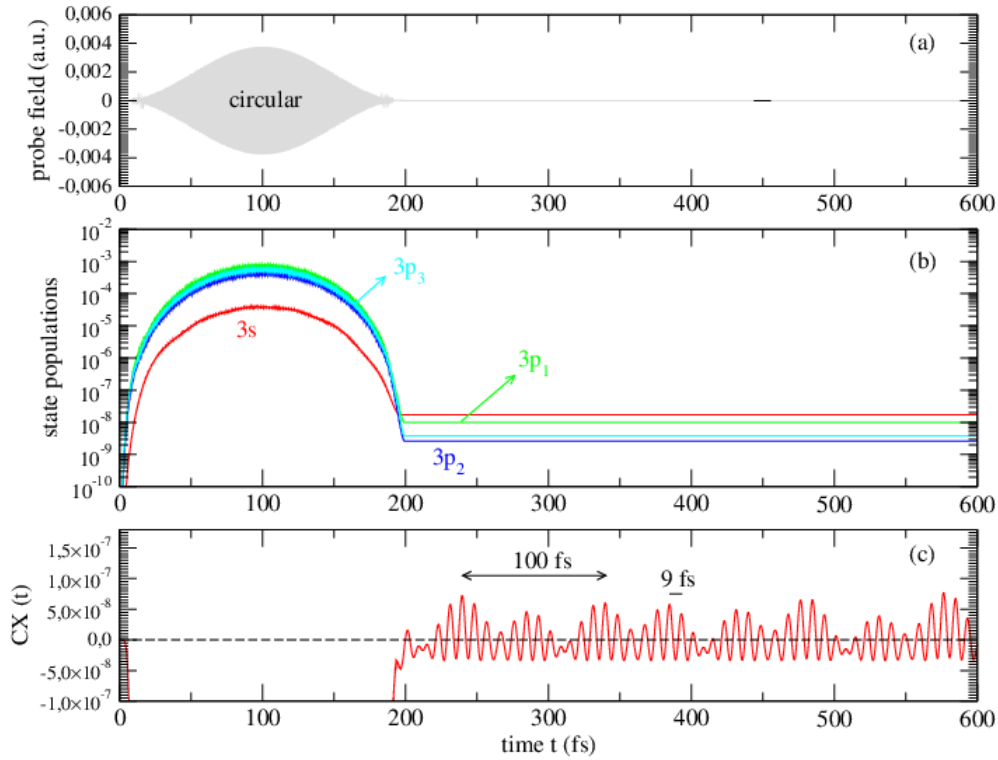


Figure 10. (a) Temporal evolution of the circularly polarized pump field. (b) Temporal evolution of the $3s$ and $3p$'s Rydberg state populations. (c) Temporal evolution of the amplitude cross term (see text). The beating periods expected from the energies of the bound states (see Table 1) are in the 8-9 fs range for $3s-3p_{1-3}$. For $3p_1-3p_2$, $3p_1-3p_3$ and $3p_2-3p_3$, they respectively are 100, 45 and 85 fs. All the illustrations refer to a given molecular orientation and the pump helicity is +1.

in details to the experimental one (because of the approximations made in the construction of the CIS states), it is instructive to notice that while the PXCD of Fig. 9(a) mainly consists of a $P_1(\cos\theta)$ contribution in the (x, z) -plane where $\theta = \cos^{-1}(z/x)$, the PXECD exhibits a clear $P_3(\cos\theta)$ contribution, as expected from the absorption of one and two photons, respectively. Since the absorption of a linearly polarized photon is not amenable to the occurrence of PECD, it is clear here that the observed PXECD is nothing else than the translation of PXCD into the continuum.

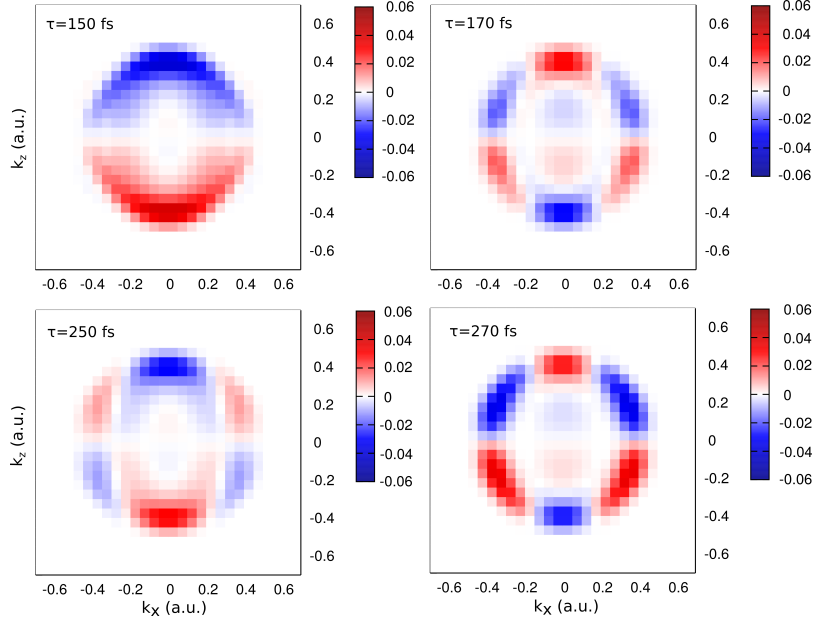


Figure 11. Temporal evolution of the PXECD as function of the pump-probe delay τ . $\tau = 150$ fs corresponds to the case of adjacent but non-overlapping pulses.

3. PXCD, PXECD and dipole beatings, stationarity of the integrated spectra

We have seen that a transient molecular wavepacket, expressed in eq. (66) for a fixed molecular orientation, is formed by the pump pulse (and required to observe PXCD and related PXECD). In the absence of probe ionization, electronic beatings between the constituents of the wavepacket should therefore be observed in the dynamics of the wavepacket for $t > \tau^{pump}$, with frequencies $2\pi/(\epsilon_i - \epsilon_j)$, because of the phase terms $\exp(-i\epsilon_i t)$ in eq. (66). To illustrate this, we display in Fig. 10 an 'history of the interaction' which consists of the temporal evolution of both the Rydberg state populations, $|a_i^p(t)|^2$ with $i \in \{3s, 3p_1, 3p_2, 3p_3\}$, and the amplitude cross term, $CX(t) = \sum_{i,j \neq i} a_i^{p*}(t)a_j^p(t)e^{-i(\epsilon_j - \epsilon_i)t}$, for given molecular orientation l and helicity p in the absence of probe ionization. After the pump pulse, the populations of the $3s$ and $3p_{1-3}$ states forming the Rydberg wavepacket remain constant for $t > \tau^{pump}$, as expected, while $CX(t)$ exhibits some kind of periodic structures with different underlying frequencies corresponding to the beatings between the $3s$ and $3p$'s states.

Since $CX(t)$ is directly involved in the occurrence of PXCD, this latter should present signatures of underlying beatings. Further, if a probe is switched on at different delays after the pump, the PXECD, which consists of the projection of PXCD into the continuum, should also present similar signatures. We therefore present in Fig. 11 some PXECD images, obtained for $\tau = (\tau^{pump} + \tau^{probe})/2$, $(\tau^{pump} + \tau^{probe})/2 + 20$ fs, $(\tau^{pump} + \tau^{probe})/2 + 100$ fs and $(\tau^{pump} + \tau^{probe})/2 + 120$ fs. We do observe that the PXECD evolves quite rapidly in time according to the beating between $3s$ and $3p$'s states. Some kind of revivals appear in Fig. 11, every ~ 100 fs, corresponding to periods of

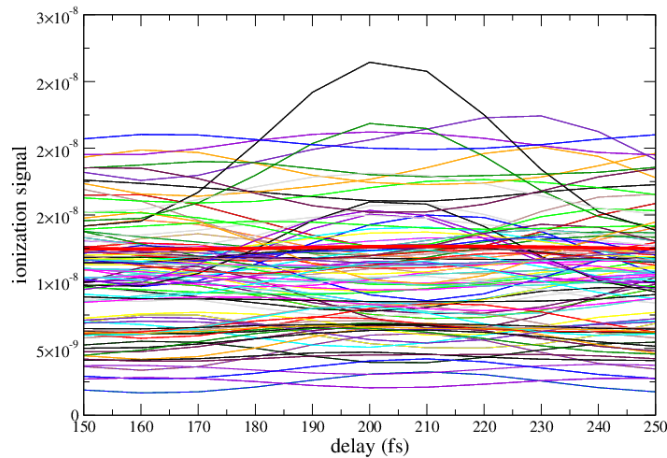


Figure 12. Total ionization signal as a function of the pump-probe delay. The thin lines refer to fixed molecular orientations while the thick (red) line is the orientation-averaged signal.

beatings between $3s$ and $3p_{1-3}$ states. Note that they are not really revivals since the mixture of various (non-multiple) beating frequencies prohibits the appearance of strictly periodic motion.

Beatings show up in the macroscopic dipole displayed in Fig. 2 of the main text. For a given molecular orientation l , the dipole associated to the Rydberg wavepacket has been computed according to $\mathbf{d}_l(t) = \sum_{i,j} a_i^{p,l*}(t)a_j^{p,l}(t)\mathbf{d}_{ij}e^{-i(\epsilon_j-\epsilon_i)t}/N$ with $i \in \{3s, 3p_1, 3p_2, 3p_3\}$ and where N is the norm of the wavepacket. The macroscopic dipole results from averaging over molecular orientations, $\mathbf{d}_{macro}(t) = \int d\alpha_l d\beta_l d\gamma_l \sin(\beta_l)\mathbf{d}_l(t)$. Only the component of \mathbf{d}_{macro} parallel to the laser propagation axis survives orientation averaging, consistently with PXCD (and PXECD) features. This dipole component is not permanent. However it does not vanish if one integrates it over a quite large temporal range, which means that it could be resolved experimentally without the need for an extreme temporal resolution, provided fast dynamics subsequent to pump excitation (as rapid transitions between vibrational modes) do not blur it. No trace of beating have been found in the present experiment, which tends to indicate the existence of fast nuclear dynamics coupled to the electronic motion.

For fixed-in-space molecules (fixed orientation), the electronic beating also appears in the (integrated) ionization signal (see similar features in [18]). This is what we show in Fig. 12. However, and importantly, this beating does not survive the orientation average (see Fig. 12), similarly to what happens in usual photoionization experiments.

4. Evolution of chiral structure after pump photon absorption and impact on PXECD features

It is clear from Fig. 4 of the main text that the PXECD induced by the probe photon absorption evolves as a function of the pump-probe delay. We inferred that such a change is due to the evolution of the chiral molecular structure within the $3s$ and $3p$ electronic manifolds after the pump excitation. The molecular structure indeed influences the magnitude and direction of the bound-free dipoles involved in probe-induced ionization (see eq. (69)). To verify this, we performed additional calculations where the probe ionization step has been computed using the bound-free dipoles associated to the nuclear equilibrium geometry of the $3s$ Rydberg state – this geometry was derived from TDDFT calculations using the 6-311++G** gaussian basis and CAM-B3LYP exchange-correlation functional. The resulting PXECD is presented in Fig. 5 of the main text. It is significantly different from the one obtained when the same (ground-state) geometry is employed for the computation of both (pump) bound-bound and (probe) bound-free dipoles. Therefore we can safely state that the temporal evolution of the α and α' coefficients displayed in Fig. 4 of the main text are due to the changes of the chiral molecular structure after the pump excitation. Moreover, we reiterate that with high vibrational frequencies at play, the oscillations of the photoelectron asymmetry calculated and shown in Fig. 12 are expected to be blurred such that the contrast is significantly reduced.

E. Conclusions on the quantum mechanical calculations

Our simulations have shown that molecular chiral Rydberg wavepackets can be formed by absorption of a circularly polarized photon. In addition, (i) the population of this wavepacket does not depend on the helicity within the dipolar approximation, (ii) this wavepacket presents inherent chirality, imaged by photoexcitation circular dichroism, that survives orientation averaging within a set of randomly aligned targets as a remanence of electronic coherence, (iii) when a linearly polarized probe is switched on, this dichroism is translated into the continuum and pictured in terms of (usual) photoelectron circular dichroism, (iv) electron beating among the underlying wavepacket states is noticeable in the excitation and related ionization dichroisms, as function of the pump-probe delay, but the beating is blurred in the total ionization signal. All of this shed new light on the origin of chirality, whose signature is no more constrained to molecular ionization but extends to the whole electron spectrum, within the usual (and intuitive) dipolar approximation.

Note finally that more elaborate calculations, employing e.g. TDDFT, could be performed to obtain more quantitative results which could be compared to experimental data. However this would not change the findings and conclusions of the present work since the interaction relies on dynamics of the outermost electron of fenchone which are qualitatively well described by CIS.

V. VIBRATIONAL COHERENCE IN PXECD

What are the conditions for observing purely vibrational PXECD? First, it requires the breakdown of the Franck-Condon approximation. This is expected to be the case for large molecules exhibiting broad vibrational lines. Indeed, the essence of this approximation is that the vibrational wavefunctions are sufficiently compact in coordinate space, so that the electronic dipole moment does

not change as a function of vibrational coordinates within this compact region. If, however, the vibrational wave-functions spread over considerable distances, the opportunity for the breakdown of the Franck-Condon approximation is created. Second, it requires multidimensional, at least two dimensional, potential energy surfaces (PESF), which is certainly the case for non-linear molecules, such as chiral molecules.

To construct the proof-of-principle example we can simply use two dimensional harmonic oscillator as a model of the PESF with the two reaction coordinates denoted as R_i and R_j . Characterizing the vibrational states by two quantum numbers v_i and v_j , it is easy to show that the excitation with one vibrational quantum $v_i = 1$ put in R_i direction and one vibrational quantum $v_j = 1$ put in R_j direction leads to non-collinearity of the two associated transition dipoles. If the vibrational function χ_1 of the first state corresponds to the normal mode along the R_i coordinate, i.e. excitation with $v_i = 1, v_j = 0$ while the vibrational function χ_2 of the second state is the normal mode in the R_j coordinate with $v_j = 1, v_i = 0$, then transition dipole involving the first vibrational state χ_1 is aligned along the R_i coordinate, while the transition dipole involving the second vibrational state χ_2 is aligned along the R_j coordinate. Indeed, consider the dipole that depends on two nuclear coordinates $\mu(R_i, R_j)$. Making the standard linear expansion: $\mu_x(R_i, R_j) = \mu_i + \alpha_{ii}R_i + \alpha_{ij}R_j$ and $\mu_y(R_i, R_j) = \mu_j + \alpha_{ji}R_i + \alpha_{jj}R_j$ we obtain in addition to the standard FC term, the following two dipoles. The dipole for the first vibrational state: $d_1 = (\langle \chi_g | R_i | \chi_1 \rangle; \langle \chi_g | R_j | \chi_1 \rangle)$, and for the second vibrational state $d_2 = (\langle \chi_g | R_i | \chi_2 \rangle; \langle \chi_g | R_j | \chi_2 \rangle)$. This simple example proves the existence of non-collinear dipoles corresponding to two vibrational states within a single potential energy surface.

-
- [1] P. W. Anderson, *Science* 177, 393-396 (1972)
 - [2] M. Stener *et al.*, *J. Chem. Phys.* 124, 024326 (2006)
 - [3] D. Dill and U. Fano, *Phys. Rev. Lett.* 29, 1203 (1972)
 - [4] A. F. Ordonez and O. Smirnova, *Phys. Rev. A* 99, 043416 (2019)
 - [5] B. Ritchie, *Phys. Rev. A* 13, 1411 (1976)
 - [6] B. R. Johnson, *J. Chem. Phys.* 69, 4678 (1978)
 - [7] B. R. Johnson, *J. Comp. Phys.* 13, 445 (1973)
 - [8] L. Nahon *et al.*, *J. Chem. Phys.* 125, 114309 (2006)
 - [9] Ullrich *et al.*, *Rep. Prog. Phys.* 66, 1463 (2003)
 - [10] M. W. Schmidt *et al.*, *J. Comput. Chem.* 14, 1347 (1993)
 - [11] R. Krishnan *et al.*, *J. Chem. Phys.* 72, 650 (1980)
 - [12] J. B. Foresman *et al.*, *J. Phys. Chem.* 96, 135 (1996)
 - [13] F. Pulm *et al.*, *Chem. Phys.* 224, 143 (1997)
 - [14] A. Kastner *et al.*, *J. Chem. Phys.* 147, 13926 (2017)
 - [15] H. Goldstein, *Classical Mechanics*, Addison-Wesley Publishing Company (1980)
 - [16] B. H. Bransden and C. J. Joachain, *Physics of Atoms and Molecules*, Prentice-Hall, Englewood Cliffs, NJ (2003)
 - [17] D. Kröner, *J. Chem. Phys. A* 115, 14510 (2011)
 - [18] U. Höfer *et al.*, *SPIE* 3272, 211 (1998)

Generalized perspective on chiral measurements without magnetic interactions

Andres F. Ordonez^{1,2,*} and Olga Smirnova^{1,2,†}

¹*Max-Born-Institut, Berlin, Germany*

²*Technische Universität Berlin, Berlin, Germany*

This is the accepted version of an article published in Physical Review A 98, 063428 (2018). The published version is available online at <http://dx.doi.org/10.1103/PhysRevA.98.063428>

We present a unified description of several methods of chiral discrimination based exclusively on electric-dipole interactions. It includes photoelectron circular dichroism (PECD), enantio-sensitive microwave spectroscopy (EMWS), photoexcitation circular dichroism (PXCD) and photoelectron-photoexcitation circular dichroism (PXECD). We show that, in spite of the fact that the physics underlying the appearance of a chiral response is very different in all these methods, the enantio-sensitive and dichroic observable in all cases has a unique form. It is a polar vector given by the product of (i) a molecular pseudoscalar and (ii) a field pseudovector specified by the configuration of the electric fields interacting with the isotropic ensemble of chiral molecules. The molecular pseudoscalar is a rotationally invariant property, which is composed from different molecule-specific vectors and in the simplest case is a triple product of such vectors. The key property that enables the chiral response is the non-coplanarity of the vectors forming such triple product. The key property that enables chiral detection without relying on the chirality of the electromagnetic fields is the vectorial nature of the enantio-sensitive observable. Our compact and general expression for this observable shows what ultimately determines the efficiency of the chiral signal and if, or when, it can reach 100%. We also discuss the differences between the two phenomena, which rely on the bound states, PXCD and EMWS, and the two phenomena using the continuum states, PECD and PXECD. Finally, we extend these methods to arbitrary polarizations of the electric fields used to induce and probe the chiral response.

I. INTRODUCTION

Right- and left-handed helices are typical examples of chiral objects; each of them cannot be superimposed on its own mirror image. Some molecules possess the same property; left-handed and right-handed molecules are called enantiomers. Distinguishing left and right enantiomers is both vital and difficult [1–3]. Since the XIX century, the helix of circularly polarized light was used to distinguish the two enantiomers of a chiral molecule, relying on the relatively weak interaction with the magnetic field as a key mechanism for chiral discrimination. However, in this case the chiral signal¹ is proportional to the ratio of the molecular size to the pitch of the light helix, i.e. its wavelength, generally leading to weak signals in the infrared, visible, and UV regions.

One can overcome this unfavorable scaling and obtain significantly higher circular dichroism, at the level of a few percent, in several ways. Firstly, one can rely on using a strong laser field to enhance the optical response involving the interference of the magnetic-dipole transitions and the electric-dipole ones, as done in chiral high harmonic generation [4–7]. Secondly, one can decrease the pitch of the light helix by using XUV/X-ray light [8, 9]. Yet, in both cases the chiral signal would be equal to zero within the electric-dipole approximation.

Thus, the discovery of approaches relying exclusively on electronic dipole transitions [10–18] and yielding a very high chiral response already in the electric-dipole approximation is both intriguing and beneficial. These techniques include photoelectron circular dichroism (PECD) [10–13], enantio-sensitive microwave spectroscopy (EMWS) [16, 19, 20], photoexcitation circular dichroism (PXCD) [18], and photoexcitation-photoelectron circular dichroism (PXECD) [18].

This new generation of chiral methods leads to very high signals, up to tens of percent in PECD, which is several orders of magnitude higher than in standard techniques relying on magnetic interactions. Here we present a unified description of several of these methods working in the perturbative one- and two-photon regimes of the light-molecule interaction. Results for the multiphoton [21–23] and the strong-field regime [24, 25] of PECD will be presented elsewhere.

We derive a common general formulation for the chiral response encompassing PECD, EMWS, PXCD, and PXECD. This formulation is based on understanding that these electric-dipole based techniques using non-chiral fields are only possible thanks to vectorial observables. Readers familiar with chiral measurements might be uncomfortable with such statement. Indeed, it is well known that chiral observables are pseudoscalars, not polar vectors. Section II addresses this issue and describes the role of the lab setup in enantio-sensitive techniques with non-chiral fields. In Sec. III we describe how symmetry enforces enantio-sensitivity and dichroism on polar vectors resulting from the electric-dipole interaction. Section IV consists of four parts which specify how the

* ordonez@mbi-berlin.de

† smirnova@mbi-berlin.de

¹ When referring to the measured signal, we will use the adjective *chiral* as a shorthand for *enantio-sensitive and dichroic*.

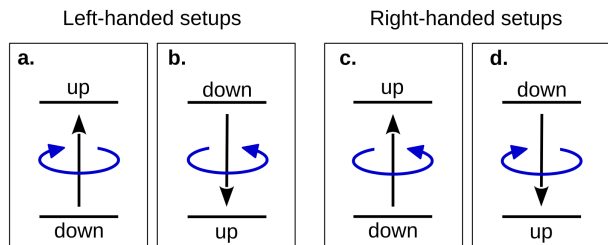


Figure 1. The combination of circularly polarized light (blue curved arrows) and a detector (horizontal lines) defining a vector perpendicular to the polarization plane (black vertical arrows) make up a chiral setup. Four possible realizations of such setup are shown. Setups **a** and **b** are left handed and setups **c** and **d** are right handed. For a fixed molecular enantiomer (not shown in the figure) setups with the same handedness yield the same result, while setups with opposite handedness yield opposite results.

information about the handedness of the lab setup and that of the molecular enantiomer can be decoupled and defined in a common way for the four perturbative dipole techniques: PECD, PXCD, EMWS, and PXECD. Section V summarizes the conclusions of this work. We use atomic units throughout the paper.

II. CHIRAL MEASUREMENTS AND ENANTIO-SENSITIVE OBSERVABLES

The goal of our work is to demonstrate the general concept underlying several chiral measurements which do not use magnetic interactions. Achieving this goal requires two things. First, one should provide a general concept, i.e. address the question “*what is the key difference between the chiral measurements involving the magnetic component of the light field and those relying only on the electric-dipole approximation?*”. We outline such concept in this section. Second, one should formalize this concept by deriving compact expressions for observables pertinent to the four different experimental setups and establishing connections between them. Such derivations will be presented in Sec. IV.

It is well known that any enantio-sensitive observable should be a pseudoscalar. However, detectors in any experimental setup measure clicks. Clicks are scalars. Where is the pseudoscalar in a click?

Let us start with the conventional concept. It is well known that the handedness of chiral objects can only be probed via interaction with another chiral object, in other words, it is well known that one always needs a chiral reagent to discriminate between opposite enantiomers. A chiral reagent interacts differently with left and right enantiomers. The chiral reagent can be simply another chiral molecule or chiral light. Consider, for example, absorption circular dichroism. Absorption of circularly polarized light by a chiral molecule is the out-

come of such an experiment, and this absorption must be different for right and left enantiomers. The difference in absorption is a scalar, however this scalar is just a product of two pseudoscalars, one from the molecule and the other from light. In this particular case the second pseudoscalar is the light helicity (see Appendix VII A), which encodes the handedness of the helix traced by the circularly polarized light in space. Thus, we use the chiral probe (chiral reagent) to “hide” a molecular pseudoscalar inside a scalar. The molecular pseudoscalar in absorption circular dichroism, as it is well known, is given by the scalar product of electric-dipole and magnetic-dipole vectors. The overall signal is small because the magnetic field interacts very weakly with molecules.

We now turn to methods which do not rely on the interaction with the magnetic component of the light field such as e.g. PECD. In PECD the photoionization of an isotropic molecular ensemble with circularly polarized light yields a net photoelectron current in the direction perpendicular to the plane of polarization. The direction of this current can be flipped by either swapping the molecular handedness or the direction of rotation of the field. It is a purely electric-dipole effect: light chirality is not needed at all, i.e. the magnetic field of the incident laser pulse is not used. Thus, we do not use the chiral property of light, yet the chiral signal is very strong. Where is our chiral reagent if the light chirality is not used? The combination of circularly polarized light and a detector that distinguishes the two opposite directions perpendicular to the polarization plane defines a chiral setup (see Fig. 1) whose handedness (a pseudoscalar) is given by the scalar product between the photon’s spin (a pseudovector) and the direction defined by the detector (a vector). Thus, the chiral reagent is substituted by the chiral observer (i.e. chiral setup). That is why we do not need to employ chiral properties of impinging electromagnetic fields.

The role of the directionality of the detector in defining the handedness of the chiral setup highlights the crucial importance of having a vectorial response to the light-matter interaction, since a scalar response would be unable to exploit the directionality of the detector, and as a consequence also the handedness of the setup. Furthermore, as we show in Sec. III, such vectorial response automatically exhibits enantio-sensitivity and dichroism with respect to the *external* vector defined by the detector. These properties indicate that in general the vectorial response results from the product of a molecular pseudoscalar and a field pseudovector. The field pseudovector determines the direction of observation of the dichroic and enantio-sensitive response and thus indicates (up to a sign) the corresponding detector arrangement required to measure such response (see Fig. 1). The field pseudovector is formed by non-collinear (and phase-delayed in the case of a single frequency) components of the electric field. For example, in PECD, it results from the vector product between the x and y components of the circularly polarized field. Ultimately, the

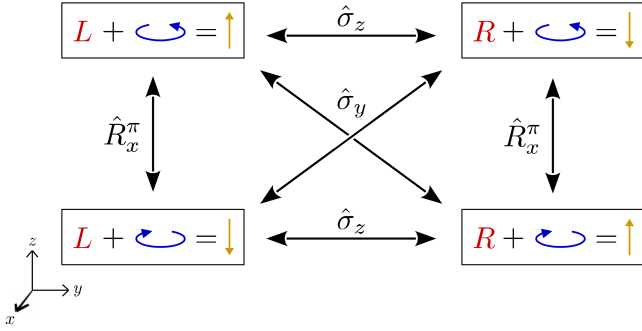


Figure 2. Symmetry properties of an isotropic ensemble of chiral molecules interacting with circularly polarized light in the electric-dipole approximation. The box represents the “enantiomer+field” system. Inside the box: red letters L and R specify the enantiomer, the curved blue arrow specifies the direction of rotation of a field circularly polarized in the xy plane, and the vertical golden arrow stands for a polar vector observable $\vec{v} = v_z \hat{z}$ displaying asymmetry with respect to the polarization xy plane. A reflection $\hat{\sigma}_z$ with respect to the xy plane, leaves the field invariant, but swaps the enantiomer and flips \vec{v} . A rotation \hat{R}_a^π by π radians around any axis \hat{a} contained in the xy plane leaves the enantiomer invariant because the ensemble is isotropic, but swaps the polarization and flips \vec{v} . Note that a rotation \hat{R}_x^π (\hat{R}_y^π) followed by a reflection $\hat{\sigma}_z$ is equivalent to a reflection $\hat{\sigma}_y$ ($\hat{\sigma}_x$) and leaves \vec{v} invariant but swaps both the enantiomer and the polarization.

result of the measurement—the scalar (click)—is given by the projection of the vectorial response on the *external* vector defined by detector, which yields the product of the molecular pseudoscalar and the handedness of the setup (see Sec. IV). The latter is the projection (positive or negative) of the field pseudovector on the *external* vector defined by the detector.

Note that the field pseudovector does not have to point in the direction of light propagation (as one might think from the above example). In Sec. IV we expose various opportunities offered by different field geometries, including arrangements of electric fields propagating non-collinearly.

In Sec. IV we illustrate this concept by deriving molecular pseudoscalars and field pseudovectors for four experiments detecting different observables in different systems using different setups. However, in all cases what enables chiral discrimination is the chiral observer defined by the combination of an achiral electromagnetic field and a directional detector.

III. SYMMETRY IN THE ELECTRIC-DIPOLE APPROXIMATION

Let us begin with a simple symmetry consideration, which applies to all enantio-sensitive effects considered here. Consider first an isotropic ensemble of a non-racemic mixture of chiral molecules, which interacts with

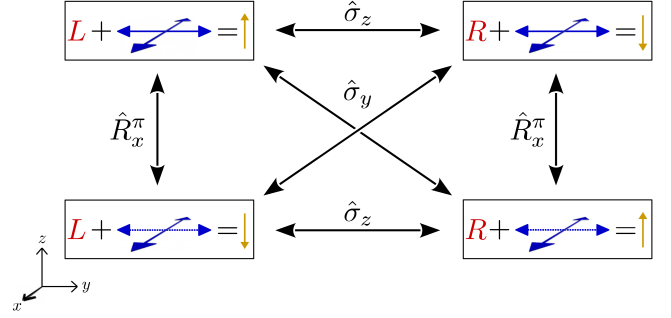


Figure 3. Same as Fig. 2 but for two perpendicular linearly polarized fields along \hat{x} (double headed arrow in perspective) and \hat{y} (horizontal double headed arrow) of arbitrary frequencies and intensities. In general $v_x \neq 0$ and $v_y \neq 0$ but only $v_z \hat{z}$ is shown (vertical arrow). A rotation \hat{R}_x^π (\hat{R}_y^π) leaves the enantiomer invariant but changes the phase of the field along \hat{y} (\hat{x}) by π . $\hat{\sigma}_x$, $\hat{\sigma}_y$, $\hat{\sigma}_z$ describe transformations of the “enantiomer+field” system upon reflections with respect to the different axes of the lab frame.

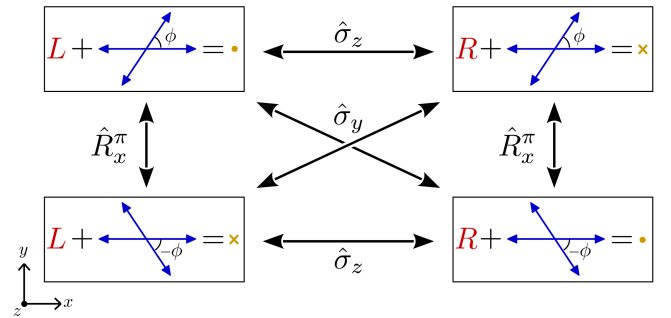


Figure 4. Same as Fig. 3 but for an arbitrary angle between the two linearly polarized fields. Note that vectors pointing out of the page are indicated by a dot (\hat{z} and \vec{v} in the upper left and lower right configurations) and vectors pointing inside the page by an \times (\vec{v} in the upper right and lower left configurations).

light circularly polarized in the xy plane. Irrespective of the specific chiral response we are looking at, it may lead to an observable associated with some polar vector \vec{v} . For example, in the case of PECD this polar vector is the net photoelectron current, while in PXCD it would be the coherent dipole induced in the bound states of the neutral. The cylindrical symmetry of the “ensemble+field” system implies that $\vec{v} = v_z \hat{z}$ ². Generalization to the case with no cylindrical symmetry is discussed below. The

² Note that for few-cycle pulses, the cylindrical symmetry may be severely compromised. However, for perturbative fields the first-order amplitudes do not encode the duration of the pulse, that is, the response of a few-cycle pulse can be emulated using monochromatic light of the appropriate intensity, and therefore the cylindrical symmetry assumption remains valid even for ultra-short pulses provided one only looks at functions of the first-order amplitudes.

“enantiomer+field” system and a chiral sensitive vectorial observable in the case of cylindrical symmetry are sketched in the upper-left box of Fig. 2. It applies, for example, to the field configuration in PECD and PXCD. Our system transforms as indicated in Fig. 2 under reflections in the xy plane and under rotations by π radians around any axis contained in the xy plane. These transformations show the relationship between the different “enantiomer+field” configurations and the corresponding effect on the dichroic and enantio-sensitive observable \vec{v} .

Figure 2 shows that for an achiral ensemble, i.e. an ensemble of achiral molecules or a racemic mixture of chiral molecules, the system “ensemble+field” is symmetric with respect to reflection $\hat{\sigma}_z$ in the xy plane. Therefore, the vector \vec{v} must vanish, yielding a photoelectron angular distribution symmetric with respect to the plane of polarization, otherwise two identical experiments would yield different results. However, for a non-racemic mixture of chiral molecules, there is no symmetry enforcing $\vec{v} = 0$. Therefore, nothing prohibits the emergence of observables which display asymmetry with respect to the plane of polarization, and the associated dichroism and enantio-sensitivity. The question is what these observables are, how strong can the signal be, and what determines its limits. We address these problems in the next section.

We also stress that the cylindrical symmetry is not essential for our reasoning. The argument can be extended to other geometries including linear fields or aligned molecules, provided one takes into account that v_x and v_y are not necessarily zero. Figure 3 shows a generalization of the case we have just considered. Now the x and y components of the field have different frequencies, intensities, and an arbitrary phase shift with respect to each other. This field configuration is relevant, for example, for the EMWS experiments carried out in Ref. [19]. The original experiment in Ref. [16] can also be analyzed similarly by replacing one of the two-headed arrows in each “enantiomer+field” configuration in Fig. 3 by a single-headed arrow to account for the static field. The details of the analysis are discussed further in Sec. IV C 1, but the conclusion remains the same: the emergence of a non-vanishing polar vector characterizing the chiral response of the “enantiomer+field” system. Finally, the emergence of this vector for arbitrary orientations of linear fields is illustrated in Fig. 4.

We can now support the introductory discussion of Sec. II with several remarks concluding the symmetry analysis above:

First, from Figs. 2-4 it is clear that \vec{v} reflects the properties of the “enantiomer+field” system, and not those of the enantiomer or field separately.

Second, while it is well known that molecular chiral observables are characterized by pseudoscalars (scalar quantities that change sign upon the parity transformation), so far we have been discussing enantio-sensitive properties of a polar vector. The appearance of a polar vector \vec{v} is not accidental: its projections on the axes of

the lab frame combine the information about the handedness of the chiral molecule and the handedness of the chiral setup.

Third, the observation of enantio-sensitivity and dichroism in Figs. 2-4 implicitly assumes a fixed z direction against which we can compare the rotation direction of the light and the direction of the vector \vec{v} . Otherwise, there would be no way to, for example, distinguish right- and left-circularly-polarized light from each other, since we could rotate the z axis by π to change right- into left-circularly polarized light. Although a fixed z direction is usually taken for granted, it remains physically meaningless until it is somehow related to the elements taking part in the experiment. In the methods we analyze here, such a z direction is fixed by the detector (vertical arrow in Fig. 1), which is of course assumed to remain unchanged when either the enantiomer or the light polarization is changed.

Therefore, the advent of electric-dipole-based techniques marks a shift of paradigm in chiral discrimination from using chiral reagents to using chiral observers, i.e. an experimental setup with well-defined handedness, even if the latter is not explicitly stated or recognized.

In the next section we will show that in all cases the polar vector \vec{v} is given by the product of (i) a molecular pseudoscalar and (ii) a field pseudovector specified by the configuration of the electric fields. We will directly specify these two key quantities, forming the vectorial observables, for each of the electric-dipole-based techniques.

IV. UNIFIED DESCRIPTION OF CHIRAL ELECTRIC-DIPOLE RESPONSE

The chiral electric-dipole response manifests itself in vectorial observables, which have the following general form:

$$\vec{v} = \chi_m \vec{Z}_l, \quad (1)$$

where χ_m is a molecular pseudoscalar defining the handedness of the molecule and \vec{Z}_l is a light field pseudovector. Measuring \vec{v} means projecting it on the *external* vector \vec{u}_d defined by the detector (vertical arrow in Fig. 1),

$$\vec{v} \cdot \vec{u}_d = \chi_m \left(\vec{Z}_l \cdot \vec{u}_d \right). \quad (2)$$

The projection of \vec{Z}_l on \vec{u}_d defines the handedness of the chiral setup, therefore, the result of the measurement is given by the product of the molecular handedness and the setup’s handedness. In this section we will derive χ_m and \vec{Z}_l for four different electric-dipole based techniques of chiral discrimination. These techniques include PECD [10–13], EMWS [16, 19, 20], PXCD [18], and PXECD [18].

A. Photoelectron circular dichroism

We begin with what is perhaps the most prominent electric-dipole-based technique, PECD. This technique was first proposed in 1976 [10] and then rediscovered in 1982 [11]. The first quantitative calculations of the effect [12] yielded staggering results: the expected effect was at the level of some few percent to maybe even some ten percent of the total photoionization signal. The first experiment appeared just a year later [13]. The technique was dramatically advanced in Refs. [26–29] from a theoretical concept to an extra-sensitive experimental technique. With the advances in table-top laser-based implementations [30, 31] including multi-photon [21–23] and strong-field regimes [24], PECD has proven very interesting from both fundamental and applied perspectives. In PECD, the photoionization of an isotropic and non-racemic ensemble of chiral molecules by circularly polarized light leads to an asymmetry in the photoelectron angular distribution (PAD) with respect to the polarization plane, the so-called forward-backward asymmetry (FBA). This asymmetry is usually described by decomposing the angle-resolved photoionization probability $W(\vec{k}^L)$ in Legendre polynomials,

$$W(\vec{k}^L) = \sum_{l=0}^2 b_l(k) P_l(\cos\theta_k^L), \quad (3)$$

where it corresponds to a non-zero b_1 coefficient. In Eq. (3), $W(\vec{k}^L)$ is the probability of obtaining a photoelectron with momentum \vec{k}^L , L indicates that the vector is in the lab frame, θ_k^L is the polar angle of \vec{k}^L , $k \equiv |\vec{k}^L|$, P_l is the Legendre polynomial of degree l , and we assume that the polarization plane coincides with the $x^L y^L$ plane. The b_1 coefficient is directly related to the net photoelectron current induced by ionization

$$\vec{j}^L(k) = \int d\Omega_k^L \vec{j}^L(\vec{k}^L), \quad (4)$$

where $\vec{j}^L(\vec{k}^L) = W(\vec{k}^L)\vec{k}^L$ is the photoelectron current in the direction specified by the photoelectron direction \vec{k}^L in the lab frame, and $\int d\Omega_k^L \equiv \int_0^\pi d\theta_k^L \int_0^{2\pi} d\varphi_k^L \sin\theta_k^L$ is the integral over all photoelectron directions. From the orthogonality of the Legendre polynomials we obtain

$$\begin{aligned} \vec{j}^L(k) &= \int d\Omega_k^L \vec{j}^L(\vec{k}^L), \\ &= \sum_{l=0}^2 b_l(k) \int d\Omega_k^L P_l(\cos\theta_k^L) \vec{k}^L, \\ &= k \sum_{l=0}^2 b_l(k) \int d\Omega_k^L P_l(\cos\theta_k^L) P_1(\cos\theta_k^L) \hat{z}^L, \\ &= \frac{4\pi}{3} k b_1(k) \hat{z}^L. \end{aligned} \quad (5)$$

The current in Eqs. (4) and (5) is the vectorial observable of our interest. The task is to find it or, equivalently, $b_1(k)$. The corresponding calculations of the

photoelectron angular distributions traditionally rely on the formalism of angular momentum algebra, both for one-photon and few-photon PECD [10–12, 32]. We have found that it is very instructive to depart from this traditional formalism, which uses language specific for photoionization. Instead, we use an alternative, vectorial formulation, pioneered in works of Manakov [33] and applied to aligned chiral systems [34]. The vectorial formalism was also used to describe two-photon absorption CD [35]. Conveniently, it provides a common language for all electric-dipole-based techniques, irrespective of their “field of origin” or observable, be it photoionization or microwave physics.

We define the incident circularly polarized field in the lab reference frame as

$$\vec{E}(t) = \mathcal{E}(t)\hat{e}_\sigma^L + \text{c.c.} \quad (6)$$

where $\hat{e}_\sigma^L = (\hat{x}^L + i\sigma\hat{y}^L)/\sqrt{2}$ is the light polarization vector, $\sigma = \pm 1$ defines the rotation direction of the field, and $\mathcal{E}(t)$ is the time-dependent amplitude. The photoelectron current density for a given photoelectron momentum \vec{k}^M in the molecular frame is (up to the negative electron charge)

$$\vec{j}_{\vec{k}^M}^M = |a_{\vec{k}^M}|^2 \vec{k}^M. \quad (7)$$

Here $a_{\vec{k}^M}$ is the ionization amplitude of the transition to the continuum state $|\vec{k}^M\rangle$ from the ground state $|0\rangle$ in the circularly polarized field Eq. (6). Its standard first-order perturbation theory expression is

$$a_{\vec{k}^M} = i\tilde{\mathcal{E}} \langle \vec{k}^M | \vec{d}^L \cdot \hat{e}_\sigma^L | 0 \rangle = \frac{i\tilde{\mathcal{E}}}{\sqrt{2}} \left(\vec{D}^L \cdot \hat{x}^L + \sigma i \vec{D}^L \cdot \hat{y}^L \right), \quad (8)$$

where $\tilde{\mathcal{E}}$ is the Fourier transform of \mathcal{E} at the transition frequency, \vec{d} is the dipole operator, and \vec{D}^L is the corresponding transition dipole matrix element in the lab frame.

Our next step is to identify the molecule-specific enantio-sensitive structure in Eqs. (7) and (8). That is, we will be looking for molecule-specific pseudoscalars; quantities that change sign upon parity inversion. Pseudoscalars may arise as a product of a vector and pseudovector. An example of such pseudoscalar is the helicity η of circularly polarized light which is non-zero only beyond the electric-dipole approximation (see Appendix VII A). Molecular pseudoscalars also arise from triple products formed by three molecular polar vectors. We shall now look for such quantities.

Let us look at the cross term arising in $|a_{\vec{k}^M}|^2$,

$$i\sigma \left[(\vec{D}^{L*} \cdot \hat{x}^L)(\vec{D}^L \cdot \hat{y}^L) - (\vec{D}^L \cdot \hat{x}^L)(\vec{D}^{L*} \cdot \hat{y}^L) \right]. \quad (9)$$

We now use the vector identity $(\vec{a} \cdot \vec{c})(\vec{b} \cdot \vec{d}) - (\vec{a} \cdot \vec{d})(\vec{b} \cdot \vec{c}) = (\vec{a} \times \vec{b}) \cdot (\vec{c} \times \vec{d})$ and the fact that $\hat{x}^L \times \hat{y}^L = \hat{z}^L$ to write

the interference term as a triple product,

$$|a_{\vec{k}_M}|^2 = \frac{|\tilde{\mathcal{E}}|^2}{2} \left\{ \left| \vec{D}^L \cdot \hat{x}^L \right|^2 + \left| \vec{D}^L \cdot \hat{y}^L \right|^2 + i\sigma \left(\vec{D}^{L*} \times \vec{D}^L \right) \cdot \hat{z}^L \right\}. \quad (10)$$

Note that $i \left(\vec{D}^* \times \vec{D} \right) = 2\Im\{\vec{D}\} \times \Re\{\vec{D}\}$ is a real vector, where $\Re\{\vec{D}\}$ and $\Im\{\vec{D}\}$ are the real and imaginary parts of \vec{D} .

The last term in Eq. (10) is a triple product, but it is not the one we were looking for. Indeed, instead of a polar vector, $\sigma \hat{z}^L$ is a pseudovector that characterizes the rotation direction of the field, i.e. the photon's spin (see Appendix VII A), and moreover, the triple product includes two vectors characterizing the molecule and one vector characterizing the "observer" (or the lab frame), as opposed to three vectors characterizing the molecule in the molecular frame.

To relate the above expression to the transition dipoles in the molecular, rather than the lab frame, one can use the rotation matrix $S(\varrho)$. It transforms the vectors from the molecular to the lab frame via a rotation through the Euler angles $\varrho \equiv (\alpha\beta\gamma)$: $\vec{D}^L = S\vec{D}^M \equiv S\langle \vec{k}^M | \vec{d}^M | 0 \rangle$.

Using Eq. (10), we can also write the current in the lab frame, corresponding to the photoelectron momentum \vec{k}^M in the molecular frame

$$\vec{J}_{\vec{k}^M}^L = S\vec{J}_{\vec{k}^M}^M = \frac{|\tilde{\mathcal{E}}|^2}{2} \left[\left| S\vec{D}^M \cdot \hat{x}^L \right|^2 + \left| S\vec{D}^M \cdot \hat{y}^L \right|^2 + \sigma i S \left(\vec{D}^{M*} \times \vec{D}^M \right) \cdot \hat{z}^L \right] S\vec{k}^M. \quad (11)$$

Note that $\vec{D}^{L*} \times \vec{D}^L = S(\vec{D}^{M*} \times \vec{D}^M)$. This current is not a usual observable. Measuring it would require a coincidence-type setup, where one would detect the lab-frame electron momentum together with the orientation of the molecular frame in the lab frame. We are interested in the standard observable – the net photoelectron current in the lab frame. Therefore, we need to integrate over all directions of the photoelectron momentum and over all molecular orientations:

$$\vec{j}^L(k) = \int d\varrho \int d\Omega_k^M \vec{J}_{\vec{k}^M}^L, \quad (12)$$

where $\int d\Omega_k^M \equiv \int_0^\pi d\theta_k^M \int_0^{2\pi} d\varphi_k^M \sin\theta_k^M$.

Within the standard approach, one performs the integration over all molecular orientations keeping the photoelectron momentum \vec{k} fixed in the lab frame. This yields the standard lab-frame photoelectron angular distributions, from which the b_1 coefficient, which is proportional to the net photoelectron current [see Eq. 5], is extracted. Here, since we are not interested in the full angular distribution of photoelectrons, we can keep the photoelectron momentum \vec{k} fixed in the molecular frame. This simplifies the orientation averaging procedure considerably

because in this case the transition matrix element vector $\vec{D}^M(\vec{k}^M)$ does not have an argument that depends on the molecular orientation ϱ , and can therefore be trivially rotated as $S(\varrho)\vec{D}^M(\vec{k}^M)$. In the other case, when \vec{k} is fixed in the lab frame, the corresponding rotation reads as $S(\varrho)\vec{D}^M(S(\varrho)^{-1}\vec{k}^L)$ and the orientation averaging step requires knowing how \vec{D} changes as a function of \vec{k} , which is usually tackled with a partial wave expansion of the continuum wave function. We do not have such complication here and we can simply use the vector identity Eq. (51) derived in Appendix VII B to obtain

$$\vec{j}^L(k) = \left\{ \frac{1}{6} \int d\Omega_k^M \left[i(\vec{D}^{M*} \times \vec{D}^M) \cdot \vec{k}^M \right] \right\} \left\{ \sigma |\tilde{\mathcal{E}}|^2 \hat{z}^L \right\}. \quad (13)$$

The equivalence between expression (13) and the original expression derived by Ritchie in [10] is demonstrated in Appendix VII E.

Expression (13) is physically transparent. In particular, it shows that the strength of the chiral signal depends on the mutual orientation of the three vectors forming the triple product of vectors defined in the molecular frame.

Let us analyze expression (13):

First, we see that only the interference term in the current [see Eq. (11)] yields a non-vanishing contribution to the net current after orientation averaging. This stresses the importance of the coherence between the two contributions to the ionization amplitude, triggered by the two components of the ionizing field.

Second, we see that the orientation averaging has modified the expression for the vector triple product: it no longer involves any lab-frame quantities, such as $\sigma \hat{z}^L$. Its place is now taken by the molecular frame photoelectron momentum \vec{k}^M , and the molecular term is now a rotationally invariant quantity.

Third, Eq. (13) shows that the net photoelectron current (per molecule) in the lab frame can be factored into a pseudovector field term expressed in the lab frame and a pseudoscalar molecular term expressed in the molecular frame. The pseudovector field term contains the intensity of the field at the transition frequency, and the rotation direction of the circularly polarized field $\sigma \hat{z}^L$. The molecular term is an integral over all states on the photoelectron energy shell $k^2/2$, where, after taking into account all molecular orientations, each state contributes by an amount proportional to the scalar triple product between $\vec{D}^M(\vec{k}^M)$, $\vec{D}^{M*}(\vec{k}^M)$, and \vec{k}^M , or equivalently between $\Re\{\vec{D}^M(\vec{k}^M)\}$, $\Im\{\vec{D}^M(\vec{k}^M)\}$, and \vec{k}^M .

From the field term we can see that $\vec{j}^L(k)$ is directed along \hat{z}^L and takes opposite values for opposite circular polarizations and a given enantiomer. On the other hand, from the relationship between the photoionization dipoles of opposite enantiomers derived in Appendix VII D, $\vec{D}_{\text{left}}^M(\vec{k}^M) = -\vec{D}_{\text{right}}^M(-\vec{k}^M)$, it is simple to see that the molecular term is a pseudoscalar, i.e. it changes sign under a parity inversion, and therefore $\vec{j}^L(k)$ takes opposite values for the opposite enantiomers and a given

circular polarization [see Eqs. (81) and (82) in Appendix VIII]. All these conclusions are in agreement with the symmetry analysis described in Sec. III, with $\vec{j}^{\text{L}}(k)$ playing the role of the generic dichroic and enantio-sensitive vector \vec{v} .

The triple product in the molecular term vanishes if the vectors are coplanar, which is for example the case for the plane wave continuum, where one can use the velocity gauge to show that \vec{D}^{M} is parallel to \vec{k}^{M} . This conclusion corresponds to the well known fact that $|\vec{j}^{\text{L}}(k)|/k \propto |b_1|$ has an overall tendency to decrease as the photoelectron energy increases and the continuum resembles more and more a plane wave. One can also show that $\vec{j}^{\text{L}}(k)$ vanishes in case of a spherically symmetric continuum in agreement with earlier studies [11]. The same conclusion holds for the strong-field PECD [25].

Our derivation and the result provide us with an important insight. The chiral signal stems from the interference between the two non-collinear dipole transitions. If we consider a single final state, such interference leading to a vector product of two transition dipoles would only be possible for a scattering state where the complex transition dipole allows for two non-collinear components: one of them is given by the real part of the transition dipole and the other by its imaginary part.

The generalization of Eq. (13) to arbitrary polarizations of the field is straightforward. We just need to separate the Fourier transform of the field into its real and imaginary parts, and keep in mind that for any complex vector $\vec{u} = \vec{u}_r + i\vec{u}_i$ we have that $\vec{u}^* \times \vec{u} = -2i\vec{u}_i \times \vec{u}_r$. Then we obtain

$$\vec{j}^{\text{L}}(k) = \left\{ \frac{1}{6} \int d\Omega_k^{\text{M}} \left[(\vec{D}^{\text{M}*} \times \vec{D}^{\text{M}}) \cdot \vec{k}^{\text{M}} \right] \right\} \left\{ \tilde{\mathcal{E}}^{\text{L}*} \times \tilde{\mathcal{E}}^{\text{L}} \right\}, \quad (14)$$

which reduces to Eq. (13) for the case of circularly polarized light. Eq. (14) shows that for an arbitrary field configuration the chiral response in PECD is not necessarily along the light propagation direction.

B. Photo-excitation circular dichroism in electronic or vibronic states

Let us now consider chiral response in bound excited states. In this case, and for a single excited state, the excitation dipole is real. Therefore, $\vec{D}^{\text{M}}(\vec{k}^{\text{M}})$ and $\vec{D}^{\text{M}*}(\vec{k}^{\text{M}})$ are parallel, yielding zero enantio-sensitive dipole signal.

On the other hand, if we were to coherently excite two states with non collinear transition dipoles, we would have a non-zero cross product. Then we could obtain a dichroic and enantio-sensitive signal as long as we find a vectorial signal that involves the interference between the two excitations. Unlike in the previous case where this vectorial signal was provided by the photoelectron current, in this case, it is provided by the dynamics of the induced polarization.

The goal of our analysis is to uncover the intimate connection between the PXCD effect discovered in [18] for electronic and vibronic states and the EMWS discovered in [16] for the rotational states. The physics in these two cases is quite different, as the former involves internal and the latter external degrees of freedom, leading to subtle but important details in the mathematical treatment.

Consider the case of two electronic or vibronic states, which can be coherently excited by an ultrashort pulse from the ground state. As before, we will consider a randomly oriented ensemble. After interaction with a field of arbitrary frequency, polarization, and intensity, the first-order amplitudes of the excited states are given by

$$a_j(t) = i \left[\vec{d}_{j,0}^{\text{L}} \cdot \tilde{\mathcal{E}}^{\text{L}}(\omega_{j0}) \right] e^{-i\omega_j t}, \quad j = 1, 2, \quad (15)$$

where $\vec{d}_{j,0}^{\text{L}}$ is now the real-valued transition dipole between the ground and j -th excited state and $\tilde{\mathcal{E}}^{\text{L}}$ is the Fourier transform of the field at the corresponding transition frequency. For an ultrashort pulse with the bandwidth covering both excited states, the expectation value of the dipole will contain an interference term of the form

$$\begin{aligned} \langle \vec{d}^{\text{L}} \rangle_{\chi} &\equiv a_1^* a_2 \vec{d}_{1,2}^{\text{L}} + \text{c.c.} \\ &= [\vec{d}_{0,1}^{\text{L}} \cdot \tilde{\mathcal{E}}^{\text{L}*}(\omega_{1,0})] [\vec{d}_{2,0}^{\text{L}} \cdot \tilde{\mathcal{E}}^{\text{L}}(\omega_{2,0})] \vec{d}_{1,2}^{\text{L}} e^{-i\omega_{2,1} t} + \text{c.c.} \end{aligned} \quad (16)$$

which we have denoted by $\langle \vec{d}^{\text{L}} \rangle_{\chi}$ to indicate that it is the chiral part of the induced polarization.

In contrast to Eq. (10) and PECD, the fact that the Fourier transform of the field is evaluated at two different transition frequencies in the above expression does not allow us to easily use the vector identity $(\vec{a} \cdot \vec{c})(\vec{b} \cdot \vec{d}) - (\vec{a} \cdot \vec{d})(\vec{b} \cdot \vec{c}) = (\vec{a} \times \vec{b}) \cdot (\vec{c} \times \vec{d})$ and directly identify a triple product. The emergence of the triple-product as an enantio-sensitive measure is somewhat subtle: it only appears after averaging over *all* molecular orientations, for a randomly oriented molecular ensemble. With the help of Eq. (52) derived in Appendix VII B, one finds that

$$\begin{aligned} \int d\varrho \langle \vec{d}^{\text{L}} \rangle_{\chi} &= \frac{1}{6} \left[\left(\vec{d}_{0,1}^{\text{M}} \times \vec{d}_{2,0}^{\text{M}} \right) \cdot \vec{d}_{1,2}^{\text{M}} \right] \\ &\times \left[\tilde{\mathcal{E}}^{\text{L}*}(\omega_{1,0}) \times \tilde{\mathcal{E}}^{\text{L}}(\omega_{2,0}) \right] e^{-i\omega_{2,1} t} + \text{c.c.} \quad (17) \end{aligned}$$

The essential features of this expression are similar to those of PECD. The expression again factorizes into a molecular part, a pseudoscalar given by the triple product of molecule-specific transition dipoles, and a field part, a pseudovector given by the vector product of the incident fields. The induced dipole oscillates at the frequency $\omega_{2,1}$ in the direction determined by the cross product between the Fourier transforms of the exciting fields, at the corresponding transition frequencies. The triple product of the transition dipoles is taken in the molecular frame and forms the pseudoscalar that changes

sign for opposite enantiomers (see Appendix VII D). This means that the phase of the oscillations will be determined by the product of the signs resulting from the molecular and field terms. For a fixed polarization and opposite enantiomers, or for a fixed enantiomer and opposite polarizations (see Figs. 2-4), the phase will change by π . That is, the enantio-sensitive and dichroic character of the vectorial observable, in this case the polarization, is encoded in the phase of its oscillations.

In the particular case of a circularly polarized field [see Eq.(6)], we have $\tilde{\mathcal{E}}^{\text{L}}(\omega) = \tilde{\mathcal{E}}(\omega) (\hat{x}^{\text{L}} + \sigma i \hat{y}^{\text{L}}) / \sqrt{2}$ and therefore

$$\int d\varrho \langle \bar{d}^{\text{L}} \rangle_{\chi} = \frac{i\sigma}{6} \left[\left(\bar{d}_{0,1}^{\text{M}} \times \bar{d}_{2,0}^{\text{M}} \right) \cdot \bar{d}_{1,2}^{\text{M}} \right] \times \tilde{\mathcal{E}}^*(\omega_{1,0}) \tilde{\mathcal{E}}(\omega_{2,0}) \hat{z}^{\text{L}} e^{-i\omega_{2,1}t} + \text{c.c.}, \quad (18)$$

which is the PXCD effect discovered in [18].

Equation (17) is the generalization of the PXCD effect to the case of an arbitrary field. It shows that one can obtain the same effect by either using a single broadband elliptically polarized pulse or, for example, by using a sequence of two spectrally narrow (and phase locked) linearly polarized pulses with orthogonal polarizations. If more than two levels are coherently excited, then Eq. (18) should include the sum over all states.

Importantly, the vectorial quantity associated with the chiral response does not have to be collinear with the direction of light propagation, as it happens in the case of a circularly polarized field. It illustrates once again, that the light propagation direction, fundamental for characterizing the chirality of a photon, does not play any role in electric-dipole-based techniques. These techniques do not use the chirality of the photon, but use the polarization vectors of the light to define the lab setup.

An important feature that distinguishes the “light-observer” from the “light-reagent” is the presence of chiral sensitive absorption. Of course, PECD is associated with light absorption, but this absorption is not chiral sensitive, e.g. it is neither enantio-sensitive nor dichroic [18].

Note that the earlier results for the quadratic susceptibility in isotropic chiral media chiral media can also be presented in the vectorial form, originally derived by Giordmaine [36],

$$\vec{P}(\omega_3 = \omega_1 - \omega_2) = \chi^{(2)} [\vec{E}_1(\omega_1) \times \vec{E}_2^*(\omega_2)], \quad (19)$$

where the vectors \vec{P} , \vec{E}_1 , and \vec{E}_2 , are the Fourier components of induced polarizations and incident fields at the respective frequencies, $\chi^{(2)}$ is the molecular pseudoscalar described by the triple product of transition dipoles and a combination of resonance denominators typical for second order instantaneous response and derived in [14, 15] in the context of tree-wave mixing in isotropic chiral media within the electric-dipole approximation.

Finally, the expression for PXCD also allows one to gauge the strength of the chiral response. It maximizes when the three transition dipoles are orthogonal to each

other. In this case, the coherent enantio-sensitive dipole along the lab \hat{z}^{L} axis, normalized to the excitation amplitudes, reaches $d_{1,2}^{\text{M}}/3$. Thus, for orthogonal excitation dipoles, the molecule can convert all of its (ensemble-averaged) initial excitation in the polarization plane of the circularly polarized pump into enantio-sensitive motion orthogonal to this plane, making a highly efficient helix.

C. Chiral response upon rotational excitation: enantio-sensitive microwave spectroscopy

In this section we will use our vectorial formulation to consider two enantio-sensitive schemes in the microwave regime suggested by Patterson et al. [16, 19], and described theoretically in detail by Lehman [20].

Consider first coherent excitation of rotational states and the enantio-sensitive signal discovered by Patterson et al. in [19]. The corresponding rotational wavefunctions are the eigenstates of the asymmetric rigid rotor [37], and are themselves functions of the Euler angles. We no longer deal with *a posteriori* averaging over this degree of freedom. The transition dipoles themselves are already the integrals over the Euler angles $\varrho \equiv (\alpha\beta\gamma)$,

$$\begin{aligned} \bar{d}_{i,j}^{\text{L}} &= \langle J_i \tau_i M_i | \bar{d}^{\text{L}} | J_j \tau_j M_j \rangle \\ &= \left[\int d\varrho \psi_{J_i \tau_i M_i}^*(\varrho) S(\varrho) \psi_{J_j \tau_j M_j}(\varrho) \right] \bar{d}^{\text{M}}, \quad (20) \end{aligned}$$

where \bar{d}^{M} is the permanent dipole moment of the electronic ground state in the molecular frame, $i, j = 1, 2$. The state $|J\tau M\rangle$ is an eigenfunction of the total angular momentum operator \hat{J}^2 and its z -component \hat{J}_z with eigenvalues $J(J+1)$ and M , respectively, and τ is associated with all other quantum numbers pertinent for this state. These transition dipoles are now used for the excitation amplitudes, which are still given by the general expression Eq. (15) and the induced dipole Eq. (17). Each of the dipoles entering Eq. (17) is associated with a distribution of possible M_i, M_j, M_k . This distribution depends on the preparation of the system.

The orientation averaging over the Euler angles is now replaced by summing over the distribution of all possible initial and final M 's

$$\begin{aligned} \sum_{M_0, M_1, M_2} \langle \bar{d}^{\text{L}} \rangle_{\chi} &= \sum_{M_0, M_1, M_2} [\bar{d}_{0,1}^{\text{L}} \cdot \tilde{\mathcal{E}}^{\text{L}*}(\omega_{1,0})] \\ &\times [\bar{d}_{2,0}^{\text{L}} \cdot \tilde{\mathcal{E}}^{\text{L}}(\omega_{2,0})] \bar{d}_{1,2}^{\text{L}} e^{-i\omega_{2,1}t} + \text{c.c.} \quad (21) \end{aligned}$$

When all possible initial and final M 's are equally represented, as is the case for an isotropic sample, the averaging is performed with the help of Eq. (56) which is

derived the Appendix (VII C) and yields

$$\sum_{M_0, M_1, M_2} \langle \bar{d}^{\mathbf{L}} \rangle_{\chi} = \sum_{M_0, M_1, M_2} \frac{1}{6} \left[\left(\bar{d}_{0,1}^{\mathbf{L}} \times \bar{d}_{2,0}^{\mathbf{L}} \right) \cdot \bar{d}_{1,2}^{\mathbf{L}} \right] \times \left[\tilde{\mathcal{E}}^{\mathbf{L}*}(\omega_{1,0}) \times \tilde{\mathcal{E}}^{\mathbf{L}}(\omega_{2,0}) \right] e^{-i\omega_{2,1}t} + \text{c.c.} \quad (22)$$

The main result here is the factorization of induced polarization into the molecular-specific pseudoscalar $\sum_{M_0, M_1, M_2} \frac{1}{6} [(\bar{d}_{0,1}^{\mathbf{L}} \times \bar{d}_{2,0}^{\mathbf{L}}) \cdot \bar{d}_{1,2}^{\mathbf{L}}]$, and the field pseudovector $[\tilde{\mathcal{E}}^{\mathbf{L}*}(\omega_{1,0}) \times \tilde{\mathcal{E}}^{\mathbf{L}}(\omega_{2,0})]$.

Note that before the averaging we had scalar products of dipoles and fields [see Eq. (21)]. The averaging over the distribution of M -states in Eq. (21) plays the same role as averaging over a random classical rotational ensemble in Eq. (17): it leads to rearrangement of terms and to the appearance of a rotationally invariant molecular pseudoscalar. It shows the link to the PXCD effect [18] in the vibronic states.

Eq. (22) is applicable for an arbitrary field configuration. In the work by Patterson et al. [19] two linearly polarized fields, orthogonal to each other, have been used to produce a sum-frequency signal polarized along the direction perpendicular to both fields. Here we derived the complementary difference-frequency signal.

Importantly, our result shows that, if two different pulses are used, the signal in Eqs. (17) and (22) depends on the relative phase between the two pulses. Therefore, the chiral signal will only be observed in a reproducible fashion if the relative phase between the two pulses is stable from shot to shot. Clearly, this is automatically satisfied in case of one-pulse excitation with a circularly polarized field, where the relative phase between the two perpendicular components is fixed at $\pi/2$, as it happens in PXCD.

Now we shall consider an alternative scheme, invented by Patterson et al. and involving a static field [16].

1. Vectorial formulation for the static field case

Consider a molecule with eigenstates $|n\rangle$ in the absence of fields and initially in the state $|0\rangle$. Application of a static field $\vec{E}_S^{\mathbf{L}}$ transforms the zeroth-order eigenstates into

$$|n'\rangle = |n\rangle + \sum_{m \neq n} \frac{\vec{E}_S^{\mathbf{L}} \cdot \bar{d}_{m,n}^{\mathbf{L}}}{E_{m,n}} |m\rangle, \quad (23)$$

where $E_{m,n}$ is the energy difference between the m -th and n -th states, and we assumed that the states are non-degenerate, or that the perturbation does not couple degenerate states with the same energy. If the perturbation of the initial state is much smaller than that of the excited state and we apply an oscillating field resonant with the transition $|0\rangle \rightarrow |n'\rangle$, then the first order (in the oscillating field) amplitude of the state $|n'\rangle$ reads as

$$\begin{aligned} a_{n'} &= i \left[\bar{d}_{n',0}^{\mathbf{L}} \cdot \tilde{\mathcal{E}}^{\mathbf{L}}(\omega_{n',0}) \right] \\ &= i \left\{ \left[\bar{d}_{n,0}^{\mathbf{L}} \cdot \tilde{\mathcal{E}}^{\mathbf{L}}(\omega_{n',0}) \right] \right. \\ &\quad \left. + \sum_{m \neq n} \frac{\vec{E}_S^{\mathbf{L}} \cdot \bar{d}_{n,m}^{\mathbf{L}}}{E_{m,n}} \left[\bar{d}_{m,0}^{\mathbf{L}} \cdot \tilde{\mathcal{E}}^{\mathbf{L}}(\omega_{n',0}) \right] \right\}. \quad (24) \end{aligned}$$

While the DC Stark field is still present, the expected value of the dipole has the form

$$\langle \bar{d}^{\mathbf{L}} \rangle = \bar{d}_{0,0}^{\mathbf{L}} + |a_{n'}|^2 \bar{d}_{n',n'}^{\mathbf{L}} + \left(a_{n'} \bar{d}_{0,n'}^{\mathbf{L}} e^{-i\omega_{n',0}t} + \text{c.c.} \right). \quad (25)$$

Upon orientation averaging, the oscillating term reads as

$$\begin{aligned} &\int d\varrho a_{n'} \bar{d}_{0,n'}^{\mathbf{L}} e^{-i\omega_{n',0}t} + \text{c.c.} \\ &= i \int d\varrho \left[\bar{d}_{n',0}^{\mathbf{L}} \cdot \tilde{\mathcal{E}}^{\mathbf{L}}(\omega_{n',0}) \right] \bar{d}_{0,n'}^{\mathbf{L}} e^{-i\omega_{n',0}t} + \text{c.c.} \\ &= \frac{i}{3} \left[\bar{d}_{n',0}^{\mathbf{M}} \cdot \bar{d}_{0,n'}^{\mathbf{M}} \right] \tilde{\mathcal{E}}^{\mathbf{L}}(\omega_{n',0}) e^{-i\omega_{n',0}t} + \text{c.c.}, \quad (26) \end{aligned}$$

so that the oscillations of the induced polarization follow the field. Note that the orientation averaging for the rotational states would follow accordingly as shown above, by replacing $\int d\varrho$ by a sum over all M 's and keeping the sum on the right hand side of Eq. (26).

On the other hand, if the static field is adiabatically removed so that all of the population in state $|n'\rangle$ is transferred to state $|n\rangle$ we get

$$\langle \bar{d}^{\mathbf{L}} \rangle = \bar{d}_{0,0}^{\mathbf{L}} + |a_{n'}|^2 \bar{d}_{n,n}^{\mathbf{L}} + \left(a_{n'} \bar{d}_{0,n}^{\mathbf{L}} e^{-i\omega_{n,0}t + \phi} + \text{c.c.} \right), \quad (27)$$

where ϕ depends on the details of the turn-off of the static field. The orientation-averaged oscillating term reads as

$$\begin{aligned}
& \int d\varrho a_{n'} \vec{d}_{0,n}^{\text{L}} e^{-i\omega_{n,0}t+\phi} + \text{c.c.} \\
&= i \int d\varrho \left\{ \left[\vec{d}_{n,0}^{\text{L}} \cdot \tilde{\mathcal{E}}^{\text{L}}(\omega_{n',0}) \right] \vec{d}_{0,n}^{\text{L}} + \sum_{m \neq n} \frac{1}{E_{m,n}} \left[\vec{d}_{n,m}^{\text{L}} \cdot \vec{E}_S^{\text{L}} \right] \left[\vec{d}_{m,0}^{\text{L}} \cdot \tilde{\mathcal{E}}^{\text{L}}(\omega_{n',0}) \right] \vec{d}_{0,n}^{\text{L}} \right\} e^{-i\omega_{n,0}t+\phi} + \text{c.c.} \\
&= i \left\{ \frac{1}{3} \left[\vec{d}_{n,0}^{\text{M}} \cdot \vec{d}_{0,n}^{\text{M}} \right] \tilde{\mathcal{E}}^{\text{L}}(\omega_{n',0}) + \frac{1}{6} \sum_{m \neq n} \frac{1}{E_{m,n}} \left[\left(\vec{d}_{n,m}^{\text{M}} \times \vec{d}_{m,0}^{\text{M}} \right) \cdot \vec{d}_{0,n}^{\text{M}} \right] \left[\vec{E}_S^{\text{L}} \times \tilde{\mathcal{E}}^{\text{L}}(\omega_{n',0}) \right] \right\} e^{-i\omega_{n,0}t+\phi} + \text{c.c.} \quad (28)
\end{aligned}$$

In this case we obtain an enantio-sensitive contribution which oscillates in the direction specified by the cross product between the direction of the static field and the polarization of the oscillating field. If, like in the original experiment [16], the static field is along \hat{x} and the oscillating field is along \hat{z} , then the polarization will exhibit oscillations along \hat{y} .

Wave mixing phenomena are usually described on the language of susceptibilities. The quadratic susceptibility $\chi^{(2)}$ is responsible for three wave mixing. However, both PXCD and EMWS can also be described as free induction decay. In fact, PXCD maximizes when the laser field is already turned off (see Fig. 2b in Ref. [18]), supporting that free induction decay after the pulse is at its main origin.

The example of a static field is interesting because it shows that the free induction decay occurring both in PXCD and in EMWS can have very different properties from the ‘‘instantaneous’’ response of an isotropic chiral medium described by the quadratic susceptibility $\chi^{(2)}$. For example, as shown in [15], the chiral quadratic susceptibility vanishes if one of the excitation fields is static, while the second term in Eq. (28) shows that the chiral response associated with the free induction decay is non-zero, be it EMWS or generalized PXCD.

D. Bound-bound + bound-unbound transition

In the previous section we saw how molecular chirality can be read out from the dynamics of the induced polarization. One can also imagine reading out this chirality not by looking at the induced polarization directly but by looking at the photoelectron current induced by a second absorption process as originally proposed in [18]. Here, we will consider the general case in which a pump pulse of arbitrary polarization excites the molecule to a bound superposition and a probe pulse of arbitrary polarization ionizes it after a time delay τ . In this case the photoionization amplitude into the state $|k^{\text{M}}\rangle$ reads as

$$\begin{aligned}
a_{k^{\text{M}}} = & - \left[\vec{d}_{1,0}^{\text{L}} \cdot \tilde{\mathcal{E}}_1^{\text{L}}(\omega_{1,0}) \right] \left[\vec{D}_1^{\text{L}} \cdot \tilde{\mathcal{E}}_2^{\text{L}}(\omega_{k,1}) \right] e^{-i\omega_1\tau} \\
& - \left[\vec{d}_{2,0}^{\text{L}} \cdot \tilde{\mathcal{E}}_1^{\text{L}}(\omega_{2,0}) \right] \left[\vec{D}_2^{\text{L}} \cdot \tilde{\mathcal{E}}_2^{\text{L}}(\omega_{k,2}) \right] e^{-i\omega_2\tau}, \quad (29)
\end{aligned}$$

where $\vec{d}_{i,0}$ is a bound-bound transition dipole between states $|i\rangle$ and $|0\rangle$, \vec{D}_i is a bound-continuum transition dipole between states $|k^{\text{M}}\rangle$ and $|i\rangle$, $\tilde{\mathcal{E}}_i$ is the Fourier transform of the i -th pulse, and we assumed that the pulses do not overlap. Application of Eq. (53) to Eqs. (7), (12), and (29), yields the most general result and it shows that not only the cross terms, as in the generalized PXCD [see Eq. (17)], but also the diagonal terms in $|a_{k^{\text{M}}}|^2$ may contribute to the net photoelectron current

$$\begin{aligned}
\vec{j}^{\text{L}}(k) &= \int d\varrho \int d\Omega_k^{\text{M}} |a_{k^{\text{M}}}(\varrho)|^2 S(\varrho) \vec{k}^{\text{M}} \\
&= \vec{j}_{\text{diag},1}^{\text{L}}(k) + \vec{j}_{\text{diag},2}^{\text{L}}(k) + \vec{j}_{\text{cross}}^{\text{L}}(k). \quad (30)
\end{aligned}$$

The contribution from the diagonal terms is of the form

$$\begin{aligned}
\vec{j}_{\text{diag},i}^{\text{L}}(k) &= \int d\varrho \int d\Omega_k^{\text{M}} \left(\vec{d}_{0,i}^{\text{L}} \cdot \tilde{\mathcal{E}}_1^{\text{L}*} \right) \left(\vec{D}_i^{\text{L}*} \cdot \tilde{\mathcal{E}}_2^{\text{L}*} \right) \left(\vec{d}_{i,0}^{\text{L}} \cdot \tilde{\mathcal{E}}_1^{\text{L}} \right) \left(\vec{D}_i^{\text{L}} \cdot \tilde{\mathcal{E}}_2^{\text{L}} \right) \vec{k}^{\text{L}} \\
&= \frac{1}{15} \Re \left\{ \int d\Omega_k^{\text{M}} \left[\left(\vec{d}_{0,i}^{\text{M}} \times \vec{D}_i^{\text{M}*} \right) \cdot \vec{D}_i^{\text{M}} \right] \left(\vec{d}_{i,0}^{\text{M}} \cdot \vec{k}^{\text{M}} \right) \left[\left(\tilde{\mathcal{E}}_1^{\text{L}*} \times \tilde{\mathcal{E}}_2^{\text{L}*} \right) \cdot \tilde{\mathcal{E}}_2^{\text{L}} \right] \tilde{\mathcal{E}}_1^{\text{L}} \right. \\
&\quad + \int d\Omega_k^{\text{M}} \left[\left(\vec{d}_{0,i}^{\text{M}} \times \vec{D}_i^{\text{M}*} \right) \cdot \vec{k}^{\text{M}} \right] \left(\vec{d}_{i,0}^{\text{M}} \cdot \vec{D}_i^{\text{M}} \right) \left(\tilde{\mathcal{E}}_1^{\text{L}} \cdot \tilde{\mathcal{E}}_2^{\text{L}} \right) \left(\tilde{\mathcal{E}}_1^{\text{L}*} \times \tilde{\mathcal{E}}_2^{\text{L}*} \right) \\
&\quad + \int d\Omega_k^{\text{M}} \left[\left(\vec{d}_{0,i}^{\text{M}} \times \vec{D}_i^{\text{M}} \right) \cdot \vec{k}^{\text{M}} \right] \left(\vec{d}_{i,0}^{\text{M}} \cdot \vec{D}_i^{\text{M}*} \right) \left(\tilde{\mathcal{E}}_1^{\text{L}} \cdot \tilde{\mathcal{E}}_2^{\text{L}*} \right) \left(\tilde{\mathcal{E}}_1^{\text{L}*} \times \tilde{\mathcal{E}}_2^{\text{L}} \right) \left. \right\} \\
&\quad + \frac{1}{30} \left| \vec{d}_{i,0}^{\text{M}} \right|^2 \left| \tilde{\mathcal{E}}_1^{\text{L}} \right|^2 \int d\Omega_k^{\text{M}} \left[\left(\vec{D}_i^{\text{M}*} \times \vec{D}_i^{\text{M}} \right) \cdot \vec{k}^{\text{M}} \right] \left(\tilde{\mathcal{E}}_2^{\text{L}*} \times \tilde{\mathcal{E}}_2^{\text{L}} \right), \quad (31)
\end{aligned}$$

where we only assumed that $\vec{d}_{0,i} = \vec{d}_{i,0}$ is real, which can always be achieved for bound states in the absence of magnetic fields. The fields $\vec{\mathcal{E}}_1$ and $\vec{\mathcal{E}}_2$ are evaluated at the frequencies $\omega_{i,0}$ and $\omega_{k,i}$ respectively. The last term is simply the generalized PECD from the j -th state multiplied by the population in the i -th state induced by the pump and a factor of $1/5$ that comes from the orientation averaging. The terms in curly brackets represent con-

tributions to the current beyond the usual PECD. Each term has selection rules that are evident from its vectorial structure, and will be discussed below after considering the cross terms contribution to the photoelectron current. As usual, the molecular terms are rotationally-invariant molecule-specific pseudoscalars and the field terms are pseudovectors.

The contribution from the cross terms in $|a_{\vec{k}M}|^2$ to the net photoelectron current $\vec{j}^L(k)$ is given in general by

$$\begin{aligned} \vec{j}_{\text{cross}}^L(k) &= \int d\varrho \int d\Omega_k^M \left(\vec{d}_{0,2}^L \cdot \vec{\mathcal{E}}_1^{L*} \right) \left(\vec{D}_2^{L*} \cdot \vec{\mathcal{E}}_2^{L*} \right) \left(\vec{d}_{1,0}^L \cdot \vec{\mathcal{E}}_1^L \right) \left(\vec{D}_1^L \cdot \vec{\mathcal{E}}_2^L \right) \vec{k}^L + \text{c.c.} \\ &= \vec{j}_{\text{noncopl}}^L(k) + \vec{j}_{\text{ellip}}^L(k) + \vec{j}_{\text{lin}}^L(k), \end{aligned} \quad (32)$$

where the fields $\vec{\mathcal{E}}_1^{L*}$, $\vec{\mathcal{E}}_2^{L*}$, $\vec{\mathcal{E}}_1^L$, and $\vec{\mathcal{E}}_2^L$ are evaluated at the frequencies $\omega_{2,0}$, $\omega_{k,2}$, $\omega_{1,0}$, and $\omega_{k,1}$, respectively, and we grouped the 10 terms according to their selection rules for the fields as follows. The first group reads as

$$\begin{aligned} \vec{j}_{\text{noncopl}}^L(k) &= \frac{1}{30} \left\{ \int d\Omega_k^M \left[\left(\vec{d}_{0,2}^M \times \vec{D}_2^{M*} \right) \cdot \vec{d}_{1,0}^M \right] \left(\vec{D}_1^M \cdot \vec{k}^M \right) \left[\left(\vec{\mathcal{E}}_1^{L*} \times \vec{\mathcal{E}}_2^{L*} \right) \cdot \vec{\mathcal{E}}_1^L \right] \vec{\mathcal{E}}_2^L \right. \\ &\quad + \int d\Omega_k^M \left[\left(\vec{d}_{0,2}^M \times \vec{D}_2^{M*} \right) \cdot \vec{D}_1^M \right] \left(\vec{d}_{1,0}^M \cdot \vec{k}^M \right) \left[\left(\vec{\mathcal{E}}_1^{L*} \times \vec{\mathcal{E}}_2^{L*} \right) \cdot \vec{\mathcal{E}}_2^L \right] \vec{\mathcal{E}}_1^L \\ &\quad + \int d\Omega_k^M \left[\left(\vec{d}_{0,2}^M \times \vec{d}_{1,0}^M \right) \cdot \vec{D}_1^M \right] \left(\vec{D}_2^{M*} \cdot \vec{k}^M \right) \left[\left(\vec{\mathcal{E}}_1^{L*} \times \vec{\mathcal{E}}_2^L \right) \cdot \vec{\mathcal{E}}_2^L \right] \vec{\mathcal{E}}_1^L \\ &\quad \left. + \int d\Omega_k^M \left[\left(\vec{D}_2^{M*} \times \vec{d}_{1,0}^M \right) \cdot \vec{D}_1^M \right] \left(\vec{d}_{0,2}^M \cdot \vec{k}^M \right) \left[\left(\vec{\mathcal{E}}_2^{L*} \times \vec{\mathcal{E}}_1^L \right) \cdot \vec{\mathcal{E}}_2^L \right] \vec{\mathcal{E}}_1^L \right\} e^{i\omega_{21}\tau} + \text{c.c.}, \end{aligned} \quad (33)$$

and contains all the terms involving scalar triple products of the field vectors, which means that each of its terms vanishes if the fields involved in its triple product are coplanar. It means that exciting $\vec{j}_{\text{noncopl}}^L(k)$ requires non-coplanar geometry of pump and probe pulses. For fields with the same polarization at the two transition frequencies, that is, $\vec{\mathcal{E}}_1^L(\omega_{1,0}) \parallel \vec{\mathcal{E}}_1^L(\omega_{2,0})$ and $\vec{\mathcal{E}}_2^L(\omega_{k,1}) \parallel \vec{\mathcal{E}}_2^L(\omega_{k,2})$, $\vec{j}_{\text{noncopl}}^L$ vanishes unless the polarization of the pump and the probe are non-coplanar, which means that at least one of the fields must be elliptically polarized. The other field can be either linearly or elliptically polarized, provided its polarization is non-coplanar to that of the first field.

The second group of contributions to \vec{j}_{cross}^L is given by

$$\begin{aligned} \vec{j}_{\text{ellip}}^L(k) &= \frac{1}{30} \left\{ \int d\Omega_k^M \left[\left(\vec{d}_{0,2}^M \times \vec{d}_{1,0}^M \right) \cdot \vec{k}^M \right] \left(\vec{D}_2^{M*} \cdot \vec{D}_1^M \right) \left(\vec{\mathcal{E}}_2^{L*} \cdot \vec{\mathcal{E}}_2^L \right) \left(\vec{\mathcal{E}}_1^{L*} \times \vec{\mathcal{E}}_1^L \right) \right. \\ &\quad \left. + \int d\Omega_k^M \left[\left(\vec{D}_2^{M*} \times \vec{D}_1^M \right) \cdot \vec{k}^M \right] \left(\vec{d}_{0,2}^M \cdot \vec{d}_{1,0}^M \right) \left(\vec{\mathcal{E}}_1^{L*} \cdot \vec{\mathcal{E}}_1^L \right) \left(\vec{\mathcal{E}}_2^{L*} \times \vec{\mathcal{E}}_2^L \right) \right\} e^{i\omega_{21}\tau} + \text{c.c.}, \end{aligned} \quad (34)$$

and contains the two terms involving a cross product between a single field at the two transition frequencies. For fields satisfying $\vec{\mathcal{E}}_1^L(\omega_{1,0}) \parallel \vec{\mathcal{E}}_1^L(\omega_{2,0})$ and $\vec{\mathcal{E}}_2^L(\omega_{k,1}) \parallel \vec{\mathcal{E}}_2^L(\omega_{k,2})$, each term vanishes unless the field in the cross product is elliptically polarized. The field in the scalar product can have any polarization.

The third group of contributions to \vec{j}_{cross}^L reads as

$$\begin{aligned} \vec{j}_{\text{lin}}^L(k) &= \frac{1}{30} \left\{ \int d\Omega_k^M \left[\left(\vec{d}_{0,2}^M \times \vec{D}_2^{M*} \right) \cdot \vec{k}^M \right] \left(\vec{d}_{1,0}^M \cdot \vec{D}_1^M \right) \left(\vec{\mathcal{E}}_1^L \cdot \vec{\mathcal{E}}_2^L \right) \left(\vec{\mathcal{E}}_1^{L*} \times \vec{\mathcal{E}}_2^{L*} \right) \right. \\ &\quad + \int d\Omega_k^M \left[\left(\vec{d}_{0,2}^M \times \vec{D}_1^M \right) \cdot \vec{k}^M \right] \left(\vec{D}_2^{M*} \cdot \vec{d}_{1,0}^M \right) \left(\vec{\mathcal{E}}_2^{L*} \cdot \vec{\mathcal{E}}_1^L \right) \left(\vec{\mathcal{E}}_1^{L*} \times \vec{\mathcal{E}}_2^L \right) \\ &\quad + \int d\Omega_k^M \left[\left(\vec{D}_2^{M*} \times \vec{d}_{1,0}^M \right) \cdot \vec{k}^M \right] \left(\vec{d}_{0,2}^M \cdot \vec{D}_1^M \right) \left(\vec{\mathcal{E}}_1^{L*} \cdot \vec{\mathcal{E}}_2^L \right) \left(\vec{\mathcal{E}}_2^{L*} \times \vec{\mathcal{E}}_1^L \right) \\ &\quad \left. + \int d\Omega_k^M \left[\left(\vec{d}_{1,0}^M \times \vec{D}_1^M \right) \cdot \vec{k}^M \right] \left(\vec{d}_{0,2}^M \cdot \vec{D}_2^{M*} \right) \left(\vec{\mathcal{E}}_1^{L*} \cdot \vec{\mathcal{E}}_2^{L*} \right) \left(\vec{\mathcal{E}}_1^L \times \vec{\mathcal{E}}_2^L \right) \right\} e^{i\omega_{21}\tau} + \text{c.c.}, \end{aligned} \quad (35)$$

and contains the remaining terms. Unlike $\vec{j}_{\text{noncopl}}^L$ and \vec{j}_{ellip}^L , which vanish in the absence of elliptical fields when

$\tilde{\mathcal{E}}_1^L(\omega_{1,0}) \parallel \tilde{\mathcal{E}}_1^L(\omega_{2,0})$ and $\tilde{\mathcal{E}}_2^L(\omega_{k,1}) \parallel \tilde{\mathcal{E}}_2^L(\omega_{k,2})$, \vec{j}_{lin}^L can be non-zero even for purely linear fields provided pump and probe are neither parallel nor orthogonal to each other. Clearly, the selection rules described for $\vec{j}_{\text{noncopl}}^L$, \vec{j}_{lin}^L , and \vec{j}_{ellip}^L are also valid for the first, the second and third, and the last terms of \vec{j}_{diag}^L , respectively.

As a whole, the 10 terms in Eq. (32) correspond to the 10 ways in which the five molecular vectors $\vec{d}_{0,1}^M$, $\vec{d}_{2,0}^M$, \vec{D}_1^M , \vec{D}_2^M , and \vec{k}^M can form a rotation-invariant molecular quantity. Each molecular term is coupled to a field term that corresponds to 1 of the 10 ways that a vector can be formed via scalar and vector products between 4 vectors. Unlike the diagonal terms, the cross terms contribution oscillates with the pump-probe time delay at a frequency corresponding to the energy difference between the two bound states excited by the pump.

If we consider the PXECD setup originally described in [18], where the pump field is circularly polarized like in Eq. (6) and the pump is linearly polarized along \hat{x}^L , then application of the above discussed selection rules and some vector algebra (see Appendix VII F) yields

$$\vec{j}^L(k) = \frac{i\sigma}{60} \tilde{\mathcal{E}}_1^* \tilde{\mathcal{E}}_2^* \tilde{\mathcal{E}}_1 \tilde{\mathcal{E}}_2 \left[\left(\vec{d}_{0,1}^M \times \vec{d}_{2,0}^M \right) \cdot \int d\Omega_k^M \vec{D}_{12}^M(\vec{k}^M) \right] \times \hat{z}^L e^{i\omega_{21}\tau} + \text{c.c.}, \quad (36)$$

$$\vec{D}_{12}^M(\vec{k}^M) = -4 \left(\vec{D}_1^M \cdot \vec{D}_2^{M*} \right) \vec{k}^M + \left(\vec{D}_2^{M*} \cdot \vec{k}^M \right) \vec{D}_1^M + \left(\vec{D}_1^M \cdot \vec{k}^M \right) \vec{D}_2^{M*}, \quad (37)$$

which coincides with the result originally obtained in [18]. Eqs. (30), (31), (32), (33), (34), and (35) are the generalization of PXECD to arbitrary polarizations of the pump and probe pulses.

Interestingly, although the symmetry of a linear pump - linear probe scheme where the two fields are orthogonal to each other does not forbid the emergence of a non-zero net photoelectron current \vec{j}^L (see Fig. 3), Eqs. (30), (31), (32), (33), (34), and (35) show that it vanishes. This symmetry can be traced back to the fact that the phase shift between the pump and the probe is not recorded by the system because the probe step corresponds to the parametric process in terms of non-linear optics diagrams (see Fig. 1 in Ref. [18]), where the initial and final states are the same: it is a superposition of the states prepared by the pump. It highlights the fact that all the effects considered in this section do not require a phase-lock between the pump and probe pulses.

V. CONCLUSIONS

We have presented a unified approach to electric-dipole-based methods of chiral discrimination. The approach is based on a vectorial formulation of the chiral response and provides a common language for under-

standing electric-dipole-based techniques used in different fields, such as photoionization and microwave spectroscopy. All these techniques make use of coherent excitation of several states leading to electronic, vibronic, rotational, or ionization dynamics.

The chiral response in all cases is characterized by a vectorial observable and takes place within a chiral setup. Unlike scalar observables (e.g. total cross sections), vectorial observables (e.g. induced polarization) are able to exploit the chirality of such setups and therefore provide the opportunity to probe the chirality of isotropic molecular samples without relying on the chirality of the light inducing the response. Chiral setups can result from the combination of at least two linearly polarized fields with non-collinear polarizations (and phase-delayed in the case of a single frequency) defining a non-zero pseudovector, and a detector defining a direction parallel or anti-parallel to the field pseudovector. Furthermore, the fields defining the pseudovector need not overlap in time, which allows for pump-probe schemes in the construction of the chiral setup.

We have shown that the generic structure of the vectorial observable is given by the product of the field pseudovector, defined by the configurations of the electric fields exciting or probing chiral dynamics, and a molecular pseudoscalar characterizing the molecular handedness. The projection of the vectorial observable on the *external* direction defined by the detector yields the result of the measurement: a product between the molecular pseudoscalar associated to the molecular handedness, and the chiral setup pseudoscalar defining the handedness of the chiral setup.

The molecular pseudoscalar is given by a rotationally invariant molecule-specific quantity such as a triple product involving three bound-bound transition dipoles, and/or the triple product between photoionization dipoles and the photoelectron momentum integrated over all directions. The strength of the chiral response is determined by the mutual orientation of such vectors in the molecular frame.

The affinity of different electric-dipole-based techniques should help us to identify general mechanisms of chiral response, driven exclusively by the electric component of the electromagnetic field, and their link to molecular chiral structure and dynamics.

VI. ACKNOWLEDGEMENTS

O.S. gratefully acknowledges illuminating discussions with Prof. Aephraim Steinberg, in particular, on the role of the chiral observer in detecting the chiral response in electric-dipole-based methods. We also thank Dr. Emilio Pisanty for his comments on the role of the chiral setup in PECD. The authors are grateful to Prof. Misha Ivanov for stimulating discussions and comments on the manuscript. O.S. thanks Dr. Alex G. Harvey and Dr. Zdeněk Mašín for useful discus-

sions. We thank Dr. Laurent Nahon and Prof. Christiane Koch for their comments on the manuscript and Prof. Amar Vutha for discussions of the EMWS scenarios. A.F.O. gratefully acknowledges the MEDEA project, which has received funding from the European Union's

Horizon 2020 research and innovation programme under the Marie Skłodowska-Curie grant agreement No 641789. O.S. gratefully acknowledges the QUTIF programme of the Deutsche Forschungsgemeinschaft, project Sm 292-5/1.

VII. APPENDIX

A. Beyond the electric-dipole approximation: the magnetic dipole, the helicity of light, and absorption circular dichroism

In order to introduce the reader into some fundamental aspects of the discussion in the main part of the manuscript, we will briefly illustrate the relation between magnetic dipole, helicity of light, and absorption circular dichroism in randomly oriented chiral molecules.

The interaction between the electron in the molecule and the radiation field can be described by the interaction Hamiltonian (see e.g. [38])

$$H'(t) = -\vec{d} \cdot \vec{E}(0, t) - \vec{m} \cdot \vec{B}(0, t) + \dots, \quad (38)$$

where \vec{d} and \vec{m} are the electric and magnetic dipoles,

$$\vec{E}(\vec{r}, t) = -\partial_t \vec{A}(\vec{r}, t) \quad \text{and} \quad \vec{B}(\vec{r}, t) = \vec{\nabla} \times \vec{A}(\vec{r}, t), \quad (39)$$

are the electric and magnetic fields, and $\vec{A}(\vec{r}, t)$ is the vector potential. Other terms of the same order as the magnetic-dipole interaction (e.g. the electric-quadrupole interaction) have been ignored because electric-quadrupole effects vanish in isotropic samples [38]. Consider a plane wave with wave number \vec{k} and frequency ω ,

$$\vec{A}(\vec{r}, t) = \vec{\mathcal{A}} e^{i(\vec{k} \cdot \vec{r} - \omega t)} + \text{c.c.}, \quad (40)$$

where $\vec{\mathcal{A}}$ encodes the polarization, intensity, and phase shift of the wave. For wavelengths λ much greater than the electron orbit, the term $\vec{k} \cdot \vec{r} = 2\pi r/\lambda$ is very small and $e^{i\vec{k} \cdot \vec{r}}$ can be expanded in powers of it. The electric-dipole and magnetic-dipole interactions in Eq. (38) stem from the zeroth and first order terms, respectively, of such expansion. That is, the magnetic-dipole interaction emerges as a consequence of taking into account the spatial structure of the electromagnetic field. Furthermore, absorption circular dichroism, which is linear in the magnetic-dipole interaction, scales as $\vec{k} \cdot \vec{r}$, i.e. as the ratio of the electron orbit size to the wavelength.

Replacing Eq. (40) in Eq. (39) yields

$$\vec{E}(0, t) = \vec{\mathcal{E}} e^{-i\omega t} + \text{c.c.} \quad \text{and} \quad \vec{B}(0, t) = \vec{\mathcal{B}} e^{-i\omega t} + \text{c.c.}, \quad (41)$$

where $\vec{\mathcal{E}} = i\omega \vec{\mathcal{A}}$ and $\vec{\mathcal{B}} = i\vec{k} \times \vec{\mathcal{A}}$. Therefore, the probability that the molecule in the initial state $|i\rangle$ is excited into the upper energy state $|f\rangle$ is given by

$$|\langle f | H'(t) | i \rangle|^2 \propto \left| \left(\vec{d}_{fi} \cdot \vec{\mathcal{E}} + \vec{m}_{fi} \cdot \vec{\mathcal{B}} \right) \right|^2 \quad (42)$$

and contains an interference term of the form

$$\left(\vec{d}_{fi} \cdot \vec{\mathcal{E}} \right)^* \left(\vec{m}_{fi} \cdot \vec{\mathcal{B}} \right) + \text{c.c.} \quad (43)$$

For the case of electronic and/or vibrational transitions, \vec{d}_{fi} and \vec{m}_{fi} are fixed in the molecular frame, while $\vec{\mathcal{E}}$ and $\vec{\mathcal{B}}$ are fixed in the lab frame. If the sample is isotropic we must average over all molecular orientations ϱ (see Appendix VII B), which yields

$$\int d\varrho \left[\vec{d}_{fi}^L(\varrho) \cdot \vec{\mathcal{E}}^L \right]^* \left[\vec{m}_{fi}^L(\varrho) \cdot \vec{\mathcal{B}}^L \right] = \frac{1}{3} \left[\vec{d}_{fi}^M \cdot \vec{m}_{fi}^M \right] \left[\vec{\mathcal{E}}^{L*} \cdot \vec{\mathcal{B}}^L \right], \quad (44)$$

where the superscripts L and M indicate vectors expressed in the lab and molecular frames respectively, and we explicitly indicated the dependence of the molecular frame vectors \vec{d}_{fi} and \vec{m}_{fi} on the molecular orientation ϱ when

they are expressed in the lab frame. The right hand side of Eq. (44) is a scalar that is the product of two pseudoscalars. One of them contains only molecular quantities in the molecular frame, and the other contains only field quantities in the lab frame. Furthermore, the latter is proportional to the helicity of the field, i.e. it is proportional to the projection of the light spin angular momentum on the propagation direction \vec{k} . To see this, we rewrite the field pseudoscalar in terms of the vector potential as

$$\vec{\mathcal{E}}^{\text{L}*} \cdot \vec{\mathcal{B}}^{\text{L}} = i\omega \vec{\mathcal{A}}^{\text{L}*} \cdot \left(i\vec{k}^{\text{L}} \times \vec{\mathcal{A}}^{\text{L}} \right) = i\omega \left(i\vec{\mathcal{A}}^{\text{L}} \times \vec{\mathcal{A}}^{\text{L}*} \right) \cdot \vec{k}^{\text{L}}. \quad (45)$$

The factor $i\vec{\mathcal{A}}^{\text{L}} \times \vec{\mathcal{A}}^{\text{L}*}$ is always real and it is proportional to the photon's spin. For example, for light circularly polarized in the xy plane $\vec{\mathcal{A}}^{\text{L}} = \mathcal{A} (\hat{x}^{\text{L}} + i\sigma\hat{y}^{\text{L}}) / \sqrt{2}$, $\sigma = \pm 1$, and $i\vec{\mathcal{A}}^{\text{L}} \times \vec{\mathcal{A}}^{\text{L}*} = |\mathcal{A}|^2 \sigma \hat{z}^{\text{L}}$, where $\sigma \hat{z}^{\text{L}}$ is the spin of the photon. If we now project on the propagation direction \hat{k}^{L} , we obtain the sign of the helicity of the circularly polarized field

$$\eta = \sigma \hat{z}^{\text{L}} \cdot \hat{k}^{\text{L}} = \pm \sigma, \quad (46)$$

where we used the fact that \hat{k}^{L} can point either in the positive (+) or negative (-) \hat{z}^{L} direction. One must be careful of not confusing σ with η . While η indicates the handedness of the helix formed by the electric (or magnetic) component of the circularly polarized field in space at a fixed time and is a time-even pseudoscalar, σ merely indicates the direction of rotation of the electric field in time at a fixed point in space, is invariant with respect to parity inversion, and is therefore a time-odd scalar.

Importantly for the discussion in the main part of the manuscript, in the electric-dipole approximation the variation of the electromagnetic field in space and along with it the propagation direction of the light, the magnetic field, and the magnetic-dipole interaction, are absent. Therefore, the chiral effects which rely only on the electric-dipole interaction do not rely on the helicity of the light, but on its spin. In other words, they do not rely on the pseudoscalar character of the light encoded in η but instead on its time-odd character encoded in the pseudovector $\sigma \hat{z}$.

B. Classical orientation averaging

Following the formalism in Sec. 4.2 of Ref. [38] we can perform the orientation averaging using tensor notation as follows: first we define the transformation from the molecular frame to the lab frame via

$$v_i = l_{i\alpha} v_\alpha, \quad (47)$$

where we used Einstein's summation convention, latin and greek indices indicate components in the lab and molecular frame respectively, and $l_{i\alpha}$ stands for the direction cosine between the axis $i = x^{\text{L}}, y^{\text{L}}, z^{\text{L}}$ in the lab frame and the axis $\alpha = x^{\text{M}}, y^{\text{M}}, z^{\text{M}}$ in the molecular frame. The direction cosines can be written in terms of the Euler angles $\varrho \equiv (\alpha\beta\gamma)$ (see for example Sec. 2.2 in Ref. [37]). From Sec. 4.2.5 of Ref. [38] (see also [39]) we have that the isotropic orientation averages of products of direction cosines are

$$\int d\varrho l_{i\alpha} l_{j\beta} = \frac{1}{3} \delta_{ij} \delta_{\alpha\beta}, \quad (48)$$

$$\int d\varrho l_{i\alpha} l_{j\beta} l_{k\gamma} = \frac{1}{6} \varepsilon_{ijk} \varepsilon_{\alpha\beta\gamma}, \quad (49)$$

$$\int d\varrho l_{i\alpha} l_{j\beta} l_{k\gamma} l_{l\delta} l_{m\epsilon} = \frac{1}{30} \left\{ \begin{aligned} &\varepsilon_{ijk} \delta_{lm} \varepsilon_{\alpha\beta\gamma} \delta_{\delta\epsilon} + \varepsilon_{ijl} \delta_{km} \varepsilon_{\alpha\beta\delta} \delta_{\gamma\epsilon} + \varepsilon_{ijm} \delta_{kl} \varepsilon_{\alpha\beta\epsilon} \delta_{\gamma\delta} + \varepsilon_{ikl} \delta_{jm} \varepsilon_{\alpha\gamma\delta} \delta_{\beta\epsilon} + \varepsilon_{ikm} \delta_{jl} \varepsilon_{\alpha\gamma\epsilon} \delta_{\beta\delta} \\ &+ \varepsilon_{ilm} \delta_{jk} \varepsilon_{\alpha\delta\epsilon} \delta_{\beta\gamma} + \varepsilon_{jkl} \delta_{im} \varepsilon_{\beta\gamma\delta} \delta_{\alpha\epsilon} + \varepsilon_{jkm} \delta_{il} \varepsilon_{\beta\gamma\epsilon} \delta_{\alpha\delta} + \varepsilon_{jlm} \delta_{ik} \varepsilon_{\beta\delta\epsilon} \delta_{\alpha\gamma} + \varepsilon_{klm} \delta_{ij} \varepsilon_{\gamma\delta\epsilon} \delta_{\alpha\beta} \end{aligned} \right\}, \quad (50)$$

where $\int d\varrho \equiv \frac{1}{8\pi^2} \int_0^{2\pi} d\alpha \int_0^\pi d\beta \int_0^{2\pi} d\gamma \sin\beta$. Straightforward application of formulas (48), (49), and (50) yields the vector identities

$$\int d\varrho (\vec{a}^{\text{L}} \cdot \vec{v}^{\text{L}}) \vec{b}^{\text{L}} = \frac{1}{3} (\vec{a}^{\text{M}} \cdot \vec{b}^{\text{M}}) \vec{v}^{\text{L}}, \quad (51)$$

$$\int d\varrho (\vec{a}^L \cdot \vec{u}^L) (\vec{b}^L \cdot \vec{v}^L) \vec{c}^L = \frac{1}{6} \left[(\vec{a}^M \times \vec{b}^M) \cdot \vec{c}^M \right] (\vec{u}^L \times \vec{v}^L), \quad (52)$$

$$\begin{aligned} & \int d\varrho (\vec{a}^L \cdot \vec{u}^L) (\vec{b}^L \cdot \vec{v}^L) (\vec{c}^L \cdot \vec{w}^L) (\vec{d}^L \cdot \vec{x}^L) \vec{e}^L \\ &= \frac{1}{30} \left\{ \left[(\vec{a}^M \times \vec{b}^M) \cdot \vec{c}^M \right] (\vec{d}^M \cdot \vec{e}^M) [(\vec{u}^L \times \vec{v}^L) \cdot \vec{w}^L] \vec{x}^L + \left[(\vec{a}^M \times \vec{b}^M) \cdot \vec{d}^M \right] (\vec{e}^M \cdot \vec{e}^M) [(\vec{u}^L \times \vec{v}^L) \cdot \vec{x}^L] \vec{w}^L \right. \\ &+ \left[(\vec{a}^M \times \vec{b}^M) \cdot \vec{e}^M \right] (\vec{c}^M \cdot \vec{d}^M) (\vec{u}^L \times \vec{v}^L) (\vec{w}^L \cdot \vec{x}^L) + \left[(\vec{a}^M \times \vec{c}^M) \cdot \vec{d}^M \right] (\vec{b}^M \cdot \vec{e}^M) [(\vec{u}^L \times \vec{w}^L) \cdot \vec{x}^L] \vec{v}^L \\ &+ \left[(\vec{a}^M \times \vec{c}^M) \cdot \vec{e}^M \right] (\vec{b}^M \cdot \vec{d}^M) (\vec{u}^L \times \vec{w}^L) (\vec{v}^L \cdot \vec{x}^L) + \left[(\vec{a}^M \times \vec{d}^M) \cdot \vec{e}^M \right] (\vec{b}^M \cdot \vec{c}^M) (\vec{u}^L \times \vec{x}^L) (\vec{v}^L \cdot \vec{w}^L) \\ &+ \left[(\vec{b}^M \times \vec{c}^M) \cdot \vec{d}^M \right] (\vec{a}^M \cdot \vec{e}^M) [(\vec{v}^L \times \vec{w}^L) \cdot \vec{x}^L] \vec{u}^L + \left[(\vec{b}^M \times \vec{c}^M) \cdot \vec{e}^M \right] (\vec{a}^M \cdot \vec{d}^M) (\vec{v}^L \times \vec{w}^L) (\vec{u}^L \cdot \vec{x}^L) \\ &+ \left. \left[(\vec{b}^M \times \vec{d}^M) \cdot \vec{e}^M \right] (\vec{a}^M \cdot \vec{c}^M) (\vec{v}^L \times \vec{x}^L) (\vec{u}^L \cdot \vec{w}^L) + \left[(\vec{c}^M \times \vec{d}^M) \cdot \vec{e}^M \right] (\vec{a}^M \cdot \vec{b}^M) (\vec{w}^L \times \vec{x}^L) (\vec{u}^L \cdot \vec{v}^L) \right\}, \quad (53) \end{aligned}$$

for arbitrary vectors \vec{a} , \vec{b} , \vec{c} , \vec{d} , \vec{e} , \vec{u} , \vec{v} , \vec{w} , and \vec{x} , respectively.

C. Quantum orientation averaging

In this appendix we will derive the identities

$$\sum_{M_i} \vec{A}_{i,i} = 0, \quad (54)$$

$$\sum_{M_i, M_j} (\vec{A}_{i,j} \cdot \vec{u}) \vec{A}_{j,i} = \frac{1}{3} \sum_{M_i, M_j} (\vec{A}_{i,j} \cdot \vec{A}_{j,i}) \vec{u}, \quad (55)$$

$$\sum_{M_i, M_j, M_k} (\vec{A}_{i,j} \cdot \vec{u}) (\vec{B}_{k,i} \cdot \vec{v}) \vec{C}_{j,k} = \frac{1}{6} \sum_{M_i, M_j, M_k} [(\vec{A}_{i,j} \times \vec{B}_{k,i}) \cdot \vec{C}_{j,k}] (\vec{u} \times \vec{v}), \quad (56)$$

where \hat{A} , \hat{B} , and \hat{C} , are vector operators, \vec{u} and \vec{v} are vectors, and we use the shorthand notation $\vec{A}_{i,j} = \langle \alpha_i J_i M_i | \hat{A} | \alpha_j J_j M_j \rangle$. The state $|\alpha JM\rangle$ is an eigenfunction of the total angular momentum operator \hat{J}^2 and of its z component \hat{J}_z , with eigenvalues $J(J+1)$ and M respectively. The label α indicates all the other quantum numbers required to describe the state.

These equations can be used to carry out the orientation averaging procedure of the expected value of the dipole in Sec. IV C.

The first identity is rather trivial, especially in view of its classical analogue. The second and third identities are the quantum analogues of Eqs. (51) and (52) respectively. The proofs below are valid both for integer and half-integer J .

Before going into the derivation we will briefly remind the reader of a few formulas that we will use throughout our derivation. The spherical components of a vector are defined by (see Eq. 4.10 in [40])

$$v_0 = v_z, \quad v_{\pm} = \mp \frac{1}{\sqrt{2}} (v_x \pm i v_y). \quad (57)$$

From this definition it follows that the dot product, the cross product, and the scalar triple product can be written in terms of their spherical components as follows:

$$\vec{u} \cdot \vec{v} = \sum_{q=-1}^1 (-1)^q u_{-q} v_q, \quad (58)$$

$$(\vec{u} \times \vec{v})_p = (-1)^p i \sum_{q,r=-1}^1 \epsilon_{pqr} u_{-q} v_{-r}, \quad (59)$$

$$(\vec{u} \times \vec{v}) \cdot \vec{w} = -i \sum_{p,q,r=-1}^1 \epsilon_{pqr} u_p v_q w_r, \quad (60)$$

where ϵ_{pqr} is the Levi-Civita tensor for the set $\{-1, 0, 1\}$ such that $\epsilon_{-1,0,1} = \epsilon_{0,1,-1} = \epsilon_{1,-1,0} = 1$ and $\epsilon_{1,0,-1} = \epsilon_{-1,1,0} = \epsilon_{0,-1,1} = -1$, and every other component is equal to zero. Note also that

$$\frac{1}{\sqrt{6}} \begin{pmatrix} 1 & 1 & 1 \\ -1 & 0 & 1 \end{pmatrix} = 1, \quad (61)$$

which along with the symmetry properties of the 3-j symbol for column permutations implies that (see also Sec. 3.2 in [40])

$$\sqrt{6} \begin{pmatrix} 1 & 1 & 1 \\ p & q & r \end{pmatrix} = \epsilon_{pqr}. \quad (62)$$

Another special value of the 3-j symbol is obtained by considering the coupling to zero angular momentum $\langle JM; 00 | JM \rangle = 1$ and the relationship between the Clebsch-Gordan coefficient and the 3-j symbol, which yields

$$\begin{pmatrix} J & 0 & J \\ -M & 0 & M \end{pmatrix} = \frac{(-1)^{J-M}}{\sqrt{2J+1}}. \quad (63)$$

We will also use the formula (see Eq. 7.35 of [40]³)

$$\sum_{\delta \epsilon \phi} (-1)^{d-\delta+e-\epsilon+f-\phi} \begin{pmatrix} d & e & c \\ -\delta & \epsilon & \gamma \end{pmatrix} \begin{pmatrix} e & f & a \\ -\epsilon & \phi & \alpha \end{pmatrix} \begin{pmatrix} f & d & b \\ -\phi & \delta & \beta \end{pmatrix} = \left\{ \begin{matrix} a & b & c \\ d & e & f \end{matrix} \right\} \begin{pmatrix} a & b & c \\ \alpha & \beta & \gamma \end{pmatrix}, \quad (64)$$

where the symbol in curly brackets is a 6-j symbol.

Finally, the Wigner-Eckart theorem for the spherical component q of a rank k tensor reads as (see [40])

$$\langle \alpha JM | T_q^k | \alpha' J' M' \rangle = \langle \alpha J || \mathbf{T}_k || \alpha' J' \rangle (-1)^{J-M} \begin{pmatrix} J & k & J' \\ -M & q & M' \end{pmatrix}. \quad (65)$$

Note that our reduced matrix element contains an extra factor of $\sqrt{2J+1}$ in comparison to that defined in Ref. [40].

Now we begin with the proof of Eq. (54). For this case we will drop the index i on the quantum numbers and let $\alpha \neq \alpha'$. On the left hand side of Eq. (54) the addends read as

$$\vec{A}_{i,i} = \langle \alpha JM | \vec{A} | \alpha' JM \rangle = \langle \alpha J || \mathbf{A} || \alpha' J \rangle (-1)^{J-M} \sum_q \begin{pmatrix} J & 1 & J \\ -M & q & M \end{pmatrix} \hat{e}_q, \quad (66)$$

and the corresponding sum over M yields

$$\begin{aligned} \sum_M (-1)^{J-M} \begin{pmatrix} J & 1 & J \\ -M & q & M \end{pmatrix} &= \sqrt{2J+1} \sum_M \begin{pmatrix} J & 0 & J \\ -M & 0 & M \end{pmatrix} \begin{pmatrix} J & 1 & J \\ -M & q & M \end{pmatrix}, \\ &= \sqrt{2J+1} \sum_{M,M'} \begin{pmatrix} J & 0 & J \\ -M & 0 & M' \end{pmatrix} \begin{pmatrix} J & 1 & J \\ -M & q & M' \end{pmatrix}, \\ &= 0, \end{aligned} \quad (67)$$

³ There is a misprint in the reference.

where we used Eqs. (63), the selection rule $-M + M' = 0$, and the orthogonality of the 3-j symbols. Eqs. (66) and (67) yield the first identity [Eq. (54)].

For the second identity, we can use Eqs. (58) and (65) to write the addends on the left hand side of Eq. (55) as

$$\begin{aligned}
(\vec{A}_{i,j} \cdot \vec{u}) \vec{A}_{j,i} &= \sum_{q,p} (-1)^q \langle \alpha_i J_i M_i | A_{-q} | \alpha_j J_j M_j \rangle u_q \langle \alpha_j J_j M_j | A_p | \alpha_i J_i M_i \rangle \hat{e}_p, \\
&= \sum_{q,p} (-1)^q \langle \alpha_i J_i \| \mathbf{A} \| \alpha_j J_j \rangle (-1)^{J_i - M_i} \begin{pmatrix} J_i & 1 & J_j \\ -M_i & -q & M_j \end{pmatrix} u_q \\
&\quad \times \langle \alpha_j J_j \| \mathbf{A} \| \alpha_i J_i \rangle (-1)^{J_j - M_j} \begin{pmatrix} J_j & 1 & J_i \\ -M_j & p & M_i \end{pmatrix} \hat{e}_p,
\end{aligned} \tag{68}$$

and the corresponding sum over M_i and M_j yields

$$\begin{aligned}
&\sum_{M_i, M_j} (-1)^{J_i - M_i + J_j - M_j} \begin{pmatrix} J_i & 1 & J_j \\ -M_i & -q & M_j \end{pmatrix} \begin{pmatrix} J_j & 1 & J_i \\ -M_j & p & M_i \end{pmatrix} \\
&= \sum_{M_i, M_j} (-1)^{J_i - M_i + J_j - M_j} \begin{pmatrix} J_i & J_j & 1 \\ -M_i & M_j & -q \end{pmatrix} \begin{pmatrix} J_i & J_j & 1 \\ -M_i & M_j & -p \end{pmatrix}, \\
&= (-1)^{-J_i + J_j - q} \sum_{M_i, M_j} \begin{pmatrix} J_i & J_j & 1 \\ -M_i & M_j & -q \end{pmatrix} \begin{pmatrix} J_i & J_j & 1 \\ -M_i & M_j & -p \end{pmatrix}, \\
&= \frac{(-1)^{-J_i + J_j - q}}{\sqrt{3}} \delta_{p,q},
\end{aligned} \tag{69}$$

where we used the symmetry property for column exchange and for negating all M 's of the 3-j symbol, the selection rule for the M 's to write $M_j = M_i + q$ in the exponent of (-1) , and the fact that $J_i + J_j + 1$ is an integer. Then we replaced $(-1)^{2M_i}$ by $(-1)^{2J_i}$, and used the orthogonality relation of 3-j symbols. Replacing Eqs. (68) and (69) on the left hand side of (55) we get

$$\sum_{M_i, M_j} (\vec{A}_{i,j} \cdot \vec{u}) \vec{A}_{j,i} = F \sum_{q,p} u_q \delta_{p,q} \hat{e}_p = F \vec{u},$$

where we defined

$$F \equiv \frac{(-1)^{J_j - J_i}}{\sqrt{3}} |\langle \alpha_i J_i \| \mathbf{A} \| \alpha_j J_j \rangle|^2. \tag{70}$$

Using Eq. (69) with $p = q$, the right hand side of Eq. (55) yields

$$\sum_{M_i, M_j} (\vec{A}_{i,j} \cdot \vec{A}_{j,i}) = \sum_{M_i, M_j, q} (-1)^q \langle \alpha_i J_i M_i | A_{-q} | \alpha_j J_j M_j \rangle \langle \alpha_j J_j M_j | A_q | \alpha_i J_i M_i \rangle = F \sum_q \delta_{q,q} = 3F, \tag{71}$$

which in comparison with Eq. (70) yields the identity (55).

For the third identity, we can use Eqs. (58) and (65) to write the addends on the left hand side of Eq. (56) as

$$\begin{aligned}
&(\vec{A}_{i,j} \cdot \vec{u}) (\vec{B}_{k,i} \cdot \vec{v}) \vec{C}_{j,k} \\
&= \sum_{p,q,r} (-1)^{p+q} \langle \alpha_i J_i M_i | A_{-p} | \alpha_j J_j M_j \rangle u_p \langle \alpha_k J_k M_k | B_{-q} | \alpha_i J_i M_i \rangle v_q \langle \alpha_j J_j M_j | C_r | \alpha_k J_k M_k \rangle \hat{e}_r, \\
&= \sum_{p,q,r} (-1)^{p+q} \langle \alpha_i J_i \| \mathbf{A} \| \alpha_j J_j \rangle (-1)^{J_i - M_i} \begin{pmatrix} J_i & 1 & J_j \\ -M_i & -p & M_j \end{pmatrix} u_p \langle \alpha_k J_k \| \mathbf{B} \| \alpha_i J_i \rangle (-1)^{J_k - M_k} \begin{pmatrix} J_k & 1 & J_i \\ -M_k & -q & M_i \end{pmatrix} v_q \\
&\quad \times \langle \alpha_j J_j \| \mathbf{C} \| \alpha_k J_k \rangle (-1)^{J_j - M_j} \begin{pmatrix} J_j & 1 & J_k \\ -M_j & r & M_k \end{pmatrix} \hat{e}_r,
\end{aligned} \tag{72}$$

and the corresponding sum over all M_i , M_j , and M_k yields

$$\begin{aligned}
& \sum_{M_i, M_j, M_k} (-1)^{J_i - M_i + J_j - M_j + J_k - M_k} \begin{pmatrix} J_i & 1 & J_j \\ -M_i & -p & M_j \end{pmatrix} \begin{pmatrix} J_k & 1 & J_i \\ -M_k & -q & M_i \end{pmatrix} \begin{pmatrix} J_j & 1 & J_k \\ -M_j & r & M_k \end{pmatrix}, \\
& = (-1)^{2J_i + 2J_j + 2J_k + 3} \sum_{M_i, M_j, M_k} (-1)^{J_i - M_i + J_j - M_j + J_k - M_k} \begin{pmatrix} J_i & J_j & 1 \\ -M_i & M_j & -p \end{pmatrix} \begin{pmatrix} J_j & J_k & 1 \\ -M_j & M_k & r \end{pmatrix} \begin{pmatrix} J_k & J_i & 1 \\ -M_k & M_i & -q \end{pmatrix}, \\
& = (-1)^{2J_k + 1} \left\{ \begin{matrix} 1 & 1 & 1 \\ J_i & J_j & J_k \end{matrix} \right\} \begin{pmatrix} 1 & 1 & 1 \\ r & -q & -p \end{pmatrix}, \\
& = \frac{(-1)^{2J_k + 1}}{\sqrt{6}} \left\{ \begin{matrix} 1 & 1 & 1 \\ J_i & J_j & J_k \end{matrix} \right\} \epsilon_{r, -q, -p}, \tag{73}
\end{aligned}$$

where we used the symmetry property for column exchange of the 3-j symbols, Eqs. (62) and (64), and the fact that $J_i + J_j + 1$ is an integer. Replacing Eqs. (72) and (73) in the left hand side of Eq. (56) and using Eq. (59), we get

$$\sum_{M_i, M_j, M_k} \left(\vec{A}_{i,j} \cdot \vec{u} \right) \left(\vec{B}_{k,i} \cdot \vec{v} \right) \vec{C}_{j,k} = G \sum_{p,q,r} (-1)^{p+q} u_p v_q \epsilon_{r, -q, -p} \hat{e}_r = iG \sum_{p,q,r} (-1)^r i \epsilon_{r,p,q} u_{-p} v_{-q} \hat{e}_r = iG (\vec{u} \times \vec{v}), \tag{74}$$

where we defined

$$G \equiv \frac{(-1)^{2J_k + 1}}{\sqrt{6}} \langle \alpha_i J_i \| \mathbf{A} \| \alpha_j J_j \rangle \langle \alpha_k J_k \| \mathbf{B} \| \alpha_i J_i \rangle \langle \alpha_j J_j \| \mathbf{C} \| \alpha_k J_k \rangle \left\{ \begin{matrix} 1 & 1 & 1 \\ J_i & J_j & J_k \end{matrix} \right\}. \tag{75}$$

On the right hand side of the identity [Eq. (56)] we have

$$\begin{aligned}
\left(\vec{A}_{i,j} \times \vec{B}_{k,i} \right) \cdot \vec{C}_{j,k} & = -i \sum_{p,q,r} \epsilon_{pqr} \langle \alpha_i J_i M_i | A_p | \alpha_j J_j M_j \rangle \langle \alpha_k J_k M_k | B_q | \alpha_i J_i M_i \rangle \langle \alpha_j J_j M_j | C_r | \alpha_k J_k M_k \rangle, \\
& = -i \sum_{p,q,r} \epsilon_{pqr} \langle \alpha_i J_i \| \mathbf{A} \| \alpha_j J_j \rangle (-1)^{J_i - M_i} \begin{pmatrix} J_i & 1 & J_j \\ -M_i & p & M_j \end{pmatrix} \\
& \quad \times \langle \alpha_k J_k \| \mathbf{B} \| \alpha_i J_i \rangle (-1)^{J_k - M_k} \begin{pmatrix} J_k & 1 & J_i \\ -M_k & q & M_i \end{pmatrix} \\
& \quad \times \langle \alpha_j J_j \| \mathbf{C} \| \alpha_k J_k \rangle (-1)^{J_j - M_j} \begin{pmatrix} J_j & 1 & J_k \\ -M_j & r & M_k \end{pmatrix}, \tag{76}
\end{aligned}$$

and, inverting the sign of q and p in (73), the corresponding sum over M_i , M_j , and M_k yields

$$\sum_{M_i, M_j, M_k} \left(\vec{A}_{i,j} \times \vec{B}_{k,i} \right) \cdot \vec{C}_{j,k} = -iG \sum_{p,q,r} \epsilon_{pqr} \epsilon_{rqp} = iG \sum_{p,q,r} \epsilon_{pqr}^2 = 6iG, \tag{77}$$

which in comparison with Eq. (74) yields Eq. (56).

D. Transition dipoles for chiral electronic states

Opposite enantiomers R and L are related to each other via an inversion, therefore their bound and scattering electronic wave functions satisfy

$$\psi_R(\vec{r}) = \psi_L(-\vec{r}), \tag{78}$$

$$\psi_{\vec{k}, R}(\vec{r}) = \psi_{-\vec{k}, L}(-\vec{r}). \tag{79}$$

Then, for the transition dipole between two electronic bound states ψ and ψ' we have

$$\vec{d}_R \equiv - \int d\vec{r} \psi_R'^*(\vec{r}) \vec{r} \psi_R(\vec{r}) = \int d\vec{r} \psi_L'^*(-\vec{r}) (-\vec{r}) \psi_L(-\vec{r}) = \int d\vec{r} \psi_L'^*(\vec{r}) \vec{r} \psi_L(\vec{r}) = -\vec{d}_L, \tag{80}$$

as expected. For the transition dipole between the bound state ψ and the scattering state $\psi_{\vec{k}}$ one has to be more careful because of the vector nature of the photoelectron momentum \vec{k} . In this case we have

$$\vec{D}_R(\vec{k}) = - \int d\vec{r} \psi_{\vec{k},R}^* (\vec{r}) \vec{r} \psi_R (\vec{r}) = \int d\vec{r} \psi_{-\vec{k},L}^* (-\vec{r}) (-\vec{r}) \psi_L (-\vec{r}) = \int d\vec{r} \psi_{-\vec{k},L}^* (\vec{r}) \vec{r} \psi_L (\vec{r}) = -\vec{D}_L(-\vec{k}). \quad (81)$$

Using Eq. (81) it is a simple matter to confirm that the molecular term in Eq. (13) does indeed have opposite sign for opposite enantiomers:

$$\begin{aligned} \chi_m^R &= \frac{1}{6} \int d\Omega_k \left[i\vec{D}_R^* (\vec{k}) \times \vec{D}_R (\vec{k}) \right] \cdot \vec{k}, \\ &= \frac{1}{6} \int d\Omega_k \left[i\vec{D}_L^* (-\vec{k}) \times \vec{D}_L (-\vec{k}) \right] \cdot \vec{k}, \\ &= -\frac{1}{6} \int d\Omega_{k'} \left[i\vec{D}_L^* (\vec{k}') \times \vec{D}_L (\vec{k}') \right] \cdot \vec{k}', \\ &= -\chi_m^L, \end{aligned} \quad (82)$$

where we did the change of variable $\vec{k}' = -\vec{k}$ in the third line.

E. Recovering Ritchie's formula

In Ritchie's original derivation [10] the b_1 factor is given by

$$\begin{aligned} b_1 &= \left| \tilde{\mathcal{E}} \right|^2 \frac{(4\pi)^2}{3} \sum_{l_j, m_j, \lambda_j, \mu_j, m_1, \mu_1} \left\langle \psi_i \left| rY_{1\mu_1}^* \left| \psi_{\lambda_j, \mu_j}^{(-)} \right. \right. \right\rangle \left\langle \psi_{l_j, m_j}^{(-)} \left| rY_{1m_1} \left| \psi_i \right. \right. \right\rangle (-1)^{1+m_1+m_j} 3\sqrt{(2l_j+1)(2\lambda_j+1)} \\ &\quad \times \begin{pmatrix} l_j & \lambda_j & 1 \\ 0 & 0 & 0 \end{pmatrix} \begin{pmatrix} 1 & 1 & 1 \\ \sigma & -\sigma & 0 \end{pmatrix} \begin{pmatrix} l_j & \lambda_j & 1 \\ m_j & -\mu_j & -(m_j - \mu_j) \end{pmatrix} \begin{pmatrix} 1 & 1 & 1 \\ m_1 & -\mu_1 & -(m_j - \mu_j) \end{pmatrix}, \end{aligned} \quad (83)$$

where the different prefactor in comparison with Eq. (11) in [10] is because we take $W(\vec{k}^L) = \left| \left\langle \psi_{\vec{k}}^{(-)} \left| \hat{e}_\sigma \left| \psi_i \right. \right. \right\rangle \right|^2$ in agreement with Eqs. (3), (5), (7), and (12). If we define

$$D_q^{l_j m_j} \equiv \sqrt{\frac{4\pi}{3}} \left\langle \psi_{l_j m_j}^{(-)} \left| rY_{1q} \left| \psi_i \right. \right. \right\rangle, \quad (84)$$

use Eq. (59) for the cross product in spherical components, along with the properties $\epsilon_{pqr} = -\epsilon_{-p, -q, -r}$, $(v_q)^* = (-1)^q (\bar{v}^*)_{-q}$, Eq. (62), and the selection rule $m_1 - \mu_1 - m_j + \mu_j = 0$ of the 3-j symbol, we obtain

$$\begin{aligned} &\sum_{m_1, \mu_1} (-1)^{m_1} \left\langle \psi_i \left| rY_{1\mu_1}^* \left| \psi_{\lambda_j, \mu_j}^{(-)} \right. \right. \right\rangle \left\langle \psi_{l_j, m_j}^{(-)} \left| rY_{1m_1} \left| \psi_i \right. \right. \right\rangle \begin{pmatrix} 1 & 1 & 1 \\ m_1 & -\mu_1 & -(m_j - \mu_j) \end{pmatrix}, \\ &= \frac{3}{4\pi} \sum_{m_1, \mu_1} (-1)^{m_1} (D_{\mu_1}^{\lambda_j \mu_j})^* D_{m_1}^{l_j m_j} \begin{pmatrix} 1 & 1 & 1 \\ m_1 & -\mu_1 & -(m_j - \mu_j) \end{pmatrix}, \\ &= \frac{3}{4\pi\sqrt{6}} \sum_{m_1, \mu_1} (-1)^{m_1 - \mu_1} \epsilon_{m_1, -\mu_1, \mu_j - m_j} \left(\vec{D}^{\lambda_j \mu_j *} \right)_{-\mu_1} D_{m_1}^{l_j m_j}, \\ &= -i \frac{1}{4\pi} \sqrt{\frac{3}{2}} (-1)^{m_j - \mu_j} i \sum_{m_1, \mu_1} \epsilon_{m_j - \mu_j, \mu_1, -m_1} \left(\vec{D}^{\lambda_j \mu_j *} \right)_{-\mu_1} D_{m_1}^{l_j m_j}, \\ &= -\frac{1}{4\pi} \sqrt{\frac{3}{2}} \left(i\vec{D}^{\lambda_j \mu_j *} \times \vec{D}^{l_j m_j} \right)_{m_j - \mu_j}. \end{aligned} \quad (85)$$

Then we can use the integral of three spherical harmonics,

$$\int d\Omega_k Y_{l_j, m_j} Y_{\lambda_j, -\mu_j} Y_{1, \mu_j - m_j} = \sqrt{\frac{3(2l_j+1)(2\lambda_j+1)}{4\pi}} \begin{pmatrix} l_j & \lambda_j & 1 \\ 0 & 0 & 0 \end{pmatrix} \begin{pmatrix} l_j & \lambda_j & 1 \\ m_j & -\mu_j & \mu_j - m_j \end{pmatrix}, \quad (86)$$

Eq. (58) for the dot product in spherical components, and the selection rule for the sum of the M 's in the 3-j symbol to obtain

$$\begin{aligned}
& -\frac{1}{4\pi} \sqrt{\frac{3}{2}} \sum_{m_j, \mu_j} (-1)^{m_j} \left(i\vec{D}^{\lambda_j \mu_j^*} \times \vec{D}^{l_j m_j} \right)_{m_j - \mu_j} \sqrt{(2l_j + 1)(2\lambda_j + 1)} \begin{pmatrix} l_j & \lambda_j & 1 \\ 0 & 0 & 0 \end{pmatrix} \begin{pmatrix} l_j & \lambda_j & 1 \\ m_j & -\mu_j & -(m_j - \mu_j) \end{pmatrix} \\
& = -\frac{1}{4\pi} \sqrt{\frac{3}{2}} \sqrt{\frac{4\pi}{3}} \sum_{m_j, \mu_j} (-1)^{m_j} \left(i\vec{D}^{\lambda_j \mu_j^*} \times \vec{D}^{l_j m_j} \right)_{m_j - \mu_j} \int d\Omega_k Y_{l_j, m_j} Y_{\lambda_j, -\mu_j} Y_{1, \mu_j - m_j}, \\
& = -\frac{1}{4\pi} \sqrt{\frac{3}{2}} \sqrt{\frac{4\pi}{3}} \sum_{m_j, \mu_j} (-1)^{m_j - \mu_j} \left(i\vec{D}^{\lambda_j \mu_j^*} \times \vec{D}^{l_j m_j} \right)_{m_j - \mu_j} \int d\Omega_k Y_{\lambda_j, \mu_j}^* Y_{l_j, m_j} Y_{1, \mu_j - m_j}, \\
& = -\frac{1}{4\pi} \sqrt{\frac{3}{2}} \sqrt{\frac{4\pi}{3}} \sum_{m_j, \mu_j, q} (-1)^q \left(i\vec{D}^{\lambda_j \mu_j^*} \times \vec{D}^{l_j m_j} \right)_q \int d\Omega_k Y_{\lambda_j, \mu_j}^* Y_{l_j, m_j} Y_{1, -q}, \\
& = -\frac{1}{4\pi} \sqrt{\frac{3}{2}} \sum_{m_j, \mu_j} \int d\Omega_k Y_{\lambda_j, \mu_j}^* Y_{l_j, m_j} \left[\left(i\vec{D}^{\lambda_j \mu_j^*} \times \vec{D}^{l_j m_j} \right) \cdot \hat{k} \right]. \tag{87}
\end{aligned}$$

Finally, according to Eq. (10) in Ritchie's [10], the scattering wave function is expanded as

$$\psi_k^{(-)}(\vec{r}) = 4\pi \sum_{l_j, m_j} \psi_{l_j m_j}^{(-)}(\vec{r}) Y_{l_j m_j}^*(\hat{k}), \tag{88}$$

and therefore the dipole transition vector reads as

$$\vec{D} = \left\langle \psi_k^{(-)} \left| \vec{d} \right| \psi_i \right\rangle = -4\pi \sum_{l_j, m_j, q} \left\langle \psi_{l_j m_j}^{(-)} \left| \sqrt{\frac{4\pi}{3}} r Y_{1, q} \hat{e}_q \right| \psi_i \right\rangle Y_{l_j m_j}(\hat{k}) = -4\pi \sum_{l_j, m_j} \vec{D}^{l_j m_j} Y_{l_j m_j}(\hat{k}). \tag{89}$$

Then, putting together Eqs. (83), (85), (87), and (89), and using Eqs. (13) and (62), we obtain

$$\begin{aligned}
b_1 & = |\tilde{\mathcal{E}}|^2 (4\pi)^2 \begin{pmatrix} 1 & 1 & 1 \\ \sigma & -\sigma & 0 \end{pmatrix} \frac{1}{4\pi} \sqrt{\frac{3}{2}} \sum_{l_j, m_j, \lambda_j, \mu_j} \int d\Omega_k Y_{\lambda_j, \mu_j}^* Y_{l_j, m_j} \left[\left(i\vec{D}^{\lambda_j \mu_j^*} \times \vec{D}^{l_j m_j} \right) \cdot \hat{k} \right] \\
& = \frac{1}{8\pi k} \sigma |\tilde{\mathcal{E}}|^2 \int d\Omega_k \left[\left(i\vec{D}^* \times \vec{D} \right) \cdot \vec{k} \right] \\
& = \frac{3}{4\pi} \frac{j_z^L}{k}, \tag{90}
\end{aligned}$$

which shows that Ritchie's expression for b_1 is equivalent to the one derived here.

F. Circular pump + linear probe

In this appendix we derive Eqs. (36) and (37) from Eqs. (30)-(35) for the case when the pump is circularly polarized according to Eq. (6) and the probe is linearly polarized along \hat{x}^L . From the selection rules already discussed in Sec. IVD we immediately see that the first and last terms in \vec{j}_{diag}^L [Eq. (31)], $\vec{j}_{\text{noncopl}}^L$ [Eq. (33)] and the second term in \vec{j}_{ellip}^L [Eq. (34)] vanish. Furthermore, the remaining terms in \vec{j}_{diag}^L [Eq. (31)] are purely imaginary and also vanish, which only leaves \vec{j}_{lin}^L [Eq. (35)] and the first term in \vec{j}_{ellip}^L [Eq. (34)]. Replacing the field terms in Eq. (34) we obtain

$$\vec{j}_{\text{ellip}}^L(k) = \frac{i\sigma\tilde{\mathcal{E}}}{30} \left(\vec{d}_{0,2}^M \times \vec{d}_{1,0}^M \right) \cdot \int d\Omega_k^M \left[\left(\vec{D}_2^{M*} \cdot \vec{D}_1^M \right) \vec{k}^M \right] e^{i\omega_{21}\tau \hat{z}^L} + \text{c.c.}, \tag{91}$$

whereas for Eq. (35) we obtain

$$\begin{aligned}
\vec{j}_{\text{lin}}^L(k) & = \frac{i\sigma\tilde{\mathcal{E}}}{60} \left\{ \int d\Omega_k^M \left[\left(\vec{d}_{0,2}^M \times \vec{D}_2^{M*} \right) \cdot \vec{k}^M \right] \left(\vec{d}_{1,0}^M \cdot \vec{D}_1^M \right) + \int d\Omega_k^M \left[\left(\vec{d}_{0,2}^M \times \vec{D}_1^M \right) \cdot \vec{k}^M \right] \left(\vec{D}_2^{M*} \cdot \vec{d}_{1,0}^M \right) \right. \\
& \quad \left. + \int d\Omega_k^M \left[\left(\vec{D}_2^{M*} \times \vec{d}_{1,0}^M \right) \cdot \vec{k}^M \right] \left(\vec{d}_{0,2}^M \cdot \vec{D}_1^M \right) - \int d\Omega_k^M \left[\left(\vec{d}_{1,0}^M \times \vec{D}_1^M \right) \cdot \vec{k}^M \right] \left(\vec{d}_{0,2}^M \cdot \vec{D}_2^{M*} \right) \right\} e^{i\omega_{21}\tau \hat{z}^L} + \text{c.c.} \tag{92}
\end{aligned}$$

where $\tilde{\mathcal{E}} = \tilde{\mathcal{E}}_1^* \tilde{\mathcal{E}}_2^* \tilde{\mathcal{E}}_1 \tilde{\mathcal{E}}_2$. Now, in order to extract $\bar{d}_{0,2}^M$ and $\bar{d}_{1,0}^M$ from the integrals we begin by reordering the expression as

$$\begin{aligned} \bar{j}_{\text{lin}}^L(k) = & \frac{i\sigma\tilde{\mathcal{E}}}{60} \left\{ \int d\Omega_k^M \left[\left(\bar{D}_2^{M*} \times \bar{k}^M \right) \cdot \bar{d}_{0,2}^M \right] \left(\bar{D}_1^M \cdot \bar{d}_{1,0}^M \right) + \int d\Omega_k^M \left[\left(\bar{D}_1^M \times \bar{k}^M \right) \cdot \bar{d}_{0,2}^M \right] \left(\bar{D}_2^{M*} \cdot \bar{d}_{1,0}^M \right) \right. \\ & \left. - \int d\Omega_k^M \left[\left(\bar{D}_2^{M*} \times \bar{k}^M \right) \cdot \bar{d}_{1,0}^M \right] \left(\bar{D}_1^M \cdot \bar{d}_{0,2}^M \right) - \int d\Omega_k^M \left[\left(\bar{D}_1^M \times \bar{k}^M \right) \cdot \bar{d}_{1,0}^M \right] \left(\bar{D}_2^{M*} \cdot \bar{d}_{0,2}^M \right) \right\} e^{i\omega_{21}\tau} \hat{z}^L + \text{c.c.}, \quad (93) \end{aligned}$$

to apply the vector identity $(\vec{a} \cdot \vec{c})(\vec{b} \cdot \vec{d}) - (\vec{a} \cdot \vec{d})(\vec{b} \cdot \vec{c}) = (\vec{a} \times \vec{b}) \cdot (\vec{c} \times \vec{d})$, which yields

$$\bar{j}_{\text{lin}}^L(k) = \frac{i\sigma\tilde{\mathcal{E}}}{60} \left(\bar{d}_{0,2}^M \times \bar{d}_{1,0}^M \right) \cdot \left\{ \int d\Omega_k^M \left[\left(\bar{D}_2^{M*} \times \bar{k}^M \right) \times \bar{D}_1^M \right] + \int d\Omega_k^M \left[\left(\bar{D}_1^M \times \bar{k}^M \right) \times \bar{D}_2^{M*} \right] \right\} e^{i\omega_{21}\tau} \hat{z}^L + \text{c.c.} \quad (94)$$

Now we use the vector identity $(\vec{a} \times \vec{b}) \times \vec{c} = (\vec{a} \cdot \vec{c})\vec{b} - (\vec{b} \cdot \vec{c})\vec{a}$ to get

$$\bar{j}_{\text{lin}}^L(k) = \frac{i\sigma\tilde{\mathcal{E}}}{60} \left(\bar{d}_{0,2}^M \times \bar{d}_{1,0}^M \right) \cdot \int d\Omega_k^M \left\{ 2 \left(\bar{D}_2^{M*} \cdot \bar{D}_1^M \right) \bar{k}^M - \left(\bar{k}^M \cdot \bar{D}_1^M \right) \bar{D}_2^{M*} - \left(\bar{k}^M \cdot \bar{D}_2^{M*} \right) \bar{D}_1^M \right\} e^{i\omega_{21}\tau} \hat{z}^L + \text{c.c.} \quad (95)$$

Adding Eqs. (91) and (95) yields Eqs. (36) and (37).

-
- [1] U. Boesl and A. Kartouzian, *Annual Review of Analytical Chemistry* **9**, 343 (2016).
- [2] M. H. Janssen and I. Powis, *Spectroscopy* **15**, 16 (2017).
- [3] G.-Q. Lin, Q.-D. You, and J.-F. Cheng, *Chiral Drugs: chemistry and biological action* (Wiley, Hoboken, New Jersey, 2011).
- [4] R. Cireasa, A. E. Boguslavskiy, B. Pons, M. C. H. Wong, D. Descamps, S. Petit, H. Ruf, N. Thiré, A. Ferré, J. Suarez, J. Higué, B. E. Schmidt, A. F. Alharbi, F. Légaré, V. Blanchet, B. Fabre, S. Patchkovskii, O. Smirnova, Y. Mairesse, and V. R. Bhardwaj, *Nature Physics* **11**, 654 (2015).
- [5] O. Smirnova, Y. Mairesse, and S. Patchkovskii, *Journal of Physics B: Atomic, Molecular and Optical Physics* **48**, 234005 (2015).
- [6] D. Ayuso, P. Decleva, S. Patchkovskii, and O. Smirnova, *Journal of Physics B: Atomic, Molecular and Optical Physics* **51**, 06LT01 (2018).
- [7] D. Ayuso, P. Decleva, S. Patchkovskii, and O. Smirnova, *Journal of Physics B: Atomic, Molecular and Optical Physics* **51**, 124002 (2018).
- [8] Y. Zhang, J. R. Rouxel, J. Autschbach, N. Govind, and S. Mukamel, *Chem. Sci.* **8**, 5969 (2017).
- [9] J. R. Rouxel, M. Kowalewski, and S. Mukamel, *Structural Dynamics* **4**, 044006 (2017).
- [10] B. Ritchie, *Physical Review A* **13**, 1411 (1976).
- [11] N. Cherepkov, *Chemical Physics Letters* **87**, 344 (1982).
- [12] I. Powis, *The Journal of Chemical Physics* **112**, 301 (2000).
- [13] N. Böwering, T. Lischke, B. Schmidtke, N. Müller, T. Khalil, and U. Heinzmann, *Physical Review Letters* **86**, 1187 (2001).
- [14] P. Fischer, D. S. Wiersma, R. Righini, B. Champagne, and A. D. Buckingham, *Physical Review Letters* **85**, 4253 (2000).
- [15] P. Fischer, A. D. Buckingham, and A. C. Albrecht, *Phys. Rev. A* **64**, 053816 (2001).
- [16] D. Patterson, M. Schnell, and J. M. Doyle, *Nature* **497**, 475 (2013).
- [17] A. Yachmenev and S. N. Yurchenko, *Phys. Rev. Lett.* **117**, 033001 (2016).
- [18] S. Beaulieu, A. Comby, D. Descamps, B. Fabre, G. A. Garcia, R. Géneaux, A. G. Harvey, F. Légaré, Z. Masín, L. Nahon, A. F. Ordonez, S. Petit, B. Pons, Y. Mairesse, O. Smirnova, and V. Blanchet, *Nature Physics* **14**, 484 (2018).
- [19] D. Patterson and J. M. Doyle, *Physical Review Letters* **111**, 023008 (2013).
- [20] K. K. Lehman, *Frontiers and Advances in Molecular Spectroscopy, Chapter 21: Theory of Enantiomer-Specific Microwave Spectroscopy*, 1st ed., edited by J. Laane (Elsevier, 2018).
- [21] C. Lux, M. Wollenhaupt, T. Bolze, Q. Liang, J. Koehler, C. Sarpe, and T. Baumert, *Angewandte Chemie International Edition* **51**, 5001 (2012).
- [22] C. S. Lehmann, R. B. Ram, I. Powis, and M. H. M. Janssen, *The Journal of Chemical Physics* **139**, 234307 (2013).
- [23] C. Lux, M. Wollenhaupt, C. Sarpe, and T. Baumert, *ChemPhysChem* **16**, 115 (2015).
- [24] S. Beaulieu, A. Ferre, R. Geneaux, R. Canonge, D. Descamps, B. Fabre, N. Fedorov, F. Legare, S. Petit, T. Ruchon, V. Blanchet, Y. Mairesse, and B. Pons, *New Journal of Physics* **18**, 102002 (2016).
- [25] I. Dreissigacker and M. Lein, *Phys. Rev. A* **89**, 053406 (2014).
- [26] V. Ulrich, S. Barth, S. Joshi, U. Hergenhahn, E. Mikajlo, C. J. Harding, and I. Powis, *The Journal of Physical Chemistry A* **112**, 3544 (2008).
- [27] L. Nahon, G. A. Garcia, C. J. Harding, E. Mikajlo, and I. Powis, *The Journal of Chemical Physics* **125**, 114309 (2006).
- [28] L. Nahon, G. A. Garcia, and I. Powis, *Journal of Electron Spectroscopy and Related Phenomena Gas phase spectroscopic and dynamical studies at Free-Electron Lasers and other short wavelength sources*, **204**, Part B, 322

- (2015).
- [29] L. Nahon, L. Nag, G. A. Garcia, I. Myrgorodska, U. Meierhenrich, S. Beaulieu, V. Wanie, V. Blanchet, R. Geneaux, and I. Powis, *Phys. Chem. Chem. Phys.* **18**, 12696 (2016).
- [30] M. M. R. Fanoood, N. B. Ram, C. S. Lehmann, I. Powis, and M. H. M. Janssen, *Nature Communications* **6**, 7511 (2015).
- [31] M. M. R. Fanoood, M. H. M. Janssen, and I. Powis, *The Journal of Chemical Physics* **145**, 124320 (2016).
- [32] R. E. Goetz, T. A. Isaev, B. Nikoobakht, R. Berger, and C. P. Koch, *The Journal of Chemical Physics* **146**, 024306 (2017).
- [33] N. L. Manakov, S. I. Marmo, and A. V. Meremianin, *Journal of Physics B: Atomic, Molecular and Optical Physics* **29**, 2711 (1996).
- [34] M. Y. Agre, *Optics and spectroscopy* **101**, 356 (2006).
- [35] I. Tinoco, *The Journal of Chemical Physics* **62**, 1006 (1975), <https://doi.org/10.1063/1.430566>.
- [36] J. A. Giordmaine, *Physical Review* **138**, A1599 (1965).
- [37] H. W. Kroto, *Molecular Rotation Spectra*, Dover Books on Physics and Chemistry (Dover Publications, 1992).
- [38] L. D. Barron, *Molecular light scattering and optical activity*, 2nd ed. (Cambridge University Press, Cambridge, UK ; New York, 2004).
- [39] D. L. Andrews and T. Thirunamachandran, *The Journal of Chemical Physics* **67**, 5026 (1977).
- [40] D. M. Brink and G. R. Satchler, *Angular Momentum*, 2nd ed. (Clarendon Press, Oxford, 1968).

Propensity rules in photoelectron circular dichroism in chiral molecules II: General picture

Andres F. Ordonez^{1,2,*} and Olga Smirnova^{1,2,†}

¹*Max-Born-Institut, Berlin, Germany*

²*Technische Universität Berlin, Berlin, Germany*

This is the accepted version of an article published in Physical Review A 99, 043417 (2019). The published version is available online at <http://dx.doi.org/10.1103/PhysRevA.99.043417>

Photoelectron circular dichroism results from one-photon ionization of chiral molecules by circularly polarized light and manifests itself in forward-backward asymmetry of electron emission in the direction orthogonal to the light polarization plane. To expose the physical mechanism responsible for asymmetric electron ejection, we first establish a rigorous relation between the responses of unaligned and partially or perfectly aligned molecules. Next, we identify a propensity field, which is responsible for the chiral response in the electric-dipole approximation, i.e. a chiral response without magnetic interactions. We find that this propensity field, up to notations, is equivalent to the Berry curvature in a two-band solid. The propensity field directly encodes optical propensity rules, extending our conclusions regarding the role of propensity rules in defining the sign of forward-backward asymmetry from the specific case of chiral hydrogen [Phys. Rev. A 99, 043416 (2019)] to generic chiral systems. Optical propensity rules underlie the chiral response in photoelectron circular dichroism. The enantiosensitive flux of the propensity field through the sphere in momentum space determines the forward-backward asymmetry in unaligned molecules and suggests a geometrical origin of the chiral response. This flux has opposite sign for opposite enantiomers and vanishes for achiral molecules.

I. INTRODUCTION

Photoelectron circular dichroism (PECD) [1–3] is an extremely efficient method of chiral discrimination, due to the very high value of circular dichroism, several orders of magnitude higher than in conventional optical methods, such as absorption circular dichroism or optical rotation (see e.g. [4]). PECD is intimately related [5] to other phenomena where a chiral response arises already in the electric-dipole approximation, such as methods based on exciting rotational [6–9], electronic, and vibronic [10, 11] chiral dynamics without relying on relatively weak interactions with magnetic fields. PECD is not only a promising technique of chiral discrimination but also a powerful tool for studying ultrafast chiral dynamics in molecules as documented in several experimental [3, 12–38] and theoretical [1, 2, 5, 39–51] studies. PECD was recently extended to the multiphoton [52–61], pump-probe [62] and strong-field ionization regimes [63, 64].

In this and in the companion paper [65] we focus on physical mechanisms underlying the chiral response in one-photon ionization at the level of electrons. While the physical mechanism itself is the same for perfectly aligned, partially aligned, and randomly oriented ensembles of chiral molecules, the chiral response will have a different magnitude and may have a different sign in each case (see e.g. [49]). In our companion paper [65] we have considered an example of chiral electronic states in hydrogen to identify physical mechanisms relevant for PECD

in aligned molecules. Here we will expose the connection between the chiral response of aligned and unaligned molecular ensembles, and show that since handedness is a rotationally invariant property, the basic structure of the molecular pseudoscalar remains the same in aligned and unaligned ensembles, providing a robust link between photoionization chiral observables in the two cases.

The rotationally invariant molecular pseudoscalar underlying the chiral response of randomly oriented ensembles [5] is a scalar triple product of three vectors: the photoionization dipole, its complex conjugate, and the photoelectron momentum. We find that the vector product of the photoionization dipole and its complex conjugate counterpart describes a propensity field in momentum space which underlies the chiral response in photoionization, and up to notations coincides with the Berry curvature in a two-band solid [66]. Similarly to the latter, this field explicitly reflects absorption circular dichroism resolved on photoelectron momentum and implicitly encodes optical propensity rules. Its flux through a sphere in momentum space determines the chiral response in PECD, and the effect of each of its components on the chiral response can be either enhanced or suppressed via molecular alignment. This way, we extend the ideas presented in our companion paper for chiral states in hydrogen [65] to the general case of arbitrary chiral molecules. The remarkable appearance of a flux of a Berry-curvature-like field in the description of PECD points to the role of geometry in the emergence of the chiral response.

This paper is organized as follows: In Sec. II we introduce the propensity field and the chiral flux and discuss the interplay between dynamical and geometrical aspects

* ordonez@mbi-berlin.de

† smirnova@mbi-berlin.de

of the chiral response. In Sec. III we establish the connection between the chiral response in unaligned and aligned molecules. In Sec. IV we analyze the chiral response in aligned molecules in terms of the propensity field and the chiral flux density. Sec. V concludes the paper.

II. THE PHYSICAL MEANING OF THE TRIPLE PRODUCT IN PECD AND THE PROPENSITY FIELD.

Recently, we derived a simple and general expression for PECD in unaligned (i.e. randomly oriented) molecular ensembles [5]. In this section we will begin by inspecting this expression further in order to gain more insight into its meaning.

The expression for the orientation-averaged net photoelectron current density in the lab frame resulting from photoionization of a randomly-oriented molecular ensemble via an electric field circularly polarized in the $x^L y^L$ plane is [see Eq. (13) in Ref. [5]]

$$\vec{j}^L(k) = \left\{ \frac{1}{6} \int d\Omega_k^M [i(\vec{D}^{M*} \times \vec{D}^M) \cdot \vec{k}^M] \right\} \left\{ \vec{\tilde{\mathcal{E}}}_x^{L*} \times \vec{\tilde{\mathcal{E}}}_y^L \right\}, \quad (1)$$

where the L and M superscripts indicate vectors expressed in the lab and molecular frames, respectively. $\vec{D} \equiv \langle \vec{k}^M | \hat{d} | g \rangle$ is the transition dipole between the ground state and the scattering state with photoelectron momentum \vec{k}^M . $\vec{\tilde{\mathcal{E}}} = \vec{\mathcal{E}}(\hat{x}^L + i\sigma\hat{y}^L)/\sqrt{2} \equiv (\vec{\tilde{\mathcal{E}}}_x^L + i\vec{\tilde{\mathcal{E}}}_y^L)/\sqrt{2}$, is the Fourier transform of the field at the transition frequency and $\sigma = \pm 1$ defines the rotation direction of the field.

Equation (1) shows that $\vec{j}^L(k)$ can be factored into a molecule-specific rotationally-invariant pseudoscalar and a field-specific pseudovector. As shown in [5], the term $i\vec{D}^{M*} \times \vec{D}^M$ has its origins in the interference between the transitions caused by the \hat{x}^L and \hat{y}^L components of the field, and it is the only “part” of \vec{D}^M that remains after averaging over all possible molecular orientations. It is instructive to rewrite this term as

$$i(\vec{D}^{M*} \times \vec{D}^M) = \frac{1}{2} \left(\begin{array}{c} \left| \vec{D}^M \cdot (\hat{y}^M + i\hat{z}^M) \right|^2 - \left| \vec{D}^M \cdot (\hat{y}^M - i\hat{z}^M) \right|^2 \\ \left| \vec{D}^M \cdot (\hat{z}^M + i\hat{x}^M) \right|^2 - \left| \vec{D}^M \cdot (\hat{z}^M - i\hat{x}^M) \right|^2 \\ \left| \vec{D}^M \cdot (\hat{x}^M + i\hat{y}^M) \right|^2 - \left| \vec{D}^M \cdot (\hat{x}^M - i\hat{y}^M) \right|^2 \end{array} \right), \quad (2)$$

which shows that each component of $i(\vec{D}^{M*} \times \vec{D}^M)$ corresponds to the interference term that would arise if the molecule (with fixed orientation) interacts with light circularly polarized in the plane perpendicular to each molecular axis.

Equation (2) leads to several important conclusions: First, the i -th component of $i(\vec{D}^{M*} \times \vec{D}^M)$ is simply

the “local” (i.e. \vec{k}^M -resolved) absorption circular dichroism for light circularly polarized with respect to the i -th molecular axis (for a fixed molecular orientation). Second, the i -th component of $i(\vec{D}^{M*} \times \vec{D}^M)$ is non-zero only in the absence of rotational symmetry around the i -th axis. Third, the \vec{k}^M -dependent field $i(\vec{D}^{M*} \times \vec{D}^M)$ encodes photoionization propensity rules and is analogous to the Berry curvature in two-band solids as we will demonstrate below. For comparison purposes, until the end of this section we will write \hbar , and the mass m and charge of the electron $-e$ explicitly.

Equation (1) was derived in the length gauge. Since for any two stationary states of the Hamiltonian we have that $\vec{p}_{fi} \equiv i m \omega_{fi} \vec{r}_{fi}$, then the photoionization dipole defined above can be rewritten as

$$\vec{D}^M(\vec{k}^M) \equiv \frac{i\hbar e}{m(E(k) - E_g)} \vec{P}^M(\vec{k}^M), \quad (3)$$

where $E(k) - E_g$ is the energy “gap” between the ground state of the molecule and the energy of photoelectron and $\vec{P} \equiv \langle \vec{k}^M | \hat{p} | g \rangle$ is the transition dipole between the ground state and the scattering state with photoelectron momentum $\hbar\vec{k}^M$, now defined in the velocity gauge. This simple relationship will allow us to uncover another interesting property of the vector product discussed above.

Let us formally introduce a propensity field $\vec{B}^M(\vec{k}^M)$:

$$\vec{B}^M(\vec{k}^M) \equiv -\frac{1}{e^2} i \left[\vec{D}^{M*}(\vec{k}^M) \times \vec{D}^M(\vec{k}^M) \right] \quad (4)$$

$$\equiv i \frac{\hbar^2}{m^2} \frac{\left[\vec{P}^M(\vec{k}^M) \times \vec{P}^{M*}(\vec{k}^M) \right]}{(E(k) - E_g)^2}. \quad (5)$$

Note that, up to notation, $\vec{B}^M(\vec{k}^M)$ is equivalent to the Berry curvature $\Omega(\vec{k})$ of the upper band in a two-band solid (see e.g. [66])

$$\vec{\Omega}(\vec{k}) = i \frac{\hbar^2}{m^2} \frac{\left[\vec{P}^{ci}(\vec{k}) \times \vec{P}^{ic}(\vec{k}) \right]}{(E_c(\vec{k}) - E_i(\vec{k}))^2}, \quad (6)$$

where $\vec{P}^{ci}(\vec{k}) = \vec{P}^{ic*}(\vec{k})$ is the transition dipole matrix element between the two bands, and $E_i(\vec{k})$ and $E_c(\vec{k})$ are the lower and upper band dispersions, respectively.

The enantiosensitive net current $\vec{j}^L(k) = j_z^L \hat{z}^L$ can be understood as arising due to an anisotropic enantiosensitive conductivity $\sigma_{z,xy}^X(k)$:

$$\vec{j}^L(k) = \sigma_{z,xy}^X(k) \left\{ \vec{\tilde{\mathcal{E}}}_x^{L*} \times \vec{\tilde{\mathcal{E}}}_y^L \right\}. \quad (7)$$

The conductivity $\sigma_{z,xy}^X(k)$ is proportional to the flux of the propensity field through the surface of the sphere of radius k in momentum space [cf. Eqs. (1) and (4)]:

$$\sigma_{z,xy}^X(k) \equiv \frac{e^3}{6\hbar k m} \int d\vec{S}^M \cdot \vec{B}^M(\vec{k}^M), \quad (8)$$

where $d\vec{S}^M = k^2 d\Omega_k^M (\vec{k}^M/k)$ is the surface element, and the continuum wave functions used to calculate the transition dipoles are k -normalized¹. The enantiosensitive flux

$$\Phi^x(k) \equiv \int d\vec{S}^M \cdot \vec{B}^M(\vec{k}^M) \quad (9)$$

is a molecular pseudoscalar, which defines the handedness of the enantiomer, i.e. the flux has opposite sign for opposite enantiomers. The relation between the propensity field and the enantiosensitive conductivity in Eq. (8) is reminiscent of the one between the Berry curvature and the Hall conductivity (see e.g. [66]). Similarly, the relation between the enantiosensitive flux and the propensity field in Eq. (9) is reminiscent of the relation between the Chern number and the Berry curvature of a given band in a two-dimensional solid.

The propensity field \vec{B}^M is related to the angular momentum of the photoelectron as follows:

$$\begin{aligned} \vec{L}^M(\vec{k}^M) &\equiv \langle \vec{k}^M | [\vec{r} \times \vec{p}] | \vec{k}^M \rangle \\ &= \sum_n \langle \vec{k}^M | \vec{r} | n \rangle \times \langle n | \vec{p} | \vec{k}^M \rangle \\ &= \frac{m}{\hbar e^2} \sum_n (E_k - E_n) i (\vec{D}_n^{M*} \times \vec{D}_n^M) \\ &= -\frac{m}{\hbar} \sum_n (E_k - E_n) \vec{B}_n^M(\vec{k}^M), \end{aligned} \quad (10)$$

where the sum is over all bound and continuum eigenstates $|n\rangle$ of the Hamiltonian, $\vec{D}_n^M \equiv \langle \vec{k}^M | \vec{r} | n \rangle$, and $\vec{B}_n^M(\vec{k}^M) \equiv -i(\vec{D}_n^{M*} \times \vec{D}_n^M)/e^2$ in analogy with Eq. (4). Introducing the angular momentum $\vec{L}_n^M(\vec{k}^M)$ associated with the transition from a specific state n :

$$\vec{L}_n^M(\vec{k}^M) \equiv -\frac{m}{\hbar} (E_k - E_n) \vec{B}_n^M(\vec{k}^M), \quad (11)$$

we find that the propensity field $\vec{B}^M(\vec{k}^M)$ reflects the angular momentum $\vec{L}_g^M(\vec{k}^M)$ associated with photoionization from the ground state. Since such angular momentum arises due to selection rules, its connection to the propensity field is natural. Thus, Eqs. (2), (7) and (8) show that the enantiosensitive net current emerges as a result of propensity rules. A specific example, explicitly demonstrating the interplay of two propensity rules has been described in the companion paper [65].

The helicity of a (spinless) photoelectron is given by the projection of its angular momentum on the direction of electron momentum: $\eta(\vec{k}^M) = \vec{L}_g^M \cdot \frac{\vec{k}^M}{\hbar k}$. Evidently, the molecular pseudoscalar in Eq. (1), the enantiosensitive conductivity (8) and flux (9), and the angle integrated

photoelectron helicity, are all proportional to each other:

$$\sigma_{z,xy}^x(k) = \frac{e^3}{6\hbar km} \Phi^x(k) = -\frac{e^3 \hbar k}{6m^2(E_k - E_g)} \int d\Omega_k^M \eta(\vec{k}^M). \quad (12)$$

The propensity field $\vec{B}^M(\vec{k}^M)$ and the chiral flux $\Phi^x(k)$ emphasize different molecular properties. The pseudovector field $\vec{B}^M(\vec{k}^M)$ determines the local absorption circular dichroism, is proportional to the angular momentum of the photoelectron $\vec{L}_g^M(\vec{k}^M)$ associated with the ionization from the ground state, and can be non-zero even in achiral systems. On the other hand, the pseudoscalar flux $\Phi^x(k)$ determines the enantiosensitivity of PECd, is proportional to the average helicity of the photoelectrons with energy E_k , and is non-zero only in chiral systems. Its emergence emphasizes the importance of geometry in the chiral response in PECd.

Further aspects underlying the connection between the enantiosensitive net current and the propensity field will be addressed in our forthcoming publication. Now we will show how the propensity field \vec{B}^M underlying the response of unaligned molecules manifests itself in the chiral response of aligned molecules.

III. THE CONNECTION BETWEEN PECd IN ALIGNED AND UNALIGNED MOLECULES.

In the following we use atomic units everywhere, and we take $-e = 1$. We first rewrite Eq. (1) in an equivalent form using Eqs. (4), (7), (8), (9), and explicitly evaluating the vector product of field components:

$$\begin{aligned} \vec{j}^L(k) &\equiv \left\{ \frac{1}{6k} \int d\vec{S}^M \cdot \vec{B}^M(\vec{k}^M) \right\} \left\{ \sigma |\tilde{\mathcal{E}}|^2 \hat{z}^L \right\} \\ &\equiv \frac{1}{6k} \Phi^x \left\{ \sigma |\tilde{\mathcal{E}}|^2 \hat{z}^L \right\}. \end{aligned} \quad (13)$$

We will focus on the analysis of the chiral flux and specifically on the flux of each cartesian component of the propensity field, i.e. on

$$\Phi_i^x \equiv \int dS_i^M B_i^M(\vec{k}^M), \quad i = x, y, z. \quad (14)$$

If we pick a specific direction, given by the i -th component of propensity field in the molecular frame, we obtain the difference between the net photoelectron currents along the i -th molecular axis resulting from left and right circularly polarized light (defined with respect to the same axis), for a fixed molecular orientation. For example, for the flux of the x component of the propensity

¹ When \hbar , m , and $-e$ are written explicitly one must include a factor of $-e/(hm)$ in Eq. (1)

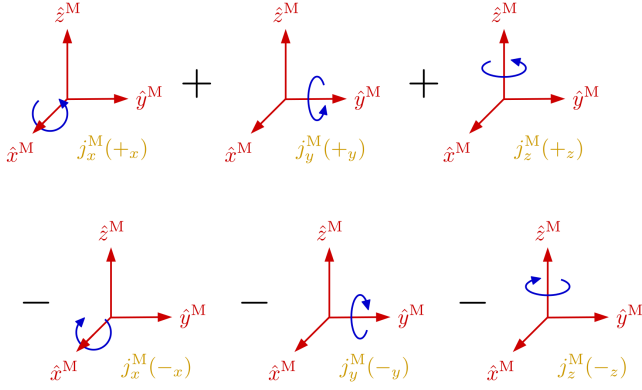


Figure 1. Scheme of the right hand side of Eq. (16) depicting the 6 different field geometries (circular blue arrows) in the molecular frame contributing to the net photoelectron current in the lab frame. For each field geometry only the component of the photoelectron current perpendicular to the polarization plane is taken into account.

field we obtain [see Eq. (2)]:

$$\begin{aligned}
\frac{1}{k} \int dS_x \vec{B}_x^M(\vec{k}^M) &\equiv \int d\Omega_k^M i \left(\vec{D}^{M*} \times \vec{D}^M \right)_x k_x^M \\
&= \int d\Omega_k^M \left| \vec{D}^M \cdot \frac{\hat{y}^M + i\hat{z}^M}{\sqrt{2}} \right|^2 k_x^M \\
&\quad - \int d\Omega_k^M \left| \vec{D}^M \cdot \frac{\hat{y}^M - i\hat{z}^M}{\sqrt{2}} \right|^2 k_x^M \\
&= \frac{1}{|\vec{\mathcal{E}}|^2} [j_x^M(+x) - j_x^M(-x)], \quad (15)
\end{aligned}$$

where the subscript of the plus and of the minus indicates the axis with respect to which the light is left or right circularly polarized. An analogous result is obtained for the flux of the y and z components of propensity field. Then, the chiral flux in Eq. (13) is simply the sum of the differences (15) along each molecular axis, normalized by the intensity of the Fourier component of the field at the transition frequency, and we can write the net photoelectron current in the lab frame in terms of the photoelectron currents in the molecular frame as²

$$\vec{j}^L = \left\{ \frac{1}{6} \sum_{i=x,y,z} [j_i^M(+i) - j_i^M(-i)] \right\} \{ \sigma \hat{z}^L \}. \quad (16)$$

The right hand side of Eq. (16) is depicted in Fig. 1, which shows the different field geometries and the corresponding components of the current in the molecular frame that account for the net current in the lab frame. This figure immediately suggests the equivalent

² We drop the argument k of the currents in the lab and molecular frames for simplicity.

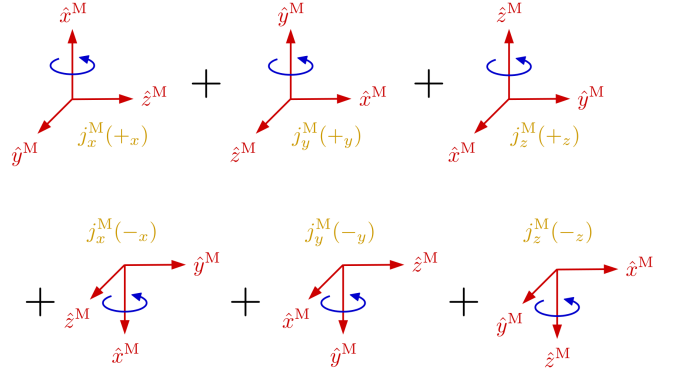


Figure 2. Scheme of the right hand side of Eq. (17) depicting the 6 different orientations of the molecular frame contributing to the net photoelectron current in the lab frame. The curved blue arrows indicate the field in the lab frame. For each orientation only the component of the photoelectron current perpendicular to the polarization plane is taken into account. These orientations are unique only up to a rotation around the axis perpendicular to the polarization plane.

but somewhat more natural picture shown in Fig. 2, where the field geometry is kept fixed and the molecule assumes the six different orientations in which \hat{x}^M , $-\hat{x}^M$, \hat{y}^M , $-\hat{y}^M$, \hat{z}^M , and $-\hat{z}^M$, coincide with \hat{z}^L . To reflect this picture Eq. (16) can be rewritten as follows:

$$\vec{j}^L = \left\{ \frac{1}{6} \sum_{i=x,y,z} [j_z^L(\sigma, \lambda_i) + j_z^L(\sigma, \lambda_{-i})] \right\} \hat{z}^L, \quad (17)$$

where λ_i and λ_{-i} are the Euler angles specifying the orientation for which the i -th molecular axis is parallel to \hat{z}^L and $-\hat{z}^L$, respectively. This change of picture corresponds to the substitutions: $j_z^L(\sigma, \lambda_{\pm i}) = \pm j_i^M((\pm\sigma)_i)$ which directly follow from comparing Figs. 1 and 2. The Euler angles $\lambda_{\pm i}$ are not unique because the z component of the current $\vec{j}^L(\sigma, \lambda_{\pm i})$ is of course invariant with respect to rotations of the molecular frame about \hat{z}^L , and therefore the specific orientation of the molecular axes that lie on the polarization plane is irrelevant. Furthermore, the definition of the orientation of the molecular frame with respect to the nuclei that form the molecule is also arbitrary. Thus, what Eq. (17) really says is that the orientation-averaged photoelectron current for a randomly-oriented ensemble is equivalent to the average over six molecular orientations, where each orientation corresponds to having one of the six spatial directions in the molecular frame pointing along \hat{z}^L .

We can work a bit more on Eq. (17) to avoid the ambiguity of $\lambda_{\pm i}$ mentioned above. If for a given orientation λ_i the current in the lab frame is $\vec{j}^L(\sigma, \lambda_i)$, then the average of $\vec{j}^L(\sigma, \lambda_i)$ over all the orientations $\lambda_i(\phi)$, that yield the same orientation as λ_i up to a rotation by ϕ of the molecular frame around \hat{z}^L , yields the z component

of $\vec{j}^L(\sigma, \lambda_i)$, i.e.

$$\frac{1}{2\pi} \int_0^{2\pi} d\phi \vec{j}^L(\sigma, \lambda_i(\phi)) = j_z^L(\sigma, \lambda_i) \hat{z}^L. \quad (18)$$

This means that we can rewrite the net orientation-averaged photoelectron current [Eq. (17)] in the more symmetric form

$$\vec{j}^L(k) = \frac{1}{3} \sum_{i=x,y,z} \frac{1}{2} \left\{ \frac{1}{2\pi} \int_0^{2\pi} d\phi \vec{j}^L(\sigma, \lambda_i(\phi)) + \frac{1}{2\pi} \int_0^{2\pi} d\phi \vec{j}^L(\sigma, \lambda_{-i}(\phi)) \right\}. \quad (19)$$

This equation provides the relationship between the isotropically-oriented-ensemble PECD and the aligned-ensemble PECD that we were looking for. The i -th term in the summation corresponds to the average photoelectron current that a molecular ensemble yields when its i -th molecular axis is perfectly aligned (parallel and anti-parallel) along the normal to the polarization plane, and the other two molecular axes take all possible orientations in the polarization plane. That is, Eq. (19) shows that the net photoelectron current for an isotropically-oriented ensemble is simply the average of the three different aligned-ensemble cases.

IV. PECD IN ALIGNED MOLECULAR ENSEMBLES

From Eq. (19) we can infer that the introduction of partial alignment along an axis perpendicular to the polarization plane in an otherwise isotropic ensemble will simply change the weight factors of the aligned-ensemble contributions in favor of the molecular axis which is being aligned. In this section we will confirm that this is indeed the case by deriving an exact formula for the net photoelectron current in the lab frame resulting from photoionization via circularly polarized light of a molecular ensemble exhibiting an arbitrary degree of alignment with respect to the normal to the polarization plane. We will also derive an analogous formula for the case in which the alignment axis is in the plane of polarization, which corresponds to the standard experimental set-up when the laser field used to align the sample co-propagates with the ionizing field. But first we will briefly discuss some general symmetry properties that explain enantiosensitivity and dichroism in these ensembles from a purely geometrical point of view.

A. Symmetry considerations for aligned and oriented ensembles

The relevant symmetry properties of an *aligned* ensemble of chiral molecules interacting with circularly polar-

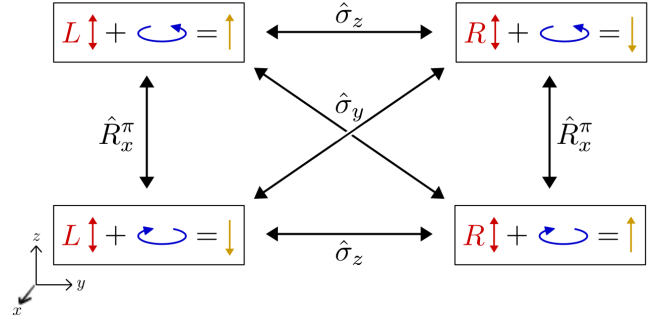


Figure 3. Symmetry properties of an ensemble of chiral molecules interacting with circularly polarized light in the electric-dipole approximation. The ensemble is partially (or totally) aligned along the (z) axis perpendicular to the (xy) polarization plane of the light. The box represents the “enantiomer+field” system. Inside the box: the red letters L and R specify the enantiomer, the red double-headed vertical arrow specifies the direction along which the molecules are aligned, the blue curved arrow specifies the direction of rotation of a field circularly polarized in the xy plane, and the golden vertical arrow stands for a polar vector observable $\vec{v} = v_z \hat{z}$ displaying asymmetry with respect to the polarization plane xy . A reflection $\hat{\sigma}_z$ with respect to the xy plane, leaves the field invariant, but swaps the enantiomer and flips \vec{v} (enantiosensitivity). A rotation \hat{R}_a^π by π radians around any vector \vec{a} contained in the xy plane leaves the enantiomer invariant, but swaps the polarization and flips \vec{v} (dichroism). Note that a rotation \hat{R}_x^π (\hat{R}_y^π) followed by a reflection $\hat{\sigma}_z$ is equivalent to a reflection $\hat{\sigma}_y$ ($\hat{\sigma}_x$) and leaves \vec{v} invariant but swaps both the enantiomer and the polarization. Thus, except for very specific cases (see Fig. 4), FBA in aligned ensembles is a signature of molecular chirality (see also Fig. 5).

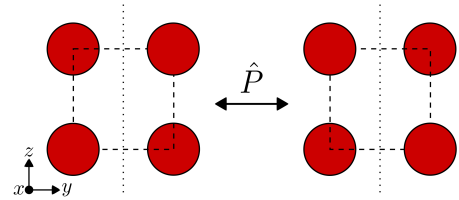


Figure 4. Left: an achiral molecule consisting of four identical atoms with Cartesian coordinates $(-a, -b, b)$, (a, b, b) , $(a, -b, -b)$, and $(-a, b, -b)$. Right: spatial inversion of the molecule on the left. A rotation by $\pi/2$ around the x axis yields the molecule on the left. However, molecular alignment restricts available rotations. Thus if we consider a sample aligned along the vertical dotted line, the rotation by $\pi/2$ is not allowed and the aligned sample becomes effectively chiral.

ized light in the electric-dipole approximation are summarized in Fig. 3 (cf. Fig. 2 in [5]) for the case of alignment perpendicular to the polarization plane. In this case, the cylindrical symmetry of the “aligned-enantiomer + field” system enforces cylindrical symmetry on the observables and therefore limits the asymmetry of the photoelectron angular distribution to be

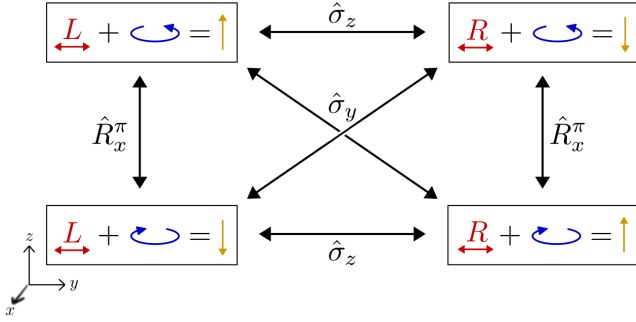


Figure 5. Symmetry properties of an ensemble of chiral molecules interacting with circularly polarized light in the electric-dipole approximation. The ensemble is partially (or totally) aligned along an axis (y) contained in the (xy) polarization plane of the light. Notations are described in Fig. 3. This shows that, except for very specific cases (see Fig. 4), FBA in aligned ensembles is a signature of molecular chirality (see also Fig. 3).

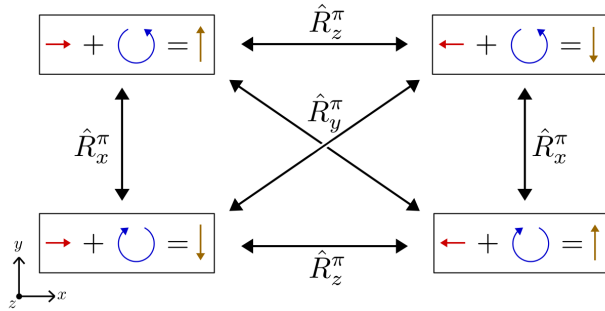


Figure 6. Symmetry considerations for an ensemble of oriented (chiral or achiral) molecules. Notations are described in Fig. 3. The orientation axis (x) is in the polarization plane of the light (xy). A rotation \hat{R}_z^π by π radians around the z axis leaves the field invariant, but flips both the molecular orientation and $v_y\hat{y}$ (orientation sensitivity). A rotation \hat{R}_x^π by π radians around the x axis leaves the orientation invariant, but swaps the polarization and flips $v_y\hat{y}$ (dichroism). Note that a rotation \hat{R}_z^π (\hat{R}_x^π) followed by a rotation \hat{R}_x^π (\hat{R}_z^π) is equivalent to a rotation \hat{R}_y^π and leaves $v_y\hat{y}$ invariant but flips the orientation and the polarization. For achiral molecules reflection symmetry forbids signals perpendicular to the polarization plane, i.e. $v_z = 0$. For chiral molecules such FBA signal is not symmetry forbidden and it is enantiosensitive and dichroic.

along the axis perpendicular to the polarization plane, i.e. forward-backward asymmetry³ (FBA). Furthermore, if the aligned sample is achiral then the “enantiomer +

field” system becomes invariant with respect to reflections through the polarization plane, and the forward-backward asymmetry disappears. That is, like in the isotropic case, in the aligned case the FBA is also a signature of the chirality of the sample.

However, unlike in the isotropic case, in the aligned case one must be careful of distinguishing between the chirality of the aligned sample and the chirality of the molecules that make up the sample. Although an aligned sample of chiral molecules is always chiral, a chiral aligned sample is not necessarily made up of chiral molecules. The reason is that restricting the degrees of freedom of the molecular orientation may lead to suppression of the orientation corresponding to the reflection of an allowed orientation and therefore induce chirality. An example of how this may occur is shown in Fig. 4, where we can see that such alignment-induced chirality seems to require a very particular interplay between the molecular symmetry and the alignment axis. In the absence of such particular conditions, alignment does not induce chirality in the sample and FBA can be traced back to the chirality of the molecules.

Figure 5 shows a symmetry diagram analogous to that in Fig. 3 for the setup in which the molecular alignment axis is in the plane of polarization of the ionizing light. In this case the molecular alignment breaks the cylindrical symmetry. Nevertheless the system remains invariant with respect to rotations by π around the z axis and the vector observable is again constrained to the \hat{z} direction. Like for the previous case, the dichroic and enantiosensitive FBA is a signature of the chirality of the molecular sample.

It is important to distinguish the FBA discussed here from the dichroic asymmetry observed in Refs. [67–69] in oriented achiral samples. While the former is with respect to the polarization plane and is a hallmark of the chirality of the sample, the latter is with respect to the plane containing the spin of the photon and the orientation axis (a plane perpendicular to the polarization plane), and takes place even for achiral samples. Figure 6 shows how such dichroic asymmetry can emerge in uniaxially oriented chiral and achiral systems. The x component of \vec{v} is not shown because it is not dichroic and the z component reflecting FBA is zero in achiral systems because of reflection symmetry with respect to the xy plane.

B. Connection between chiral current and molecular field for aligned ensembles

Now that we have established a general starting point based on the symmetry properties of the “aligned-enantiomer + field” system, we will proceed to the deriva-

³ We note that the term FBA can be misleading because it seems to imply that the direction of propagation of the light, i.e. the sign of the wave vector plays a role. This is clearly not the case as the effect is within the electric-dipole approximation, and therefore whether the light propagates in the $+\hat{z}$ direction or the $-\hat{z}$ direction is completely irrelevant. The only thing that

matters is the rotation direction of the light, i.e. the spin of the photon and not its helicity (see Appendix 1 of Ref. [5]).

tion of the lab-frame net photoelectron current for such an ensemble for the case of one-photon absorption. The molecular alignment can be introduced in the orientation-averaging procedure via a weight function $w(\lambda)$ that depends on the Euler angles $\lambda \equiv \alpha\beta\gamma$, which are the angles that determine the relative orientation between the lab frame and the molecular frame. In the ZYZ convention, β determines the angle between the z axes of the two frames, so that to describe molecular alignment we can use a distribution $w(\beta)$ that only depends on this angle and that is symmetric with respect to $\beta = \pi/2$. With the molecular alignment defined along the \hat{z}^L axis (or vice-versa), we can consider that the circularly polarized field is in the $x^L y^L$ plane or in the $y^L z^L$ plane, depending on whether we are interested in the setup where the molecular alignment is perpendicular or parallel to the light polarization plane, respectively.

1. Alignment perpendicular to the plane of polarization

For light circularly polarized in the $x^L y^L$ plane the photoelectron current density in the lab frame corresponding to a given photoelectron momentum \vec{k}^M in the molecular frame and a given molecular orientation $\lambda \equiv (\alpha, \beta, \gamma)$ is [5]

$$\begin{aligned} \vec{j}^L(\vec{k}^M, \lambda) &= \frac{|\tilde{\mathcal{E}}|^2}{2} |\vec{D}^L \cdot (\hat{x}^L + \sigma i \hat{y}^L)|^2 \vec{k}^L \\ &= \frac{|\tilde{\mathcal{E}}|^2}{2} [|S\vec{D}^M \cdot \hat{x}^L|^2 + |S\vec{D}^M \cdot \hat{y}^L|^2 \\ &\quad + \sigma i S(\vec{D}^{M*} \times \vec{D}^M) \cdot \hat{z}^L] S\vec{k}^M, \end{aligned} \quad (20)$$

where $S(\lambda)$ is the rotation matrix that takes vectors from the molecular frame to the lab frame, i.e. $\vec{v}^L = S(\lambda) \vec{v}^M$, $\tilde{\mathcal{E}}$ is the Fourier transform of the electric field evaluated at the transition frequency, and $\sigma = \pm 1$ stands for left(+)/right(-) circularly polarized light. Before moving on to the case at hand, Eq. (20) gives us the opportunity to briefly point out another reason why only the coherent term survives the orientation averaging in both isotropically-oriented and aligned ensembles. For each orientation λ_i of the molecular frame there will be another orientation λ_{-i} related to it by a rotation by π around (for example) \hat{y}^L that will change the sign of the x^L and z^L components of all molecular vectors. Therefore, if we consider the average of $j_z^L(\vec{k}^M, \lambda)$ over those two orientations, $[j_z^L(\vec{k}^M, \lambda_i) + j_z^L(\vec{k}^M, \lambda_{-i})]/2$, we can see from (20) that the incoherent terms $|S\vec{D}^M \cdot \hat{x}^L|^2 (S\vec{k}^M \cdot \hat{z}^L)$ and $|S\vec{D}^M \cdot \hat{y}^L|^2 (S\vec{k}^M \cdot \hat{z}^L)$ will cancel because they have opposite signs for opposite orientations, while the coherent term $\sigma [S(\vec{D}^{M*} \times \vec{D}^M) \cdot \hat{z}^L] (S\vec{k}^M \cdot \hat{z}^L)$ will not because it is the same for both orientations. That is, while obviously each term of $j_z^L(\vec{k}^M, \lambda)$ is invariant with respect to rotations of the molecular frame by π around \hat{z}^L , only the coherent term is invariant with respect to

rotations by π with respect to any axis. Thus, either for isotropically-oriented samples or aligned samples (with molecular alignment perpendicular to the polarization plane or not), the incoherent terms will always cancel by pairs in the orientation averaging while the coherent term will not.

For a distribution of orientations $w(\beta)$, the net photoelectron current in the lab frame takes the form:

$$\vec{j}^L(k) = \int d\Omega_k^M \int d\lambda w(\beta) \vec{j}^L(\vec{k}^M, \lambda), \quad (21)$$

where $\int d\lambda \equiv \int_0^{2\pi} d\alpha \int_0^\pi d\beta \int_0^{2\pi} d\gamma \sin\beta/8\pi^2$ is the integral over molecular orientations, and $\int d\Omega_k^M \equiv \int_0^{2\pi} d\phi_k^M \int_0^\pi d\theta_k^M \sin\theta_k^M$ is the integral over directions of the photoelectron momentum \vec{k}^M . For an alignment distribution $w(\beta) \propto \cos^2\beta$, Eq. (21) becomes equivalent to the photoelectron current found in the case where a pump linearly polarized along \hat{z}^L resonantly excites the molecule via a transition dipole parallel to \hat{z}^M into a bound excited electronic state and is then photoionized from the latter by a circularly polarized probe pulse. Therefore, for such a distribution we could simply make use of Eq. (31) derived in [5] in the context of the generalized PXECD (see Appendix VII A). This equivalence reveals the close relation between aligned ensembles where the molecular orientation is anisotropic and isotropically-oriented ensembles that have been electronically excited. This happens because the field imprints its anisotropy on the originally isotropic molecular ensemble via the excitation.

In the following we will make no assumption about $w(\beta)$ except that it is symmetric with respect to $\beta = \pi/2$, which simply imposes the condition of alignment. The first two terms in Eq. (20) describe interaction with a linearly polarized field and therefore, from symmetry considerations⁴, they lead to $\vec{j}^L(k) = 0$. The integral over orientations of the third term in Eq. (20) can be carried out with the help of Eq. (33) derived in Appendix VII A and yields

$$\begin{aligned} \vec{j}^L(k) &= \frac{\sigma |\tilde{\mathcal{E}}|^2}{2} \left[\frac{1}{3} w_i \int d\Omega_k^M (\vec{i}\vec{D}^{M*} \times \vec{D}^M) \cdot \vec{k}^M \right. \\ &\quad \left. + (1 - w_i) \int d\Omega_k^M (\vec{i}\vec{D}^{M*} \times \vec{D}^M)_z k_z^M \right] \hat{z}^L, \end{aligned} \quad (22)$$

where we assumed that $w(\beta)$ is properly normalized [see Eq. (35)] and we defined w_i as

$$w_i \equiv \frac{3}{4} \int_0^\pi d\beta w(\beta) \sin^3\beta. \quad (23)$$

⁴ For example, for polarization along \hat{x}^L , the system is invariant with respect to a rotation by π around \hat{x}^L which means that $j_y^L = j_z^L = 0$, and also with respect to rotation by π around \hat{z}^L which means that $j_x^L = j_y^L = 0$.

w_i is a parameter determined exclusively by $w(\beta)$. Equation (22) can be written in an equivalent form [cf. Eqs. (4) (9), and (14)]:

$$\vec{j}^L(k) = \frac{\sigma|\tilde{\mathcal{E}}|^2}{2k} \left[\frac{1}{3} w_i \Phi^X(k) + (1 - w_i) \Phi_z^X(k) \right] \hat{z}^L. \quad (24)$$

Table I shows $w(\beta)$, w_i , and j_z^L for perfectly aligned, isotropic, and perfectly antialigned samples. While the isotropic case reduces to Eq. (13) and gives the average of Φ_x^X , Φ_y^X , and Φ_z^X [i.e. the total flux, see Eqs. (9) and (14)], the perfectly aligned case singles out the Φ_z^X , in full agreement with our discussion in Sec. III. On the other hand, the perfectly antialigned case, where the molecular z axis is constrained to be perpendicular to the laboratory z axis, prevents Φ_z^X from contributing to the photoelectron current.

As shown in Appendix VII A, for the case $w(\beta) \propto \cos^2 \beta$, Eq. (22) coincides with the predictions of the generalized PXECD formula derived in [5] and discussed above.

2. Alignment parallel to the plane of polarization

The derivation for the setup in which the molecular alignment axis is contained in the polarization plane follows analogously with only subtle differences. This time we define the orientation of the lab frame such that the molecular alignment remains along the \hat{z}^L axis but now the light is polarized in the $y^L z^L$ plane, and therefore we have that the photoelectron current in the lab frame corresponding to a given photoelectron momentum \vec{k}^M in the molecular frame and a given molecular orientation $\lambda \equiv (\alpha, \beta, \gamma)$ reads as

$$\vec{j}^L(\vec{k}^M, \lambda) = \frac{|\tilde{\mathcal{E}}|^2}{2} \left[|S\vec{D}^M \cdot \hat{y}^L|^2 + |S\vec{D}^M \cdot \hat{z}^L|^2 + \sigma i S (\vec{D}^{M*} \times \vec{D}^M) \cdot \hat{x}^L \right] S\vec{k}^M. \quad (25)$$

With the help of Eq. (37) derived in Appendix VII A we obtain

$$\vec{j}^L(k) = \frac{\sigma|\tilde{\mathcal{E}}|^2}{2} \left[\frac{1}{3} \frac{(3 - w_i)}{2} \int d\Omega_k^M (\vec{i}\vec{D}^{M*} \times \vec{D}^M) \cdot \vec{k}^M + \frac{1}{2} (w_i - 1) \int d\Omega_k^M (\vec{i}\vec{D}^{M*} \times \vec{D}^M)_z k_z^M \right] \hat{x}^L. \quad (26)$$

Like in the previous case, and as follows from the symmetry considerations of Sec. IV A, the current is directed along the direction perpendicular to the polarization plane of the incident field. Comparing with Eq. (22) we can see that the factors in front of the isotropic and anisotropic contributions are slightly different from what we obtained in the previous case. We can rewrite this

equation in an equivalent form [cf. Eqs. (4), (9), and (14)]:

$$\vec{j}^L(k) = \frac{\sigma|\tilde{\mathcal{E}}|^2}{2k} \left[\frac{1}{3} \frac{(3 - w_i)}{2} \Phi^X(k) + \frac{1}{2} (w_i - 1) \Phi_z^X(k) \right] \hat{x}^L. \quad (27)$$

Some limiting cases of this equation are shown in the last column of Table I, where we can see that, as expected, this formula reduces to Eq. (13) in the isotropic case. We can also see that the aligned case with the alignment parallel to the polarization plane yields the same result as the antialigned case with the alignment perpendicular to the polarization plane, as expected from symmetry, and that antialignment doubles the weight of Φ_z^X with respect to that of Φ_x^X and Φ_y^X . Appendix VII A shows how Eq. (26) can also be derived from the generalized PXECD formulas derived in [5] when $w(\beta) \propto \cos^2 \beta$.

Equations (24) and (27) suggest that choosing the alignment properly could lead to an increase of the PECD signal. Such increase has been recently discovered both theoretically and experimentally in Ref. [49]. The increase can be rationalized in terms of the propensity field $\vec{B}^M(\vec{k}^M)$ and its strength along different \vec{k}^M directions. For example, if a molecule is such that $|\Phi_z^X| > |\Phi_x^X|$ and $|\Phi_z^X| > |\Phi_y^X|$, and the z molecular axis can be aligned, then Eq. (24) shows that the PECD signal will increase with the alignment. Similarly, if for example Φ_z^X has an opposite sign to that of Φ_x^X and Φ_y^X , then Eq. (24) shows that the PECD signal will also benefit from the alignment.

V. CONCLUSIONS

The enantiosensitive photoelectron current, or in other words, the forward-backward asymmetry in photoelectron circular dichroism (PECD), is determined by the the propensity field, which is analogous to the Berry curvature in a two-band solid. This field is independent of light properties, is defined in the molecular frame, and is unique to each molecule. The enantiosensitive photoelectron current stemming from aligned ensembles of chiral molecules is only sensitive to specific components of the propensity field and therefore the increase or decrease of the chiral response vs. molecular alignment depends on the structure of this field. Each component of the propensity field reflects photoelectron-momentum-resolved absorption circular dichroism and is only non-zero in the absence of rotational symmetry about the corresponding axis. The propensity field underlies the emergence of PECD. Thus, in this paper we have generalized the ideas presented in our companion paper [65], which illustrates the role of optical propensity rules in PECD in aligned molecular ensembles for specific examples of chiral states.

In the case of unaligned molecular ensembles, the enantiosensitive photoelectron current for a given absolute value k of the photoelectron momentum is proportional to the flux of the propensity field through the sphere

	$w(\beta)$	w_i	$\vec{\mathcal{E}} = \frac{\hat{\epsilon}}{\sqrt{2}}(\hat{x} + \sigma i\hat{y})$ $j_z/\frac{\sigma \hat{\epsilon} ^2}{2k}$	$\vec{\mathcal{E}} = \frac{\hat{\epsilon}}{\sqrt{2}}(\hat{y} + \sigma i\hat{z})$ $j_x/\frac{\sigma \hat{\epsilon} ^2}{2k}$
Aligned	$\frac{2[\delta(\beta)+\delta(\beta-\pi)]}{\sin\beta}$	0	Φ_z	$\frac{1}{2}(\Phi_x + \Phi_y)$
Isotropic	1	1	$\frac{1}{3}(\Phi_x + \Phi_y + \Phi_z)$	$\frac{1}{3}(\Phi_x + \Phi_y + \Phi_z)$
Antialigned	$\frac{2\delta(\beta-\frac{\pi}{2})}{\sin\beta}$	$\frac{3}{2}$	$\frac{1}{2}(\Phi_x + \Phi_y)$	$\frac{1}{4}(\Phi_x + \Phi_y + 2\Phi_z)$

Table I. Photoelectron current density in aligned, isotropic, and antialigned samples for circular polarization perpendicular [fourth column, Eq. (24)] and parallel [fifth column, Eq. (27)] to the alignment axis z . We have dropped the L and the χ superscripts for simplicity.

of radius k . The flux is a pseudoscalar and has opposite sign for opposite enantiomers. Molecular alignment allows one to probe the flux generated by specific components of the propensity field.

VI. ACKNOWLEDGEMENTS

The authors thank Alvaro Jiménez-Galán, Rui Silva, David Ayuso and Misha Ivanov for illuminating discussions and essential collaboration on this topic. The authors gratefully acknowledge the MEDEA project, which has received funding from the European Union's Horizon 2020 research and innovation programme under the Marie Skłodowska-Curie grant agreement 641789. The authors gratefully acknowledge support from the DFG SPP 1840 "Quantum Dynamics in Tailored Intense Fields" and DFG grant SM 292/5-2.

VII. APPENDIX

A. Orientation averaging in aligned ensembles

In this appendix we will derive the orientation averaged net photoelectron current in the lab frame for the aligned ensembles considered in Sec. (IV B). Before deriving the expression for an arbitrary distribution $w(\beta)$, we will consider the particular distribution $w(\beta) = 3 \cos^2 \beta$ in order to draw some connections between the results obtained in a randomly oriented sample and an aligned sample. In this case the net photoelectron current can be written as [see Eqs. (20) and (21)]

$$\vec{j}^L(k) = 3 \int d\Omega_k^M \int d\lambda \cos^2 \beta \vec{j}^L(\vec{k}^M, \lambda) = 3 \int d\Omega_k^M \int d\lambda \left| \hat{d}_{\text{eff}}^L \cdot \hat{\mathcal{E}}_{\text{eff}}^L \right|^2 \left| \vec{D}^L \cdot \vec{\mathcal{E}}^L \right|^2 \vec{k}^L,$$

which simply shows that the anisotropic orientation average of $\vec{j}^L(\vec{k}^M, \lambda)$ is equivalent to the isotropic averaging of $|\hat{d}_{\text{eff}}^L \cdot \hat{\mathcal{E}}_{\text{eff}}^L|^2 |\vec{D}^L \cdot \vec{\mathcal{E}}^L|^2$, where we introduced an effective bound-bound transition dipole $\hat{d}_{\text{eff}}^M = \hat{z}^M$ and the effective field which interacts with it $\hat{\mathcal{E}}_{\text{eff}}^L = \hat{z}^L$, in order to make evident that, mathematically, we are dealing with a particular case of the generalized PXECD effect considered in [5], where first a pump pulse of arbitrary polarization excites the system into a superposition of two excited states and then a probe pulse of arbitrary polarization photoionizes the system from intermediate state. In the present case the effective pump pulse excites the system from an effective ground state into a single excited state (the actual ground state) through the interaction $\hat{d}_{\text{eff}}^L \cdot \hat{\mathcal{E}}_{\text{eff}}^L$ and then the probe pulse (the actual pulse) photoionizes the system from the excited state. That is, we only have to deal with Eq. (31) in [5], which in our case reads as

$$\begin{aligned}
\vec{j}^L(k) &= 3 \int d\Omega_k^M \int d\lambda \left| \hat{d}_{\text{eff}}^L \cdot \hat{\mathcal{E}}_{\text{eff}}^L \right|^2 \left| \vec{D}^L \cdot \vec{\mathcal{E}}^L \right|^2 \vec{k}^L \\
&= \frac{1}{5} \Re \left\{ \int d\Omega_k^M \left[\left(\hat{d}_{\text{eff}}^M \times \vec{D}^{M*} \right) \cdot \vec{D}^M \right] \left(\hat{d}_{\text{eff}}^M \cdot \vec{k}^M \right) \left[\left(\hat{\mathcal{E}}_{\text{eff}}^L \times \vec{\mathcal{E}}^{L*} \right) \cdot \vec{\mathcal{E}}^L \right] \hat{\mathcal{E}}_{\text{eff}}^L \right. \\
&\quad + \int d\Omega_k^M \left[\left(\hat{d}_{\text{eff}}^M \times \vec{D}^{M*} \right) \cdot \vec{k}^M \right] \left(\hat{d}_{\text{eff}}^M \cdot \vec{D}^M \right) \left(\hat{\mathcal{E}}_{\text{eff}}^L \cdot \vec{\mathcal{E}}^L \right) \left(\hat{\mathcal{E}}_{\text{eff}}^L \times \vec{\mathcal{E}}^{L*} \right) \\
&\quad + \int d\Omega_k^M \left[\left(\hat{d}_{\text{eff}}^M \times \vec{D}^M \right) \cdot \vec{k}^M \right] \left(\hat{d}_{\text{eff}}^M \cdot \vec{D}^{M*} \right) \left(\hat{\mathcal{E}}_{\text{eff}}^L \cdot \vec{\mathcal{E}}^{L*} \right) \left(\hat{\mathcal{E}}_{\text{eff}}^L \times \vec{\mathcal{E}}^L \right) \left. \right\} \\
&\quad + \frac{1}{10} \int d\Omega_k^M \left[\left(\vec{D}^{M*} \times \vec{D}^M \right) \cdot \vec{k}^M \right] \left(\vec{\mathcal{E}}^{L*} \times \vec{\mathcal{E}}^L \right), \tag{28}
\end{aligned}$$

If the molecular alignment (which we have already set along \hat{z}^L) is perpendicular to the polarization plane we set $\vec{\mathcal{E}}^L = (\hat{x}^L + \sigma i \hat{y}^L) / \sqrt{2}$. The second and third terms vanish because $(\hat{\mathcal{E}}_{\text{eff}}^L \cdot \vec{\mathcal{E}}^L) = 0$ and Eq. (28) yields

$$\vec{j}^L(k) = \frac{\sigma |\vec{\mathcal{E}}^L|^2}{2} \left\{ \frac{1}{5} \int d\Omega_k^M \left[\left(i \vec{D}^{M*} \times \vec{D}^M \right) \cdot \vec{k}^M \right] + \frac{2}{5} \int d\Omega_k^M \left[\left(i \vec{D}^{M*} \times \vec{D}^M \right)_z k_z^M \right] \right\} \hat{z}^L, \tag{29}$$

On the other hand, for the case in which molecular alignment is in the plane of the light polarization we set $\vec{\mathcal{E}}^L = (\hat{y}^L + \sigma i \hat{z}^L) / \sqrt{2}$. The first term vanishes because $[(\hat{\mathcal{E}}_{\text{eff}}^L \times \vec{\mathcal{E}}^{L*}) \cdot \vec{\mathcal{E}}^L] = 0$, and with the help of the vector identities $(\vec{a} \times \vec{b}) \cdot (\vec{c} \times \vec{d}) = (\vec{a} \cdot \vec{c})(\vec{b} \cdot \vec{d}) - (\vec{a} \cdot \vec{d})(\vec{b} \cdot \vec{c})$ and $(\vec{a} \times \vec{b}) \times \vec{c} = (\vec{a} \cdot \vec{c})\vec{b} - (\vec{b} \cdot \vec{c})\vec{a}$ we obtain

$$\vec{j}^L(k) = \frac{\sigma |\vec{\mathcal{E}}^L|^2}{2} \left\{ \frac{2}{5} \int d\Omega_k^M \left[\left(i \vec{D}^{M*} \times \vec{D}^M \right) \cdot \vec{k}^M \right] - \frac{1}{5} \int d\Omega_k^M \left(i \vec{D}^{M*} \times \vec{D}^M \right)_z k_z^M \right\} \hat{x}^L. \tag{30}$$

In both cases, Eq. (29) and (30) show that $\vec{j}^L(k)$ is along the direction perpendicular to the light polarization plane and that there is an imbalance in the scalar product $(i \vec{D}^{M*} \times \vec{D}^M) \cdot \vec{k}^M$ that singles out the molecular axis being aligned. Equations (29) and (30) coincide with Eqs. (22) and (26), respectively, when we set $w(\beta) = 3 \cos^2 \beta$ and consequently $w_i = 3/5$ in Eqs. (22) and (26).

Now we proceed to the general derivation where the only assumption on $w(\beta)$ is that it is symmetric with respect to $\beta = \pi/2$, which simply imposes the condition of alignment. Since symmetry implies that the incoherent terms corresponding to linear polarization along \hat{x}^L and \hat{y}^L in Eq. (20) vanish⁵, we will focus exclusively on the coherent term. For the case in which the molecular alignment is perpendicular to the light polarization plane, the relevant integral over orientations is of the form [see Eq. (20)]

$$\int d\lambda w(\beta) (\vec{a}^L \cdot \hat{z}^L) \vec{b}^L, \tag{31}$$

where $\int d\lambda \equiv \int_0^{2\pi} d\alpha \int_0^\pi d\beta \int_0^{2\pi} d\gamma \sin \beta / 8\pi^2$, \vec{a} and \vec{b} are vectors fixed in the molecular frame. To transform a vector from the molecular frame to the lab frame we use $\vec{v}^L = R(\lambda) \vec{v}^M$, where

$$R(\lambda) = \begin{pmatrix} -s\alpha s\gamma + c\alpha c\beta c\gamma & -s\alpha c\gamma - s\gamma c\alpha c\beta & s\beta c\alpha \\ s\alpha c\beta c\gamma + s\gamma c\alpha & -s\alpha s\gamma c\beta + c\alpha c\gamma & s\alpha s\beta \\ -s\beta c\gamma & s\beta s\gamma & c\beta \end{pmatrix}, \tag{32}$$

and s and c stand for sin and cos, respectively. With the help of $R(\lambda)$ we calculate the expression $(\vec{a}^L \cdot \hat{z}^L) \vec{b}^L$ in terms of the molecular frame components of \vec{a} and \vec{b} and then note that most of the terms vanish after integration over α and γ . The non-vanishing terms read as

⁵ Consider the analog of Fig. 3 for linearly polarized light along x (y). The total system becomes symmetric with respect to rota-

tions of π around x (y) and therefore there can be no asymmetry along z .

$$\begin{aligned}
& \int d\lambda w(\beta) (\vec{a}^L \cdot \hat{z}^L) \vec{b}^L \\
&= \left\{ \left[\int d\lambda w(\beta) \sin^2 \beta \cos^2 \gamma \right] a_x^M b_x^M + \left[\int d\lambda w(\beta) \sin^2 \beta \sin^2 \gamma \right] a_y^M b_y^M \right. \\
&\quad \left. + \left[\int d\lambda w(\beta) \cos^2 \beta \right] a_z^M b_z^M \right\} \hat{z}^L \\
&= \left\{ \left[\frac{1}{2} \int_0^\pi d\beta w(\beta) \sin^3 \beta \right] \frac{1}{2} (a_x^M b_x^M + a_y^M b_y^M) \right. \\
&\quad \left. + \left[\frac{1}{2} \int_0^\pi d\beta w(\beta) \sin \beta \cos^2 \beta \right] a_z^M b_z^M \right\} \hat{z}^L \\
&= \left[\frac{1}{3} w_i (\vec{a}^M \cdot \vec{b}^M) + (1 - w_i) a_z^M b_z^M \right] \hat{z}^L, \tag{33}
\end{aligned}$$

where we defined

$$w_i \equiv \frac{3}{4} \int_0^\pi d\beta w(\beta) \sin^3 \beta, \tag{34}$$

and we assumed that $w(\beta)$ is normalized so that $\int d\lambda w(\beta) = 1$, which implies that

$$\frac{1}{2} \int_0^\pi d\beta \sin(\beta) w(\beta) = 1. \tag{35}$$

In the case in which molecular alignment is in the plane of the light polarization the relevant integral is of the form [see Eq. (25)]

$$\int d\lambda w(\beta) (\vec{a}^L \cdot \hat{x}^L) \vec{b}^L, \tag{36}$$

and we proceed analogously as before to find that the only terms that do not vanish after integration yield

$$\begin{aligned}
& \int d\lambda w(\beta) (\vec{a}^L \cdot \hat{x}^L) \vec{b}^L \\
&= \frac{1}{2} \int_0^\pi d\beta \sin \beta w(\beta) \left[\frac{1}{4} (1 + \cos^2 \beta) (a_x^M b_x^M + a_y^M b_y^M) + \frac{1}{2} \sin^2 \beta a_z^M b_z^M \right] \hat{x}^L \\
&= \frac{1}{2} \int_0^\pi d\beta \sin \beta w(\beta) \left[\frac{1}{4} (2 - \sin^2 \beta) \vec{a}^M \cdot \vec{b}^M - \frac{1}{4} (2 - 3 \sin^2 \beta) a_z^M b_z^M \right] \hat{x}^L \\
&= \left[\frac{1}{2} \left(1 - \frac{w_i}{3} \right) \vec{a}^M \cdot \vec{b}^M - \frac{1}{2} (1 - w_i) a_z^M b_z^M \right] \hat{x}^L. \tag{37}
\end{aligned}$$

-
- | | |
|---|---|
| [1] B. Ritchie, Physical Review A 13 , 1411 (1976). | 063428 (2018). |
| [2] I. Powis, The Journal of Chemical Physics 112 , 301 (2000). | [6] D. Patterson, M. Schnell, and J. M. Doyle, Nature 497 , 475 (2013). |
| [3] N. Böwering, T. Lischke, B. Schmidtke, N. Müller, T. Khalil, and U. Heinzmann, Physical Review Letters 86 , 1187 (2001). | [7] D. Patterson and J. M. Doyle, Physical Review Letters 111 , 023008 (2013). |
| [4] E. U. Condon, Reviews of Modern Physics 9 , 432 (1937). | [8] A. Yachmenev and S. N. Yurchenko, Phys. Rev. Lett. 117 , 033001 (2016). |
| [5] A. F. Ordonez and O. Smirnova, Physical Review A 98 , | [9] S. Eibenberger, J. Doyle, and D. Patterson, Phys. Rev. |

- Lett.* **118**, 123002 (2017).
- [10] P. Fischer, A. D. Buckingham, and A. C. Albrecht, *Phys. Rev. A* **64**, 053816 (2001).
- [11] S. Beaulieu, A. Comby, D. Descamps, B. Fabre, G. A. Garcia, R. Géneaux, A. G. Harvey, F. Légaré, Z. Masín, L. Nahon, A. F. Ordóñez, S. Petit, B. Pons, Y. Mairesse, O. Smirnova, and V. Blanchet, *Nature Physics* **14**, 484 (2018).
- [12] G. A. Garcia, L. Nahon, M. Lebeck, J.-C. Houver, D. Dowek, and I. Powis, *The Journal of Chemical Physics* **119**, 8781 (2003).
- [13] S. Turchini, N. Zema, G. Contini, G. Alberti, M. Alagia, S. Stranges, G. Fronzoni, M. Stener, P. Decleva, and T. Prosperi, *Phys. Rev. A* **70**, 014502 (2004).
- [14] U. Hergenhahn, E. E. Rennie, O. Kugeler, S. Marburger, T. Lischke, I. Powis, and G. Garcia, *The Journal of Chemical Physics* **120**, 4553 (2004).
- [15] T. Lischke, N. Böwering, B. Schmidtke, N. Müller, T. Khalil, and U. Heinzmann, *Phys. Rev. A* **70**, 022507 (2004).
- [16] S. Stranges, S. Turchini, M. Alagia, G. Alberti, G. Contini, P. Decleva, G. Fronzoni, M. Stener, N. Zema, and T. Prosperi, *The Journal of Chemical Physics* **122**, 244303 (2005).
- [17] A. Giardini, D. Catone, S. Stranges, M. Satta, M. Tacconi, S. Piccirillo, S. Turchini, N. Zema, G. Contini, T. Prosperi, P. Decleva, D. D. Tommaso, G. Fronzoni, M. Stener, A. Filippi, and M. Speranza, *ChemPhysChem* **6**, 1164 (2005).
- [18] C. J. Harding, E. Mikajlo, I. Powis, S. Barth, S. Joshi, V. Ulrich, and U. Hergenhahn, *The Journal of Chemical Physics* **123**, 234310 (2005).
- [19] L. Nahon, G. A. Garcia, C. J. Harding, E. Mikajlo, and I. Powis, *The Journal of Chemical Physics* **125**, 114309 (2006).
- [20] G. Contini, N. Zema, S. Turchini, D. Catone, T. Prosperi, V. Carravetta, P. Bolognesi, L. Avaldi, and V. Feyer, *The Journal of Chemical Physics* **127**, 124310 (2007).
- [21] G. A. Garcia, L. Nahon, C. J. Harding, and I. Powis, *Phys. Chem. Chem. Phys.* **10**, 1628 (2008).
- [22] V. Ulrich, S. Barth, S. Joshi, U. Hergenhahn, E. Mikajlo, C. J. Harding, and I. Powis, *The Journal of Physical Chemistry A* **112**, 3544 (2008).
- [23] I. Powis, C. J. Harding, G. A. Garcia, and L. Nahon, *ChemPhysChem* **9**, 475 (2008).
- [24] I. Powis, C. J. Harding, S. Barth, S. Joshi, V. Ulrich, and U. Hergenhahn, *Phys. Rev. A* **78**, 052501 (2008).
- [25] S. Turchini, D. Catone, G. Contini, N. Zema, S. Irrera, M. Stener, D. D. Tommaso, P. Decleva, and T. Prosperi, *ChemPhysChem* **10**, 1839 (2009).
- [26] G. A. Garcia, H. Soldi-Lose, L. Nahon, and I. Powis, *The Journal of Physical Chemistry A* **114**, 847 (2010), pMID: 20038111.
- [27] L. Nahon, G. A. Garcia, H. Soldi-Lose, S. Daly, and I. Powis, *Phys. Rev. A* **82**, 032514 (2010).
- [28] S. Daly, I. Powis, G. A. Garcia, H. Soldi-Lose, and L. Nahon, *The Journal of Chemical Physics* **134**, 064306 (2011).
- [29] D. Catone, M. Stener, P. Decleva, G. Contini, N. Zema, T. Prosperi, V. Feyer, K. C. Prince, and S. Turchini, *Phys. Rev. Lett.* **108**, 083001 (2012).
- [30] D. Catone, S. Turchini, M. Stener, P. Decleva, G. Contini, T. Prosperi, V. Feyer, K. C. Prince, and N. Zema, *Rendiconti Lincei* **24**, 269 (2013).
- [31] G. A. Garcia, L. Nahon, S. Daly, and I. Powis, *Nature Communications* **4**, 2132 (2013).
- [32] S. Turchini, D. Catone, N. Zema, G. Contini, T. Prosperi, P. Decleva, M. Stener, F. Rondino, S. Piccirillo, K. C. Prince, and M. Speranza, *ChemPhysChem* **14**, 1723 (2013).
- [33] M. Tia, B. Cunha de Miranda, S. Daly, F. Gaie-Levrel, G. A. Garcia, I. Powis, and L. Nahon, *The Journal of Physical Chemistry Letters* **4**, 2698 (2013).
- [34] I. Powis, S. Daly, M. Tia, B. Cunha de Miranda, G. A. Garcia, and L. Nahon, *Phys. Chem. Chem. Phys.* **16**, 467 (2014).
- [35] M. Tia, B. Cunha de Miranda, S. Daly, F. Gaie-Levrel, G. A. Garcia, L. Nahon, and I. Powis, *The Journal of Physical Chemistry A* **118**, 2765 (2014), pMID: 24654892.
- [36] L. Nahon, L. Nag, G. A. Garcia, I. Myrgorodska, U. Meierhenrich, S. Beaulieu, V. Wanie, V. Blanchet, R. Geneaux, and I. Powis, *Phys. Chem. Chem. Phys.* **18**, 12696 (2016).
- [37] G. A. Garcia, H. Dossmann, L. Nahon, S. Daly, and I. Powis, *ChemPhysChem* **18**, 500 (2016).
- [38] D. Catone, S. Turchini, G. Contini, T. Prosperi, M. Stener, P. Decleva, and N. Zema, *Chemical Physics* **482**, 294 (2017), electrons and nuclei in motion - correlation and dynamics in molecules (on the occasion of the 70th birthday of Lorenz S. Cederbaum).
- [39] N. A. Cherepkov, *Chemical Physics Letters* **87**, 344 (1982).
- [40] I. Powis, *The Journal of Physical Chemistry A* **104**, 878 (2000).
- [41] M. Stener, G. Fronzoni, D. D. Tommaso, and P. Decleva, *The Journal of Chemical Physics* **120**, 3284 (2004).
- [42] C. J. Harding and I. Powis, *The Journal of Chemical Physics* **125**, 234306 (2006).
- [43] D. D. Tommaso, M. Stener, G. Fronzoni, and P. Decleva, *ChemPhysChem* **7**, 924 (2006).
- [44] M. Stener, D. Di Tommaso, G. Fronzoni, P. Decleva, and I. Powis, *The Journal of Chemical Physics* **124**, 024326 (2006).
- [45] I. Dreisigacker and M. Lein, *Physical Review A* **89**, 053406 (2014).
- [46] A. N. Artemyev, A. D. Müller, D. Hochstuhl, and P. V. Demekhin, *The Journal of Chemical Physics* **142**, 244105 (2015).
- [47] R. E. Goetz, T. A. Isaev, B. Nikoobakht, R. Berger, and C. P. Koch, *The Journal of Chemical Physics* **146**, 024306 (2017).
- [48] M. Ilchen, G. Hartmann, P. Rupprecht, A. N. Artemyev, R. N. Coffee, Z. Li, H. Ohldag, H. Ogasawara, T. Osipov, D. Ray, P. Schmidt, T. J. A. Wolf, A. Ehresmann, S. Moeller, A. Knie, and P. V. Demekhin, *Phys. Rev. A* **95**, 053423 (2017).
- [49] M. Tia, M. Pitzer, G. Kastirke, J. Gatzke, H.-K. Kim, F. Trinter, J. Rist, A. Hartung, D. Trabert, J. Siebert, K. Henrichs, J. Becht, S. Zeller, H. Gassert, F. Wiegandt, R. Wallauer, A. Kuhlins, C. Schober, T. Bauer, N. Wechselberger, P. Burzynski, J. Neff, M. Weller, D. Metz, M. Kircher, M. Waitz, J. B. Williams, L. P. H. Schmidt, A. D. Müller, A. Knie, A. Hans, L. Ben Ltaief, A. Ehresmann, R. Berger, H. Fukuzawa, K. Ueda, H. Schmidt-Böcking, R. Dörner, T. Jahnke, P. V. Demekhin, and M. Schöffler, *The Journal of Physical Chemistry Letters* **8**, 2780 (2017), pMID: 28582620.

- [50] S. Daly, I. Powis, G. A. Garcia, M. Tia, and L. Nahon, *The Journal of Chemical Physics* **147**, 013937 (2017).
- [51] J. Miles, D. Fernandes, A. Young, C. Bond, S. Crane, O. Ghafur, D. Townsend, J. Sá, and J. Greenwood, *Analytica Chimica Acta* **984**, 134 (2017).
- [52] C. Lux, M. Wollenhaupt, T. Bolze, Q. Liang, J. Koehler, C. Sarpe, and T. Baumert, *Angewandte Chemie International Edition* **51**, 5001 (2012).
- [53] C. S. Lehmann, R. B. Ram, I. Powis, and M. H. M. Janssen, *The Journal of Chemical Physics* **139**, 234307 (2013).
- [54] M. M. Rafiee Fanoood, I. Powis, and M. H. M. Janssen, *The Journal of Physical Chemistry A* **118**, 11541 (2014), PMID: 25402546.
- [55] M. M. Rafiee Fanoood, M. H. M. Janssen, and I. Powis, *Phys. Chem. Chem. Phys.* **17**, 8614 (2015).
- [56] C. Lux, M. Wollenhaupt, C. Sarpe, and T. Baumert, *ChemPhysChem* **16**, 115 (2015).
- [57] C. Lux, A. Senftleben, C. Sarpe, M. Wollenhaupt, and T. Baumert, *Journal of Physics B: Atomic, Molecular and Optical Physics* **49**, 02LT01 (2016).
- [58] M. M. R. Fanoood, M. H. M. Janssen, and I. Powis, *The Journal of Chemical Physics* **145**, 124320 (2016).
- [59] A. Kastner, C. Lux, T. Ring, S. Züllighoven, C. Sarpe, A. Senftleben, and T. Baumert, *ChemPhysChem* **17**, 1119 (2016).
- [60] S. Beaulieu, A. Comby, A. Clergerie, J. Caillat, D. Descamps, N. Dudovich, B. Fabre, R. Gèneaux, F. Légaré, S. Petit, B. Pons, G. Porat, T. Ruchon, R. Taïeb, V. Blanchet, and Y. Mairesse, *Science* **358**, 1288 (2017).
- [61] A. Kastner, T. Ring, B. C. Krüger, G. B. Park, T. Schäfer, A. Senftleben, and T. Baumert, *The Journal of Chemical Physics* **147**, 013926 (2017).
- [62] A. Comby, S. Beaulieu, M. Boggio-Pasqua, D. Descamps, F. Legare, L. Nahon, S. Petit, B. Pons, B. Fabre, Y. Mairesse, and V. Blanchet, *The Journal of Physical Chemistry Letters* **7**, 4514 (2016).
- [63] S. Beaulieu, A. Ferre, R. Geneaux, R. Canonge, D. Descamps, B. Fabre, N. Fedorov, F. Legare, S. Petit, T. Ruchon, V. Blanchet, Y. Mairesse, and B. Pons, *New Journal of Physics* **18**, 102002 (2016).
- [64] S. Beaulieu, A. Comby, B. Fabre, D. Descamps, A. Ferre, G. Garcia, R. Geneaux, F. Legare, L. Nahon, S. Petit, T. Ruchon, B. Pons, V. Blanchet, and Y. Mairesse, *Faraday Discuss.* **194**, 325 (2016).
- [65] A. F. Ordonez and O. Smirnova, *Physical Review A* **99**, 043416 (2019).
- [66] W. Yao, D. Xiao, and Q. Niu, *Phys. Rev. B* **77**, 235406 (2008).
- [67] R. L. Dubs, S. N. Dixit, and V. McKoy, *Physical Review Letters* **54**, 1249 (1985).
- [68] R. L. Dubs, S. N. Dixit, and V. McKoy, *Physical Review B* **32**, 8389 (1985).
- [69] L. Holmegaard, J. L. Hansen, L. Kalhøj, S. Louise Kragh, H. Stapelfeldt, F. Filsinger, J. Küpper, G. Meijer, D. Dimitrovski, M. Abu-samha, C. P. J. Martiny, and L. Bojer Madsen, *Nature Physics* **6**, 428 (2010).

Synthetic chiral light for efficient control of chiral light matter interaction

David Ayuso,^{1,*} Ofer Neufeld,^{2,†} Andres F. Ordonez,^{1,3} Piero Decleva,⁴
Gavriel Lerner,² Oren Cohen,² Misha Ivanov,^{1,5,6,‡} Olga Smirnova^{1,3,§}

¹*Max-Born-Institut, Berlin, Germany*

²*Physics Department and Solid State Institute, Technion - Israel Institute of Technology, Haifa, Israel*

³*Technische Universität Berlin, Berlin, Germany*

⁴*Dipartimento di Scienze Chimiche e Farmaceutiche, Università degli Studi di Trieste, Trieste, Italy.*

⁵*Institute für Physik, Humboldt-Universität zu Berlin, Berlin, Germany.*

⁶*Department of Physics, Imperial College London, London, UK.*

This is the accepted version of an article published in Nature Photonics 13, 866 (2019). The published version is available online at <http://dx.doi.org/10.1038/s41566-019-0531-2>

Light is one of the most powerful and precise tools allowing us to control [1], shape [2, 3] and create new phases [4] of matter. In this task, the magnetic component of a light wave has so far played a unique role in defining the wave’s helicity, but it weakly influences the optical response of matter. Chiral molecules offer a typical example where the weakness of magnetic interactions hampers our ability to control the strength of their chiro-optical response [5], limiting it several orders of magnitude below the full potential. Here we introduce and theoretically analyze a new type of chiral light: freely propagating, *locally* and *globally* chiral electric fields, which interact with chiral matter extremely efficiently. We show that this *synthetic* chiral light enables full control over intensity, polarization and propagation direction of the nonlinear enantio-sensitive optical response of randomly oriented chiral molecules. This response can be quenched or enhanced at will in a desired enantiomer, opening efficient ways for controlling chiral matter and for ultrafast imaging of chiral dynamics in gases, liquids and solids.

Chiral molecules appear in pairs of left and right-handed enantiomers, where their nuclear arrangements present two non-superimposable mirror twins. The general importance of chiral structures makes identification of molecular handedness vital [5]. Two groups of approaches [7] address this challenge using light. The first one analyses vectorial observables [8–22], such as the direction of the photo-electron current [8–13] upon ionization with circularly polarized light with respect to a reference frame defined by the experimental setup. While the total signal intensity –the total number of photo-electrons– is the same in opposite enantiomers, the current direction is enantio-sensitive. Another important example is nonlinear-optical wave-mixing [14–18], where two incident waves with frequencies ω_1 and ω_2 generate response at the sum frequency $\omega_3 = \omega_1 + \omega_2$ in randomly oriented chiral media, a process that is strictly prohibited in isotropic non-chiral media. In addition to purely dipole effects, for which the intensity of chiral signal is the same in opposite enantiomers, one can also take advantage of their interference with non-dipole contributions to sum frequency generation [19].

The second group of techniques rely on the helical structure of circularly or elliptically polarized light to

probe chirality. They allow us to access fundamentally different observables: enantio-sensitive total signal intensities. A well-known example is photo-absorption circular dichroism [5], manifested in the different absorption intensities of left-handed and right-handed circularly polarized light. This group of techniques rely on the interplay between electric and magnetic interactions, and include the recent pioneering work of Cireasa et al [6], which demonstrated that high harmonic generation can be enantio-sensitive. Here, light serves as a chiral *reagent*.

However, circularly (or elliptically) polarized light makes a poor chiral reagent in the optical domain, because the micron-scale pitch of the light helix is too large compared to the angstrom-scale size of a molecule. The dominant part of the optical response arises in the dipole approximation, where the spatial extent of the molecule is negligible compared to the light wavelength. In the dipole approximation, the Lissajous curve drawn by the tip of the electric field vector forms a circle, that is, a two-dimensional planar structure. Confinement of light polarization to a plane makes it non-chiral, and thus the dominant part of the emitted or absorbed light intensity is not enantio-sensitive.

Here we show that freely propagating optical fields can be made chiral already in the dipole approximation. We introduce *synthetic* chiral light, a new type of light in which the tip of the electric field vector draws a chiral, three-dimensional Lissajous curve in time, at each fixed point in space. Such light is *locally* chiral: unlike circularly polarized light, its chirality does not rely

* david.ayuso@mbi-berlin.de

‡ mikhaail.ivanov@mbi-berlin.de

§ olga.smirnova@mbi-berlin.de

† These authors contributed equally to this work.

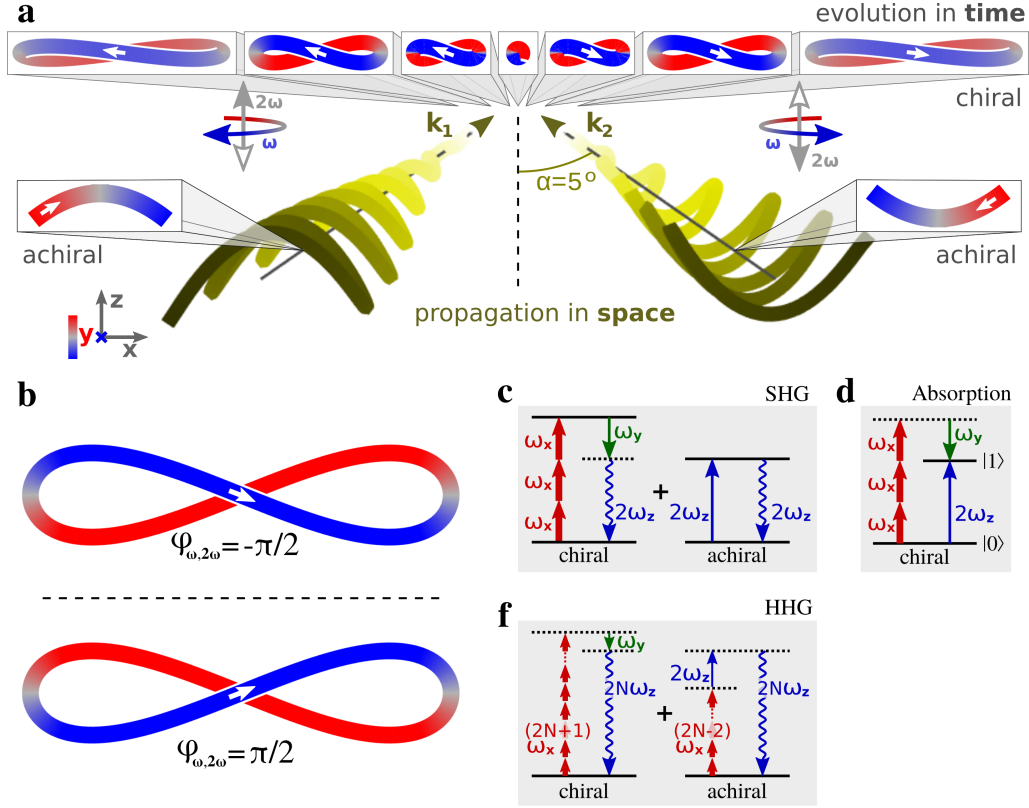


FIG. 1. **Synthetic chiral light.** **a**, Locally and globally chiral light can be synthesized using two non-collinear laser beams, each carrying orthogonally polarized ω and 2ω fields. The total ω field is elliptic in the xy plane, the 2ω field is linear along z , generating locally the Lissajous curves in the insets. **b**, Lissajous curves of Eq. (2) for $F_\omega, F_{2\omega}, \epsilon > 0$ and $\phi_{\omega,2\omega} = \mp\pi/2$ correspond to reflection through the xy plane, which interconverts the two field enantiomers. **c**, **d**, Interference of chiral and achiral pathways in second harmonic generation (SHG) (c) and 2ω absorption (d), controlled by $h^{(5)}$. **e**, Interference of chiral and achiral pathways in even high harmonic generation (HHG).

on the spatial helix of the light field. Thus, it remains chiral in the dipole approximation. We formulate a general theory that describes the properties of these new electromagnetic chiral objects and their interaction with matter. We show how to generate such light practically, characterize and control its handedness, and maintain it *globally* across the entire interaction region. Synthetic chiral light enables the highest possible degree of control over the macroscopic enantio-sensitive response at the level of optical signal intensities, quenching it in one enantiomer while maximizing it in its mirror twin. We emphasize that such a giant enantio-sensitivity is possible because the interaction of synthetic chiral light with chiral matter is enantio-sensitive in the dipole approximation at the level of total signal intensities, making our work fundamentally different from previous works.

We begin by establishing the general requirements for creating synthetic chiral light and introduce new measures that quantify its handedness. These are required because the previously employed measure of optical chirality [23] vanishes in the electric-dipole approximation. To quantify the degree of chirality of a locally chiral field, we developed several complementary approaches. First,

we take advantage of tools developed in chemistry for characterizing the degree of chirality of molecular structures, and extend them to electromagnetic fields, see Supplementary Information (SI). Second, we developed a group theoretical approach [22, 24] that provides guidelines for synthesizing locally chiral fields (see Methods and SI). Third, we introduce a measure that characterizes not only light chirality on its own, but also predicts the strength of the interaction of synthetic chiral light with matter. To this end, we sample the electric field vector at three different instants of time, and evaluate the triple product of these three vectors. Such triple product forms a ubiquitous chiral measure [7, 12, 17, 25, 26], which has never been used to characterize light fields. We average this triple product over time to sample the entire Lissajous curve. The measure yields a special, chiral, three-point correlation function (see Methods) which (i) distinguishes left-handed and right-handed light and (ii) allows one to engineer desired waveforms to control the total intensity of dipole chiro-optical response.

We present here the main ingredients of this new formalism (see Methods for full description). The lowest order chiral field-correlation function in the frequency do-

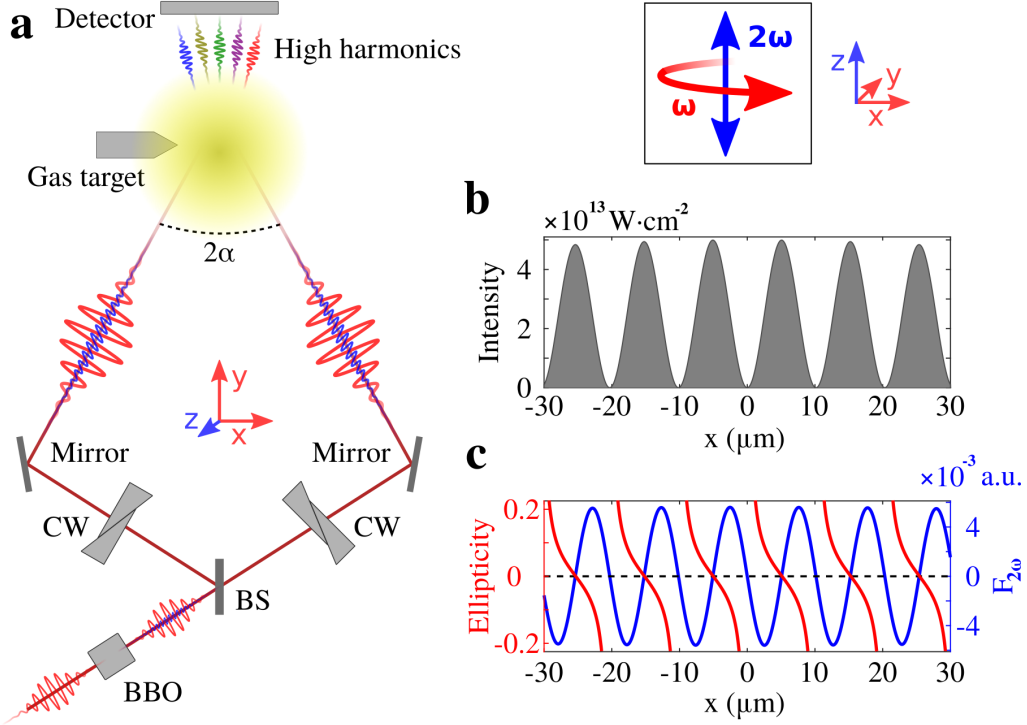


FIG. 2. **Practical setup.** **a**, A linearly polarized ω beam is frequency doubled in a nonlinear (BBO) crystal, generating an orthogonally polarized 2ω field. After the beam splitter (BS), $\phi_{\omega,2\omega}^{(1,2)}$ are tuned with calcite wedges (CW). The two beams are refocused in a non-collinear geometry ($2\alpha = 10^\circ$). The gas target is placed before the focus to favour phase matching of “short HHG trajectories”. The two noncollinear beams generate intensity (**b**) and ellipticity gratings of the ω field (**c**, red curve) and amplitude grating of the 2ω field (**c**, blue curve) in the transverse direction. The nodes of the ω -field ellipticity grating and the 2ω -field amplitude grating are aligned (**c**), so that the synthetic chiral light maintains handedness across the interaction region. The intensity in each beam is $I_1 = I_2 = 1.25 \cdot 10^{13} \text{ Wcm}^{-2}$, and thus the total intensity (**b**) reaches the maximum value of $I_{\text{max}} = (\sqrt{I_1} + \sqrt{I_2})^2 = 5 \cdot 10^{13} \text{ Wcm}^{-2}$, as in the experiment of Ref. [6].

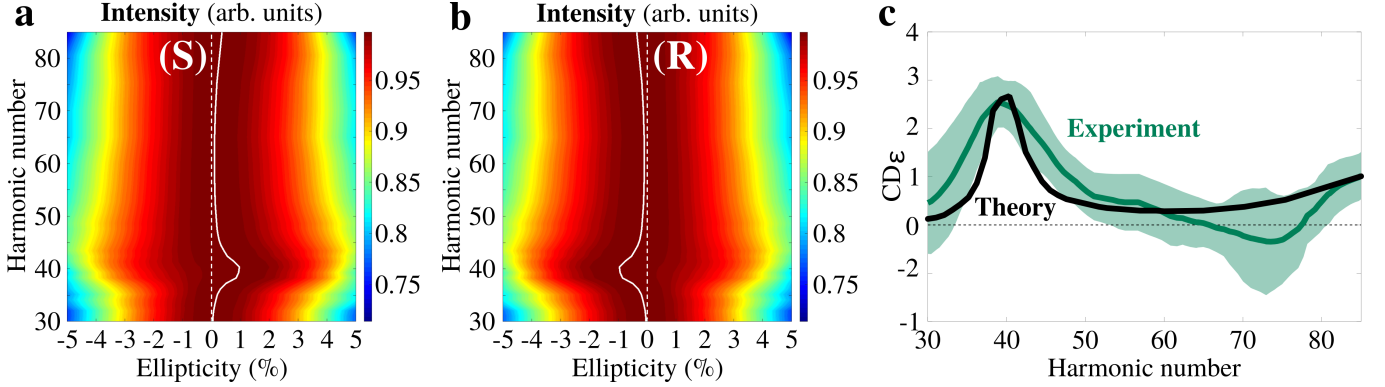


FIG. 3. **Chiral response in high harmonic generation using standard chiral light.** **a, b**, High harmonic intensity calculated for randomly oriented *S* and *R* propylene oxide molecules in elliptically polarized laser fields with intensity $I_0 = 5 \cdot 10^{13} \text{ W}\cdot\text{cm}^{-2}$ and wavelength $\lambda = 1770 \text{ nm}$. For each harmonic order N , the intensity is normalized to its maximum value. The white line shows the ellipticity $\epsilon_0(N)$ that maximizes the harmonic intensity. **c**, Chiral dichroism normalized to ϵ , $CD_\epsilon(N) = \frac{2}{\epsilon} \frac{I_S(N) - I_R(N)}{I_S(N) + I_R(N)}$: theoretical results (black line) vs experimental values of Ref. [6] (green line). The shaded area shows the experimental error-bars. Chiral dichroism $CD(N) = 2 \frac{I_S(N) - I_R(N)}{I_S(N) + I_R(N)}$ reaches $\sim 3\%$ for $\epsilon \sim 1\%$.

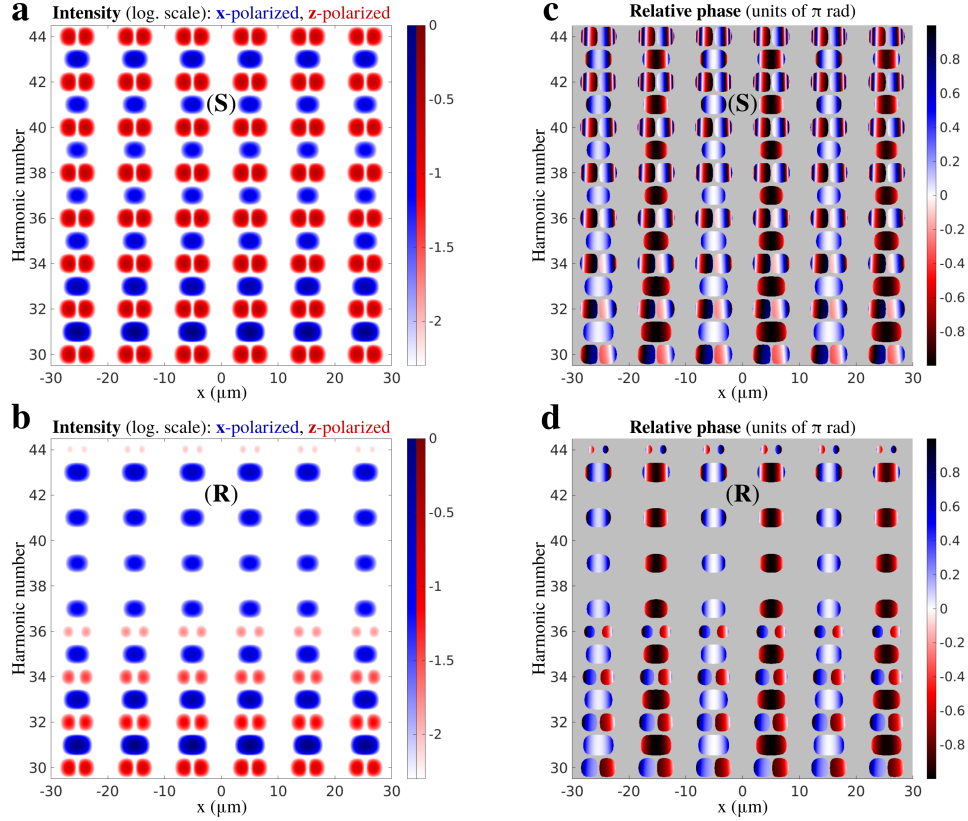


FIG. 4. **Near field enantio-sensitive high harmonic generation using synthetic chiral light.** Enantio-sensitive polarization grating created in enantiopure samples of *S* and *R* propylene oxide molecules: intensity (**a**, **b**) and relative phase (**c**, **d**) of harmonic response in randomly oriented propylene oxide as functions of harmonic number and transverse (x) coordinate of the interaction region. The fundamental wavelength is $\lambda = 1770\text{nm}$, intensity $I_\omega = 1.25 \cdot 10^{13}\text{W}\cdot\text{cm}^{-2}$, $I_{2\omega} = 0.01I_\omega$, $\phi_{\omega,2\omega} = \pi$, pulse duration 23 fsec at constant intensity, $\alpha = 5^\circ$, focal diameter $400\mu\text{m}$.

main is

$$h^{(3)}(-(\omega_1 + \omega_2), \omega_1, \omega_2) \equiv \mathbf{F}^*(\omega_1 + \omega_2) \cdot [\mathbf{F}(\omega_1) \times \mathbf{F}(\omega_2)], \quad (1)$$

where $\mathbf{F}(\omega_i)$ are the Fourier components of the electric field vector at three different frequencies. $h^{(3)}$ governs perturbative light-matter interaction, such as absorption circular dichroism induced solely by laser electric fields, replacing the optical chirality [23] in the dipole approximation (see Methods). Using the formalism of [7], one can show that $h^{(3)}$ also quantifies the control of enantio-sensitive population of rotational states in chiral molecules [25] using microwave fields.

To have non-zero $h^{(3)}$, synthetic chiral light needs three different non-co-planar frequency components: ω_1 , ω_2 , and $\omega_3 = \omega_1 + \omega_2$. Nevertheless, synthetic chiral light can be realized with just two frequency components, ω and 2ω . One possible realization is an elliptically polarized ω field and a linear 2ω field polarized orthogonal to the ellipse:

$$F_\omega \cos(\omega t)\mathbf{x} + \varepsilon F_\omega \sin(\omega t)\mathbf{y} + F_{2\omega} \cos(2\omega t + \phi_{\omega,2\omega})\mathbf{z} \quad (2)$$

Such light can be created with the beam configuration shown in Fig. 1a. The electric field vector draws a chiral

Lissajous curve (Fig. 1a,b), with the shape controlled by $\phi_{\omega,2\omega}$. Changing $\phi_{\omega,2\omega}$ by π changes the handedness of the Lissajous curve, see Fig. 1b. Although $h^{(3)} = 0$ for this field, its chirality is manifested in higher order correlations, which can be perfectly put to use in higher order nonlinear light-matter interactions. Indeed, the next order chiral correlation function for this field (see Methods)

$$h^{(5)}(-2\omega, -\omega, \omega, \omega, \omega) \equiv \{\mathbf{F}^*(2\omega) \cdot [\mathbf{F}^*(\omega) \times \mathbf{F}(\omega)]\} [\mathbf{F}(\omega) \cdot \mathbf{F}(\omega)] \quad (3)$$

is nonzero. It describes the interference of the two pathways shown in Fig. 1c. In the chiral pathway, the system absorbs three photons from the (main) x component of the ω field and emits one photon into the (minor) y component. The last two steps record the ellipticity of the ω field. In isotropic chiral media, the induced polarization associated with this path is directed along z . This process is unique to chiral media, where chiral response occurs due to interactions involving an even number of photons, both in the weak-field [17] and strong-field [22] regimes. In isotropic achiral media, such processes are symmetry-forbidden. In the second, achiral, pathway, the system absorbs one 2ω photon from the z field component, also

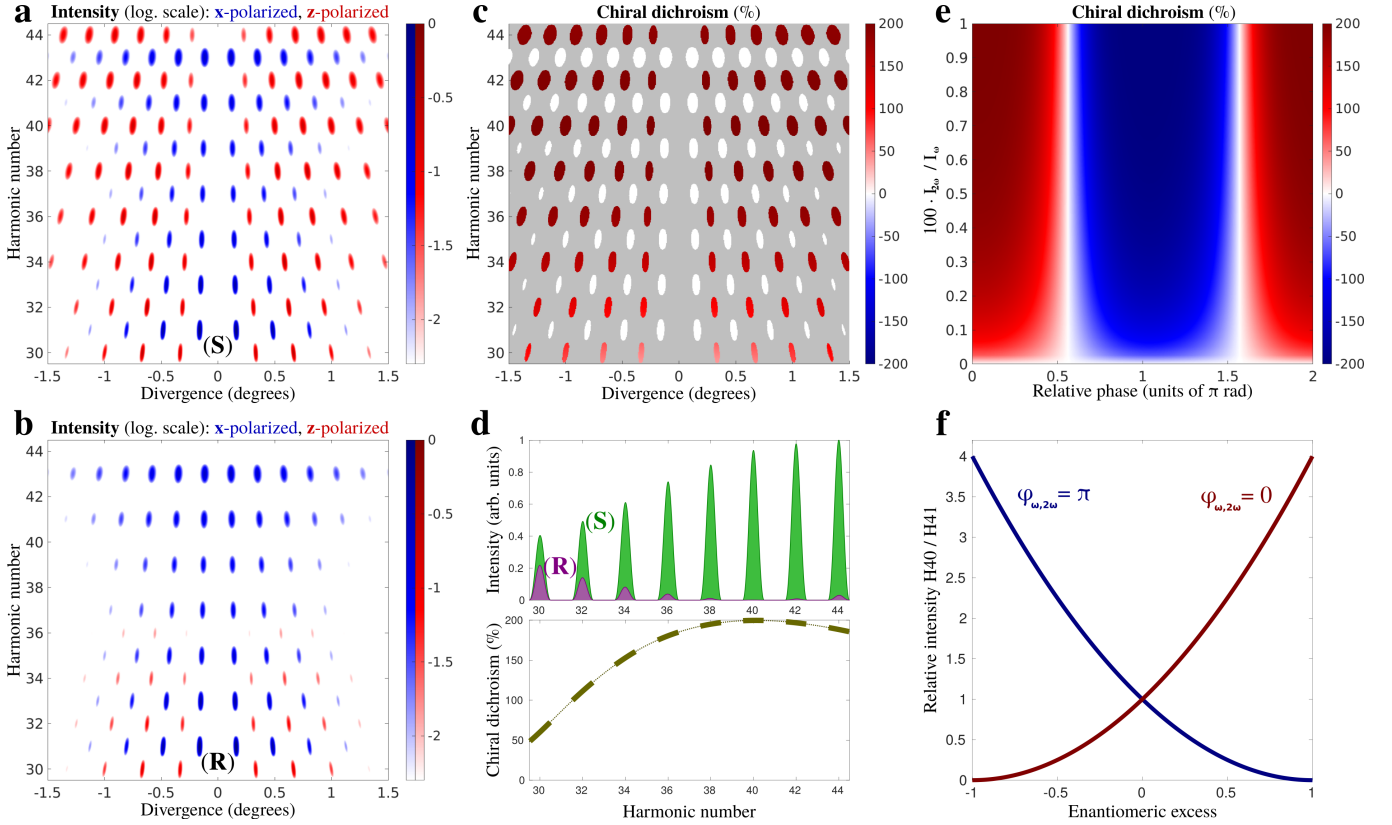


FIG. 5. **Far-field harmonic intensity and chiral dichroism.** **a, b**, Harmonic intensity for randomly oriented enantiopure *S* and *R* propylene oxide molecules, for the same field as in Fig. 4, with $I_{2\omega}/I_\omega = 0.01$ and $\phi_{\omega,2\omega} = \pi$. Shifting $\phi_{\omega,2\omega}$ by π is equivalent to exchanging the enantiomer. **c**, Chiral dichroism in the harmonic intensity, $CD = 2 \frac{I_S - I_R}{I_S + I_R}$. **d**, Total angle-integrated even harmonic intensity and chiral dichroism. **e**, Chiral dichroism in H40 versus $\phi_{\omega,2\omega}$ and relative intensity between the two colors. **f**, Intensity ratio between H40 and H41 as a function of the enantiomeric excess when $I_{2\omega}/I_\omega = 0.01$ and $\phi_{\omega,2\omega} = 0$ (red) and $\phi_{\omega,2\omega} = \pi$ (blue).

leading to polarization along z . As the chiral and achiral polarizations are directed along the same axis, they interfere. Their interference, controlled by $\phi_{\omega,2\omega}$, yields the chiral fifth-order field correlation function $h^{(5)}$, which describes enantio-sensitive emission and absorption at frequency 2ω (Fig. 1c,d and Methods). $h^{(5)}$ changes sign when $\phi_{\omega,2\omega}$ is shifted by π , reflecting the reversal of the field handedness in Fig. 1b.

Tuning $\phi_{\omega,2\omega}$ and the relative field strengths, we can achieve perfect constructive or destructive interference of the two paths (Fig. 1c,d) and fully suppress or maximally enhance the signal intensity in a selected enantiomer (see Methods). Enantio-sensitive interference in higher-order harmonics, such as shown in Fig. 1e, is described by higher-order correlation functions (see SI). Thus, we now have a chiral photonic reagent, whose handedness can be tailored to control multiphoton interactions, with extremely high efficiency.

A practical realization of the field configuration in Fig. 1a is shown in Fig. 2a. The suggested experimental setup produces two non-collinear beams with wavevectors \mathbf{k}_n ($n = 1, 2$) propagating in the xy plane at small angles $\pm\alpha$ to the y axis (here $\alpha = 5^\circ$). Each beam carries

orthogonally polarized ω and 2ω fields with controlled $\phi_{\omega,2\omega}^{(n)}$. The total ω field is elliptically polarized in the xy plane, with its minor component along the propagation direction y (Fig. 2a, inset).

Obtaining enantio-sensitive harmonic signals in the macroscopic emission requires the local handedness of the light field to be maintained across the interaction region. That is, synthetic light needs to be chiral not only *locally*, but also *globally*. This is achieved in our setup. Indeed, the two beams (Fig 2a) form amplitude (Fig. 2b) and ellipticity (Fig. 2c) gratings for the ω field and an amplitude grating (Fig. 2c) for the 2ω field. To maintain the field handedness, these two gratings must be aligned, so that their nodes coincide (Fig. 2c). This is achieved by setting $\phi_{\omega,2\omega}^{(2)} - \phi_{\omega,2\omega}^{(1)} = \pi$ using calcite wedges (Fig. 2a). As a result, the Lissajous curve maintains its handedness across the interaction region (Fig. 1a). Changing $\phi_{\omega,2\omega}^{(1)}$ and $\phi_{\omega,2\omega}^{(2)}$ synchronously while keeping $\phi_{\omega,2\omega}^{(2)} - \phi_{\omega,2\omega}^{(1)} = \pi$, controls the field handedness locally and globally. Dispersion does not change $\phi_{\omega,2\omega}^{(n)}$ across the interaction region [27, 28] for medium thickness $d \leq 3$ mm at pressures < 1 bar, sufficient for strong HHG signal [6, 27, 28]. In

liquids, dispersion would limit d to few μm .

To describe high harmonic generation (HHG) in randomly oriented chiral molecules, we developed a quantitative model in propylene oxide (see Methods). Fig. 3 shows the strength of the enantio-sensitive high harmonic intensities obtained when using single-beam, single-color light at $\lambda = 1770$ nm, elliptically polarized transverse to its propagation direction. In this setup, the chiral response is only possible beyond the dipole approximation [6]. These results provide two benchmarks. First, they show the excellent agreement between our model and the experimental results of [6]. Second, they provide a reference point for comparing the efficiency of natural and synthetic chiral light in generating enantio-sensitive high harmonic signals, for the same fundamental frequency, total intensity, ellipticity, and the same medium. The chiral dichroism obtained when using the spatial helix of light reaches 2 – 3% for weak ellipticities (see Fig. 3c).

We now turn to synthetic chiral light. The periodic locally chiral structure of the synthetic light field along the x axis (Fig. 1a, top row, Fig. 2c) leads to the enantio-sensitive intensity (Figs. 4a,b) and phase (Figs. 4c,d) gratings of the generated high harmonic response. The intensity of the second harmonic field is 1% of the fundamental, and $\phi_{\omega,2\omega} = \pi$. In our setup, even harmonics of the fundamental can only be z -polarized, whereas odd harmonics are polarized along x due to symmetry constraints [24]. The gratings in Fig. 4 for z -polarized even harmonics are completely different for opposite enantiomers, demonstrating strong enantio-sensitivity of the optical response already at the single-molecule level. Note that, while the near-field phase grating is not usually directly detected, it determines the signal intensity in the far field. Such a strong enantio-sensitivity is possible because (i) the driving field is chiral in the dipole approximation (locally chiral), and (ii) its handedness is fully controlled in our setup. Note also the different amplitude and phase grating of the orthogonal polarization components: whereas the x -polarized component maximizes at the intensity peaks of the driving field, at these positions the enantio-sensitive z -polarized component is symmetry forbidden, as the driver is linearly polarized.

Figs. 5a,b show how the enantio-sensitive gratings translate into the far field. The far field image is a series of diffraction minima and maxima, generated by the propagated near-field emission (see Methods). As a result of the different amplitude and phase gratings (Fig. 4), even and odd harmonics are emitted in different directions. Their spatial separation can also be understood from momentum conservation upon net absorption of the corresponding number of photons. Thus, the strongly enantio-sensitive signal at even harmonics is separated from the non-enantio-sensitive signal at odd harmonics in frequency, polarization and space.

The mechanism of control over enantio-sensitive HHG

can be described in terms of interfering chiral and achiral pathways (see SI). It can also be viewed semiclassically. In strong laser fields, HHG can be understood as a sequence of three steps: tunnel ionization, laser-driven electron propagation in the continuum, and radiative electron-core recombination. Synthetic chiral light makes the electron trajectory in the continuum chiral. We can control its handedness by tuning $\phi_{\omega,2\omega}$, imprinting the chirality of light on the electron. The control over the handedness and the three-dimensional structure of the electron trajectory in the continuum controls the strength of the enantio-sensitive electron recombination with the chiral parent ion. Here we completely suppress the signal from the right-handed molecule I_R for H40 when setting $\phi_{\omega,2\omega} = \pi$. Shifting $\phi_{\omega,2\omega}$ by π reverses the handedness of the driver, and thus the handedness of the electron trajectory in the continuum. As a result, we obtain the opposite result: suppression of I_S and enhancement of I_R (see Fig. 5e). For H40, chiral dichroism, $CD = 2\frac{I_S - I_R}{I_S + I_R}$, reaches the ultimate limit of 200% (see Fig. 5c-e).

The harmonic order(s) that exhibit 200% dichroism can be selected by tuning the laser field parameters and used for concentration-independent determination of both the amplitude and sign of the enantiomeric excess ee in macroscopic mixtures, from simple intensity measurements (Fig. 5f). For such harmonics, the intensity ratio between consecutive harmonics is $\frac{I_{2N}}{I_{2N+1}} \simeq (1 \pm ee)^2 \frac{I_{2N}}{I_{2N+1}} \Big|_{ee=0}$, where $\frac{I_{2N}}{I_{2N+1}} \Big|_{ee=0}$ is the intensity ratio in a racemic mixture (see Methods).

One can also create synthetic chiral fields which carry several elements of chirality or change their handedness in space (see SI). They may present alternative opportunities for studying matter with similar spatial chirality patterns, or for exciting such patterns on demand.

Our theory introduces and describes a new intrinsic property of electromagnetic fields – their local and global chirality. By laying down the foundation for generating, utilizing and controlling such synthetic chiral light, it opens new routes for enantio-sensitive sensing in all phases of matter. This includes selective monitoring of enantiomers with a specific handedness in non-enantiopure samples undergoing a chemical reaction, with ultrafast time resolution. The possibility of driving enantio-selective excitations in chiral molecules brings new opportunities for laser-based separation of enantiomers. Synthetic chiral light can also be used to imprint chirality on achiral matter efficiently [29], extending the recent proposal of Ref. [30] from molecular rotations to other degrees of freedom. Looking broadly, these opportunities can be used to realize laser-driven "achiral-chiral" phase transitions in matter.

METHODS

Chiral-field correlation functions

For a locally chiral field with electric field vector $\mathbf{F}(t)$ the lowest order chiral-field correlation function is a pseudoscalar

$$H^{(3)}(\tau_1, \tau_2) \equiv \frac{1}{2\pi} \int dt \mathbf{F}(t) \cdot [\mathbf{F}(t + \tau_1) \times \mathbf{F}(t + \tau_2)]. \quad (4)$$

Its complex counterpart in the frequency domain,

$$h^{(3)}(-(\omega_1 + \omega_2), \omega_1, \omega_2) \equiv \int d\tau_1 \int d\tau_2 H^{(3)}(\tau_1, \tau_2) e^{-i\omega_1 \tau_1} e^{-i\omega_2 \tau_2}, \quad (5)$$

yields Eq. (1) of the main text.

$h^{(3)}$ describes perturbative enantio-sensitive three-photon light matter interaction. As shown here, it appears as a light pseudoscalar in absorption circular dichroism in the electric-dipole approximation, analogously to how the optical chirality [23] of circularly polarized light contributes to standard absorption circular dichroism beyond the electric-dipole approximation.

Consider a field with frequencies ω_1 , ω_2 , and $\omega_3 \equiv \omega_2 + \omega_1$

$$\mathbf{F}(t) = \mathbf{F}_1 e^{-i\omega_1 t} + \mathbf{F}_2 e^{-i\omega_2 t} + \mathbf{F}_3 e^{-i\omega_3 t} + \text{c.c.} \quad (6)$$

The contribution from second order induced polarization is enantio-sensitive [17] and can be written as (see also [31]):

$$\mathbf{P}^{(2)}(\omega_3) = \frac{1}{3} \epsilon_{\alpha\beta\gamma} \chi_{\alpha\beta\gamma}^{(2)}(\omega_3 = \omega_1 + \omega_2) [\mathbf{F}(\omega_1) \times \mathbf{F}(\omega_2)]. \quad (7)$$

Note that $\mathbf{P}^{(2)}(\omega_3)$ vanishes if $\omega_1 = \omega_2$ [17]. Thus, for the field in Eq. (6) we obtain:

$$\mathbf{P}^{(2)}(\omega_1) = \frac{1}{3} \epsilon_{\alpha\beta\gamma} \chi_{\alpha\beta\gamma}^{(2)}(\omega_1 = \omega_3 - \omega_2) (\mathbf{F}_3 \times \mathbf{F}_2^*), \quad (8)$$

$$\mathbf{P}^{(2)}(\omega_2) = \frac{1}{3} \epsilon_{\alpha\beta\gamma} \chi_{\alpha\beta\gamma}^{(2)}(\omega_2 = \omega_3 - \omega_1) (\mathbf{F}_3 \times \mathbf{F}_1^*), \quad (9)$$

$$\mathbf{P}^{(2)}(\omega_3) = \frac{1}{3} \epsilon_{\alpha\beta\gamma} \chi_{\alpha\beta\gamma}^{(2)}(\omega_3 = \omega_2 + \omega_1) (\mathbf{F}_2 \times \mathbf{F}_1). \quad (10)$$

The second-order response at the difference frequency $\omega_2 - \omega_1$ does not contribute to absorption because this frequency is absent in the driving field. Using the standard definition for the total energy \mathcal{E} exchanged between the field and the molecule,

$$\mathcal{E} = \int_{-\infty}^{\infty} dt \mathbf{F}(t) \cdot \dot{\mathbf{P}}(t) = -2\pi i \int d\omega \omega \mathbf{F}(-\omega) \cdot \mathbf{P}(\omega), \quad (11)$$

and replacing Eqs. (8), (9), and (10) in Eq. (11) we obtain

$$\mathcal{E}^{(2)} = \frac{4\pi}{3} \text{Im} \left\{ \left[-\omega_1 \epsilon_{\alpha\beta\gamma} \chi_{\alpha\beta\gamma}^{(2)*}(\omega_1 = \omega_3 - \omega_2) + \omega_2 \epsilon_{\alpha\beta\gamma} \chi_{\alpha\beta\gamma}^{(2)*}(\omega_2 = \omega_3 - \omega_1) + \omega_3 \epsilon_{\alpha\beta\gamma} \chi_{\alpha\beta\gamma}^{(2)}(\omega_3 = \omega_2 + \omega_1) \right] [\mathbf{F}_3^* \cdot (\mathbf{F}_2 \times \mathbf{F}_1)] \right\}. \quad (12)$$

Equation (12) shows that enantio-sensitive light absorption is controlled by the third-order correlation function $h^{(3)}$ in Eq. (1). Indeed, it is proportional to the imaginary part of a product of two pseudoscalars: the first one is associated with the chiral medium and involves second order susceptibilities, the second one is associated with the locally chiral field and is given by its correlation function $h^{(3)} = [\mathbf{F}_3^* \cdot (\mathbf{F}_2 \times \mathbf{F}_1)]$. An analogous expression applies for a field with frequencies ω_1 , ω_2 , and $\omega_1 - \omega_2$.

Control over the enantio-sensitive optical response

Here we describe the mechanism of control over enantio-sensitive optical response in the perturbative multiphoton regime. In ordinary isotropic media, dipole-allowed interactions must involve an odd number of photons. In contrast, in the electric-dipole approximation, isotropic chiral media can generate chiral response due to interactions involving an even number of photons, both in the weak-field [17] and strong-field [22] regimes. This difference allows one to differentiate between chiral and non-chiral media in the intensity of nonlinear optical response associated with even number of absorbed photons. However, the signal intensity is the same for right-handed and left-handed enantiomers, and their response differs only by a global phase [20, 22].

Locally chiral fields make the signal intensity enantio-sensitive and allow one to control its strength depending on the molecular handedness. Indeed, consider the intensity of the optical response triggered by the ω - 2ω field (Fig. 1a,b) at frequency 2ω . Since the enantio-sensitive second order susceptibility $\chi^{(2)}(2\omega; \omega, \omega) = 0$ (see e.g. [17]), the lowest order enantio-sensitive multiphoton process involves four photons of frequency ω in the chiral channel and one photon of frequency 2ω in the achiral channel:

$$|\mathbf{P}(2\omega)|^2 = \left| \chi^{(4)} [\mathbf{F}^*(\omega) \times \mathbf{F}(\omega)] [\mathbf{F}(\omega) \cdot \mathbf{F}(\omega)] + \chi^{(1)} \mathbf{F}(2\omega) \right|^2 = (\text{diagonal terms}) + \chi^{(1)*} \chi^{(4)} h^{(5)} + \text{c.c.} \quad (13)$$

Here $\mathbf{P}(2\omega)$ is the induced polarization at 2ω , $\chi^{(4)} = \sigma_M |\chi^{(4)}| e^{i\phi_4}$ is the enantio-sensitive fourth-order susceptibility (see SI), and $\chi^{(1)} = |\chi^{(1)}| e^{i\phi_1}$ is the achiral linear susceptibility. The interference term

$$2\sigma_M \sigma_L |\chi^{(1)}| |\chi^{(4)}| |h^{(5)}| \cos(\phi_M + \phi_{\omega, 2\omega}) \quad (14)$$

is controlled by the chiral-field correlation function $h^{(5)} = \sigma_L |h^{(5)}| e^{i\phi_{\omega, 2\omega}}$. It depends on the molecular phase $\phi_M = \phi_4 - \phi_1$ associated with complex susceptibilities, the relative phase $\phi_{\omega, 2\omega}$ between the ω and 2ω field components, the handedness of the molecule $\sigma_M = \pm 1$, and the sense of in-plane rotation of light $\sigma_L = \pm 1$. Eqs. (13) and (14) show that tuning the strengths and the relative phase $\phi_{\omega, 2\omega}$ between the ω and 2ω fields we can achieve perfect constructive/destructive interference and fully suppress or maximally enhance the signal intensity in the selected enantiomer (see Fig. 1c). No additional achiral background channels are allowed due to selection rules. The same interference controls absorption of the 2ω field (Fig. 1d), but the mathematical expression is, of course, different. The derivation of Eq. (13) and the associated susceptibility tensors $\chi^{(1)}$ and $\chi^{(4)}$ in randomly oriented media is discussed in the SI.

Fifth-order chiral-field correlation function

The different chiral-field correlation functions $h^{(n)}$, with n odd, control the sign of the enantio-sensitive and dichroic response in multiphoton interactions. For the locally chiral field employed in our work (see Eq. (2)), $h^{(5)}$ is the lowest-order non-vanishing chiral-field correlation function. Here we show that $h^{(5)}$ has a unique form for this field.

We write the field in Eq. (2) in the exponential form

$$\mathbf{F}(t) = (F_x \hat{\mathbf{x}} + iF_y \hat{\mathbf{y}}) e^{-i(\omega t + \delta_\omega)} + F_z \hat{\mathbf{z}} e^{-2i(\omega t + \delta_{2\omega})} + c.c., \quad (15)$$

and the fifth-order chiral-field correlation function as

$$h^{(5)}(\omega_0, \omega_1, \omega_2, \omega_3, \omega_4) \equiv \{\mathbf{F}(\omega_0) \cdot [\mathbf{F}(\omega_1) \times \mathbf{F}(\omega_2)]\} [\mathbf{F}(\omega_3) \cdot \mathbf{F}(\omega_4)], \quad (16)$$

where

$$\omega_0 + \omega_1 + \omega_2 + \omega_3 + \omega_4 = 0. \quad (17)$$

First, note that $h^{(5)}$ is symmetric with respect to exchange of ω_3 and ω_4 , and symmetric/anti-symmetric with respect to even/odd permutations of ω_0 , ω_1 , and ω_2 . Non-trivially different forms of $h^{(5)}$ result only from considering exchanges between $\{\omega_0, \omega_1, \omega_2\}$ and $\{\omega_3, \omega_4\}$. In the following we show that the field (Eq. (2) of the main text) yields a unique non-zero form of $h^{(5)}$.

For $h^{(5)}$ to be non-vanishing, the triple product in $h^{(5)}$ must contain the three different vectors available in our field, namely $F_x \hat{\mathbf{x}} + iF_y \hat{\mathbf{y}}$, $F_x \hat{\mathbf{x}} - iF_y \hat{\mathbf{y}}$ (from the c.c. part), and $\hat{\mathbf{z}}$. The remaining scalar product must have frequencies such that Eq. (17) is satisfied. This means that we have the following four options for $h^{(5)}$:

$$h_a^{(5)} = h^{(5)}(-2\omega, -\omega, \omega, \omega) \quad (18)$$

$$h_b^{(5)} = h^{(5)}(-2\omega, \omega, -\omega, \omega) \quad (19)$$

$$h_c^{(5)} = h^{(5)}(2\omega, \omega, -\omega, -\omega) \quad (20)$$

$$h_d^{(5)} = h^{(5)}(2\omega, -\omega, \omega, -\omega) \quad (21)$$

Since $\mathbf{F}(\omega_2) \times \mathbf{F}(\omega_1) = -\mathbf{F}(\omega_1) \times \mathbf{F}(\omega_2)$ and $\mathbf{F}(t)$ is real, then

$$h_b^{(5)} = -h_a^{(5)} \quad (22)$$

$$h_c^{(5)} = h_a^{(5)*} \quad (23)$$

$$h_d^{(5)} = -h_c^{(5)} \quad (24)$$

so that all options are actually equivalent to each other up to either a sign, a complex conjugation, or both. The ambiguity in the sign reflects the fact that in general right-handed and left-handed cannot be defined in an absolute way, i.e. without reference to another chiral object, so it is equally valid to define a chiral measure $h^{(5)} = h_a^{(5)}$ or a chiral measure $h^{(5)} = h_b^{(5)} = -h_a^{(5)}$ to characterize the ‘‘absolute’’ handedness of the field. Choosing $h_a^{(5)}$ or $h_b^{(5)}$, i.e. ordering vectors in the vector product, corresponds to choosing a left- or a right-handed reference frame. On the other hand, if we consider the interaction with matter, $h^{(5)}$ and $h^{(5)*}$ appear on the same footing (see Eq. (13)), therefore it is only natural that we have found both options in this derivation. Even if we consider the field by itself, since $h^{(5)}$ is the Fourier transform of a real quantity, $h^{(5)}$ and $h^{(5)*}$ contain the same information, so it is again to be expected that we find both options in our derivation.

Replacing Eqs. (15) and (16) in Eq. (18) we obtain

$$h_a^{(5)} = 2iF_x F_y F_z (F_x^2 - F_y^2) e^{2i(\delta_{2\omega} - \delta_\omega)}, \quad (25)$$

so that $h_a^{(5)}$ is sensitive to the phase difference between the two colors and also to the sign of the ellipticity of the ω field $\varepsilon \equiv F_y/F_x$. In the supplementary information we show that, although the chiral-field correlation function $h^{(n)}$ does not have a unique non-zero form for higher odd orders $n = 7, 9, \dots$, only a single form is non-negligible provided that the fields along y and z are weak in comparison to the field along x , such as the field employed in the main text.

Practical generation of synthetic chiral light

We can generate synthetic light fields that are locally and globally chiral using the non-collinear setup presented in Fig. 2a. It consists of two beams that propagate along \mathbf{k}_1 and \mathbf{k}_2 , in the xy plane, creating angles $\pm\alpha$ with the y axis. Each beam is composed of a linearly polarized field, whose polarization is contained in the xy plane, and a z -polarized second harmonic. We shall assume that the two beams ($n = 1, 2$) are Gaussian beams [32], and thus their electric fields can be written at the focus as

$$\mathbf{F}_n^\omega(\mathbf{r}, t) = F_0 e^{-\rho_n^2/\tilde{\omega}^2} \cos(\mathbf{k}_n \cdot \mathbf{r} - \omega t - \phi_n^\omega) \hat{\mathbf{e}}_n \quad (26)$$

$$\mathbf{F}_n^{2\omega}(\mathbf{r}, t) = r_0 F_0 e^{-\rho_n^2/\tilde{\omega}^2} \cos(2\mathbf{k}_n \cdot \mathbf{r} - 2\omega t - 2\phi_n^{2\omega}) \hat{\mathbf{z}} \quad (27)$$

where F_0 is the electric field amplitude, r_0^2 is the intensity ratio between the two colours, ρ_n is the radial distance to beams’ axis ($\rho = \rho_1 \simeq \rho_2$ in the focus), $\tilde{\omega}$ is the waist radius, the propagation vectors of the fundamental field are defined as

$$\mathbf{k}_1 = k \sin(\alpha) \hat{\mathbf{x}} + k \cos(\alpha) \hat{\mathbf{y}} \quad (28)$$

$$\mathbf{k}_2 = -k \sin(\alpha) \hat{\mathbf{x}} + k \cos(\alpha) \hat{\mathbf{y}} \quad (29)$$

where $k = \frac{2\pi}{\lambda}$, λ being the fundamental wavelength, and the polarization vectors are given by

$$\hat{\mathbf{e}}_1 = \cos(\alpha)\hat{\mathbf{x}} - \sin(\alpha)\hat{\mathbf{y}} \quad (30)$$

$$\hat{\mathbf{e}}_2 = \cos(\alpha)\hat{\mathbf{x}} + \sin(\alpha)\hat{\mathbf{y}} \quad (31)$$

Near the focus, the total electric field can be written as

$$\mathbf{F}(\mathbf{r}, t) = 2F_0 e^{-\rho^2/\tilde{\omega}^2} \left[f_x(x) \cos(k \cos(\alpha)y - \omega t - \delta_+^\omega) \hat{\mathbf{x}} + f_y(x) \sin(k \cos(\alpha)y - \omega t - \delta_+^\omega) \hat{\mathbf{y}} + f_z(x) \cos(2k \cos(\alpha)y - 2\omega t - 2\delta_+^{2\omega}) \hat{\mathbf{z}} \right] \quad (32)$$

with

$$f_x(x) = \cos(\alpha) \cos(k \sin(\alpha)x + \delta_-^\omega) \quad (33)$$

$$f_y(x) = \sin(\alpha) \sin(k \sin(\alpha)x + \delta_-^\omega) \quad (34)$$

$$f_z(x) = r_0 \cos(2k \sin(\alpha)x + 2\delta_-^{2\omega}) \quad (35)$$

where

$$\delta_\pm^{m\omega} = \frac{\phi_2^{m\omega} \pm \phi_1^{m\omega}}{2} \quad (36)$$

Equations (32)-(35) show that the total electric field is locally chiral. It is elliptically polarized in the xy plane at frequency ω (with major polarization component along x) and linearly polarized along z at frequency 2ω . Equation (2) of the main text is a simplified version of Eq. (32) that assumes $y = 0$ and $\delta_+^\omega = 0$, with $F_\omega = 2F_0 e^{-\rho^2/\tilde{\omega}^2} f_x(x)$, $\varepsilon = -f_y(x)/f_x(x)$, $F_{2\omega} = 2F_0 e^{-\rho^2/\tilde{\omega}^2} f_z(x)$, and $\phi_{\omega,2\omega} = 2\delta_+^{2\omega}$.

Note that the relative phases between the three field components do not change along z , as the two beams propagate in the xy plane. They do not change along y either, since $\mathbf{k}_1 \cdot \mathbf{y} = \mathbf{k}_2 \cdot \mathbf{y}$. Indeed, one can easily see in Eq. (32) that a spatial translation $\mathbf{y} \rightarrow \mathbf{y} + \Delta\mathbf{y}$ is equivalent to a temporal displacement $t \rightarrow t - \Delta t$, with $k \cos(\alpha)\Delta y = \omega\Delta t$. However, the relative phases between the field components do change along x , because $\mathbf{k}_1 \cdot \mathbf{x} \neq \mathbf{k}_2 \cdot \mathbf{x}$ (we have $\mathbf{k}_1 \cdot \mathbf{x} = -\mathbf{k}_2 \cdot \mathbf{x}$ instead), and their modulation is given by $f_x(x)$, $f_y(x)$ and $f_z(x)$.

To maximize the enantio-sensitivity of the macroscopic harmonic emission, we ensure that the *handedness* is maintained in globally space. As f_x and f_y change along x , so does the ellipticity in the xy plane, which can be defined as

$$\varepsilon(x) = -\frac{f_y(x)}{f_x(x)} = -\tan(\alpha) \tan(k \sin(\alpha)x + \delta_-^\omega) \quad (37)$$

The field changes handedness when either $\varepsilon(x)$ or $f_z(x)$ flip sign. To maintain the field handedness in space, we need to ensure that both quantities change sign at the same positions. The spatial points where forward ellipticity flips sign satisfy

$$k \sin(\alpha)x + \delta_-^\omega = n\frac{\pi}{2}, \quad \text{with } n \in \mathbb{Z}. \quad (38)$$

Whereas for f_z we have

$$2k \sin(\alpha)x + 2\delta_-^{2\omega} = \frac{\pi}{2} + n\pi, \quad \text{with } n \in \mathbb{Z}. \quad (39)$$

Combining Eqs. (38) and (39), we obtain the general condition for the field handedness to be maintained in space:

$$2\delta_-^\omega - 2\delta_-^{2\omega} = \frac{\pi}{2} + n\pi, \quad \text{with } n \in \mathbb{Z} \quad (40)$$

Let us consider the situation where the ω fields in the two beams are out of phase, i.e. $\phi_1^\omega = \delta_+^\omega - \pi/2$ and $\phi_2^\omega = \delta_+^\omega + \pi/2$, and therefore $\delta_-^\omega = \pi/2$ (see Eq. (36)). The condition given by Eq. (40) is verified if $2\delta_-^{2\omega} = \pi/2$, i.e. if the 2ω fields in the two beams are also out of phase. Then, we have $2\phi_1^{2\omega} = 2\delta_+^{2\omega} - \pi/2$ and $2\phi_2^{2\omega} = 2\delta_+^{2\omega} + \pi/2$. This means that the relative phase between the two colours in both beams has to be shifted by π , i.e. $\phi_n^{2\omega} - \phi_n^\omega = \delta_+^{2\omega} - \delta_+^\omega + \pi$. This analysis shows that the locally chiral field shown in Fig. 1a of the main text maintains its handedness globally in space. The same condition can be derived using chiral-field correlation functions, as we show in the next section.

Global handedness in chiral-field correlation functions

Here we analyze how the handedness of the locally chiral field described in the main text changes in space by analyzing the spatial modulation of its fifth-order chiral correlation function $h^{(5)}$ (Eq. (3)). We can see in Eqs. (15), (25), and (32)-(35) that $h^{(5)}$ depends on x through F_x , F_y , and F_z . F_x and F_y oscillate as a function of x with frequency $k \sin \alpha$, and F_z oscillates with frequency $2k \sin \alpha$. As a result, $h^{(5)}$ also oscillates as a function of x . To quantify the global handedness of the field, we integrate $h^{(5)}$ along x . By decomposing F_x , F_y , and F_z into exponential functions with positive and negative frequencies, we find that there is a null-frequency component in $h^{(5)}$ that does not oscillate as a function of x . Unless the beams are tightly focused, it is this null-frequency component that defines the global handedness of the field. It is given by

$$\left[h_a^{(5)} \right]_0 = 2i [F_x F_y F_z (F_x^2 - F_y^2)]_0 e^{2i(\delta_+^{2\omega} - \delta_+^\omega)} = \frac{1}{8} F_0^5 r_0 \sin(4\alpha) \sin(2\delta_-^{2\omega} - 2\delta_-^\omega) e^{i(2\delta_+^{2\omega} - 2\delta_+^\omega + \frac{\pi}{2})}. \quad (41)$$

This expression shows that the global handedness of the field vanishes when the relative phases satisfy $2\delta_-^{2\omega} - 2\delta_-^\omega = n\pi$, for $n \in \mathbb{Z}$. On the other hand, the absolute value of the global handedness reaches a maximum when $2\delta_-^{2\omega} - 2\delta_-^\omega = (n+1)\pi/2$, for $n \in \mathbb{Z}$, in agreement with the analysis presented in the previous section (see Eq. (40)). This condition is satisfied by the field shown in Fig. 1 of the main text.

Model for high harmonic generation in propylene oxide

We have adapted the method described in Ref. [33] to describe high harmonic generation in the chiral molecule propylene oxide [34–36]. The macroscopic dipole moment in a medium of randomly oriented molecules results from the coherent addition of the contributions from all possible molecular orientations, i.e.

$$\mathbf{D}(N\omega) = \int d\Omega \int d\alpha \mathbf{D}_{\Omega\alpha}(N\omega) \quad (42)$$

where ω is the fundamental frequency, N is the harmonic number, and $\mathbf{D}_{\Omega\alpha}$ is the harmonic dipole associated with a given molecular orientation. The integration in the solid angle Ω was performed using the Lebedev quadrature [37] of order 17. For each value of Ω , the integration in α was evaluated using the trapezoid method.

The dipole moment associated with a given molecular orientation results from the coherent addition of all channel contributions [33]:

$$\mathbf{D}_{\Omega\alpha}^{mn}(N\omega) = \sum_{mn} \mathbf{D}_{mn}(N\omega) \quad (43)$$

where \mathbf{D}_{mn} is the contribution from a given ionization (m) - recombination (n) channel, in the frequency domain. We have considered the electronic ground state of the ionic core (X) and the first three excited states (A, B and C), i.e. 16 channels, and found that only those involving ionization from the X and A states and recombination with the X, A and B states play a key role under the experimental conditions of Ref. [6]. Each channel contribution can be factorized as the product of three terms:

$$\mathbf{D}_{\Omega\alpha}^{mn}(N\omega) = a_{ion,\Omega\alpha}^{mn}(N\omega) \cdot a_{prop,\Omega\alpha}^{mn}(N\omega) \cdot \mathbf{a}_{rec,\Omega\alpha}^{mn}(N\omega) \quad (44)$$

which are associated with strong-field ionization, propagation and radiative recombination, respectively [33].

Recombination amplitudes are given by

$$\mathbf{a}_{rec,\Omega\alpha}^{nm} = \left(\frac{2\pi}{i\partial^2 S_m(t_r, t_i, \mathbf{p})/\partial t_r^2} \right)^{1/2} e^{-iS_m(t_r, t_r', \mathbf{p}) + iN\omega t_r} \mathbf{d}_{rec,n}^{\Omega\alpha}(\mathbf{k}(t_r')) \quad (45)$$

where $t_i = t_i' + it_i''$ and $t_r = t_r' + it_r''$ are the complex ionization and recombination times resulting from applying the saddle-point method [33], \mathbf{p} represents the canonical momentum, which is related to the kinetic momentum by $\mathbf{k}(t) = \mathbf{p}(t) + \mathbf{A}(t)$, $\mathbf{A}(t)$ being the vector potential, with $\mathbf{F}(t) = -\partial\mathbf{A}(t)/\partial t$, $\mathbf{d}_{rec,n}$ is the corresponding photo-recombination matrix element, and S_m is given by

$$S_m(t, t', \mathbf{p}) = \frac{1}{2} \int_{t'}^t d\tau [\mathbf{p} + \mathbf{A}(\tau)]^2 + \mathbf{IP}_m(t - t') \quad (46)$$

Photo-recombination matrix elements have been evaluated using the static-exchange density functional theory (DFT) method [38–45], as in [35].

Propagation amplitudes are given by

$$a_{prop,\Omega\alpha}^{nm} = \left(\frac{2\pi}{i(t_r - t_i)} \right)^{3/2} e^{-iS_m(t_r', t_i', \mathbf{p})} a_{mn}^{\Omega\alpha}(t_r', t_i') \quad (47)$$

where $a_{mn}^{\Omega\alpha}$ is the transition amplitude describing the laser-driven electron dynamics between ionization and recombination, which is calculated by solving the time-dependent Schrödinger equation numerically in the basis set of ionic states [33].

A reasonable estimation of the ionization amplitudes can be obtained using the following expression:

$$a_{ion,\Omega\alpha}^{nm} = 2\pi \left(\frac{1}{i\partial^2 S_m(t_r, t_i, \mathbf{p})/\partial t_i^2} \right)^{1/2} e^{-iS_m(t_i', t_i', \mathbf{p})} \mathcal{F}\{\Psi_m\}(\Re\{\mathbf{k}(t_i')\}) \quad (48)$$

where $\mathcal{F}\{\Psi_m\}$ is the Fourier transform of the Dyson orbital associated with the initial state wave function Ψ_m . The evaluation of sub-cycle ionization amplitudes in organic molecules is very challenging because non-adiabatic and multi-electron effects influence the dynamics of laser-driven electron tunneling, and the estimations provided by Eq. (48) are not sufficiently accurate for the purpose of this work. Nonetheless, these quantities can be reconstructed from multi-dimensional HHG spectroscopy measurements, when available, [28, 46, 47]. Here we have reconstructed the sub-cycle ionization amplitudes from the experimental results of Ref. [6], using the estimations provided by Eq. (48) as a starting point for the procedure.

Far field image

The harmonic intensity in the far field has been evaluated using the Fraunhofer diffraction equation:

$$\mathbf{I}(N\omega, \beta) \propto (N\omega)^4 \left| \int_{-\infty}^{\infty} \mathbf{D}(N\omega, x) e^{-iKx} dx \right|^2, \quad (49)$$

where β is the far field angle (divergence), $K = \frac{N\omega}{c}\beta$, c being the speed of light, and $\mathbf{D}(N\omega, x)$ is the harmonic dipole driven by the strong field in the focus (Eq. (42)), which has been computed along the transversal coordinate x using the procedure described in the previous section.

Accurate determination of the enantiomeric excess

Let us consider a macroscopic mixture of right-handed and left-handed molecules, with concentrations C_R and C_S . The intensity of the odd harmonics, which is not enantio-sensitive in the dipole approximation, depends on the total concentration of molecules,

$$I_{2N+1} \propto (C_R + C_S)^2 |D_{x,2N+1}|^2, \quad (50)$$

where $D_{x,2N+1}$ is the projection of the macroscopic dipole along x . This dipole component is essentially driven by the x -polarized component of the driving field and unaffected by the weak y and z polarization components.

The intensity of the z -polarized even harmonics results from the interference between chiral and achiral multiphoton pathways (see SI):

$$I_{2N} \propto |(C_R + C_S)D_{z,2N}^0 + (C_R - C_S)D_{z,2N}^{(R)}|^2 \quad (51)$$

where $D_{z,2N}^0$ and $D_{z,2N}^{(R)}$ are the dipole components associated with the achiral and chiral pathways, for the R enantiomer. Whereas the z -polarized component of the driver barely modifies $D_{z,2N}^{(R)}$, it controls the amplitude and phase of $D_{z,2N}^0$ (see SI). This allows us to achieve perfect constructive or destructive interference, $D_{z,2N}^0 \simeq \pm D_{z,2N}^{(R)}$, by tuning the laser parameters. If $D_{z,2N}^0 \simeq D_{z,2N}^{(R)}$, we have

$$\frac{I_{2N}}{I_{2N+1}} \propto (1 + ee)^2 \frac{I_{2N}}{I_{2N+1}} \Big|_{ee=0} \quad (52)$$

where ee is the enantiomeric excess, $ee = \frac{C_R - C_S}{C_R + C_S}$, and $\frac{I_{2N}}{I_{2N+1}} \Big|_{ee=0}$ is the intensity ratio between consecutive harmonics in a racemic mixture. Alternatively, we can adjust the driving field so that $D_{z,2N}^0 \simeq -D_{z,2N}^{(R)} = D_{z,2N}^{(S)}$, and then

$$\frac{I_{2N}}{I_{2N+1}} \propto (1 - ee)^2 \frac{I_{2N}}{I_{2N+1}} \Big|_{ee=0} \quad (53)$$

Eqs. (52) and (53) allows us to quantify the enantiomeric excess in macroscopic mixtures from single-shot measurements, with high accuracy and with sub-femtosecond time resolution. If $ee > 0$, we can determine its value more accurately if we set $D_{z,2N}^0 \simeq D_{z,2N}^{(R)}$ and use Eq. (52). Setting $D_{z,2N}^0 \simeq D_{z,2N}^{(S)}$ and using Eq. (53) provides a more accurate determination if $ee < 0$ (see Fig. 5f).

Experimental setup

The experimental setup proposed here to generate synthetic light that is locally and globally chiral is depicted in Fig. 2. A single, linearly polarized fundamental beam (we have considered $\lambda = 1770$ nm) is frequency doubled in a nonlinear BBO crystal. The second harmonic field is orthogonally polarized to the fundamental. The resulting two-colour beam is then split into two. In each beam, $\phi_{\omega,2\omega}$ is tuned using calcite wedges. The beams are then refocused in a non-collinear geometry, with opening angle $2\alpha = 10^\circ$. The molecular gas medium is placed before the focus to favour phase matching of the so-called "short trajectories" in HHG [48], with Rayleigh length well above the medium thickness. As shown in two-color gas-phase HHG experiments (e.g. [27, 28]), dispersion of ω and 2ω beams does not change the $\phi_{\omega,2\omega}$ phase across the interaction region, for medium thickness lower than around 5mm, at pressures well below atmospheric. Using liquids is also possible thanks to modern flat liquid jet technology, which provides medium thickness from a few tens of nanometers to a few micrometers [49]. In liquid jets, the ω - 2ω dispersion limits the medium thickness to a few micrometers. This thickness is sufficient to achieve strong HHG signal, see e.g. [50].

In our manuscript we have chosen to use a molecular gas as an example. We have performed our calculations for the laser radiation parameters used in the first experiment on HHG in chiral molecules [6], assuming gas phase molecules (density about 10^{18} cm $^{-3}$, corresponding to intermolecular distances of approximately 100 Angstrom, i.e. larger than the electron oscillation amplitude). Sample preparation can follow [6] using a gas cells filled by enantiopure chiral molecules, heated to 100°C and reaching a vapour pressure of 60 mbar, and closed by teflon drilled by the laser on both sides of the cell. To detect radiation in the frequency range of our interest, a standard HHG detection technique can be used (see e.g. [6]), including a grazing-incidence concave grating with a microchannel plate (MCP) coupled to a phosphor screen, imaged with a charge coupled device (CCD) camera. The expected photon count is about 10^7 photons per second, i.e. 10^4 photons per pulse (for 1kHz laser rep rate), based on typical results and standard conversion efficiency in the near IR and mid IR ranges, taking into account the scaling of the single-molecule response with the driving wavelength as λ^6 in the IR range.

While we have considered a gas-phase medium of randomly oriented chiral molecules in our calculations, high harmonic generation is ubiquitous in gas-phase atoms and molecules, liquids [50] and solids [51, 52]. The mechanism of interference between chiral and achiral pathways that we demonstrate in randomly oriented gas-phase molecules is completely general. Thus, we expect to find an equally strong enantio-sensitive response in isotropic chiral liquids and amorphous solids.

Dynamical symmetry description of chiral light

Locally chiral fields can be characterized using the dynamical symmetry group theory formalism [24]. In this approach, a light field is considered locally chiral if its symmetry group is completely free of any reflection or inversion based symmetry elements. Here we summarize the symmetry requirements that a field needs to uphold in order to be locally chiral (see SI for a detailed description):

1. $\mathbf{F}(t)$ must be a non-collinear field that exhibits polarization in three dimensions, and not within a plane.
2. $\mathbf{F}(t)$ must exhibit both even and odd harmonics of the fundamental frequency in its carrier waves.

3. If the even and odd harmonics are not perpendicular, then $\mathbf{F}(t)$ is locally chiral. If they are perpendicular, then $\mathbf{F}(t)$ is locally chiral if at least one of the odd harmonics is not linearly polarized and one of the following conditions is fulfilled:
- One of the odd harmonics is not circularly polarized.
 - The odd harmonics are circularly polarized, but they do not have alternating helicities.
 - The odd harmonics are circularly polarized and have alternating helicities, but $\mathbf{F}(t)$ contains odd harmonics of frequencies other than $(2nq \pm 1)\omega$ and even harmonics of frequencies other than $n(2q + 1)\omega$, where q and n are integer numbers, n being even.

-
- [1] M. Shapiro and P. Brumer, Principles of the Quantum Control of Molecular Processes, by Moshe Shapiro, Paul Brumer, pp. 250. ISBN 0-471-24184-9. Wiley-VCH, February 2003. p. 250 (2003).
- [2] M. Matthews, F. Morales, A. Patas, A. Lindinger, J. Gateau, N. Berti, S. Hermelin, J. Kasparian, M. Richter, T. Bredtmann, et al., Nature Physics **14**, 695 (2018), ISSN 1745-2481, URL <https://doi.org/10.1038/s41567-018-0105-0>.
- [3] D. N. Basov, R. D. Averitt, and D. Hsieh, Nature Materials **16**, 1077 (2017), URL <http://dx.doi.org/10.1038/nmat5017>.
- [4] J. Zhang, P. W. Hess, A. Kyprianidis, P. Becker, A. Lee, J. Smith, G. Pagano, I.-D. Potirniche, A. C. Potter, A. Vishwanath, et al., Nature **543**, 217 (2017), URL <http://dx.doi.org/10.1038/nature21413>.
- [5] N. Berova, P. L. Polavarapu, K. Nakanishi, and R. W. Woody, *Comprehensive Chiroptical Spectroscopy* (Wiley, 2013), ISBN 9781118012932.
- [6] R. Cireasa, A. E. Boguslavskiy, B. Pons, M. C. H. Wong, D. Descamps, S. Petit, H. Ruf, N. Thire, A. Ferre, J. Suarez, et al., Nature Physics **11**, 654 (2015), ISSN 1745-2473, letter, URL <http://dx.doi.org/10.1038/nphys3369>.
- [7] A. F. Ordonez and O. Smirnova, Physical Review A **98**, 063428 (2018), URL <https://link.aps.org/doi/10.1103/PhysRevA.98.063428>.
- [8] B. Ritchie, Phys. Rev. A **13**, 1411 (1976), URL <https://link.aps.org/doi/10.1103/PhysRevA.13.1411>.
- [9] I. Powis, The Journal of Chemical Physics **112**, 301 (2000), URL <https://doi.org/10.1063/1.480581>.
- [10] N. Böwering, T. Lischke, B. Schmidtke, N. Müller, T. Khalil, and U. Heinzmann, Phys. Rev. Lett. **86**, 1187 (2001), URL <https://link.aps.org/doi/10.1103/PhysRevLett.86.1187>.
- [11] C. Lux, M. Wollenhaupt, T. Bolze, Q. Liang, J. Köhler, C. Sarpe, and T. Baumert, Angewandte Chemie International Edition **51**, 5001 (2012), ISSN 1521-3773, URL <http://dx.doi.org/10.1002/anie.201109035>.
- [12] S. Beaulieu, A. Comby, D. Descamps, B. Fabre, G. A. Garcia, R. Géneaux, A. G. Harvey, F. Légaré, Z. Masín, L. Nahon, et al., Nature Physics (2018), ISSN 1745-2481, URL <https://doi.org/10.1038/s41567-017-0038-z>.
- [13] A. Kastner, C. Lux, T. Ring, S. Zillighoven, C. Sarpe, A. Senfleben, and T. Baumert, ChemPhysChem **17**, 1119 (2016), URL <https://onlinelibrary.wiley.com/doi/abs/10.1002/cphc.201501067>.
- [14] P. Fischer, D. S. Wiersma, R. Righini, B. Champagne, and A. D. Buckingham, Phys. Rev. Lett. **85**, 4253 (2000), URL <https://link.aps.org/doi/10.1103/PhysRevLett.85.4253>.
- [15] M. A. Belkin, S. H. Han, X. Wei, and Y. R. Shen, Phys. Rev. Lett. **87**, 113001 (2001), URL <https://link.aps.org/doi/10.1103/PhysRevLett.87.113001>.
- [16] P. Fischer, K. Beckwitt, F. Wise, and A. Albrecht, Chemical Physics Letters **352**, 463 (2002), ISSN 0009-2614, URL <http://www.sciencedirect.com/science/article/pii/S000926140101497X>.
- [17] P. Fischer and F. Hache, Chirality **17**, 421 (2005), <https://onlinelibrary.wiley.com/doi/pdf/10.1002/chir.20179>, URL <https://onlinelibrary.wiley.com/doi/abs/10.1002/chir.20179>.
- [18] N. Ji, V. Ostroverkhov, M. Belkin, Y.-J. Shiu, and Y.-R. Shen, Journal of the American Chemical Society **128**, 8845 (2006), pMID: 16819878, URL <https://doi.org/10.1021/ja060888c>.
- [19] M. A. Belkin, T. A. Kulakov, K.-H. Ernst, L. Yan, and Y. R. Shen, Phys. Rev. Lett. **85**, 4474 (2000), URL <https://link.aps.org/doi/10.1103/PhysRevLett.85.4474>.
- [20] D. Patterson, M. Schnell, and J. M. Doyle, Nature **497**, 475 (2013), ISSN 0028-0836, letter, URL <http://dx.doi.org/10.1038/nature12150>.
- [21] I. Tutunnikov, E. Gershnel, S. Gold, and I. S. Averbukh, The Journal of Physical Chemistry Letters **9**, 1105 (2018), pMID: 29417812, <https://doi.org/10.1021/acs.jpcllett.7b03416>, URL <https://doi.org/10.1021/acs.jpcllett.7b03416>.
- [22] O. Neufeld, D. Ayuso, P. Decleva, M. Y. Ivanov, O. Smirnova, and O. Cohen, Phys. Rev. X **9**, 031002 (2019), URL <https://link.aps.org/doi/10.1103/PhysRevX.9.031002>.
- [23] Y. Tang and A. E. Cohen, Physical Review Letters **104**, 163901 (2010), URL <http://link.aps.org/doi/10.1103/PhysRevLett.104.163901>.
- [24] O. Neufeld, D. Podolsky, and O. Cohen, Nature Communications **10**, 405 (2019), ISSN 2041-1723, URL <https://doi.org/10.1038/s41467-018-07935-y>.
- [25] S. Eibenberger, J. Doyle, and D. Patterson, Phys. Rev. Lett. **118**, 123002 (2017), URL <https://link.aps.org/doi/10.1103/PhysRevLett.118.123002>.
- [26] A. B. Harris, R. D. Kamien, and T. C. Lubensky, Rev. Mod. Phys. **71**, 1745 (1999), URL <https://link.aps.org/doi/10.1103/RevModPhys.71.1745>.
- [27] D. Shafir, H. Soifer, B. D. Bruner, M. Dagan, Y. Mairesse, S. Patchkovskii, M. Y. Ivanov, O. Smirnova, and N. Dudovich, Nature **485**, 343 (2012), ISSN 0028-0836, URL <http://dx.doi.org/10.1038/nature11025>.

- [28] O. Pedatzur, G. Orenstein, V. Serbinenko, H. Soifer, B. D. Bruner, A. J. Uzan, D. S. Brambila, A. G. Harvey, L. Torlina, F. Morales, et al., *Nat Phys* **11**, 815 (2015), ISSN 1745-2473, letter, URL <http://dx.doi.org/10.1038/nphys3436>.
- [29] A. F. Ordonez and O. Smirnova, *Phys. Rev. A* **99**, 043416 (2019), URL <https://link.aps.org/doi/10.1103/PhysRevA.99.043416>.
- [30] A. Owens, A. Yachmenev, S. N. Yurchenko, and J. Küpper, *Phys. Rev. Lett.* **121**, 193201 (2018), URL <https://link.aps.org/doi/10.1103/PhysRevLett.121.193201>.
- [31] J. A. Giordmaine, *Phys. Rev.* **138**, A1599 (1965), URL <https://link.aps.org/doi/10.1103/PhysRev.138.A1599>.
- [32] R. W. Boyd, *Nonlinear Optics* (Academic Press, Burlington, 2008), third edition ed., ISBN 978-0-12-369470-6.
- [33] O. Smirnova and M. Ivanov, *Multielectron High Harmonic Generation: Simple Man on a Complex Plane* (Wiley-VCH Verlag GmbH & Co. KGaA, 2014), pp. 201–256, ISBN 9783527677689, URL <http://dx.doi.org/10.1002/9783527677689.ch7>.
- [34] O. Smirnova, Y. Mairesse, and S. Patchkovskii, *Journal of Physics B: Atomic, Molecular and Optical Physics* **48**, 234005 (2015), URL <http://stacks.iop.org/0953-4075/48/i=23/a=234005>.
- [35] D. Ayuso, P. Decleva, S. Patchkovskii, and O. Smirnova, *Journal of Physics B: Atomic, Molecular and Optical Physics* (2018), URL <http://iopscience.iop.org/10.1088/1361-6455/aaae5e>.
- [36] D. Ayuso, P. Decleva, S. Patchkovskii, and O. Smirnova, *Journal of Physics B: Atomic, Molecular and Optical Physics* (2018).
- [37] V. I. Lebedev and D. N. Laikov, *Doklady Mathematics* **59**, 477 (1999).
- [38] D. Toffoli, M. Stener, G. Fronzoni, and P. Decleva, *Chemical Physics* **276**, 25 (2002), ISSN 0301-0104, URL <http://www.sciencedirect.com/science/article/pii/S0301010401005493>.
- [39] S. Turchini, N. Zema, G. Contini, G. Alberti, M. Alagia, S. Stranges, G. Fronzoni, M. Stener, P. Decleva, and T. Prosperi, *Phys. Rev. A* **70**, 014502 (2004), URL <https://link.aps.org/doi/10.1103/PhysRevA.70.014502>.
- [40] M. Stener, G. Fronzoni, D. D. Tommaso, and P. Decleva, *The Journal of Chemical Physics* **120**, 3284 (2004), URL <https://doi.org/10.1063/1.1640617>.
- [41] S. Stranges, S. Turchini, M. Alagia, G. Alberti, G. Contini, P. Decleva, G. Fronzoni, M. Stener, N. Zema, and T. Prosperi, *The Journal of Chemical Physics* **122**, 244303 (2005), URL <https://doi.org/10.1063/1.1940632>.
- [42] D. Di Tommaso, M. Stener, G. Fronzoni, and P. Decleva, *ChemPhysChem* **7**, 924 (2006), ISSN 1439-7641, URL <http://dx.doi.org/10.1002/cphc.200500602>.
- [43] S. Turchini, D. Catone, G. Contini, N. Zema, S. Irrera, M. Stener, D. Di Tommaso, P. Decleva, and T. Prosperi, *ChemPhysChem* **10**, 1839 (2009), ISSN 1439-7641, URL <http://dx.doi.org/10.1002/cphc.200800862>.
- [44] R. K. Kushawaha, M. Patanen, R. Guillemin, L. Journel, C. Miron, M. Simon, M. N. Piancastelli, C. Skates, and P. Decleva, *Proceedings of the National Academy of Sciences* **110**, 15201 (2013), <http://www.pnas.org/content/110/38/15201.full.pdf>, URL <http://www.pnas.org/content/110/38/15201.abstract>.
- [45] D. Ayuso, A. Palacios, P. Decleva, and F. Martin, *Phys. Chem. Chem. Phys.* **19**, 19767 (2017), URL <http://dx.doi.org/10.1039/C7CP01856H>.
- [46] V. Serbinenko and O. Smirnova, *Journal of Physics B: Atomic, Molecular and Optical Physics* **46**, 171001 (2013), URL <http://stacks.iop.org/0953-4075/46/i=17/a=171001>.
- [47] B. D. Bruner, Z. Masin, M. Negro, F. Morales, D. Brambila, M. Devetta, D. Facciala, A. G. Harvey, M. Ivanov, Y. Mairesse, et al., *Faraday Discuss.* **194**, 369 (2016), URL <http://dx.doi.org/10.1039/C6FD00130K>.
- [48] Y. Mairesse, A. de Bohan, L. J. Frasinski, H. Merdji, L. C. Dimu, P. Monchicourt, P. Breger, M. Kovačev, R. Taïeb, B. Carré, et al., *Science* **302**, 1540 (2003), ISSN 0036-8075, <http://science.sciencemag.org/content/302/5650/1540.full.pdf>, URL <http://science.sciencemag.org/content/302/5650/1540>.
- [49] J. D. Koralek, J. B. Kim, P. Bruza, C. B. Curry, Z. Chen, H. A. Bechtel, A. A. Cordones, P. Sperling, S. Toleikis, J. F. Kern, et al., *Nature Communications* **9**, 1353 (2018), ISSN 2041-1723, URL <https://doi.org/10.1038/s41467-018-03696-w>.
- [50] T. T. Luu, Z. Yin, A. Jain, T. Gaumnitz, Y. Pertot, J. Ma, and H. J. Wörner, *Nature Communications* **9**, 3723 (2018), ISSN 2041-1723, URL <https://doi.org/10.1038/s41467-018-06040-4>.
- [51] G. Vampa, T. J. Hammond, N. Thiré, B. E. Schmidt, F. Légaré, C. R. McDonald, T. Brabec, and P. B. Corkum, *Nature* **522**, 462 EP (2015), URL <https://doi.org/10.1038/nature14517>.
- [52] G. Vampa and T. Brabec, *Journal of Physics B: Atomic, Molecular and Optical Physics* **50**, 083001 (2017), URL <https://doi.org/10.1088/2F1361-6455%2Faa528d>.

Acknowledgements

We thank Felipe Morales for stimulating discussions. DA, A.F.O. and OS acknowledge support from the DFG SPP 1840 “Quantum Dynamics in Tailored Intense Fields” and DFG grant SM 292/5-2; A.F.O. and OS acknowledge support from MEDEA. The MEDEA project has received funding from the European Union’s Horizon 2020 research and innovation programme under the Marie Skłodowska-Curie grant agreement No 641789. This work was supported by the Israel Science Foundation (grant no. 1781/18), and the Wolfson foundation. ON gratefully acknowledges the support of the Adams Fellowship Program of the Israel Academy of Sciences and Humanities.

Author contributions

D.A., A.O. and O.S. developed the concepts of locally and globally chiral fields. D.A., A.O. and O.S. developed the theory of chiral correlation functions. O.N., G.L and O.C. developed a concept of reflection and inversion free fields, which are locally chiral, and the group-theory based analysis of such fields. O.N. proved the connection between the symmetry-based description of locally chiral fields and reflection and inversion free fields. O.N. and O. C. formulated the degree of chirality of light fields. D.A., P.D., M.I. and O.S.

developed and computed the hybrid DFT-strong-field description of the microscopic and macroscopic HHG response in propylene oxide, O.N. computed the DFT-based microscopic HHG response in bromochlorofluoromethane. D.A., A.O., M.I. and O.S. wrote the initial version of the manuscript. All authors contributed to writing the manuscript.

Competing Interests

The authors declare that they have no competing financial interests. The data that support the plots within this paper and other findings of this study are available from the corresponding authors upon reasonable request. Correspondence should be addressed to david.ayuso@mbi-berlin.de, mikhail.ivanov@mbi-berlin.de and olga.smirnova@mbi-berlin.de.

Synthetic chiral light for efficient control of chiral light matter interaction: supplementary information

David Ayuso,^{1,*,\dagger} Ofer Neufeld,^{2,\dagger} Andres F. Ordonez,^{1,3} Piero Decleva,⁴
Gavriel Lerner,² Oren Cohen,² Misha Ivanov,^{1,5,6,\ddagger} Olga Smirnova^{1,3,\S}

¹*Max-Born-Institut, Berlin, Germany*

²*Physics Department and Solid State Institute, Technion - Israel Institute of Technology, Haifa, Israel*

³*Technische Universität Berlin, Berlin, Germany*

⁴*Dipartimento di Scienze Chimiche e Farmaceutiche, Università degli Studi di Trieste, Trieste, Italy.*

⁵*Institute für Physik, Humboldt-Universität zu Berlin, Berlin, Germany.*

⁶*Department of Physics, Imperial College London, London, UK.*

I. DERIVATION OF THE CHIRAL SUSCEPTIBILITY TENSOR IN EQS. (13) AND (14)

Here we derive Eq. (13) used in Methods. The polarization corresponding to absorption of a single 2ω photon is given by

$$P_i^{(1)}(2\omega) = \chi_{ij}^{(1)}(2\omega) F_j(2\omega), \quad (1)$$

where the orientation-averaged susceptibility is given by

$$\chi_{ij}^{(1)} = \left(\int d\varrho l_{i\alpha} l_{j\beta} \right) \chi_{\alpha\beta}^{(1)} = \frac{1}{3} \delta_{i,j} \delta_{\alpha,\beta} \chi_{\alpha\beta}^{(1)} \quad (2)$$

and yields

$$\mathbf{P}^{(1)}(2\omega) = \frac{1}{3} \chi_{\alpha\alpha}^{(1)}(2\omega) \mathbf{F}(2\omega). \quad (3)$$

Here $l_{i\alpha}$ is the direction cosine between axis i in the lab frame and axis α in the molecular frame. We use latin indices for the lab frame and greek indices for the molecular frame. The fourth-order term corresponding to absorption of three and emission of one ω photon reads as

$$P_i^{(4)}(2\omega) = 4\chi_{ijklm}^{(4)}(2\omega = -\omega + \omega + \omega + \omega) F_j^*(\omega) F_k(\omega) F_l(\omega) F_m(\omega), \quad (4)$$

where the degeneracy factor 4 comes from the four possible photon orderings. The orientation-averaged fourth-order susceptibility in the lab frame is given by

$$\chi_{ijklm}^{(4)} = \left(\int d\varrho l_{i\alpha} l_{j\beta} l_{k\gamma} l_{l\delta} l_{m\epsilon} \right) \chi_{\alpha\beta\gamma\delta\epsilon}. \quad (5)$$

Using standard expressions for the orientation averaging (see e.g. Refs. [1] and [2]) we obtain (see also [3]):

$$\begin{aligned} \mathbf{P}^{(4)}(2\omega) &= \frac{2}{15} \chi_{\alpha\beta\gamma\delta\epsilon}^{(4)}(2\omega = -\omega + \omega + \omega + \omega) \\ &\quad \times (\epsilon_{\alpha\beta\gamma} \delta_{\delta\epsilon} + \epsilon_{\alpha\beta\delta} \delta_{\gamma\epsilon} + \epsilon_{\alpha\beta\epsilon} \delta_{\gamma\delta}) [\mathbf{F}^*(\omega) \times \mathbf{F}(\omega)] [\mathbf{F}(\omega) \cdot \mathbf{F}(\omega)]. \end{aligned} \quad (6)$$

In Eq. (13) we have used shorthand notations for the first-order and the fourth-order susceptibilities:

$$\chi^{(1)} \equiv \frac{1}{3} \chi_{\alpha\alpha}^{(1)}(2\omega), \quad (7)$$

* david.ayuso@mbi-berlin.de

\ddagger mikhail.ivanov@mbi-berlin.de

\S olga.smirnova@mbi-berlin.de

\dagger These authors contributed equally to this work.

$$\chi_{\pm}^{(4)} \equiv \frac{2}{15} \chi_{\alpha\beta\gamma\delta\epsilon}^{(4)} (2\omega = -\omega + \omega + \omega + \omega) (\epsilon_{\alpha\beta\gamma}\delta_{\delta\epsilon} + \epsilon_{\alpha\beta\delta}\delta_{\gamma\epsilon} + \epsilon_{\alpha\beta\epsilon}\delta_{\gamma\delta}). \quad (8)$$

Note that, for a field containing only frequencies ω and 2ω , the second-order response at frequency 2ω vanishes (see Eq. (7)) and therefore there is no interference between $\mathbf{P}^{(2)}(2\omega)$ and $\mathbf{P}^{(3)}(2\omega)$. Although $P^{(3)}(2\omega)$ is non-zero, it behaves either as $|F(\omega)|^2 F(2\omega)$ or as $|F(2\omega)|^2 F(2\omega)$. The last term should be omitted, since we keep only terms linear in $F(2\omega)$. As for the first term, which includes additional absorption and emission of ω photons, it merely describes the standard nonlinear modification of the linear response to the weak 2ω field due to the polarization of the system by the strong ω field, leading e.g. to the Stark shifts of the states involved. Thus, while these terms do modify the effective linear susceptibility $\chi^{(1)}(2\omega)$, which should include the dressing of the system by the strong ω field, they do not modify the overall result.

II. HIGHER ORDER CHIRAL-FIELD CORRELATION FUNCTIONS

Higher order chiral-field correlation functions $h^{(n)}$ control the sign of the enantio-sensitive and dichroic response in multiphoton interactions. Here, we consider higher-order ($n > 5$) correlation functions $h^{(n)}$ for the locally chiral field employed in our work (Eq. (2)). We show that, for such a field, $h^{(n)}$ has a unique form in every order, which is helpful for achieving ultimate control.

The n -th order chiral correlation function in the time domain is defined as

$$H^{(n)}(0, \tau_1, \dots, \tau_{n-1}) \equiv \int dt \{ \mathbf{F}(t) \cdot [\mathbf{F}(t + \tau_1) \times \mathbf{F}(t + \tau_2)] \} \\ \times [\mathbf{F}(t + \tau_3) \cdot \mathbf{F}(t + \tau_4)] \dots [\mathbf{F}(t + \tau_{n-2}) \cdot \mathbf{F}(t + \tau_{n-1})] \quad (9)$$

for $n \geq 3$ odd. The Fourier transform with respect to all variables τ_i yields the n -th order chiral correlation function in the frequency domain:

$$h^{(n)}(\omega_0, \omega_1, \dots, \omega_{n-1}) = \frac{1}{(2\pi)^n} \int d\tau_1 \dots \int d\tau_{n-1} e^{i\omega_1\tau_1} \dots e^{i\omega_{n-1}\tau_{n-1}} H^{(n)}(0, \tau_1, \dots, \tau_{n-1}) \\ = \{ \mathbf{F}(\omega_0) \cdot [\mathbf{F}(\omega_1) \times \mathbf{F}(\omega_2)] \} \times [\mathbf{F}(\omega_3) \cdot \mathbf{F}(\omega_4)] \dots [\mathbf{F}(\omega_{n-2}) \cdot \mathbf{F}(\omega_{n-1})] \quad (10)$$

where ω_0 is defined by the equation

$$\sum_{i=0}^{n-1} \omega_i = 0 \quad (11)$$

We now consider all possible permutations of the frequencies in $h^{(n)}$, which is equivalent to considering all possible permutations of times in $H^{(n)}$. We will show that the handedness of the field employed in our work (see Eq. (15) in Methods) is invariant with respect to such permutations.

The seventh-order chiral-field correlation function reads as:

$$h^{(7)}(\{\omega_0, \omega_1, \omega_2\}, [\omega_3, \omega_4], [\omega_5, \omega_6]) = \{ \mathbf{F}(\omega_0) \cdot [\mathbf{F}(\omega_1) \times \mathbf{F}(\omega_2)] \} \times [\mathbf{F}(\omega_3) \cdot \mathbf{F}(\omega_4)] [\mathbf{F}(\omega_5) \cdot \mathbf{F}(\omega_6)] \quad (12)$$

where we grouped the frequency arguments of $h^{(7)}$ with curly and squared brackets to improve readability. In this case there are new symmetries, we can exchange ω_3 with ω_5 and ω_4 with ω_6 simultaneously, or ω_3 with ω_6 and ω_4 with ω_5 simultaneously. Again, the first step is to make sure that the triple product is non-zero, which yields the same four triple products we got for $h^{(5)}$ (see Methods). But this time, if we choose $\omega_0 = -2\omega$, $\omega_1 = -\omega$, and $\omega_2 = \omega$, instead of one we get five different options that satisfy Eq. (17) for the rest of the frequencies :

$$h_{a_1}^{(7)} = h^{(7)}(\{-2\omega, -\omega, \omega\}, [\omega, \omega], [-\omega, \omega]), \quad (13)$$

$$h_{a_2}^{(7)} = h^{(7)}(\{-2\omega, -\omega, \omega\}, [-2\omega, 2\omega], [\omega, \omega]), \quad (14)$$

$$h_{a_3}^{(7)} = h^{(7)}(\{-2\omega, -\omega, \omega\}, [-\omega, -\omega], [2\omega, 2\omega]), \quad (15)$$

$$h_{a_4}^{(7)} = h^{(7)}(\{-2\omega, -\omega, \omega\}, [-2\omega, \omega], [\omega, 2\omega]), \quad (16)$$

$$h_{a_5}^{(7)} = h^{(7)}(\{-2\omega, -\omega, \omega\}, [-\omega, 2\omega], [-\omega, 2\omega]). \quad (17)$$

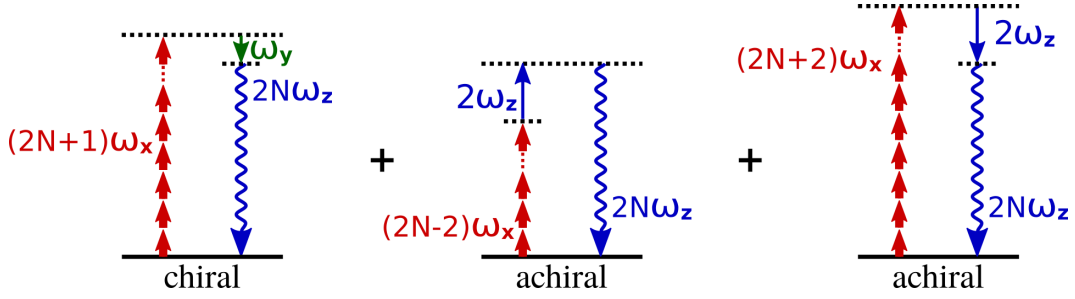


FIG. 1. Control over enantio-sensitive high harmonic generation with locally chiral fields. Interference of chiral (left diagram) and achiral (central and right diagrams) pathways in even high harmonic generation.

Since the triple product can be written in three additional different forms (see analogous discussion for $h^{(5)}$ in Methods) there are a total of 20 different possible versions of $h^{(7)}$: $h_{a_i}^{(7)}$, $h_{b_i}^{(7)}$, $h_{c_i}^{(7)}$, and $h_{d_i}^{(7)}$, with $1 \leq i \leq 5$. If we now consider the interaction with matter and limit the number of 2ω photons to a maximum of one, i.e. we consider the 2ω component to be much weaker than the ω component $|F_z| \ll |F_x|$, we are left only with $h_{a_1}^{(7)}$, $h_{b_1}^{(7)}$, $h_{c_1}^{(7)}$, and $h_{d_1}^{(7)}$. These four options are related to each other the same way that $h_a^{(5)}$, $h_b^{(5)}$, $h_c^{(5)}$ and $h_d^{(5)}$ were related to each other (see Eqs. (18)-(24) and the corresponding discussion in Methods), and therefore we arrive to the same conclusion as for $h^{(5)}$: up to a sign and complex conjugation, there is a unique expression for $h^{(7)}$ given by (see Eqs (15) in Methods)

$$h_{a_1}^{(7)} = 2iF_x F_y F_z (F_x^2 - F_y^2) (F_x^2 + F_y^2) e^{2i(\delta_{2\omega} - \delta_\omega)}. \quad (18)$$

The next order chiral measure reads as

$$h^{(9)}(\{\omega_0, \omega_1, \omega_2\}, [\omega_3, \omega_4], [\omega_5, \omega_6], [\omega_7, \omega_8]) = \{\mathbf{F}(\omega_0) \cdot [\mathbf{F}(\omega_1) \times \mathbf{F}(\omega_2)]\} \\ \times [\mathbf{F}(\omega_3) \cdot \mathbf{F}(\omega_4)] [\mathbf{F}(\omega_5) \cdot \mathbf{F}(\omega_6)] [\mathbf{F}(\omega_7) \cdot \mathbf{F}(\omega_8)] \quad (19)$$

As for the seventh-order case, we obtain some new (trivial) symmetries derived from the commutativity of scalar products. If we allow only a single 2ω photon and choose $\omega_0 = -2\omega$, $\omega_1 = -\omega$, and $\omega_2 = \omega$ then the possible options for $h^{(9)}$ are

$$h_{a_1}^{(9)} = h^{(9)}(\{-2\omega, -\omega, \omega\}, [\omega, \omega], [-\omega, \omega], [-\omega, \omega]), \quad (20)$$

$$h_{a_2}^{(9)} = h^{(9)}(\{-2\omega, -\omega, \omega\}, [\omega, \omega], [-\omega, -\omega], [\omega, \omega]). \quad (21)$$

Like before, since the triple product can be written in three additional different forms there are a total of 8 different possible versions of $h^{(9)}$ that involve a single 2ω photon (absorbed or emitted): $h_{a_i}^{(9)}$, $h_{b_i}^{(9)}$, $h_{c_i}^{(9)}$, and $h_{d_i}^{(9)}$, with $i = 1, 2$; related to each other as in the case of $h^{(5)}$ (see Eqs. (18)-(24) and the corresponding discussion in Methods). The explicit expressions for $h_{a_1}^{(9)}$ and $h_{a_2}^{(9)}$ read as (see Eq. (15) in Methods)

$$h_{a_1}^{(9)} = 2iF_x F_y F_z (F_x^2 - F_y^2) (F_x^2 + F_y^2)^2 e^{2i(\delta_{2\omega} - \delta_\omega)} \quad (22)$$

$$h_{a_2}^{(9)} = 2iF_x F_y F_z (F_x^2 - F_y^2)^3 e^{2i(\delta_{2\omega} - \delta_\omega)} \quad (23)$$

If we impose small ellipticity $|\varepsilon| \equiv |F_y/F_x| \ll 1$, then to first order in ε we get $F_x^2 \pm F_y^2 \approx F_x^2$ and therefore $h_{a_1}^{(9)} = h_{a_2}^{(9)}$, which leaves a unique expression for $h^{(9)}$ up to a sign and complex conjugation:

$$h_{a_1}^{(9)} = 2iF_x^7 F_y F_z e^{2i(\delta_{2\omega} - \delta_\omega)}. \quad (24)$$

Higher-order measures will follow the same pattern and will not introduce any new feature provided we enforce the restrictions $|F_y|, |F_z| \ll |F_x|$, which is satisfied by the field employed in our work to demonstrate the highest possible degree of control over enantio-sensitive light matter interactions (see Figs. 4 and 5 of the main text).

III. CONTROL OVER CHIRAL LIGHT MATTER INTERACTION IN THE STRONG FIELD REGIME

Here we describe the mechanism of control over enantio-sensitive HHG driven by the synthetic chiral field in Fig. 1a,b of the main text. Even HHG results from the interference between the chiral and achiral pathways depicted

in Fig. 1. The chiral pathway is associated with the enantio-sensitive polarization along z driven by the ω field component, which is elliptically polarized in the xy plane. It involves the absorption of $2N + 1$ x -polarized photons of ω frequency, the emission of one y -polarized photon of ω frequency and the emission of a $2N\omega$ z -polarized harmonic. The process of absorption of an x -polarized photon and emission of a y -polarized photon records the helicity of the driver and the molecular handedness. Note that this pathway is not affected by the presence of the 2ω , z -polarized component of the driver, as long as its amplitude is weak.

There are two achiral pathways giving rise to even HHG with z -polarization (Fig. 1), which are controlled by the relative strength and phase of the 2ω field component of the driver. The first one involves the absorption of $2N - 2$ photons of ω frequency and x polarization, absorption of one photon of 2ω frequency and z polarization, and emission of a $2N$ harmonic with z polarization. The polarization associated with this pathway can be written as

$$\mathbf{P}_{2N}^{\uparrow} = P_{2N-2} \chi_{\uparrow}^{(1)} \mathbf{F}(2\omega) = a_{\uparrow} e^{i\phi_{\omega,2\omega}} \hat{\mathbf{z}} \quad (25)$$

where P_{2N-2} is a (complex) scalar describing the absorption of $2N - 2$ photons with x polarization, which depends on the properties of the molecule and of the strong field component, $\chi_{\uparrow}^{(1)}$ is the first order susceptibility of the system dressed by the ω field describing the absorption of a 2ω photon with z polarization, and $a_{\uparrow} = P_{2N-2} \chi_{\uparrow}^{(1)} |\mathbf{F}(2\omega) \cdot \hat{\mathbf{z}}|$. The relative phase between the two colours $\phi_{\omega,2\omega}$ fully controls the phase of $\mathbf{P}_{2N}^{\uparrow}$.

The second achiral pathway (Fig. 1) involves the absorption of $2N + 2$ x -polarized photons of ω frequency, emission of a z -polarized photon of 2ω frequency and emission of a z -polarized $2N$ harmonic. The polarization term associated with this pathway is

$$\mathbf{P}_{2N}^{\downarrow} = P_{2N+2} \chi_{\downarrow}^{(1)} \mathbf{F}^*(2\omega) = a_{\downarrow} e^{-i\phi_{\omega,2\omega}} \hat{\mathbf{z}} \quad (26)$$

where $a_{\downarrow} = P_{2N+2} \chi_{\downarrow}^{(1)} |\mathbf{F}^*(2\omega) \cdot \hat{\mathbf{z}}|$. The arrows \uparrow and \downarrow indicate whether the 2ω photon is absorbed or emitted.

The total achiral contribution to polarization at $2N\omega$ frequency is given by $\mathbf{P}_{2N}^{\uparrow\downarrow} = \mathbf{P}_{2N}^{\uparrow} + \mathbf{P}_{2N}^{\downarrow}$. If one of the two pathways is dominant, then $\phi_{\omega,2\omega}$ fully controls the phase of $\mathbf{P}_{2N}^{\uparrow\downarrow}$. If both pathways are equally intense, i.e. $a_{\uparrow} = a_0 e^{i\phi_{\uparrow}}$ and $a_{\downarrow} = a_0 e^{i\phi_{\downarrow}}$, then we have

$$\mathbf{P}_{2N}^{\uparrow\downarrow} = a_0 \left(e^{i\phi_{\uparrow}} e^{i\phi_{\omega,2\omega}} + e^{i\phi_{\downarrow}} e^{-i\phi_{\omega,2\omega}} \right) \hat{\mathbf{z}} = 2a_0 e^{\phi_{\pm}} \cos(\phi_{\pm} - \phi_{\omega,2\omega}) \hat{\mathbf{z}} \quad (27)$$

where $\phi_{\pm} = \frac{\phi_{\downarrow} \pm \phi_{\uparrow}}{2}$. Here we control the amplitude and the sign of the achiral contribution in full range. The phase control is associated with the dependence of the phase of the recombination matrix element on the direction of electron approach (in the molecular frame). Further, once one includes changes in ionization and recombination times due to the presence of the 2ω field, one finds δ -dependent corrections to the Volkov phase and thus the phase of a given harmonic.

IV. DYNAMICAL SYMMETRY GROUP THEORY FOR SYNTHETIC CHIRAL LIGHT

The chirality of molecules is standardly analyzed using molecular point-group theory [4]. Within this approach, a molecule is chiral if and only if its point-group does not include any improper rotations \hat{s}_n . Note that reflection $\hat{\sigma}$ and inversion \hat{i} operations are improper rotations with $n = 1$ and $n = 2$, respectively. In this section, we develop an analogous approach to characterize the chirality of light that is complementary to the formalism based on chiral correlation functions described in the main text.

A. Locally chiral fields.

Here we show how to use the dynamical symmetry (DS) group theory formalism [5] to characterize whether a field is locally chiral or not. The spatial dependence of the field is neglected within the dipole approximation, and thus it can be fully characterized by a time-dependent electric field vector $\mathbf{F}(t)$. We assume that $\mathbf{F}(t)$ is periodic, with period T , but our analysis can also be applied to finite pulses that contain several cycles. Following the molecular group theory approach, we define a locally chiral field from a symmetry perspective as a field whose DS point-group excludes the following improper-rotational elements (i.e. it is free from reflection and inversion based symmetry elements):

- $\mathbf{F}(t)$ cannot be invariant under improper rotations \hat{s}_n of any order n . This includes reflection $\hat{\sigma}$ and inversion \hat{i} operations. Therefore, $\mathbf{F}(t)$ cannot be contained within a plane, and thus a non-collinear set-up with at least two different carrier frequency components is required.

- $\mathbf{F}(t)$ cannot be invariant under time-translations accompanied by spatial improper-rotations. There is a finite amount of such operations [5]:

1. Time translation of half a period accompanied by spatial inversion, $\mathbf{F}(t) \rightarrow \hat{i} \cdot \mathbf{F}(t + T/2) = -\mathbf{F}(t + T/2)$. A field exhibiting this DS is comprised of odd-only harmonics of its fundamental frequency [5]. Thus, to be locally chiral, $\mathbf{F}(t)$ must contain both even and odd harmonics.
2. Time translation of half a period accompanied by spatial reflection, $\mathbf{F}(t) \rightarrow \hat{\sigma} \cdot \mathbf{F}(t + T/2)$. A field exhibiting this DS can only contain even harmonics within the reflection plane and odd harmonics in the perpendicular axis [5]. Thus, even and odd harmonics must either not be perpendicular or, if they are perpendicular, then at least one odd harmonic cannot be linearly polarized.
3. Dynamical $(2n + 1)$ -fold improper rotations (odd orders) comprised of time-translations by $T/(4n + 2)$ accompanied by odd-order improper rotations, $\mathbf{F}(t) \rightarrow \hat{s}_{2n+1} \cdot \mathbf{F}(t + T/(4n + 2))$. If this DS is a member of the point-group of $\mathbf{F}(t)$, then dynamical reflection is also a member due to closure. As a result, exclusion of these symmetries leads to the same constraints derived above.
4. Dynamical $2n$ -fold improper rotations (even orders) comprised of time-translations by $T/2n$ accompanied by even-order improper rotations, $\mathbf{F}(t) \rightarrow \hat{s}_{2n} \cdot \mathbf{F}(t + T/2n)$. A field exhibiting this DS for odd values of n is also invariant with respect to dynamical inversion due to closure, and no further restrictions are required. A field exhibiting this DS for even values of n is comprised of counter-rotating pairs of circular $(2nq \pm 1)\omega$ harmonics within the plane transverse to the improper-rotation axis, and even $n(2q + 1)\omega$ harmonics along it [5]. Thus, to be locally chiral, it is sufficient that the even and odd harmonics are not perpendicular. If they are perpendicular, then $\mathbf{F}(t)$ must either contain some even harmonics other than $n(2q + 1)\omega$, where q is any integer, or it must contain some odd harmonics other than $(2nq \pm 1)\omega$, or at least one of these odd harmonics cannot be circularly polarized. Another option is that the odd harmonics do not alternate from right to left circular polarization.

The symmetry requirements presented in Methods that determine whether a field is locally chiral or not are derived from these constraints. We note that it is also possible to obtain chiral response in HHG within the dipole approximation using fields that are not locally chiral [6], but the total intensity signal cannot be enantio-sensitive. Whereas correlation functions describe the interaction of synthetic chiral light with matter, the DS based definition strictly describes the chirality of light. Thus, the symmetry based approach complements the correlation function formalism, providing insight into the properties of the field and the design of an experimental set-up.

B. Connection between locally chiral fields and reflection and inversion free fields.

We now prove that if a field is achiral from a symmetry perspective, then all correlation functions $h^{(n)}$ are zero. The most simple case is when the field is contained within a plane. Then, $h^{(n)} = 0$ for any order n , as all possible triple products involving field components are zero. The following proofs involve more complex relations.

Proof 1. Let $\mathbf{F}(t)$ be invariant under dynamical inversion such that $\mathbf{F}(t) = -\mathbf{F}(t + T/2)$. We show that $h^{(n)} = 0$ for all orders n . We start with $h^{(3)}$.

$$\begin{aligned} H^{(3)}(\tau_1, \tau_2) &= \frac{1}{2\pi} \int_0^T dt \mathbf{F}(t) \cdot (\mathbf{F}(t + \tau_1) \times \mathbf{F}(t + \tau_2)) \\ &= \frac{1}{2\pi} \int_0^{T/2} dt \mathbf{F}(t) \cdot (\mathbf{F}(t + \tau_1) \times \mathbf{F}(t + \tau_2)) + \frac{1}{2\pi} \int_{T/2}^T dt \mathbf{F}(t) \cdot (\mathbf{F}(t + \tau_1) \times \mathbf{F}(t + \tau_2)). \end{aligned} \quad (28)$$

Changing variables on the second integral $t \rightarrow t + T/2$ and using the periodicity of the field, we can write

$$H^{(3)}(\tau_1, \tau_2) = \frac{1}{2\pi} \int_0^{T/2} dt \mathbf{F}(t) \cdot (\mathbf{F}(t + \tau_1) \times \mathbf{F}(t + \tau_2)) + \frac{1}{2\pi} \int_0^{T/2} dt \mathbf{F}(t + T/2) \cdot (\mathbf{F}(t + T/2 + \tau_1) \times \mathbf{F}(t + T/2 + \tau_2)). \quad (29)$$

Now we use the dynamical inversion relation

$$H^{(3)}(\tau_1, \tau_2) = \frac{1}{2\pi} \int_0^{T/2} dt \mathbf{F}(t) \cdot (\mathbf{F}(t + \tau_1) \times \mathbf{F}(t + \tau_2)) - \frac{1}{2\pi} \int_0^{T/2} dt \mathbf{F}(t) \cdot (\mathbf{F}(t + \tau_1) \times \mathbf{F}(t + \tau_2)) = 0. \quad (30)$$

A similar approach is valid for the higher-order correlation functions, because they all involve an odd number of field vector products.

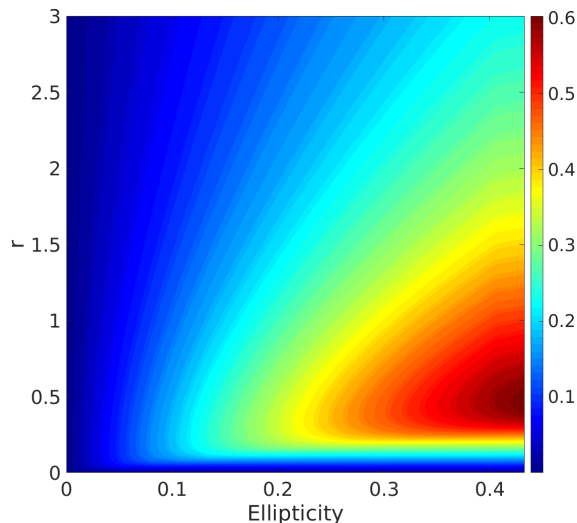


FIG. 2. **Light's degree of chirality** (Eq. (33)) for the locally chiral field used in the main text (Eq. (2) of the main text) as a function of ellipticity ε and the relative strength between the two colours $r = F_{2\omega}/F_\omega$, for $\phi_{\omega,2\omega} = \pi/2$.

Proof 2. Let $\mathbf{F}(t)$ be invariant under dynamical reflection such that $\mathbf{F}(t) = \sigma\mathbf{F}(t+T/2)$. Without loss of generality, we assume that the reflection is in the xy plane. We start with $h^{(3)}$. Using a similar strategy, we apply the dynamical reflection relation to Eq. (29), obtaining

$$H^{(3)}(\tau_1, \tau_2) = \frac{1}{2\pi} \int_0^{T/2} dt \mathbf{F}(t) \cdot (\mathbf{F}(t+\tau_1) \times \mathbf{F}(t+\tau_2)) + \frac{1}{2\pi} \int_0^{T/2} dt (\hat{\sigma} \cdot \mathbf{F}(t)) \cdot (\hat{\sigma} \cdot \mathbf{F}(t+\tau_1)) \times (\hat{\sigma} \cdot \mathbf{F}(t+\tau_2)) = 0 \quad (31)$$

The two terms cancel each other because the triple product forms a pseudoscalar that changes sign every time we reflect one of the three vector components. Equivalently, $h^{(n)} = 0$, for any n . A similar proof holds if the field is invariant under some higher order improper rotational DS.

C. Characterization of light's degree of chirality using a symmetry-based approach.

In this section we show that the degree of chirality (DOC) of locally chiral light can be analyzed in a way similar to that used for chiral molecules. While there is no absolute definition of the DOC for molecules, it can be described using so-called overlap measures [7], which quantify the extent to which an object is different from its mirror image:

$$\text{DOC}_{\text{mol}} = \frac{\min_{\theta, \phi, \psi} \left\{ \int d^3r \left| \hat{R}_z(\psi) \cdot \hat{R}_x(\phi) \cdot \hat{R}_z(\theta) \cdot V(\mathbf{r}) - V(-\mathbf{r}) \right| \right\}}{\int d^3r |V(\mathbf{r})|}, \quad (32)$$

where $V(\mathbf{r})$ is the molecular potential and θ , ϕ and ψ are three independent Euler angles. It is easy to verify that this quantity vanishes if $V(\mathbf{r})$ is invariant under improper rotations, i.e. if the molecule is not chiral. We extend this definition to light by applying the same concept to the Lissajous curve traced by the electric field over one period, which is an object spanned in (3+1)D,

$$\text{DOC}_{\text{light}} = \frac{\min_{\theta, \phi, \psi, \Delta t} \left\{ \int dt \left| \hat{R}_z(\psi) \cdot \hat{R}_x(\phi) \cdot \hat{R}_z(\theta) \cdot \mathbf{F}(t + \Delta t) + \mathbf{F}(t) \right| \right\}}{\int dt |\mathbf{F}(t)|}, \quad (33)$$

where $\Delta t \in [0, T]$. Similarly, $\text{DOC}_{\text{light}} = 0$ if the field is not locally chiral. This measure quantifies how far away the light field is from one of the DSs that render it achiral. We note that, as in molecules, this definition is not unique.

We have calculated the DOC of the locally chiral field of Eq. (2) of the main text, as a function of ellipticity and the relative strength between the two colours $r = F_{2\omega}/F_\omega$, for $\phi_{\omega,2\omega} = \pi/2$, see Fig. 2. If $\varepsilon = 0$ or $r = 0$, then the field is not locally chiral, and thus $\text{DOC} = 0$. For small values of ε or r , the DOC increases linearly with both variables. Note that, for each value of r , there is an optimal $\varepsilon_0(r)$ that maximizes the DOC. For $\varepsilon > \varepsilon_0(r)$, the DOC decreases as ε increases, since the y field component (proportional to ε) becomes negligible for large values of $F_{2\omega}$.

V. ANOTHER EXAMPLE OF LOCALLY CHIRAL FIELD: COUNTER-ROTATING BI-ELLIPTICAL FIELD

The field shown in Fig. 1a,b of the main text is only one example of a locally chiral field. Fig. 3 presents an alternative locally chiral field that has different properties. This field results from combining two counter-rotating elliptically polarized drivers with frequencies ω and 2ω that propagate in different directions, with their polarization planes creating a small angle α . Near the focus, the electric fields can be written as [8]

$$\mathbf{F}_1(\mathbf{r}, t) = \frac{1}{2}F_{1,0} e^{-\rho_1^2/\tilde{\omega}^2} e^{i(\mathbf{k}_1 \cdot \mathbf{r} - \omega t - \delta_\omega)} (\hat{\mathbf{e}}_1 + i\varepsilon_1 \hat{\mathbf{z}}) + c.c. \quad (34)$$

$$\mathbf{F}_2(\mathbf{r}, t) = \frac{1}{2}F_{2,0} e^{-\rho_2^2/\tilde{\omega}^2} e^{i(\mathbf{k}_2 \cdot \mathbf{r} - 2\omega t - 2\delta_{2\omega})} (\hat{\mathbf{e}}_2 - i\varepsilon_2 \hat{\mathbf{z}}) + c.c. \quad (35)$$

where $F_{n,0}$ is the electric field amplitude, ε_n is the ellipticity, ρ_n is the radial distance to beams' axis, $\tilde{\omega}$ is the waist radius, the propagation vectors are defined as $\mathbf{k}_1 = k \sin(\alpha)\hat{\mathbf{x}} + k \cos(\alpha)\hat{\mathbf{y}}$ and $\mathbf{k}_2 = -2k \sin(\alpha)\hat{\mathbf{x}} + 2k \cos(\alpha)\hat{\mathbf{y}}$, where $k = \frac{2\pi}{\lambda}$, λ being the fundamental wavelength, and the polarization vectors are given by $\hat{\mathbf{e}}_1 = \cos(\alpha)\hat{\mathbf{x}} - \sin(\alpha)\hat{\mathbf{y}}$ and $\hat{\mathbf{e}}_2 = \cos(\alpha)\hat{\mathbf{x}} + \sin(\alpha)\hat{\mathbf{y}}$. The locally chiral field resulting from combining both beams can be written as

$$\mathbf{F}(\mathbf{r}, t) = F_0 e^{-\rho^2/\tilde{\omega}^2} [\mathbf{f}_1(\mathbf{r}, t) + \mathbf{f}_2(\mathbf{r}, t)] \quad (36)$$

where we have assumed $F_0 = F_{1,0} = F_{2,0}$ and that $\rho = \rho_1 \simeq \rho_2$ at the focus; \mathbf{f}_1 and \mathbf{f}_2 are

$$\mathbf{f}_1(\mathbf{r}, t) = \frac{1}{2}e^{i(\Phi_1 - \omega t)} (\hat{\mathbf{e}}_1 + i\varepsilon_1 \hat{\mathbf{z}}) + c.c. \quad (37)$$

$$\mathbf{f}_2(\mathbf{r}, t) = \frac{1}{2}e^{2i(\Phi_2 - \omega t)} (\hat{\mathbf{e}}_2 - i\varepsilon_2 \hat{\mathbf{z}}) + c.c. \quad (38)$$

with

$$\Phi_1 = k \sin(\alpha)x + k \cos(\alpha)y - \delta_\omega \quad (39)$$

$$\Phi_2 = -k \sin(\alpha)x + k \cos(\alpha)y - \delta_{2\omega} \quad (40)$$

The handedness of this locally chiral field depends on the relative phase between the two colours

$$\Delta\Phi = \Phi_2 - \Phi_1 = -2k \sin(\alpha)x + \delta_\omega - \delta_{2\omega} \quad (41)$$

This relative phase does not depend on the direction of light propagation y because $\frac{\mathbf{k}_1 \cdot \mathbf{y}}{\omega_1} = \frac{\mathbf{k}_2 \cdot \mathbf{y}}{\omega_2}$, but it depends on the transversal coordinate x , as $\frac{\mathbf{k}_1 \cdot \mathbf{x}}{\omega_1} \neq \frac{\mathbf{k}_2 \cdot \mathbf{x}}{\omega_2}$. Thus, the field handedness is not maintained globally in space, it changes along x . Changing $\Delta\Phi$ by $\pm\pi/2$ transforms the locally chiral field into its mirror image (Fig. 3b). This means that the field has opposite handedness at positions (x, y, z) and $(x + \Delta x, y', z')$, with $\Delta x = \frac{\lambda}{8 \sin(\alpha)}$.

In order to illustrate that this locally chiral field can drive enantio-sensitive response in chiral media, we have performed calculations for randomly oriented bromochlorofluoromethane molecules using a DFT-based model implemented in Octopus [9–11], as in [6]. We employed the Perdew-Burke-Ernzerhof exchange-correlation functional [12] of the generalized gradient approximation and pseudopotentials [13] for the Br, Cl, F, and C atoms.

Fig. 3c shows the single-molecule high harmonic response of enantiopure, randomly oriented media of left and right handed bromochlorofluoromethane molecules. To demonstrate enantiosensitivity in odd harmonic frequencies, we have applied a polarization filter and show the intensity of the z -polarized radiation. The calculated single-molecule high harmonic response shows extremely high degree of chiral dichroism in even and odd harmonic orders, reaching 60%. The error bars at the level of 18% are associated with limited number of molecular orientations used for averaging over orientations. The extreme computational cost of these calculations makes optimization of enantio-sensitive response prohibitively expensive. In contrast to the field in Fig. 1a, this field is not globally chiral, as its handedness periodically alternates in space, see below.

A. Analysis of local and global handedness of the counter-rotating bi-elliptical field.

Here we apply the chiral correlation function $h^{(5)}$ (see Eq. (16)) to illustrate the properties of the locally chiral field in Eq. (36) from this perspective. The analysis of the field correlation function $h^{(5)}$ shows that this locally chiral field carries different elements of chirality, which manifest itself in two types of correlation functions. (see Eq. (17))

$$h_a^{(5)} = h^{(5)}(-2\omega, -\omega, \omega, \omega, \omega) \quad (42)$$

$$h_b^{(5)} = h^{(5)}(-\omega, -2\omega, 2\omega, 2\omega, -\omega) \quad (43)$$

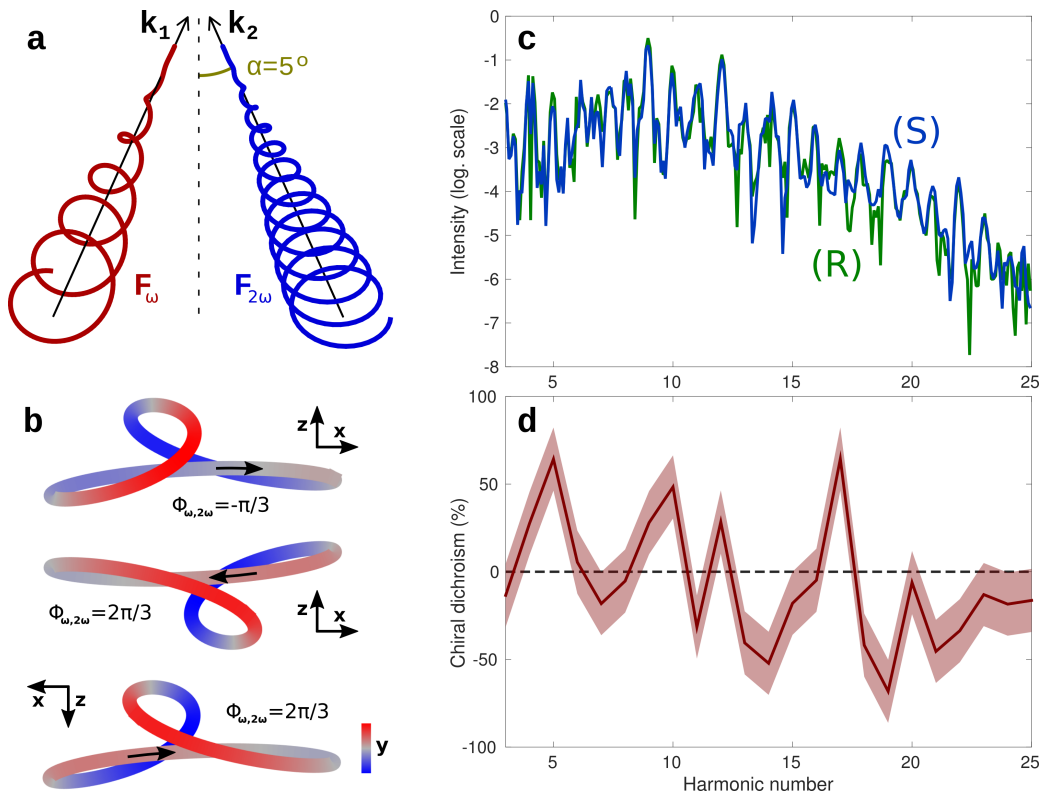


FIG. 3. Enantio-sensitive HHG in randomly oriented CBrClFH molecules. Two counter-rotating elliptically polarized ω and 2ω fields (a) generate the locally chiral field shown in panel b, for $\phi_{\omega,2\omega} = -\pi/3$ (upper image) and $2\pi/3$ (central and bottom images). The bottom image has been rotated 180° around the y axis to show that the fields for $\phi_{\omega,2\omega} = -\pi/3, 2\pi/3$ are mirror images. c) z -polarized harmonic intensity in opposite enantiomers of CBrClFH for $\lambda = 1500$ nm, $I_{max} = 1.2 \times 10^{13}$ W/cm 2 , $\phi_{\omega,2\omega} = 2\pi/3$, $\varepsilon_1 = 0.4$, $\varepsilon_2 = 0.3$, $\alpha = 5^\circ$, and a trapezoidal envelope with 4 cycle turn-on/off and 3 cycle flat-top. d) Chiral dichroism in the harmonic intensity. An error of $\pm 18\%$ is estimated based on convergence with the number of orientations.

Other options are related to either of these two by a change of sign, by complex conjugation, or by both as discussed in Methods. Note that the second option was not available for the field discussed in the main text because this option requires the 2ω field to be elliptically polarized. Furthermore, it requires more than one 2ω photon. Replacing Eq. (36) in Eqs. (42) and (43) yields

$$h_a^{(5)} = 2i \left(\frac{F_0}{2} \right)^5 \varepsilon_1 (1 - \varepsilon_1^2) \sin(2\alpha) e^{i[4kx \sin \alpha + 2(\delta_{2\omega} - \delta_\omega)]}, \quad (44)$$

$$h_b^{(5)} = -2i \left(\frac{F_0}{2} \right)^5 \varepsilon_2 \sin(2\alpha) [\cos(2\alpha) + \varepsilon_1 \varepsilon_2] e^{i[-4kx \sin \alpha - 2(\delta_{2\omega} - \delta_\omega)]}. \quad (45)$$

Interestingly, $h_a^{(5)}$ is independent of the ellipticity of the 2ω beam. We can also see from these expressions that we can obtain a locally chiral field with a unique $h^{(5)}$ by setting either of the two ellipticities to zero. That is, the fields with either ε_1 or ε_2 equal to zero are also locally chiral. Two different versions of $h^{(5)}$ mean that the field displays chirality at two different levels, i.e. like a helix made of a tighter helix. Finally, from these expressions it is clear that $h_a^{(5)}$ and $h_b^{(5)}$ oscillate as a function of x with a frequency $4k \sin \alpha$, in agreement with the reasoning in the previous section. Consequently, this field is not globally chiral.

-
- [1] A. F. Ordonez and O. Smirnova, Generalized perspective on chiral measurements without magnetic interactions, *Phys. Rev. A* **98**, 063428 (2018).
 [2] D. L. Andrews and T. Thirunamachandran, On three-dimensional rotational averages, *J. Chem. Phys.* **67**, 5026 (1977).
 [3] P. Fischer and F. Hache, Nonlinear optical spectroscopy of chiral molecules, *Chirality* **17**, 421 (2005).

- [4] D. M. Bishop, *Group Theory and Chemistry* (Dover Publications, Oxford, 1993).
- [5] O. Neufeld, D. Podolsky, and O. Cohen, Floquet group theory and its application to selection rules in harmonic generation, *Nat. Commun.* **10**, 405 (2019).
- [6] O. Neufeld, D. Ayuso, P. Decleva, M. Y. Ivanov, O. Smirnova, and O. Cohen, Ultrasensitive chiral spectroscopy by dynamical symmetry breaking in high harmonic generation, *Phys. Rev. X* **9**, 031002 (2019).
- [7] T. P. E. Auf der heyde, A. B. Buda, and K. Mislow, Desymmetrization and degree of chirality, *J. Math. Chem.* **6**, 255 (1991).
- [8] R. W. Boyd, *Nonlinear Optics*, 3rd ed. (Academic Press, Burlington, 2008) pp. 605 – 613.
- [9] M. A. Marques, A. Castro, G. F. Bertsch, and A. Rubio, Octopus: a first-principles tool for excited electron–ion dynamics, *Comput. Phys. Commun.* **151**, 60 (2003).
- [10] X. Andrade, D. Strubbe, U. De Giovannini, A. H. Larsen, M. J. T. Oliveira, J. Alberdi-Rodriguez, A. Varas, I. Theophilou, N. Helbig, M. J. Verstraete, L. Stella, F. Nogueira, A. Aspuru-Guzik, A. Castro, M. A. L. Marques, and A. Rubio, Real-space grids and the octopus code as tools for the development of new simulation approaches for electronic systems, *Phys. Chem. Chem. Phys.* **17**, 31371 (2015).
- [11] A. Castro, H. Appel, M. Oliveira, C. A. Rozzi, X. Andrade, F. Lorenzen, M. A. L. Marques, E. K. U. Gross, and A. Rubio, Octopus: a tool for the application of time-dependent density functional theory, *Phys. Status Solidi B* **243**, 2465 (2006).
- [12] J. P. Perdew, K. Burke, and M. Ernzerhof, Generalized gradient approximation made simple, *Phys. Rev. Lett.* **77**, 3865 (1996).
- [13] M. Schlipf and F. Gygi, Optimization algorithm for the generation of oncv pseudopotentials, *Comput. Phys. Commun.* **196**, 36 (2015).